Investigation of Early Signaling Mechanisms in Plant Osmotic Stress Response

By

Kelly E. Stecker

A dissertation submitted in partial fulfillment of

the requirements for the degree of

Doctor of Philosophy

(Biochemistry)

at the

UNIVERSITY OF WISCONSIN – MADISON

2016

Date of final oral examination: 2/26/2016

The dissertation is approved by the following members of the Final Oral Committee:
Michael R. Sussman, Professor, Biochemistry
Richard M. Amasino, Professor, Biochemistry
Brian G. Fox, Professor, Biochemistry
Patrick H. Masson, Professor, Genetics
Patrick J. Krysan, Associate Professor, Horticulture

Investigation of Early Signaling Mechanisms in Plant Osmotic Stress Response

Kelly E. Stecker
Under the supervision of Professor Michael R. Sussman
University of Wisconsin – Madison

ABSTRACT

How plants perceive and respond to water loss on a molecular level is a fundamental question in plant biology. Understanding the cellular signaling mechanism involved in sensing dehydration and initiating adaptive responses provides a tool for plant biologists to use in engineering crops with enhanced drought tolerance and water use efficiency as well as with developing new chemical approaches towards alleviating the negative effects of drought on crop yields. The increasing frequency and severity of drought, along with the depletion of fresh water resources, fortifies the need to understand the molecular networks that control drought response in plants.

Currently the molecular mechanisms involved in the initial perception of dehydration are poorly understood. In this dissertation I present my work towards identifying previously unknown proteins involved in the initial dehydration response, using mass spectrometry based quantitative proteomic and reverse genetic approaches. Employing the model system *Arabidopsis thaliana* and hyperosmotic stress conditions to simulate water loss, I first identified proteins whose level of phosphorylation changes in response to short-term stress treatments, using quantitative untargeted mass spectrometry based phosphoproteomics technologies. From this work I identified proteins whose phosphorylation state changed within 5 minutes of stress treatment. To further characterize these proteins, I developed

targeted proteomic assays to more routinely measure protein phosphorylated across many biotic and abiotic stress conditions. From this analysis I characterized a set of proteins that are uniquely regulated at the posttranslational level by rapid dehydration. These proteins are involved in cellular process such as mRNA degradation, microtubule restructuring, transcription factor activation, phospholipid signaling, and mitogen-activated protein kinase signaling and help elucidate the role that these processes play in the initial dehydration response. This work is presented in Chapter 2 of my dissertation.

To validate the biological significance of proteins identified in my phosphoproteome analysis, I used reverse genetics to investigate Vac14, an uncharacterized protein in plants that displayed the largest change in phosphorylation under osmotic stress conditions. Vac14 is a highly conserved protein involved in the biosynthesis of the low abundant phospholipid phosphatidylinositol-3,5 bisphosphate, which regulates vacuole function and endomembrane vesicle transport in yeast and mammals. I demonstrate that Vac14 is an essential gene in plants and is responsible for regulating water homeostasis in cells. Vac14 overexpression mutants have increased drought tolerance and improved ability to germinate under water-limited conditions. This work is presented in Chapter 3 and supports the biological significance of proteins identified in my discovery phosphoproteomic work in Chapter 2.

Finally, in Chapter 4 I describe my preliminary results in developing a new method for detecting proteins involved in cell signaling events through direct measurement of protein conformational changes. This method uses thermal denaturation profiling and untargeted quantitative mass spectrometry to identify proteins whose conformation has changed in response to *in vitro* or *in vivo* treatment conditions. Together, the data presented in this thesis demonstrate the utility of mass spectrometric based proteomic technologies for discovering

previously unidentified proteins involved in cell signaling events and provides valuable insight into pathways activated during the initial few minutes of the osmotic stress response in plants.

ACKNOWLEDGMENTS

I would like to thank all of the people who have helped me through graduate school personally and professionally. To my advisor Mike Sussman, thank you for your endless positive support and for having confidence in me from the beginning. To my fellow Sussman Lab members, thank you for all of the guidance you have provided during my graduate studies. I would like to thank Greg Barrett-Wilt and Greg Sabat in the mass spec facility for the countless hours of discussion and troubleshooting. I would like to thank Lindsay Traeger for being my coworker, bench mate, personal councilor, and good friend. Thank you to Magdalena Murray, who has been such a help in conducing my genetic research. I would also like to thank my committee and for their advice and guidance through the years.

I could not have made it through graduate school without the constant support of my parents, Lisa and Greg. I don't know what I would do without them. Thank you also to my Wisconsin relatives who have adopted me during my time in Madison and really taught me the definition of work hard play hard. Thank you to my Madison friends for bringing me joy over the years. A special thanks to Colin Smith who has supported me through many life transitions.

I would also like to thank the NSF for funding my graduate research and giving me the opportunity to work aboard at the University of Amsterdam. This NSF supported experience has changed my trajectory in science and I look forward to the new challenges to come.

.

TABLE OF CONTENTS

TABLE OF FIGURES

Chapter 2

Chapter 3

Chapter 4

Appendix 1

Appendix 2

LIST OF TABLES

CHAPTER 1

Introduction: Initial Hyperosmotic Stress Response in Plants

Introduction

Plant growth and productivity is inexorably linked to sufficient water supply, making limited water availability one of the premier threats to agricultural productivity (1). In fact, drought represents one of the most significant causes of reduced crop yield worldwide. In the United States, drought conditions in 2012 resulted in a 25% reduction in corn yield, leading to economic losses estimated in the billions (2). With the rise of global temperatures, the frequency and severity of drought is only predicted to increase. This fact, in combination with the depletion of fresh water resources, presents an extensive problem for agriculture productivity in the future. Understanding how plants sense and respond to water loss is paramount for our ability to engineer crops with improved drought tolerance and water use efficiency.

Although drought has been a longstanding research focus, little is known about the initial signaling mechanisms plants use to sense and respond to water loss. Efforts to investigate initial drought sensing in the laboratory often utilize hyperosmotic growth conditions to simulate water loss in an isolated setting where variables can be controlled more readily. Cellular water loss induced by hyperosmotic stress, herein referred to as osmotic stress, differs from drought conditions in several significant ways but provides a valuable tool for initiating dehydration and examining rapid cellular responses (3). Non-membrane permeable solutes such as mannitol draw water out of cells, causing reduced water availability. These conditions function as a first approximation for situations of low water potential encountered by plants in their natural environment, such as drying soil or the surface of a leaf on a hot arid day.

It is known that environments of low water potential cause a loss of turgor pressure in plant cells. Turgor pressure, which is the pressure exerted by the protoplast against the cell wall, is the primary driving force behind plant growth and movement and is actively maintained by high solute concentrations in the cytoplasm and vacuole (4). Changes in turgor are also the driving force behind the opening and closing of gas exchanging pores in leaves called stomata. The stomatal pore is regulated by the loss or gain of turgor pressure in guard cells. Thus, when plants experience drought, this causes the guard cells (and all other cells) to lose turgor, resulting in the closure of stomatal pores (5). This is one of the first avoidance mechanism plants employ to mitigate water loss.

Changes in turgor are hypothesized to function as a signal to actively down regulate growth in water limited environments. It is known that plant growth is restricted in the presence of reduced water availability, even when carbon resources are not limiting and water stress is mild; however, the mechanisms by which turgor changes are perceived and signaled are not known (6). Although there are some components of downstream signaling pathways that are known, we are far from understanding the details by which signal transduction proceeds once a plant cell recognizes there is a reduction in water supply. Since the plasma membrane of yeast and higher plants is so similar, with the proton pump acting as the major energy source that creates a large protonmotive force that drives solute transport, it is reasonable to examine what is known about osmotic stress sensing in yeast. Examination of yeast systems may provide additional insight into signaling mechanisms that are shared by these two organisms, whose cells experience high turgor as they are both surrounded by an inflexible cell wall.

Osmotic stress response in yeast

The molecular mechanism of osmotic stress perception and signal transduction has been extensively studied in yeast (7). The hyperosmotic stress signaling pathway of *Saccharomyces cereviciae* relies on two parallel signaling pathways that converge upon a mitogen activated protein kinase (MAPK) signaling cascade. This MAPK cascade ultimately activates the MAPK Hog1 (High osmolariry Gycerol response 1) protein, a master regulator that translocates to the nucleus upon activation and drives transcriptional changes under osmotic stress conditions (8). The Hog1 activating pathways are controlled by two different osmosensors Sln1 and Sho1. Sln1 is a histidine kinase that participates in a two-component phosphor-relay system to activate downstream MAPK proteins. The mechanisms of Sln1 osmosensing is thought to be achieved through an essential trans-membrane domain and ectodomain interaction with specific cell wall components (9, 10). The osmosensor Sho1 forms a high order homo-oligomeric structure in the plasma membrane and performs its osmosensing function through osmotic stress induced conformational changes to transmembrane domains that mediate new protein-protein interactions with downstream signaling components (11).

There is evidence to suggest that parallels to Sln1 osmosensing exist in plants. In *Arabidopsis* Athk1 is a homologue of Sln1 and has been considered a putative osmosensor based on drought sensitive mutant phenotypes and yeast complementation assays (12, 13). However, more recent reports have suggested other functions for Athk1 (14). Though the identity of plant osmosensors are not known, plants may be employing similar physiochemical concepts of cell wall to plasma membrane connections or transmembrane domain conformation changes to sense turgor status in cells. One such example of a

transmembrane protein with conformational states sensitive to osmolality is the recently identified hyperosmolality-gated calcium channel OSCA1 (15). OSCA1 is proposed to operate as a plasma membrane-localized osmosensor in Arabidopsis through triggering osmotically induced calcium increases (15). However, proof of bona fide osmosensing function is challenging and the cellular mechanism for plant osmosensing continues to remain largely elusive (6).

ABA response

Though an initial osmo-sensing signaling pathway is not well defined in plants, significant progress has been made in outlining the signaling mechanisms associated with the primary hormone involved in signaling the presence of drought and low water status, abscisic acid (ABA). ABA controls the cellular response to water loss through the activation of subfamily 2 sucrose nonfermenting1-related kinases (SnRK2). In the absence of ABA, clade A protein phosphatase 2Cs (PP2C) suppress SnRK2 autophosphorylation, keeping SnRK2s in an inactive state (16, 17). In the presence of ABA, PP2C suppression is relieved and SnRK2s become active, phosphorylating known downstream targets, including transcription factors that bind to ABA-responsive elements (AREBs) and ion channels (18-20). ABA is capable of relieving PP2C mediated SnRK2 inhibition because the ABA-receptor complex directly binds and inhibits PP2Cs. Therefore, negative regulation of a negative regulator results is activation of the downstream phosphorylation cascades.

Defining the mechanistic details of ABA perception, which acts through soluble receptors that negatively regulate PP2Cs and activate SnRK2 phosphorylation, has been a landmark discovery that has recently provided new avenues for achieving further progress in the field of abiotic stress research. Structural understanding of ABA receptors has led to new

strategies for engineering enhanced water use efficiency traits in crop species (21). However, significant questions surrounding ABA signaling still remain unanswered. For example, the onset of endogenous ABA accumulation in response to water loss occurs on the order of 0.5-2 hours (22), leaving open still the question of how dehydration is initially sensed. Furthermore, it is unknown what regulatory mechanisms are responsible for initiating ABA accumulation. More work needs to be done to define rapid stress response pathways that occur within minutes after dehydration occurs, i.e., preceding the later ABA mediated signaling that is well defined in plants.

Kinases implicated in osmotic stress response

Protein kinases act as positive regulators of signal transduction in both yeast osmosensing and ABA signaling. The SnRK2 kinases activated in ABA signaling are part of a 10-member family. In addition to SnRK2 kinases participating in the core ABA signaling pathway, this family contains kinases that are implicated in early osmotic stress signaling that are thought to be independent of ABA (23-27). Among these are SnRK2.4 and SnRK2.10, which are some of earliest kinases to be activated in response to osmotic stress. In-gel kinases assays show SnRK2.4 activation after only 1 minute of NaCl treatment (25). Phosphorylation targets of SnRK2.4 and SnRK2.10 are not yet known, but mutant analysis reveals that kinases affect levels of proline accumulation and root growth under stress conditions (23, 25, 27). SnRK2.4 and 2.10 have been shown to bind phosphatidic acid and therefor may be stimulated under dehydration conditions by lipid signaling events (28).

Another kinase family likely involved in initial osmotic stress signaling events are MAPKs. MAPK proteins canonically function in a phosphorylation hierarchy where MAP kinase kinase kinase proteins activate downstream MAP kinase kinase proteins, which then

act on MAP kinases (29). An additional MAPK family, MAPKKKK (MAP4K), can be placed at the top of the signaling hierarchy, however very little is known about the function of this protein group in plants (30). The *Arabidopsis* MAPK family is very complex, consisting of 10 MAPKKKK, 60 MAPKKK, 10 MAPKK, and 20 MAPK genes (29). Through null mutant analysis and protein overexpression studies, various MAPK family members have shown osmotic stress-sensitive phenotypes and appear to function as both positive and negative regulators of drought stress signaling, depending on the gene (31). For example, Arabidopsis MAPKKK20 mutants demonstrate increased NaCl and osmotic stress sensitivity while overexpression lines show improved tolerance under similar conditions (32). Furthermore, mapkkk20 mutants had reduced MPK6 activation under stress conditions, as measured by *in vitro* kinase activity (32). MPK6 is known to phosphorylate 5'mRNA decapping enzymes involved in mRNA degradation during dehydration stress. Phosphorylation of the decapping enzyme enhances rates of mRNA degradation (33). These observations demonstrate that MAPK proteins play important roles during water stress. However, a central MAPK cascade has not yet emerged as the primary regulators of osmotic response, as is the case with the Ste20/Ste11/Pbs2/Hog1 MAPK cascade in yeast.

A third class of kinases involved in rapid osmotic stress response is calcium dependent protein kinases. Mannitol stress has been shown to cause cytosolic calcium levels to rapidly spike and reach a peak within approximately 30 seconds after drought stimulus in root endodermal tissue (34). Though cytosolic calcium increases are a general response to stresses such as touch, cold and drought, cellular interpretations, i.e., the signaling transduction pathway utilized, are believed to be elicitor specific (35). Specificity is partially achieved through phosphorylation events directed by different calcium dependent protein

kinases (CPKs) and cacinuirin B-like proteins (CBLs) binding to CBL-interacting protein kinases (CIPKs). Genetic evidence exists for CPK involvement in osmotic stress response. Null mutations in closely related CPK21 and CPK23 genes resulted in improved growth on high osmolyte media, indicating that these genes may function as negative regulators of osmo-stress response (36, 37). In guard cells CPK6, CPK21, and CPK23 activate anion channel SLAC1 to promote stomata closure in response to dehydration (38). Interestingly, quadruple mutants in cpk6/5/21/23 genes impair ABA signal transduction in guard cells as well, indicating significant crosstalk between hormone and Ca^{2+} signaling pathways (39).

Similar to the complexity observed in MAPK families, the CPK and CIPK gene families together comprise more than 60 genes in Arabidopsis (40). The complexity of MAPK and calcium dependent kinase networks speaks to the pivotal role phosphorylation plays in transducing stress signals. This fact underscores the need to investigate osmotic stress response at the post-translational level to understand relevant cellular dehydration signaling networks.

Second messengers involved in osmotic stress response.

The cytosolic calcium bursts activating CPKs during stress response is an example of a second messenger that functions to initiate cellular responses and prime cells during stress signaling. Several second messengers are thought to play important roles during osmotic stress signaling. In addition to cytosolic calcium increases, reactive oxygen species (ROS) and inositol phospholipids represent classes of second messengers that are also active during osmotic stress response.

ROS accumulate during stress conditions when metabolic pathways become uncoupled, and imbalances between ROS production and ROS scavenging occur (41). ROS

imbalances in cells are responsible for cellular damage through oxidizing proteins and lipids, but they are also thought to simultaneously function as signals, activating stress response pathways and making cells more stress tolerant (41). Several experiments have show that H_2O_2 pretreatment of plants makes them more tolerant of osmotic and drought stress conditions (42, 43). The duel nature of ROS damaging effect and signaling function indicate that steady state levels of ROS are tightly controlled in cells. Similar to cytosolic Ca^{2+} spiking, ROS increases are associated with many biotic and abiotic stress conditions. Despite the generic nature of stress induced ROS accumulation, ROS responsive genes give unique expression signatures based on the type of stress being experienced (44). This indicates that specific signal transduction pathways exist to transduce ROS signals to cellular responses during osmotic stress.

Phosphorylated inositol phospholipid (PIP) molecules in lipid bilayers are also thought to be involved in initial signal transduction events associated with osmotic stress response. Both PIPs and their phosphorylated derivatives, PIP_2, function not only as signaling molecules but also as substrates for cleavage by phospholipase enzymes (45). Phospholipase C (PLC) cleaves PIP/PIP_2 molecules to generate soluble polyphosphoinositides and membrane retained diacyl glycerol (DAG), which is rapidly converted to phosphatidic acid (PA) (46). PA is also be generated through cleavage of structural phospholipids by phospholipase D (PLD) enzymes. Genetic manipulation of PLC, PLD, and PI4P-5 kinase family members produce phenotypes that are associated with osmotic stress, salinity stress, ABA signaling, and drought sensitivity phenotypes (46-49). Additionally, PA and PIP_2 species PI(4,5)P2 and PI(3,5)P2 have all been documented to rapidly increase in response to salt and osmotic stress (46, 50). These accumulated findings

support a significant role for phospholipid signaling during osmotic stress response.

Additional physiological responses associated with osmotic stress

In addition to increases in kinase activity and second messengers, several cellular responses have been associated with initial osmotic stress response in plants. These include restructuring of the microtubule cytoskeleton, changes in ion flux and subcellular pH, and changes in mRNA metabolism and rates of translation.

Observations of cytoskeleton networks under osmotic stress condition reveal a relationship between cellular turgor and microtubule (MT) polymerization. In guard cells it has been shown that MTs rapidly depolymerize during turgor mediated stomata closure and that this event is essential for correct guard cell behavior (51). Guard cell tubulin is actively targeted for degradation by COP1 E3 ubiquitin ligase complex during stomata closure (52). Furthermore, use of MT stabilizing and destabilizing drugs greatly affected rates of stomata closure and opening, respectively. The same relationship has been observed in roots where MT stabilization prevented seedling survival on mannitol high salt media (53, 54). In response to osmotic stress tubulin was shown to be phosphorylated at its protein dimer interface. The resulting phosphorylated protein isoforms are unable to polymerize, thus positively reinforcing MT depolymerization in response to stress (55). Taken together, these findings indicate that MT depolarization is an important cellular response to osmotic stress, but whether it plays an active role in sensing or signal transduction remains unclear.

Control of ion transport in cells is another key element of regulating turgor and responding to osmotic stress. In guard cells that surround the stomatal pore, loss of turgor is controlled through activation of anion efflux carriers. Anion efflux triggers plasma membrane depolarization events that result in further ion efflux through activation of

outward rectifying voltage-gated K^+ channels (56, 57). These regulated ion efflux events draw water out of guard cells and allow stomata pores to adopt a closed state.

In tissues other than guard cells, osmotic stress has been shown to have the opposite effect on plasma membrane polarity and ion flux. In root epidermal cells, osmotic stress caused plasma membrane hyperpolarization and K+ influx within the first few minutes of mannitol treatment. These ion influx events draw water back into cells and allow cellular turgor to recover (58). The turgor recovery driven by ion influx is believed to far precede accumulation of compatible solutes, which act to lower cellular water potential and are attributed to long-term osmotic adaption, a phenomenon first established in experiments with lower eukaryotes such as *E. coli*.

Control of the apoplastic, cytoplasmic and vacuolar pH via proton transport has also been proposed to be an important signaling event during osmotic stress response. In guard cells, vacuole acidification and cytosolic alkalization are required steps for ABA mediated stomata closure. Knockout mutations in plasma membrane K+/H+ efflux symporters cause enhanced drought sensitivity and impaired ABA and osmotic stress response, indicating that these transporters are positive regulators of normal osmotic stress signaling (59). Similarly, mutations in genes encoding vacuole localized Na+, K+/H+ antiporters cause impaired stomata regulation and reduced drought tolerance (60). In both of these examples, improper pH regulation of the vacuole and cytoplasm resulted in impaired osmotic stress response. Interestingly, osmotic stress induced ABA accumulation has been shown to be dependent on vacuole and endomembrane pH (61). A mutation in the vacuole sorting receptor VSR1 caused an inability to activate ABA biosynthesis upon osmotic stress treatment and this result was due to defects in endomembrane pH (61). This recent finding supports an essential role

for pH changes in triggering cell-signaling events during osmotic stress response.

Finally, osmotic stress response has been associated with changes in mRNA processing. Transcripts in the cell exist in mRNA-protein complexes (mRNP) that can adopt different rates of translation depending on the proteins present in the complex (62). Actively transcribed mRNP are associated with polysomes while quiescent transcripts and transcripts primed for degradation are associated in processing bodies (PB) and stress granules (62). Osmotic stress has been shown to cause changes in mRNP states, shifting transcripts away from actively translating polysomes into inactive PB and stress granules (63, 64). These changes result in targeted degradation of mRNA transcripts and represent a mechanism of stress induced post-transcriptional control in cells. In addition to altered rates of translation and mRNA degradation, alternate splicing of mRNAs has been shown to increase with osmotic stress. Deep sequencing of mRNA in a time-course analysis revealed that osmotic stress and salt treatment induced alternative splicing of hundreds of genes (65). Together these findings indicate that significant changes in translation occur during the initial osmotic stress response.

The challenge of deciphering molecular mechanisms of osmotic stress response

Osmotic stress invokes a broad range of cellular responses that share significant overlap with other forms of biotic and abiotic stress. A great challenge of understanding the initial osmotic stress response is identifying how cells translate ubiquitous stress signals into tailored outcomes that ultimately protect the plant against water loss. A key to identifying proteins involved in this complex response network is to examine signaling events occurring very early on. By looking at cellular response in the first few minutes of stress, specific signatures of protein activation can be identified. This analysis requires examining stress

response at the level of protein post-translation modifications since such modifications are known to play pivotal roles in signal transduction, and changes in protein synthesis are unlikely to be occurring on this time scale. Part of the difficulty in defining osmotic stress signaling pathways in plants has been that most research approaches in this area primarily focuses on genetic and transcriptional analysis. However, the genetic redundancy and complexity of gene families implicated in osmotic stress signal transduction severely impairs the ability of forward and reverse genetic strategies to identify candidate genes involved in early signaling events. Compounding this fact, the post-transcriptional and post-translational mechanisms of early abiotic stress response limit the utility of transcriptional studies (66). For example, a study comparing protein to transcript abundance after NaCl treatment in *Arabidopsis* roots yielded an R^2 correlation value of -0.1 (67), indicating that transcriptional changes may not be a good proxy for short-term stress response.

To implicate new genes in osmotic stress signal transduction pathways it is important to examine responses at the protein level. Furthermore, to understand early signaling events, it is important to look at post-translational modifications (PTMs) of proteins. Mass spectrometry-based analysis of proteins provides an unparalleled tool for identifying regulatory protein PTM events that occur in stress responsive signal transduction pathways. Given the fact that the protein kinase gene family is the largest single family in the plant genome, it is reasonable to suspect that protein phosphorylation plays a critical part of the early signaling pathway during osmotic stress perception and response in plants. For this reason, exploratory quantitative proteomic studies are a necessary first step to identify candidate genes involved stress response and have the potential to help define the very first components required for osmotic stress sensing and signaling network in plants.

References

1. Nuccio ML*, et al.* (2015) Expression of trehalose-6-phosphate phosphatase in maize ears improves yield in well-watered and drought conditions. *Nature Biotechnology* 33(8):862-869.

2. Elliott J*, et al.* (2013) Predicting agricultural impacts of large-scale drought: 2012 and the case for better modeling.

3. Verslues PE, Agarwal M, Katiyar-Agarwal S, Zhu J, & Zhu JK (2006) Methods and concepts in quantifying resistance to drought, salt and freezing, abiotic stresses that affect plant water status. *Plant J* 45(4):523-539.

4. Zonia L & Munnik T (2007) Life under pressure: hydrostatic pressure in cell growth and function. *Trends Plant Sci* 12(3):90-97.

5. Zhu JK (2002) Salt and drought stress signal transduction in plants. *Annu Rev Plant Biol* 53:247-273.

6. Haswell ES & Verslues PE (2015) The ongoing search for the molecular basis of plant osmosensing. *J Gen Physiol* 145(5):389-394.

7. Hohmann S (2002) Osmotic stress signaling and osmoadaptation in yeasts. *Microbiol Mol Biol Rev* 66(2):300-372.

8. Bahn YS (2008) Master and commander in fungal pathogens: the two-component system and the HOG signaling pathway. *Eukaryot Cell* 7(12):2017-2036.

9. Shankarnarayan S, Malone CL, Deschenes RJ, & Fassler JS (2008) Modulation of yeast Sln1 kinase activity by the CCW12 cell wall protein. *J Biol Chem* 283(4):1962-1973.

10. Tao W, Malone CL, Ault AD, Deschenes RJ, & Fassler JS (2002) A cytoplasmic coiled-coil domain is required for histidine kinase activity of the yeast osmosensor, SLN1. *Mol Microbiol* 43(2):459-473.

11. Tatebayashi K*, et al.* (2015) Osmosensing and scaffolding functions of the oligomeric four-transmembrane domain osmosensor Sho1. *Nat Commun* 6:6975.

12. Wohlbach DJ, Quirino BF, & Sussman MR (2008) Analysis of the Arabidopsis histidine kinase ATHK1 reveals a connection between vegetative osmotic stress sensing and seed maturation. *Plant Cell* 20(4):1101-1117.

13. Urao T*, et al.* (1999) A transmembrane hybrid-type histidine kinase in Arabidopsis functions as an osmosensor. *Plant Cell* 11(9):1743-1754.

14. Kumar MN, Jane WN, & Verslues PE (2013) Role of the putative osmosensor Arabidopsis histidine kinase1 in dehydration avoidance and low-water-potential response. *Plant Physiol* 161(2):942-953.

15. Yuan F*, et al.* (2014) OSCA1 mediates osmotic-stress-evoked Ca2+ increases vital for osmosensing in Arabidopsis. *Nature* 514(7522):367-371.

16. Park SY*, et al.* (2009) Abscisic acid inhibits type 2C protein phosphatases via the PYR/PYL family of START proteins. *Science* 324(5930):1068-1071.

17. Umezawa T*, et al.* (2009) Type 2C protein phosphatases directly regulate abscisic acid-activated protein kinases in Arabidopsis. *Proc Natl Acad Sci U S A* 106(41):17588-17593.

18. Geiger D*, et al.* (2009) Activity of guard cell anion channel SLAC1 is controlled by drought-stress signaling kinase-phosphatase pair. *Proc Natl Acad Sci U S A* 106(50):21425-21430.

19. Sato A*, et al.* (2009) Threonine at position 306 of the KAT1 potassium channel is essential for channel activity and is a target site for ABA-activated SnRK2/OST1/SnRK2.6 protein kinase. *Biochem J* 424(3):439-448.

20. Yoshida T*, et al.* (2010) AREB1, AREB2, and ABF3 are master transcription factors that cooperatively regulate ABRE-dependent ABA signaling involved in drought stress tolerance and require ABA for full activation. *Plant J* 61(4):672-685.

21. Okamoto M*, et al.* (2013) Activation of dimeric ABA receptors elicits guard cell closure, ABA-regulated gene expression, and drought tolerance. *Proc Natl Acad Sci U S A* 110(29):12132-12137.

22. Waadt R*, et al.* (2014) FRET-based reporters for the direct visualization of abscisic acid concentration changes and distribution in Arabidopsis. *Elife* 3:e01739.

23. Fujii H, Verslues PE, & Zhu JK (2011) Arabidopsis decuple mutant reveals the importance of SnRK2 kinases in osmotic stress responses in vivo. *Proc Natl Acad Sci U S A* 108(4):1717-1722.

24. Fujii H & Zhu JK (2009) Arabidopsis mutant deficient in 3 abscisic acid-activated protein kinases reveals critical roles in growth, reproduction, and stress. *Proc Natl Acad Sci U S A* 106(20):8380-8385.

25. McLoughlin F*, et al.* (2012) The Snf1-related protein kinases SnRK2.4 and SnRK2.10 are involved in maintenance of root system architecture during salt stress. *Plant J* 72(3):436-449.

26. Boudsocq M, Barbier-Brygoo H, & Lauriere C (2004) Identification of nine sucrose nonfermenting 1-related protein kinases 2 activated by hyperosmotic and saline stresses in Arabidopsis thaliana. *J Biol Chem* 279(40):41758-41766.

27. Mao X, Zhang H, Tian S, Chang X, & Jing R (2010) TaSnRK2.4, an SNF1-type serine/threonine protein kinase of wheat (Triticum aestivum L.), confers enhanced multistress tolerance in Arabidopsis. *J Exp Bot* 61(3):683-696.

28. Julkowska MM*, et al.* (2015) Identification and functional characterization of the Arabidopsis Snf1-related protein kinase SnRK2.4 phosphatidic acid-binding domain. *Plant Cell Environ* 38(3):614-624.

29. Ichimura K*, et al.* (2002) Mitogen-activated protein kinase cascades in plants: a new nomenclature. *Trends in plant science* 7(7):301-308.

30. Champion A, Picaud A, & Henry Y (2004) Reassessing the MAP3K and MAP4K relationships. *Trends Plant Sci* 9(3):123-129.

31. Moustafa K, AbuQamar S, Jarrar M, Al-Rajab AJ, & Tremouillaux-Guiller J (2014) MAPK cascades and major abiotic stresses. *Plant Cell Rep* 33(8):1217-1225.

32. Kim JM*, et al.* (2012) Arabidopsis MKKK20 is involved in osmotic stress response via regulation of MPK6 activity. *Plant Cell Rep* 31(1):217-224.

33. Xu J & Chua NH (2012) Dehydration stress activates Arabidopsis MPK6 to signal DCP1 phosphorylation. *EMBO J* 31(8):1975-1984.

34. Kiegle E, Moore CA, Haseloff J, Tester MA, & Knight MR (2000) Cell-type-specific calcium responses to drought, salt and cold in the Arabidopsis root. *Plant J* 23(2):267-278.

35. Gilroy S*, et al.* (2014) A tidal wave of signals: calcium and ROS at the forefront of rapid systemic signaling. *Trends Plant Sci* 19(10):623-630.

36. Franz S*, et al.* (2011) Calcium-dependent protein kinase CPK21 functions in abiotic stress response in Arabidopsis thaliana. *Mol Plant* 4(1):83-96.

37. Ma SY & Wu WH (2007) AtCPK23 functions in Arabidopsis responses to drought and salt stresses. *Plant Mol Biol* 65(4):511-518.

38. Brandt B*, et al.* (2012) Reconstitution of abscisic acid activation of SLAC1 anion channel by CPK6 and OST1 kinases and branched ABI1 PP2C phosphatase action. *Proc Natl Acad Sci U S A* 109(26):10593-10598.

39. Brandt B*, et al.* (2015) Calcium specificity signaling mechanisms in abscisic acid signal transduction in Arabidopsis guard cells. *Elife* 4.

40. Boudsocq M & Sheen J (2013) CDPKs in immune and stress signaling. *Trends Plant Sci* 18(1):30-40.

41. Suzuki N, Koussevitzky S, Mittler R, & Miller G (2012) ROS and redox signalling in the response of plants to abiotic stress. *Plant Cell Environ* 35(2):259-270.

42. Hossain MA*, et al.* (2015) Hydrogen peroxide priming modulates abiotic oxidative stress tolerance: insights from ROS detoxification and scavenging. *Frontiers in plant science* 6.

43. Terzi R, Kadioglu A, Kalaycioglu E, & Saglam A (2014) Hydrogen peroxide pretreatment induces osmotic stress tolerance by influencing osmolyte and abscisic acid levels in maize leaves. *Journal of Plant Interactions* 9(1):559-565.

44. Miller G, Suzuki N, Ciftci-Yilmaz S, & Mittler R (2010) Reactive oxygen species homeostasis and signalling during drought and salinity stresses. *Plant Cell Environ* 33(4):453-467.

45. Munnik T & Testerink C (2009) Plant phospholipid signaling: "in a nutshell". *J Lipid Res* 50 Suppl:S260-265.

46. Munnik T & Vermeer JE (2010) Osmotic stress-induced phosphoinositide and inositol phosphate signalling in plants. *Plant Cell Environ* 33(4):655-669.

47. McLoughlin F & Testerink C (2013) Phosphatidic acid, a versatile water-stress signal in roots. *Front Plant Sci* 4:525.

48. Testerink C & Munnik T (2005) Phosphatidic acid: a multifunctional stress signaling lipid in plants. *Trends Plant Sci* 10(8):368-375.

49. Bargmann BO*, et al.* (2009) Multiple PLDs required for high salinity and water deficit tolerance in plants. *Plant Cell Physiol* 50(1):78-89.

50. Meijer HJ ND, Ende H, Musgrave A, Munnik T (1999) Hyperosmotic stress induces rapid synthesis of phosphatidyl-D-inositol 3,5-bisphosphate in plant cells. *Planta* 208(208):813-823.

51. Eisinger WR, Kirik V, Lewis C, Ehrhardt DW, & Briggs WR (2012) Quantitative changes in microtubule distribution correlate with guard cell function in Arabidopsis. *Mol Plant* 5(3):716-725.

52. Khanna R*, et al.* (2014) COP1 jointly modulates cytoskeletal processes and electrophysiological responses required for stomatal closure. *Mol Plant* 7(9):1441-1454.

53. Wang C, Li J, & Yuan M (2007) Salt tolerance requires cortical microtubule reorganization in Arabidopsis. *Plant and Cell Physiology* 48(11):1534-1547.

54. Liu J*, et al.* (2014) Microtubule dynamics is required for root elongation growth under osmotic stress in Arabidopsis. *Plant Growth Regulation* 74(2):187-192.

55. Fujita S*, et al.* (2013) An atypical tubulin kinase mediates stress-induced microtubule depolymerization in Arabidopsis. *Curr Biol* 23(20):1969-1978.

56. Ache P*, et al.* (2000) GORK, a delayed outward rectifier expressed in guard cells of Arabidopsis thaliana, is a K(+)-selective, K(+)-sensing ion channel. *FEBS Lett* 486(2):93-98.

57. Kollist H, Nuhkat M, & Roelfsema MR (2014) Closing gaps: linking elements that control stomatal movement. *New Phytol* 203(1):44-62.

58. Shabala SN & Lew RR (2002) Turgor regulation in osmotically stressed Arabidopsis epidermal root cells. Direct support for the role of inorganic ion uptake as revealed by concurrent flux and cell turgor measurements. *Plant Physiol* 129(1):290-299.

59. Osakabe Y*, et al.* (2013) Osmotic stress responses and plant growth controlled by potassium transporters in Arabidopsis. *Plant Cell* 25(2):609-624.

60. Barragan V*, et al.* (2012) Ion exchangers NHX1 and NHX2 mediate active potassium uptake into vacuoles to regulate cell turgor and stomatal function in Arabidopsis. *Plant Cell* 24(3):1127-1142.

61. Wang ZY*, et al.* (2015) The Arabidopsis Vacuolar Sorting Receptor1 is required for osmotic stress-induced abscisic acid biosynthesis. *Plant Physiol* 167(1):137-152.

62. Muench DG, Zhang C, & Dahodwala M (2012) Control of cytoplasmic translation in plants. *Wiley Interdiscip Rev RNA* 3(2):178-194.

63. Franks TM & Lykke-Andersen J (2008) The control of mRNA decapping and P-body formation. *Mol Cell* 32(5):605-615.

64. Weber C, Nover L, & Fauth M (2008) Plant stress granules and mRNA processing bodies are distinct from heat stress granules. *Plant J* 56(4):517-530.

65. Filichkin SA*, et al.* (2010) Genome-wide mapping of alternative splicing in Arabidopsis thaliana. *Genome Res* 20(1):45-58.

66. Deyholos MK (2010) Making the most of drought and salinity transcriptomics. *Plant Cell Environ* 33(4):648-654.

67. Jiang Y, Yang B, Harris NS, & Deyholos MK (2007) Comparative proteomic analysis of NaCl stress-responsive proteins in Arabidopsis roots. *J Exp Bot* 58(13):3591-3607.

CHAPTER 2

Phosphoproteomic Analyses Reveal Early Signaling Events in the Osmotic Stress Response

The work presented in this chapter has been published:

Stecker, Kelly E., Benjamin B. Minkoff, and Michael R. Sussman. "Phosphoproteomic analyses reveal early signaling events in the osmotic stress response." *Plant physiology* 165, no. 3 (2014): 1171-1187.

Abstract

Elucidating how plants sense and respond to water loss is important for identifying genetic and chemical interventions that may help sustain crop yields in water-limiting environments. Currently, the molecular mechanisms involved in the initial perception and response to dehydration are not well understood. Modern mass spectrometric methods for quantifying changes in the phosphoproteome provide an opportunity to identify key phosphorylation events involved in this process. Here, we have used both untargeted and targeted isotope-assisted mass spectrometric methods of phosphopeptide quantitation to characterize proteins in Arabidopsis (*Arabidopsis thaliana*) whose degree of phosphorylation is rapidly altered by hyperosmotic treatment. Thus, protein phosphorylation events responsive to 5 min of 0.3 M mannitol treatment were first identified using ^{15}N metabolic labeling and untargeted mass spectrometry with a high-resolution ion-trap instrument. The results from these discovery experiments were then validated using targeted Selected Reaction Monitoring mass spectrometry with a triple quadrupole. Targeted Selected Reaction Monitoring experiments were conducted with plants treated under nine different environmental perturbations to determine whether the phosphorylation changes were specific for osmosignaling or involved cross talk with other signaling pathways. The results indicate that regulatory proteins such as members of the mitogen-activated protein kinase family are specifically phosphorylated in response to osmotic stress. Proteins involved in 5′ messenger RNA decapping and phosphatidylinositol 3,5-bisphosphate synthesis were also identified as targets of dehydration-induced phosphoregulation. The results of these experiments demonstrate the utility of targeted phosphoproteomic analysis in understanding protein

regulation networks and provide new insight into cellular processes involved in the osmotic stress response.

Introduction

Plants experiencing drought in natural environments must respond to the osmotic and ionic stresses that result from dehydration and exposure to high-salt concentrations. The response to osmotic stress is currently best understood at the level of intermediate and long-term adaptation, where changes in gene expression reorient growth and metabolism for survival. Less is known, however, about the mechanisms of initial stress perception and adaptation that occur within the first few minutes of dehydration.

During the initial phases of osmotic stress, plant cells experience a transient loss of water and turgor pressure that is recovered within minutes through increased inorganic ion fluxes into the cytoplasm (Shabala and Lew, 2002; Zonia and Munnik, 2007). Along with turgor recovery, adjustments of vital cellular processes occur, including arrest of cell growth and expansion, restructuring of the cytoskeleton, and shifts in active protein translation, that suggest heightened levels of posttranscriptional regulation (Kawaguchi et al., 2004; Fricke et al., 2006; Urano et al., 2010). Second messengers such as Ca2+, reactive oxygen species (ROS), phospholipids, and protein kinases are thought to play important signaling roles during this initial response phase (Dodd et al., 2010; Munnik and Vermeer, 2010; Steinhorst and Kudla, 2013).

In contrast to plants, the molecular nature of an osmotic stress signaling pathway is fairly well understood in yeast. The osmotic stress response is initiated by two yeast transmembrane osmosensors that act upstream of a mitogen-activated protein kinase (MAPK) signaling cascade to control gene expression in the Hog1 (for high-osmolality glycerol response1) signaling pathway (Hohmann, 2002). There is evidence to suggest that a similar pathway may be present in plants (Urao et al., 1999; Tran et al., 2007; Wohlbach et

al., 2008; Kumar et al., 2013), and MAPK phosphorylation likely plays an important role in the osmotic stress response, as MAPK cascades are known to regulate several abiotic and biotic stress response pathways (Rodriguez et al., 2010).

Abscisic acid (ABA) is a hormone that controls the cellular response to water loss through the activation of subfamily 2 sucrose nonfermenting1-related kinases (SnRK2), although changes in ABA synthesis and transport generally occur much later than the initial dehydration perception and turgor response. In the absence of ABA, clade A protein phosphatase 2Cs suppress SnRK2 autophosphorylation, keeping SnRK2s in an inactive state (Park et al., 2009; Umezawa et al., 2009). In the presence of ABA, protein phosphatase 2C suppression is relieved and SnRK2s become active, phosphorylating known downstream targets, including transcription factors that bind to ABA-responsive elements (AREBs) and ion channels (Geiger et al., 2009; Sato et al., 2009; Yoshida et al., 2010). The 10-member SnRK2 family includes kinases that act directly in this ABA pathway (SnRK2.2, SnRK2.3, and SnRK2.6) as well as others that have not been implicated in ABA signaling but are activated during osmotic stress (Fujii and Zhu, 2009; Fujii et al., 2011; McLoughlin et al., 2012).

The significance of MAPK signaling in the yeast paradigm and the role of SnRK2 proteins in ABA- and non-ABA-mediated dehydration responses point to the importance of protein phosphorylation in osmotic stress signaling. In addition to MAPKs and SnRK2s, kinase families that are responsive to changes in cytosolic Ca2+ concentration likely play active roles during the early stages of a plant's osmotic stress response (Cheong et al., 2010; Franz et al., 2011; Boudsocq and Sheen, 2013). The number and individual complexity of these gene families, along with the various second messengers associated with osmotic

perturbation, suggest a multifaceted network of proteins undergoing phosphoregulation during the stress response, even in the earliest stage of perception.

Untangling these important phosphorylation networks has been a major challenge for scientists in recent years. Advances in quantitative proteomic techniques have improved our ability to carefully analyze signaling networks via quantitative *in vivo* measurements of phosphorylation changes on a large proteome-wide scale (Ross et al., 2004; Kline et al., 2010). Identifying proteins differentially phosphorylated in response to specific perturbations has led to key discoveries in signaling pathways, such as receptor-ligand interactions and mechanisms of transcription factor activation (Umezawa et al., 2013; Haruta et al., 2014).

These studies have used the most frequently employed proteomic method of untargeted data acquisition, also referred to as shotgun or discovery proteomics, to analyze phosphopeptides. In this method, peptides are selected for mass spectrometry (MS) sequence analysis based on real-time determination of peptide ion abundance. Any peptide ion meeting an abundance threshold at a given point in time is measured and sequenced through tandem mass spectrometry (MS/MS) fragmentation using an ion-trap mass spectrometer. Because this sampling feature depends on a peptide's abundance rather than its identity, acquiring information does not require any prior knowledge of a peptide's mass or charge state. This makes untargeted proteomics appropriate for survey studies where one does not know the exact peptides being sought but an assessment of the global proteome is being queried.

Despite its appeal for analyzing a very large number of peptides in a short period of time, a common limitation of untargeted proteomic methods is the inability to routinely measure lower abundance peptides. This is because the ion intensity thresholds used to select peptides for MS/MS sequencing can cause low-abundance species to be excluded from

analysis. For protein phosphorylation measurements, where phosphorylated species exist at low stoichiometry in the cell, routine peptide detection can be extremely problematic. This impedes the ability to determine the statistical significance of observed changes and to make comparative measurements of phosphorylation changes across various experimental conditions.

To address these limitations, we employ a targeted MS method known as Selected Reaction Monitoring (SRM) to specifically measure select protein phosphorylation events in a highly sensitive, routine fashion. SRM uses knowledge of a peptide's mass, charge, and fragmentation behavior to enhance peptide detection via filtered selection using a triple quadrupole mass spectrometer. In contrast to untargeted MS, where all possible peptides are analyzed, targeted MS examines a predetermined list of peptides with improved sensitivity and throughput. This makes it an amenable platform for comparative analysis of protein phosphorylation across different samples and treatment conditions. This method has been recently used in the field to successfully measure the abundance of a protein across genotypes (Su et al., 2013; Taylor et al., 2014) and the phosphorylation state of a specific target protein (Dubiella et al., 2013).

In this study, we investigate proteins involved in the early response to hyperosmotic stress in Arabidopsis (*Arabidopsis thaliana*) by measuring stress-induced phosphorylation using untargeted and targeted proteomics. Phosphorylation responses were first quantified using untargeted MS and then validated and characterized with respect to specificity and onset using SRM. Our data implicate new proteins and points of regulation in the osmotic stress response and provide a new method of comparing phosphorylation networks in Arabidopsis that is also applicable with any plant whose proteome sequence is known.

Results

Untargeted Phosphoproteomic Measurements Identify Early Phosphorylation Changes after Osmotic Stress Treatment

To identify proteins involved in the initial stages of the osmotic stress response, we performed an untargeted proteomics experiment measuring protein phosphorylation following 5 min of perturbation with 0.3 M mannitol. To quantify phosphorylation changes, we used full metabolic labeling of Arabidopsis seedlings in the reciprocal experimental strategy outlined in **Figure 2.1A**. Plants were grown in liquid culture in experimental pairs consisting of one sample grown in natural abundance ^{14}N medium and the other grown in isotopically heavy ^{15}N medium. After 10 to 11 d of growth, the sample medium was replaced with either treatment or control medium for 5 min. Treated and control sample pairs were combined and processed together for tandem liquid chromatography (LC)-MS analysis using an LTQ-Orbitrap mass spectrometer. A reciprocal experimental pair was processed in parallel to serve as a biological replicate and correct for any isotopic effects.

In total, two sample pairs were analyzed, constituting one set of reciprocally labeled experiments. To reduce sample complexity prior to MS analysis, these samples were prefractionated by first separating the cytoplasmic soluble proteins from microsomal membranes. Following tryptic digestion, the soluble fraction was further fractionated using HPLC and a strong cation exchange (SCX) column. Microsomal pellets and SCX fractions from each sample were enriched for phosphopeptides and analyzed on the mass spectrometer. From the acquired data, only peptides meeting a 1% false discovery rate cutoff and observed in each of the two samples were included in our analysis.

Overall, 1,299 phosphorylated peptides, representing 833 unique proteins, were identified in both ^{14}N /^{15}N experimental pairs. From this data set, we identified 29 proteins

showing reciprocal changes in phosphorylation greater than 2-fold, of which 12 proteins possessed greater than 3-fold change in phosphorylation. The annotated functions of these proteins, displayed in **Table 2.I**, indicate that dehydration could be influencing diverse cellular functions, including vesicle trafficking, RNA degradation, ubiquitination, and membrane transport. A complete list of changing phosphopeptides (1.5-fold or greater change) identified in this study can be found in Supplemental **Table S2.1**. Since the chosen time points (5 min) are short and most likely precede changes in de novo protein synthesis, it is reasonable to suggest that the observed changes in phosphopeptide abundance represent phosphorylation increases rather than changes in protein abundance. However, this assumption can be experimentally tested by the identification of additional, nonchanging peptides derived from the same protein. For approximately one-third of the osmotic stress-responsive phosphoproteins listed in Supplemental **Table S2.1**, we identified an additional peptide that indicates protein levels were not changing between treated and control samples. These additional peptides are listed in Supplemental **Table S2.2**.

Coordinate Regulation of Protein Phosphorylation among Gene Family Members

Several proteins undergoing dynamic changes in phosphorylation in response to osmotic stress are closely related members of large gene families. Observing a similar pattern of regulation in related proteins indicates that particular subfamilies may be playing important roles in the stress response. An example of a coordinated phosphorylation response is seen in the MAPKKK (MAP3K) and basic leucine zipper (bZIP) transcription factor proteins identified in this study.

The Arabidopsis MAP3K family is very large, consisting of 60 genes that are broken up into two main divisions: the MAPK/ERK kinase kinase and Raf kinase subfamilies. The

MAP3K proteins showing mannitol-responsive phosphorylation in this study (Raf18, Raf20, and Raf24) all belong to the RAF B4 subgroup, which is one of 11 subdivisions in the Raf family (Ichimura et al., 2002). Phylogenic analysis of 46 Raf members shows close grouping of all three RAF proteins (**Fig. 2.2A**). Phosphorylation increases of Raf18 and Raf24 are around 2-fold and occur at nearly identical centralized regions in each protein and not in any conserved domains. Although the Raf20 phosphorylation increase is small, its close relationship to Raf18 and Raf24 indicates that these proteins may be coordinately regulated at the posttranslational level during osmotic stress. Currently, no known function has been ascribed to these kinases or to any of the RAF B4 subgroup members.

As with the MAP3Ks, the Arabidopsis bZIP transcription factor family is quite large, consisting of approximately 70 genes. Two closely related proteins of the bZIP class I subfamily (Jakoby et al., 2002), bZIP29 and bZIP30, show increased phosphorylation at a conserved Ser residue (**Fig. 2.2B**). bZIP30 phosphorylation has been shown to be responsive to exogenous ABA treatment to a lesser extent (Kline et al., 2010; Xue et al., 2013) and to 30 min of mannitol treatment (Xue et al., 2013), but an earlier osmotic challenge has not been examined previously. Within the bZIP class I subfamily, two proteins closely related to bZIP29 and bZIP30 have been reported to play a role in the abiotic stress response (**Fig. 2.2C**). VirE2-interacting protein1 (VIP1), which has been associated with the pathogen response in the past, has recently been shown to be involved in the osmotic stress response (Tsugama et al., 2012), and bZIP59 is reported to function downstream of the salt overly sensitive signaling pathway (Van Oosten et al., 2013). VIP1 and bZIP59 were not detected in our data set, but taken together, our observations suggest that bZIP class I proteins may be important components of the dehydration stress-related phosphosignaling pathway.

Phosphorylation of the 5' mRNA Decapping Protein Complex

Several proteins involved in cytosolic mRNA regulation through the 5' to 3' exonuclease degradation pathway experienced large changes in phosphorylation following a 5-min hyperosmotic challenge. These proteins include members of the 5' decapping complex: VARICOSE (VCS), VCS-related (VCR), and decapping enzyme DCP2 (**Table 2.I**). Removing the 5' cap of mRNA is an important step in posttranscriptional regulation, as it represents movement away from active translation and functions as the rate-limiting prerequisite for exoribonuclease degradation (Jonas and Izaurralde, 2013). VCS is a scaffold protein that holds together DCP1 and DCP2 in a protein complex that is conserved in plants and animals (Franks and Lykke-Andersen, 2008). Our results demonstrate that VCS is phosphorylated at multiple Ser residues, with some sites increasing and some decreasing their levels of phosphorylation in response to mannitol (**Fig. 2.3, A–C**), reflecting a complex mechanism of phosphoregulation. Nearly all of the dynamic phosphorylation changes occur in the flexible Ser-rich linker region residing between protein-binding domains (**Fig. 2.3D**). VCS has an essential function in the posttranscriptional regulation of mRNA through both 5' decapping and microRNA degradation (Brodersen et al., 2008). VCS associates with processing bodies, which are protein-RNA complexes that function as sites of transcript repression and degradation and are known to accumulate in response to abiotic stress (Weber et al., 2008). Currently, the molecular mechanisms controlling VCS association with 5' decapping complex proteins and with processing bodies are unknown.

Limitations of Untargeted Proteomic Analysis

Untargeted data acquisition is a valuable tool for the initial identification of proteins involved in the cellular stress response but offers limited utility in subsequent analysis of low-abundance species. This is due to the indiscriminate nature of MS sampling, in which any peptide meeting abundance thresholds in a certain time interval is selected for analysis, a process called data-dependent acquisition. Acquiring intensity and sequence information for all possible peptides as they enter the mass spectrometer results in frequent sampling of high-abundance species at the expense of others, because instrument space is finite and sampling occurs in a serial fashion. In our study, nearly half of all identified phosphopeptides had to be excluded from analysis because they were found in only one experimental sample (**Fig. 2.4A**). Even repeated injections of the same sample yield poor overlap in peptide detection, a common feature inherent in the technique when complex biological samples are analyzed (**Fig. 2.4B**). The consequence of this inadequate sample overlap is a reduction in usable data and weak statistical support for observed phosphorylation changes.

One approach to improving peptide detection is to reduce sample complexity prior to MS analysis. In this study, samples were prefractionated by SCX chromatography and separated over a 4-h reverse-phase HPLC gradient in tandem with MS analysis (**Fig. 2.1A**). The addition of SCX chromatography significantly improved sample detection and quantification (**Fig. 2.5A**), so much so that nearly all phosphopeptides identified in **Table 2.I** were not found in our unfractionated data set (K.E. Stecker and G.A. Barrett-Wilt, unpublished data). Improvements in detection, however, come at the cost of significantly increased labor and instrument time.

Targeted Proteomics Provides Sensitive and Reproducible Detection of Protein Phosphorylation Changes

To improve the detection of phosphopeptides across multiple experimental samples and to independently evaluate the phosphorylation changes identified in our initial study, SRM methods were developed to specifically target peptides of interest. SRM analysis is performed on a triple quadrupole tandem mass spectrometer and employs a two-step mass filtering strategy in which only peptides and selected peptide fragments with desired mass-to-charge ratios are allowed to pass through the instrument. Target peptides are selected in the first filtering step in quadrupole 1. Peptides are subsequently fragmented in quadrupole 2, and only fragment ions with desired mass-to-charge ratios are selected in the second filtering step in quadrupole 3 (**Fig. 2.1B**). The detection of targets using this dual mass filtering significantly reduces background ions, thus enhancing peptide quantitation through improved signal-to-noise ratios. A comparison of peptide detection across experimental platforms is seen in **Figure 2.5**, A and B.

To quantify target peptides in SRM analysis, we synthesized stable isotope-labeled peptide for use as a spike in standard. Standards were made for 70 phosphopeptides selected from the mannitol discovery data and several of our untargeted proteomic experiments (Kline et al., 2010; Haruta et al., 2014). From the starting 70 phosphopeptides, 12 phosphopeptides were not included in our final assay for the following reasons: (1) five phosphopeptide standards failed to be detected; (2) four endogenous phosphopeptides were below the levels of detection; and (3) three phosphopeptides possessed very high sample-to-sample variability and could not be reproducibly quantified between biological replicates. Our final assay consisted of 58 phosphopeptides (Supplemental **Table S2.3**), of which 21 were derived from the untargeted mannitol data. The selection of mannitol-responsive phosphopeptides for

targeted analysis was based on biological interest, the magnitude of phosphorylation response observed in the discovery data, the feasibility of peptide synthesis (20 amino acids or fewer in length), and overlap with other studies in the laboratory. These 58 phosphopeptide standards and corresponding endogenous peptides were measured in a single 90-min LC-MS run. No SCX prefractionation was required, as endogenous peptides could be routinely detected from the phosphopeptide enrichment of crude, total protein extracts (**Fig. 2.5**, A and B). This multiplexed targeted assay was used as a secondary experiment to evaluate the discovery data and characterize phosphorylation changes in plants treated with different environmental perturbations.

To better understand if mannitol-responsive phosphorylation events were specific to osmotic stress or were generically responding to perturbations and changes in common second messengers used by several signaling pathways, we measured phosphorylation under nine different treatment conditions (**Table 2.2**). In each case, the treatment was applied for 5 min. Hormone, biotic, and abiotic treatments that were chosen are predicted to share both overlapping and unique physiology with the osmotic stress response.

In contrast to untargeted MS detection, phosphopeptides were reliably identified in our targeted MS analysis with good statistical support. We observed minimal technical variability and low biological variability, with median coefficient of variance values around 10% for all experiments (**Fig. 2.5C**). Due to shorter LC methods (90 versus 240 min) and no HPLC prefractionation, the throughput of targeted peptide analysis is significantly higher. Analysis of nine treatment conditions with three biological replicates each was performed using less instrument time than required for analysis of the two reciprocal experimental samples in our untargeted work.

Hierarchical Clustering of Targeted Phosphoproteomic Data

To extract patterns from protein phosphorylation changes induced by various treatments, we performed hierarchical clustering of targeted phosphoproteomic data. Nearly all phosphorylation changes greater than 1.5-fold were statistically significant with $P \leq 0.05$ (**Fig. 2.5D**). Clustering of treatment conditions revealed some expected trends. The three conditions inducing osmotic stress, mannitol, NaCl, and KCl, cluster together with minimal differences observed between treatments (**Fig. 2.6A**). This shared response between the neutral osmolyte, mannitol, and the charged salts, sodium and potassium chloride, indicates that the ionic component of salt stress does not have a unique influence on the phosphorylation of many of the selected proteins. In contrast to the overlap observed among the mannitol and salt phosphorylation responses, ABA treatment appears to have a unique response and little overlap with the other treatments at 5 min. Known components of the ABA receptor signaling pathway show large changes in phosphorylation, while a minimal response is seen with all other protein targets (**Fig. 2.6A**). These components include SnRK2 kinases involved in ABA signaling (SnRK2.2, SnRK2.3, and SnRK2.6), AREB transcription factors, and class B heat shock factor HSFB2B. Interestingly, AREBs and HSFB2B experience large changes in phosphorylation under osmotic and defense-related conditions, while ABA-responsive SnRK2s do not. This indicates that these transcription factors are likely regulated by alternate phosphorylation pathways and may represent a mechanism of cross talk between various abiotic and biotic signaling networks.

Clustering shows that the bacterial flagellin flg22 peptide, which acts as a pathogen elicitor, most closely groups with the response to hydrogen peroxide (H2O2). The pathogen-associated molecular pattern (PAMP) response is known to stimulate ROS waves that

quickly propagate throughout the plant (Torres et al., 2006; Segonzac and Zipfel, 2011). Our data show that the phosphorylation of PENETRATION3 (PEN3), an ATP-binding cassette transporter involved in PAMP resistance, is dramatically induced by Flg22, H2O2, and methyl jasmonate treatment. Another protein known to be involved in defense signaling, PHOSPHOLIPASE C2 (PLC2), is shown to be responsive to Flg22 and H2O2. PLC2 is a calcium-activated phosphoinositide lipase involved in the production of diacyglycerol and soluble inositol phosphates (Munnik, 2014). Both PEN3 and PLC2 PAMP-responsive phosphorylation have been reported previously (Nühse et al., 2007) and represent positive controls for the treatment conditions and quantitation methods used in this study.

We observed some overlapping phosphorylation patterns between ROS and osmotic perturbations with SnRK2.4, α-tubulin (TUA), and Vac14 (for vacuole morphology and inheritance mutant14). This overlap is consistent with previous reports that osmotic stress induces increased ROS production (Xiong and Zhu, 2002). Notably, these proteins show increased phosphorylation in mannitol, salt, and H2O2 but not in Flg22, demonstrating that they are not responsive to all ROS-inducing conditions. This suggests a responsiveness to ROS that is unique to osmotic stress.

Regulation of the Plasma Membrane Proton Pump (H+-ATPase) by Phosphorylation Changes at Two Distinct Sites

Similar to the dynamic regulation of VCS at multiple phosphorylation sites (**Fig. 2.3C**), the plasma membrane H+-ATPase pump is controlled by phosphorylation at several residues in a C-terminal water-soluble domain of approximately 100 amino acids (Nühse et al., 2007). Increased phosphorylation of the most C-terminal Thr, referred to as the penultimate Thr, activates the pump through increased binding with a 14-3-3 protein (Olsson

et al., 1998). In contrast, phosphorylation of Ser-899, also located in this C-terminal regulatory domain, is proposed to inhibit pump activity, although the mechanism by which this acts is less well understood (Haruta et al., 2014). In our targeted analysis, the two most highly expressed H+-ATPase (AHA) family members in Arabidopsis, AHA1 and AHA2, display coordinated regulation at the penultimate position (AHA1 pT948 and AHA2 pT947) and are responsive to several treatments (**Fig. 2.6B**). We observed phosphorylation increases in response to fusicoccin, a fungal pathogen known to cause pump hyperactivation, and phosphorylation decreases in response to cold, H2O2, and mannitol. Pump inhibition via pS899 phosphorylation is seen in response to Flg22 and to a lesser extent in H2O2 and salt treatments, although these findings have less statistical support. Interestingly, these results indicate that AHA2 down-regulation occurs by two distinct mechanisms (dephosphorylation of Thr-947/948 versus phosphorylation of Ser-899) that vary based on treatment conditions.

It has been speculated that AHA proton pumps are hyperactivated during the osmotic stress response and may play an active role in the initial turgor recovery by providing the proton motive force necessary to drive ion influx into cells (Shabala and Lew, 2002; Shabala and Shabala, 2011). Our phosphorylation data show that AHAs are not being activated through penultimate Thr phosphorylation in the first 5 min of the mannitol stress response. In contrast, AHA activity appears to be down-regulated through decreased penultimate Thr phosphorylation in AHA1 and AHA2. This pattern of phosphoregulation is distinct from the AHA response to KCl treatment, suggesting that these different forms of osmotic stress have unique effects on AHA activity. This observation is supported by genetic data showing that aha2 null mutants are hypersensitive to KCl but not sorbitol or NaCl treatment (Haruta and Sussman, 2012).

Patterns of Osmotic-Specific Phosphorylation Changes Define a Rapid Dehydration-Associated Molecular Phenotype

Our primary interest in this investigation is the quantification of protein phosphorylation events that are selectively responsive to osmotic stress, as they provide insight to cellular processes involved in early signaling and adaptation. From the 21 mannitol-responsive phosphopeptides selected from untargeted data, 19 showed reproducible mannitol-induced phosphorylation (**Table 2.I**) and 11 possessed a relatively osmotic-specific response and cluster together in our phosphorylation heat map (**Fig. 2.6A**). This phosphorylation pattern is characterized as a rapid dehydration-associated molecular phenotype and includes the phosphorylation of VCS, bZIP30, and RAF18 proteins, which were described previously in our untargeted data. In addition to RAF18, another protein in the MAPK superfamily appears highly responsive to osmotic perturbation: MAP4Kα1. MAP4Kα1 is one of three mannitol-responsive MAP4Ks identified in this study (Supplemental **Table S2.1**) that belong to the poorly characterized MAP4K 10-member gene family in Arabidopsis (Champion et al., 2004). In yeast (Saccharomyces cerevisiae), the MAP4K Ste20 functions downstream of the osmosensor Sho1 to activate the Hog1 MAPK cascade responsible for osmotic adaptation (Bahn, 2008). It is unknown if a similar osmotic stress MAP4K signaling hierarchy is active in plants.

In addition to MAPK family members, proteins involved in cytoskeleton restructuring and phospholipid production cluster in the osmotic-responsive phosphorylation group. These proteins are the microtubule subunit TUA and a protein involved in phosphatidylinositol bisphosphate production, Vac14.

Tubulin Phosphorylation

We observed approximately 2-fold increases in phosphorylation of the TUA proteins TUA3 and TUA4 at Thr-349 in response to NaCl and mannitol treatment. Recently, TUA phosphorylation at this residue was shown to influence overall microtubule stability (Fujita et al., 2013). This previous work showed that TUA phosphorylation occurred under osmotic stress conditions and resulted in a polymerization-incompetent protein isoform that contributed to microtubule destabilization and depolymerization (Ban et al., 2013; Fujita et al., 2013). This finding was significant because microtubule depolymerization and restructuring are known to occur in response to several abiotic stresses (Nick, 2008; Wang et al., 2011) and are required for seedling survival under salt stress (Wang et al., 2007), but the mechanistic details underlying stress-induced depolymerization were previously unknown. Our data support these recent findings and provide further description of rapid TUA phosphorylation (**Fig. 6A**).

Vac14 Phosphorylation

The largest phosphorylation increase observed in our discovery data (approximately 12.5-fold) was of Vac14, a protein involved in the synthesis of the phospholipid phosphatidylinositol 3,5-bisphosphate [$PI(3,5)P_2$]. Vac14 is a scaffold protein that holds together a phosphatidylinositol 3-phosphate 5-kinase Fab1/PIKfyve, and a $PI(3,5)P_2$ phosphatase, Fig4/Sac3, in a conserved complex responsible for $PI(3,5)P_2$ production that is found in all eukaryotes (Dove and Johnson, 2007). The coordination of lipid kinase and phosphatase within the same complex speaks to the highly controlled nature of $PI(3,5)P_2$ metabolism. Although Vac14 function has yet to be described in plants, our data indicate that it is highly responsive to osmotic perturbations (**Fig. 2.7A**). $PI(3,5)P_2$ levels are known to rapidly increase in response to osmotic stress in plants, green algae, and yeast (Meijer et al.,

1999; Bonangelino et al., 2002; Zonia and Munnik, 2004), with as much as 20-fold induction within 5 min of treatment in Saccharomyces cerevisiae (Duex et al., 2006). Interestingly, Vac14 is required for stress-induced PI(3,5)P_2 production in yeast (Bonangelino et al., 2002), although the details regarding its regulation are unknown. The protein sequence of Vac14 is highly conserved from yeast to human, but phosphorylation occurs at a variable C-terminal region of the protein (**Fig. 2.7B**). This phosphorylation site is not present in yeast and mammals and is conserved in land plants (**Fig. 2.7C**). These data indicate the presence of a Vac14 phosphoregulation mechanism involved in the hyperosmotic response that is unique to plants.

Time-Course Analysis of Osmotic-Responsive Proteins

To better understand the temporal nature of osmotic-induced phosphorylation, we preformed a time-course experiment measuring the response to 2, 5, and 10 min of mannitol treatment using SRM. Half of the osmotic-block proteins displayed increasing or plateauing phosphorylation over the entire time period (**Fig. 2.8A**), while the other half showed a peak at earlier time points followed by a dropoff at 10 min (**Fig. 2.8B**). Vac14, SnRK2.4, and MyoB1, a plant-specific myosin adaptor protein recently shown to be involved in cytoplasmic streaming (Peremyslov et al., 2013), displayed maximal phosphorylation at 2 min. The rapid phosphorylation of SnRK2.4 is consistent with previous *in vitro* kinase activity results that showed rapid and transient SnRK2.4 activation following salt and mannitol treatment of Arabidopsis roots (McLoughlin et al., 2012). Interestingly, the phosphorylation profile of Vac14 over time closely mirrors stress-induced PI(3,5)P_2 production in yeast and Chlamydomonas reinhardtii, which peaks at 5 min and is reduced by 15 min following treatment (Meijer et al., 1999; Duex et al., 2006).

Transcription Data Do Not Identify Phosphoproteins Responsive to Osmotic Stress

To determine if gene expression data can be used to predict proteins undergoing stress-responsive phosphorylation, we analyzed transcriptomics data from available Affymetrix arrays using Genevestigator (Zimmermann et al., 2004). Experiments using whole-seedling and earlier time points (3 h or less) were selected when possible. When minimal to no response was observed at early time points, later sampling values were selected (24 h or less). A complete list of selected microarray experiments is found in Supplemental **Table S2.5**. Heat-map arrangement of expression data in the same orientation as phosphopeptide clustering reveals minimal overlap between protein phosphorylation and mRNA measurements (**Fig. 2.8C**). This is particularly true for osmotic-block genes, which show no salt- or mannitol-induced changes in gene expression, with the exception of TUA and the unknown protein Constitutive photomorphogenesis protein1-interacting related. Expanding this analysis to all available experiments related to salt, osmotic, and drought stress reveals a similar trend of minimal to no correlation of the phosphorylation and transcriptional responses (Supplemental **Fig. 2.S2**). However, it is possible that with some genes, the chip-based measurements are misrepresenting the *in vivo* transcriptional response. For example, increases in MAP4Kα1 gene expression during salt and osmotic stress have been observed previously using real-time quantitative PCR (Charrier et al., 2002), although no response is seen in array data. Nevertheless, genes implicated in stress responses are significantly different in phosphorylation studies compared with expression analyses, indicating that the rapid protein phosphorylation response to dehydration is distinct from the slower molecular phenotypes associated with mRNA changes.

Discussion

The work described in this study provides new insights into cellular processes involved in the early osmotic stress response. Using targeted MS analysis of Arabidopsis seedlings, we compared protein phosphorylation across nine different perturbations to elucidate a response network specific to osmotic stress. This network includes MAP4K and MAP3K family proteins, bZIP transcription factors, 5' mRNA decapping proteins, and Vac14. Phosphorylation of these targets suggests new points of regulation for stress-induced posttranscriptional reprograming and phosphatidylinositol synthesis. Proteins implicated in the osmotic response through our analysis did not show stress-induced changes in gene expression, demonstrating that phosphoproteomic signaling is an important orthogonal approach to understanding the stress response.

In our untargeted analysis, we identified 79 proteins responsive to osmotic stress with phosphorylation changes of 1.5-fold or greater following 5 min of treatment (Supplemental **Table S2.1**). From this list, 21 phosphopeptides were selected for validation and characterization using targeted SRM analysis. The reproducibility of the discovery data was high, with all phosphopeptides showing similar responses except ADH1 pS229, PIP2F pS283, and oxidoreductase pS29 (**Table 2.I**). These phosphopeptides likely represent false positives in our discovery data sets, as quantification was based on only two biological replicates in which over 1,200 phosphopeptides were quantified. It is possible that the original phosphorylation changes identified for ADH1 and oxidoreductase were the result of differential protein abundance rather than phosphorylation change, as no additional peptides were identified for either of these proteins; thus, no conclusion can be made regarding protein levels in each sample. The inability to comprehensively address protein abundance is

an inherent limitation of phosphopeptide enrichment. This fact underscores the importance of rapid phosphorylation analysis to observe phosphorylation responses before the onset of significant changes in protein synthesis/breakdown. Our data set was collected following 5 min of mannitol treatment, but SRM time-course data reveal that some phosphopeptides show the highest response to mannitol after only 2 min of treatment. This suggests a need to sample at more immediate time points, as important phosphorylation responses may have been missed at 5 min.

Hierarchical clustering was applied to SRM data to compare phosphorylation responses across different perturbations. The high sensitivity and throughput of SRM made routine measurements of phosphopeptides possible. This is an analysis that would be difficult to perform using standard untargeted methods because of the low reproducibility of phosphopeptide detection. From our analysis, we identified 11 proteins displaying relatively osmotic-specific phosphorylation responses. These proteins give insight into several cellular processes known to be involved in the early stress response as well as highlight new processes that may play important roles.

The poor correlation of transcript levels with protein abundance following salt treatment (Jiang et al., 2007) and the major readjustment of transcripts away from active polysomes during dehydration stress (Kawaguchi et al., 2004) indicate that mechanisms of posttranscriptional regulation are activated during early stages of the dehydration stress response (Deyholos, 2010; Sunkar et al., 2012). Our data identifying VCS, VCR, and DCP2 phosphorylation increases following mannitol treatment suggest that 5′ mRNA decapping is altered during osmotic stress. Targeted analysis of VCS phosphorylation indicates that this response is specific to hyperosmotic conditions and increases with treatment duration. VCS

functions as a scaffold protein for the decapping proteins DCP1 and DCP2. These proteins localize to processing bodies, which are aggregations of mRNA and proteins associated with transcript repression and degradation that increase following stress treatment (Franks and Lykke-Andersen, 2008). It is unclear what regulates 5′ decapping complex assembly and processing body formation, although some evidence exists suggesting that phosphorylation plays an important role. In yeast, phosphorylation of DCP2 by MAP4K Ste20 increases the DCP2 association with processing bodies (Yoon et al., 2010). In plants, DCP1 is phosphorylated by MAPK6 in response to dehydration stress, and work with phosphomimetic mutants suggests that phosphorylation enhances 5′ mRNA decapping (Xu and Chua, 2012). Similar phosphoregulation of VCS has not yet been described, although it has recently been shown to be phosphorylated in response to 30 min of mannitol treatment in Arabidopsis (Xu and Chua, 2012). It is possible that stress-induced VCS phosphorylation modulates VCS activity in a way that promotes decapping complex assembly and association with processing bodies to control posttranscriptional reprogramming during dehydration stress.

Our data highlight another phenomenon associated with the osmotic stress response: rapid accumulation of the phospholipid species PI(3,5)P_2. In yeast, PI(3,5)P_2 is predominantly localized to the vacuole, where it is required for proper vacuole function and morphology. Osmotic stress causes increased PI(3,5)P_2 production, and these increases are essential for vacuolar volume adjustment (Dove et al., 1997; Bonangelino et al., 2002; Ho et al., 2012). Vac14 is a scaffold protein for PI(3,5)P_2 synthesis and is required for this stress-induced PI(3,5)P_2 production (Bonangelino et al., 2002). Our finding of Vac14 phosphorylation following osmotic perturbation suggests a point of regulation in the

$PI(3,5)P_2$ accumulation process. It is possible that phosphorylation mediates complex assembly with PI3P-5-kinase Fab1 during the stress response. Recent work disrupting Fab1 function in plants reveals that $PI(3,5)P_2$ production is required for proper stomata closure in response to ABA (Bak et al., 2013). $PI(3,5)P_2$ is also required for polarized cell growth and influences actin filament rearrangement in moss (van Gisbergen et al., 2012). Thus, $PI(3,5)P_2$ levels have been linked directly to growth- and drought-related processes. Our identification of Vac14 phosphorylation changes is a starting point toward understanding how this protein involved in $PI(3,5)P_2$ production is regulated in plants.

In addition to fortifying our understanding of processes associated with the stress response, some of the untargeted and targeted proteomic results indicate new pathways that may be important for osmotic adaptation. Several family members of a recently characterized group of myosin-binding proteins (MyoB; Peremyslov et al., 2013) were shown to undergo increased phosphorylation in response to mannitol in our untargeted analysis (Supplemental **Table S2.1**). These proteins act as plant-specific myosin adaptors that anchor vesicles involved in cytoplasmic streaming to high-speed myosin XI motors (Peremyslov et al., 2013). Our data indicate that MyoB1 is phosphorylated specifically in response to osmotic stress and shows the highest degree of phosphorylation at 2 min. Interestingly, rates of cytoplasmic streaming have recently been identified as a major determinate of plant growth (Tominaga et al., 2013). Little is known about cytoplasmic streaming in the context of the stress response, and it is possible that MyoB1 phosphorylation represents a connection between this important growth-controlling process and osmotic stress.

In conclusion, this study demonstrates the use of targeted proteomic analysis as a reliable method for following up on untargeted proteomic experiments and examining rapid

protein phosphorylation across multiple treatment conditions to elucidate stress-specific signaling networks. Our results highlight points of both cross talk and specificity in dehydration-induced phosphorylation. We identified several proteins experiencing osmotic stress-induced phosphoregulation (**Figure 2.9**) that provide insight into the cellular mechanisms occurring during the initial stress response.

Materials and Methods

Plant Growth and Sample Preparation

Wild-type Arabidopsis (Arabidopsis thaliana) Columbia-0 seeds were grown in liquid culture under constant light for 10 to 11 d before experimental treatment and protein extraction. For untargeted proteomic experiments using full metabolic labeling, samples were processed as described previously (Minkoff et al., 2014). Briefly, plants were grown in modified Murashige and Skoog medium containing 1% (w/v) Suc, 0.05% (w/v) MES salt, and either ammonium and potassium nitrate or ^{15}N -enriched ammonium nitrate and potassium nitrate (more than 98% ^{15}N; Cambridge Isotope Laboratories) as the sole nitrogen source. After 10 d, mannitol treatment was applied by decanting the existing medium and replacing with control medium or medium containing 0.3 m mannitol. After 5 min of treatment, plant samples were flash frozen and homogenized. Samples were then combined in an experimental pair consisting of one treated sample grown in ^{14}N medium and one control sample grown in ^{15}N medium. For the second reciprocal experimental pair, the samples were combined in the inverse fashion (^{15}N treated and ^{14}N control). Ground frozen tissue was combined at a 1:1 weight ratio prior to further homogenization. For targeted proteomic experiments, sample medium consisted of one-half-strength Murashige and Skoog salts, 1% (w/v) Suc, and 0.05% (w/v) MES salt. After 11 d of growth, sample medium was replaced with fresh medium and allowed to equilibrate for 4 to 5 h prior to experimental treatment. Treatment was applied in the same manner as described for the untargeted experiments. Three biological replicates were processed for each treatment condition. For all experiments, samples were further homogenized in grinding buffer (Huttlin et al., 2007) supplemented with phosphatase inhibitors using a sonicator (1-cm probe, 5 × 10 s, and 50%

duty cycle) while kept on ice. The resulting supernatant was filtered through two layers of Miracloth (Calbiochem) and underwent a soft spin (1,500g, 20 min, and 4°C) to remove unbroken cells.

Sample Prefractionation for Untargeted MS Analysis

Sample supernatants from experimental pairs 1 and 2 were further centrifuged at 100,000g for 90 min at 4°C (Beckman Ultracentrifuge) to isolate the microsome pellet. The microsome pellet was resuspended in 50 mm Tris-HCl, pH 8, and proteins were extracted from both the microsome resuspension and soluble fraction using a previously described methanol/chloroform/water method (Wessel and Flügge, 1984; Minkoff et al., 2014). Precipitated proteins were solubilized in 8 m urea-containing phosphatase inhibitor mixture (1× PhosStop; Roche). Samples were diluted to 2 m urea, and protein concentration was measured using a bicinchoninic acid assay kit (BCA, Thermo Scientific Pierce). Five milligrams of protein from microsome and soluble fractions was reduced with 5 mm dithiothreitol (45 min at 50°C) and alkylated using 15 mm iodoacetamide (45 min at room temperature). Samples were then diluted to 1.2 m urea using 50 mm NH4HCO3 and digested with trypsin (Promega) at a 1:100 enzyme:protein ratio overnight at 37°C. Samples were acidified using 0.5% (v/v) formic acid to stop enzymatic digestion and desalted using C-18 solid-phase extraction columns (Waters). Soluble fractions were then subject to further fractionation via SCX chromatographic separation using a polysulfoethyl aspartamide column (4.6 × 200 mm; PolyLC) on a Waters Alliance 2795 HPLC device. Separation was achieved using a 0% to 25% (v/v) buffer B (5 mm KH2PO4, 350 mm KCl, and 30% [v/v] acetonitrile [ACN], pH 2.65) gradient over 33 min at a flow rate of 3 mL min−1. The gradient was followed by a 100% buffer B wash and reequilibration with buffer A (5 mm

KH2PO4 and 30% [v/v] ACN, pH 2.65). Independent fractions were collected every 4 min, and blanks were run between samples to ensure no carryover. Sample fractions were flash frozen, lyophilized, and desalted using solid-phase extraction. SCX fractions 3 to 8 and microsome samples were enriched for phosphopeptides using titanium dioxide (TiO2) particles (5 μm; GL Sciences) as described previously (Sugiyama et al., 2007; Minkoff et al., 2014).

Untargeted MS and Data Analysis

Phosphopeptide-enriched samples were analyzed on an LTQ-Orbitrap XL mass spectrometer (Thermo Scientific) using the same method as described by Kline et al. (2010). Briefly, samples were separated by HPLC using an 11-cm C-18 packed analytical column and a 240-min ACN gradient in line with MS analysis. Two to three injection replicates were performed for each sample. Acquired data files containing MS/MS spectra were searched against The Arabidopsis Information Resource 9 protein database using MASCOT software (Matrix Science). Search parameters were set at two allowed missed cleavages, precursor and fragment ion mass tolerances of 15 ppm and 0.6 D, respectively, fixed modifications of Cys carbamidomethylation, and variable modifications of Met oxidation, Ser/Thr/Tyr phosphorylation, and Asn/Gln deamidation. Searches were performed using settings for both ^{14}N and ^{15}N protein masses. MASCOT search results were filtered to maintain a 1% false discovery rate at the peptide level using a reverse-protein sequence database and in-house software. The software determines the minimum MASCOT score in which 1% of MS/MS peptide identifications match the decoy reverse-protein sequence database. All peptide identifications scoring lower than this calculated MASCOT score were excluded from analysis. Quantitative ratio measurements from MS1 peak areas were performed using

Census software (Park et al., 2008) as described by Kline et al. (2010). To correct for errors in mixing ratios (i.e. initial combination of ^{14}N and ^{15}N ground, frozen tissue), all data sets for each experimental sample were normalized to the median ^{14}N -^{15}N area ratio value. Only phosphopeptides quantified in both experiments 1 and 2 were considered for analysis. Phosphopeptides showing reciprocal changes of 1.5-fold or greater were manually validated by visual inspection of Census chromatograms. MS/MS spectra were manually validated for all phosphopeptides in Supplemental **Tables S2.1** and **S2.3** and can be found in Supplemental **Figure 2.S1**.

Targeted SRM Analysis

Proteins were precipitated from sample supernatant with 80% (v/v) acetone overnight at −20°C and then resuspended in 2% (w/v) SDS-Tris-HCl buffer prior to methanol/chloroform/water protein extraction. This initial precipitation step was added to reduce sample volume. Extracted protein was resuspended and quantified by a bicinchoninic acid assay kit as described for the untargeted sample preparation above. For each sample, 3 mg of protein was spiked with isotopically labeled phosphopeptide standards, synthesized by the Sigma-Aldrich PEPscreen platform, Sigma-Aldrich AQUA, or the University of Wisconsin-Madison Biotechnology Center's peptide synthesis core facility. Phosphopeptide standards were pooled into a master mix, divided into aliquots, and frozen. Each batch of samples received a spike from the same phosphopeptide standard master mix aliquot to avoid the variability that may arise from peptide loss due to freeze-thaw cycles or retention in plastic tubes. The concentration of each phosphopeptide standard in the master mix was individually tailored to generate optimum signal levels during SRM analysis. Calculations were based on empirically determined chromatographic and mass spectrometric behavior of

the phosphopeptide standards. Samples were reduced with 5 mm dithiothreitol (45 min at 50°C) and alkylated using 15 mm iodoacetamide (45 min at room temperature). Samples were then diluted to 1.2 m urea using 50 mm NH4HCO3 and digested with trypsin (Promega) at a 1:100 enzyme:protein ratio overnight at 37°C. Samples were acidified using 0.5% (v/v) formic acid to stop enzymatic digestion and desalted using C-18 solid-phase extraction columns (Waters). Phosphopeptide enrichment was performed using homemade TiO2 columns containing 2.4 mg of TiO2 particles (5 μm; GL Sciences), as described by Minkoff et al. (2014).

Phosphopeptide quantitation was performed using the Eksigent NanoLC-Ultra 2D system with the cHiPLC nanoflex microfluidic C18 column (75 μm, 120 Å) coupled to the AB SCIEX 5500 QTRAP mass spectrometer. SRM method development was performed using peptide standards and MRMPilot software (AB SCIEX). Multiple fragment ions were tested for each peptide using both in silico predictions and acquired MS/MS spectra. The three to five most abundant parent ion-to-fragment ion transitions were selected, and collision energies were optimized to maximize fragment ion intensity. The developed method was pilot tested, and the number of transitions for each peptide was reduced to three through the removal of the lowest quality transitions that performed poorly in complex sample backgrounds. In the final method, three transitions per peptide were monitored using scheduled data acquisition with a target scan time of 3.1 s and a detection window of 170 s. A list of SRM transitions used for each endogenous peptide and peptide standard can be found in Supplemental **Table S2.3**. Analytical separation was performed using a linear gradient of 2% to 35% (v/v) buffer B (ACN and 0.1% [v/v] formic acid; Honeywell Burdick and Jackson) over 70 min at a flow rate of 300 nL min−1. The gradient was followed by a

90% (v/v) buffer B wash and reequilibration with buffer A (0.1% [v/v] formic acid; Honeywell Burdick and Jackson). Peak areas were integrated using the automatic MQ4 function in MultiQuant software (AB SCIEX). Peak integration parameters were set as follows: 40% noise, a baseline subtraction window of 0.5 min, and peak splitting of 0 to 2 points with a Gaussian smooth width of 0.8 to 1 point. In all cases, identical integration parameters were used for standard and endogenous peptide area quantification. To determine the levels of endogenous peptide in each sample, the peak areas for endogenous peptides were normalized to the peak areas for the corresponding peptide standard for each transition within each run. Transitions that had low signal intensity or contained isobaric interference were not used for quantification and are indicated in Supplemental **Table S2.3**. For each treatment condition, peptides were quantified from two to four injection replicates for three independent biological replicates. To determine phosphorylation changes, standard-normalized endogenous phosphopeptide abundances were first averaged across biological replicates and then compared across treated and control conditions as a ratio.

The mass spectrometry proteomics data have been deposited to the ProteomeXchange Consortium (Vizcaino et. al, 2010) via the Proteomics Identification Database partner repository with the dataset identifier PXD001057.

Figure 2. 1

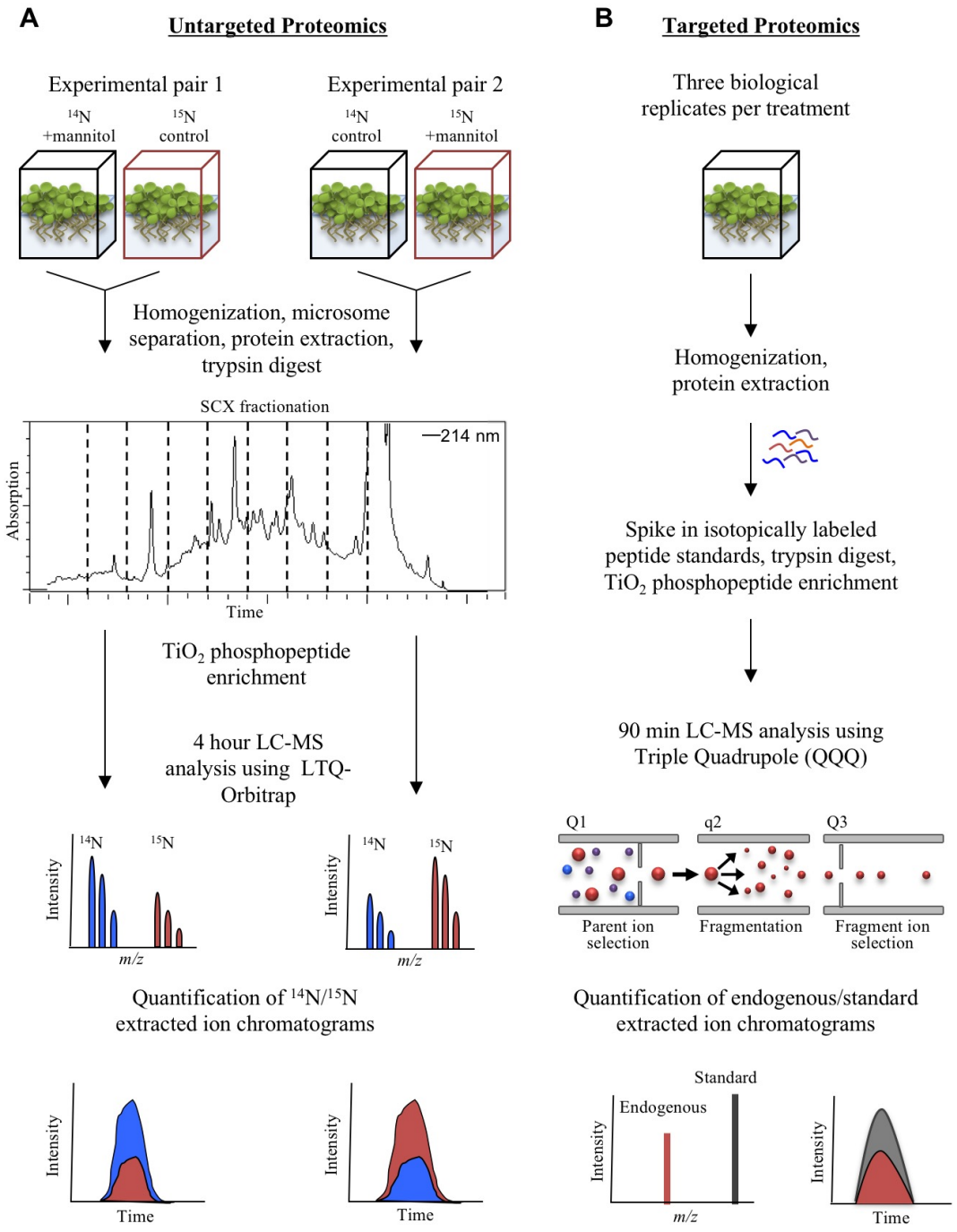
A
Untargeted Proteomics
Experimental pair 1
14N +mannitol
15N control
Experimental pair 2
14N control
15N +mannitol
Homogenization, microsome separation, protein extraction, trypsin digest
SCX fractionation
214 nm
Absorption
Time
TiO2 phosphopeptide enrichment
4 hour LC-MS analysis using LTQ-Orbitrap
Intensity
m/z
Quantification of 14N/15N extracted ion chromatograms
Time
B
Targeted Proteomics
Three biological replicates per treatment
Homogenization, protein extraction
Spike in isotopically labeled peptide standards, trypsin digest, TiO2 phosphopeptide enrichment
90 min LC-MS analysis using Triple Quadrupole (QQQ)
Q1
q2
Q3
Parent ion selection
Fragmentation
Fragment ion selection
Quantification of endogenous/standard extracted ion chromatograms
Standard
Endogenous

Figure 2.1. *Overview of quantitative proteomic methods used in this study*. **A,** Untargeted proteomics experimental design using ^{15}N full metabolic labeling. Phosphorylation changes were determined from $^{14}N/^{15}N$ area ratios of phosphopeptide extracted ion chromatograms (XIC). **B,** Targeted proteomics experimental design using stable isotope labeled peptide standards. Parent ion to fragment ion transitions are measured for endogenous and standard synthetic peptides. Phosphorylation changes are determined from endogenous/standard area ratios of fragment ion XIC.

Figure 2. 2

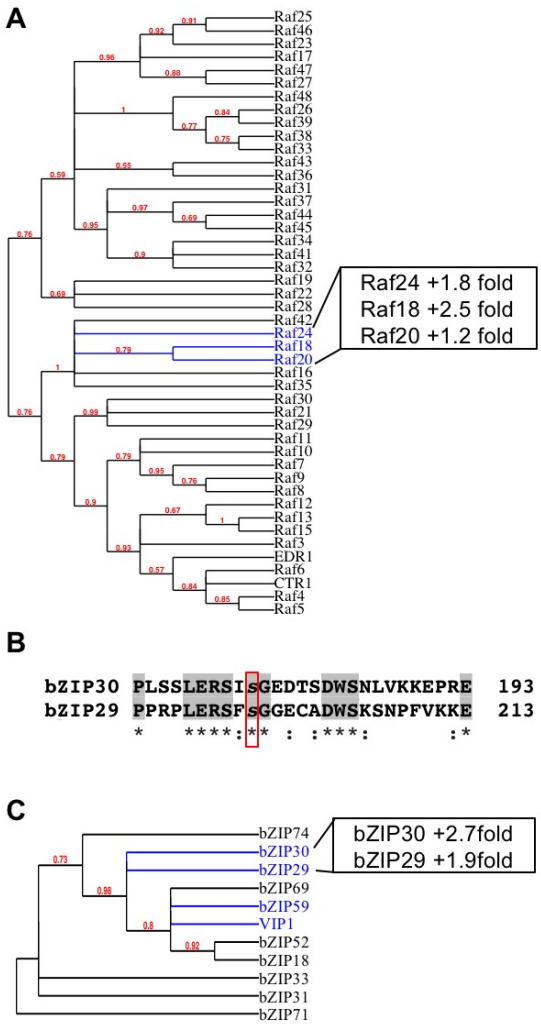

Figure 2.2. *Coordinate regulation of related gene family members*. **A,** MAPKKK RAF family phylogenetic tree. RAF proteins showing osmotic stress induced phosphorylation increases are highlighted in blue. **B,** Alignment of bZIP29 and bZIP30 proteins sequence using Clustal Omega. Conserved phosphorylation site is highlighted in the red box. Grey highlights and * indicate identical residues and : indicates highly similar residues. **C,** Phylogenetic tree of bZIP group I family member. Proteins showing osmotic stress induced phosphorylation and proteins previously implicated in salt and osmotic stress are highlighted in blue. A,C, Trees were made from protein sequence alignment using Phylogeny.fr (Dereeper et al., 2008).

Figure 2. 3

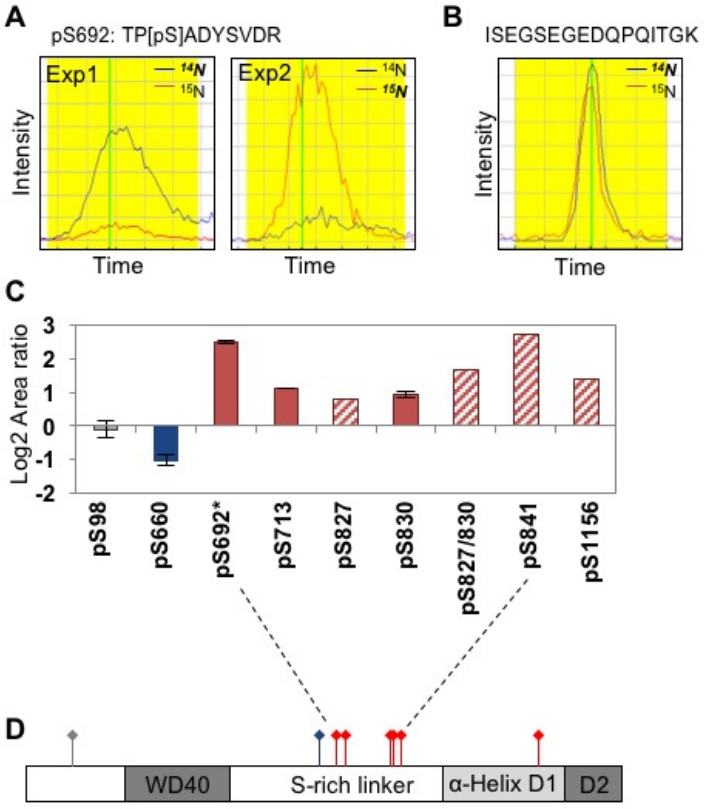
A
pS692: TP[pS]ADYSVDR
Exp1
Exp2
14N
15N
Intensity
Time
B
ISEGSEGEDQPQITGK
C
Log2 Area ratio
pS98
pS660
pS692*
pS713
pS827
pS830
pS827/830
pS841
pS1156
D
WD40
S-rich linker
α-Helix D1
D2

Figure 2.3. *VCS is phosphorylated at multiple serines in response to osmotic stress*. **A,** Reciprocal change in phosphorylation at position S629. Graphs show extracted ion chromatograms (XIC) for reciprocal experiments generated by Census software. Blue lines represent ^{14}N peptide, red lines represent ^{15}N peptide, bold and italicized label indicates treated sample in reciprocal pair. Yellow shading indicates area used to calculate peptide abundance ratio in Census. Vertical green line indicates scan at which MS/MS data was acquired. **B**, No change seen in VCS non-phosphorylated peptide, indicating phosphorylation changes are not due to differences in protein abundance. **C,** Log_2 graph of VCS phosphorylation changes. Grey = no change, blue = decreasing phosphorylation, red = increasing phosphorylation. Red strips indicate that phosphopeptide was only identified in one experimental pair. Error bars represent standard error between Exp1 and Exp2 averages. Error could not be calculated for phosphopeptides identified in only one experiment. **D,** Diagram of VCS protein with phosphorylation sites locations. Most phosphorylation changes occur in serine-rich linker region. DCP2 binding site is located in conserved protein domains α-helix domain 1 (D1) and D2. D2 contains conserved residues required for P-body localization . Phosphorylation sites are indicated by colored diamonds. Color coding is same as in B.

Figure 2. 4

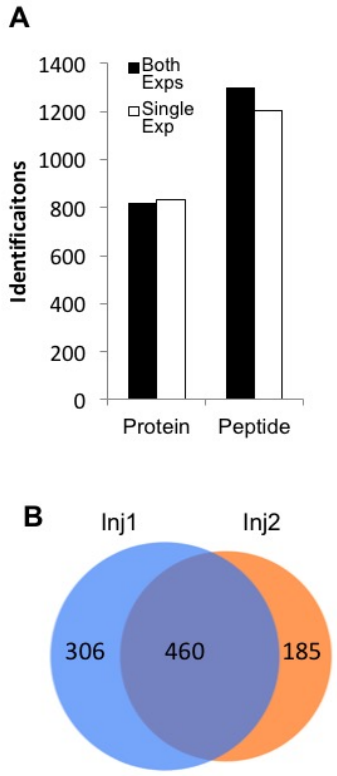

Figure 2.4. *Reproducibility in untargeted phosphoproteomic data.* **A**, Number of proteins and phosphopeptides identified in both experimental samples or only in one sample. **B**, Phosphopeptide identification overlap between two injection replicates of the same sample.

Figure 2. 5

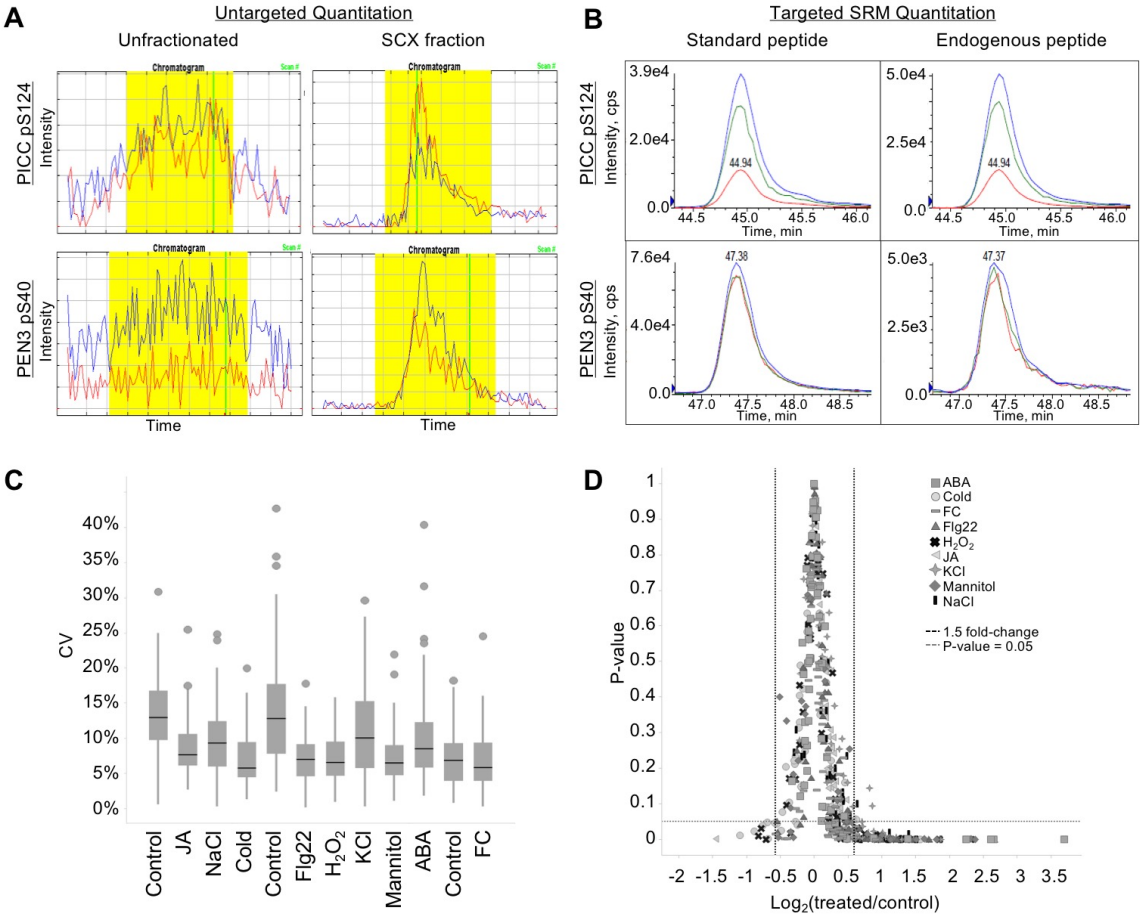
A
Untargeted Quantitation
Unfractionated
SCX fraction
PICC pS124
PEN3 pS40
Intensity
Chromatogram
Time
B
Targeted SRM Quantitation
Standard peptide
Endogenous peptide
PICC pS124
PEN3 pS40
Intensity, cps
Time, min
C
CV
Control
JA
NaCl
Cold
Control
Flg22
H2O2
KCl
Mannitol
ABA
Control
FC
D
P-value
Log2(treated/control)
ABA
Cold
FC
Flg22
H2O2
JA
KCl
Mannitol
NaCl
1.5 fold-change
P-value = 0.05

Figure 2.5. *Improved phosphopeptide detection using targeted SRM analysis*.
A-B, Quantification of PICC phosphopeptide DIDLSFS[pS]PTK (top) and PEN3 phosphopeptide NIEDIFSSG[pS]R (bottom) across different MS platforms. **A,** Extracted ion chromatograms (XIC) from phosphopeptide enrichment of unfractionated, total protein extract (left) compared to phosphopeptide enrichment of SCX fractionated samples (right) using untargeted proteomic methods. PEN3 peptide was only identify in one experimental sample in SCX fractionated data. XICs generated by Census software. Blue lines = ^{14}N peptide, red lines = ^{15}N peptide. Yellow shading indicates area used to calculate peptide abundance ratio in Census. Vertical green line indicates scan at which MS/MS data was acquired. **B,** XICs from phosphopeptide enrichment of unfractionated, total protein extract using targeted SRM method. Peptide standards (left) and endogenous peptides (right) co-elute with identical fragment ion patterns. Three fragment ions were measured for each peptide. **C-D**, Statistical analysis of targeted proteomic data. **C,** Box plot of the coefficient of variance for each phosphopeptides quantified across 3 biological replicates in 12 different treatments. 58 phosphopeptides are plotted in each treatment. Control treatment is present three times because samples were grown and processed in three separate batches. Black bar = median value for each treatment. **D,** Phosphorylation changes ≥ 1.5 fold are statistically significant (P-value ≤ 0.05) in almost all targeted experiments.

Figure 2. 6

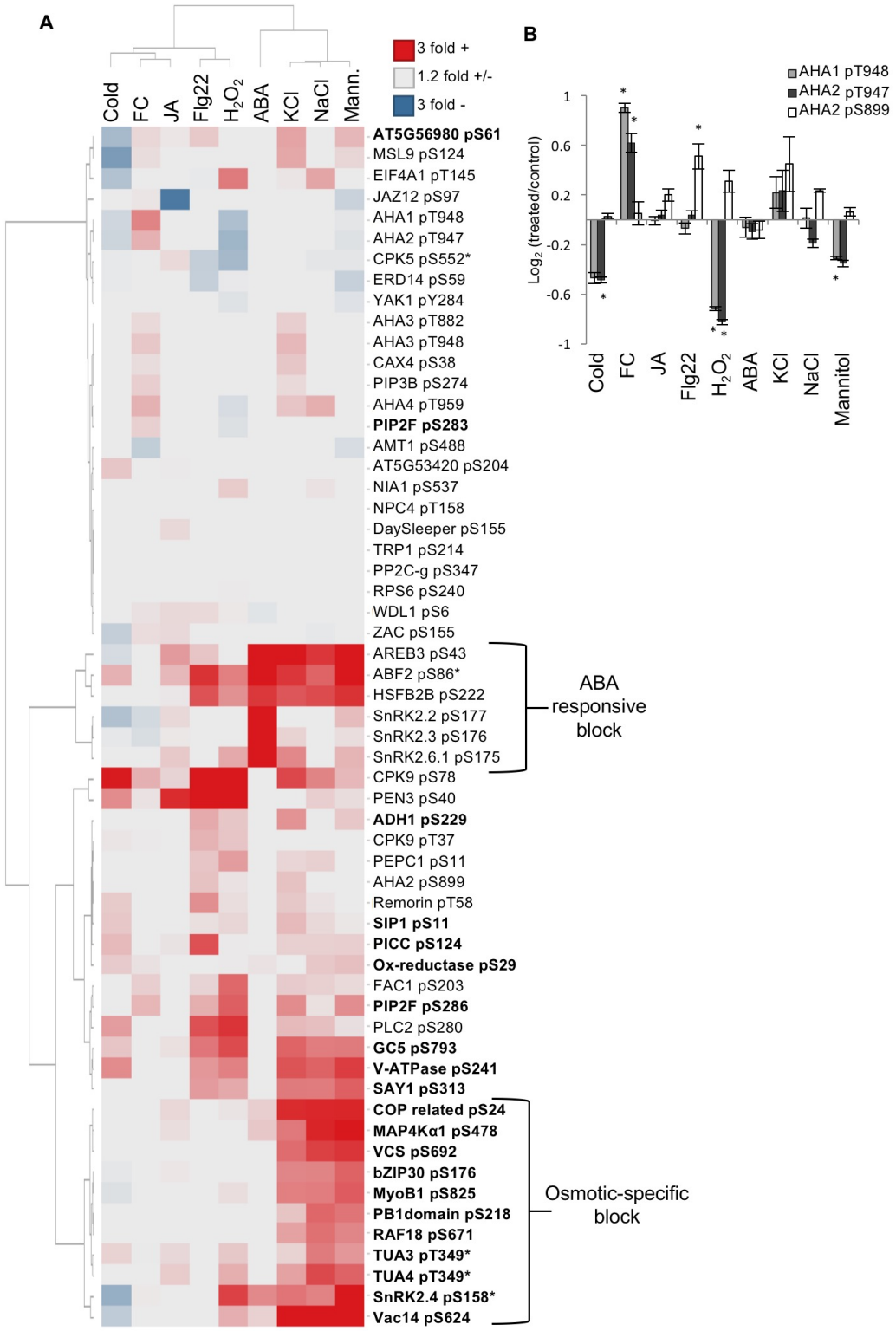
A
Cold
FC
JA
Flg22
H2O2
ABA
KCl
NaCl
Mann.
3 fold +
1.2 fold +/-
3 fold -
AT5G56980 pS61
MSL9 pS124
EIF4A1 pT145
JAZ12 pS97
AHA1 pT948
AHA2 pT947
CPK5 pS552*
ERD14 pS59
YAK1 pY284
AHA3 pT882
AHA3 pT948
CAX4 pS38
PIP3B pS274
AHA4 pT959
PIP2F pS283
AMT1 pS488
AT5G53420 pS204
NIA1 pS537
NPC4 pT158
DaySleeper pS155
TRP1 pS214
PP2C-g pS347
RPS6 pS240
WDL1 pS6
ZAC pS155
AREB3 pS43
ABF2 pS86*
HSFB2B pS222
SnRK2.2 pS177
SnRK2.3 pS176
SnRK2.6.1 pS175
ABA responsive block
CPK9 pS78
PEN3 pS40
ADH1 pS229
CPK9 pT37
PEPC1 pS11
AHA2 pS899
Remorin pT58
SIP1 pS11
PICC pS124
Ox-reductase pS29
FAC1 pS203
PIP2F pS286
PLC2 pS280
GC5 pS793
V-ATPase pS241
SAY1 pS313
COP related pS24
MAP4Kα1 pS478
VCS pS692
bZIP30 pS176
MyoB1 pS825
PB1domain pS218
RAF18 pS671
TUA3 pT349*
TUA4 pT349*
SnRK2.4 pS158*
Vac14 pS624
Osmotic-specific block
B
AHA1 pT948
AHA2 pT947
AHA2 pS899
Log2 (treated/control)
1
0.6
0.2
-0.2
-0.6
-1
Cold
FC
JA
Flg22
H2O2
ABA
KCl
NaCl
Mannitol

Figure 2.6. *Hierarchical clustering of targeted phosphoproteomic data*. **A,** Heat map of 58 phosphopeptides measured using SRM. Values represent Log_2 area ratios of treatment vs. control averages. Averages represent three biological replicates per treatment with ≥ 2 injection replicates per sample. Data for heatmap found in SI Table2.3. *Indicates non-unique peptides that match multiple gene family members. Phosphopeptides in bold were selected from mannitol untargeted proteomic data (Table 2.1). Clustering performed using Wards Method. **B,** AHA1 and AHA2 phosphorylation across all treatments. Error bars represent standard error for three biological replicates. *Indicates phosphorylation changes with P-value < 0.05 (Student's T-Test).

Figure 2. 7

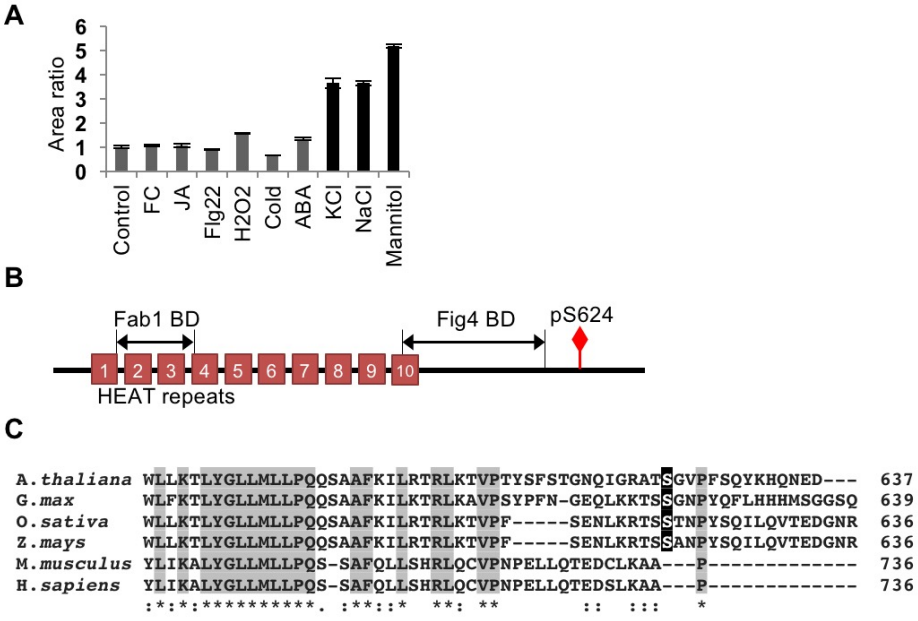

Figure 2.7. *Vac14 phosphorylation*. **A,** Vac14 protein domain structure. Phosphorylation occurs at variable C-terminal region. **B,** Alignment of C-terminal Vac14 proteins sequence using Clustal Omega. Plant specific phosphorylation site is highlighted in black. Grey highlights and * indicate identical residues, and : indicates highly similar residues. **C,** Vac14 phosphorylation is highly responsive to osmotic stress. Black bars represent osmotic stress inducing conditions. Error bars represent standard error for three biological replicates.

Figure 2. 8

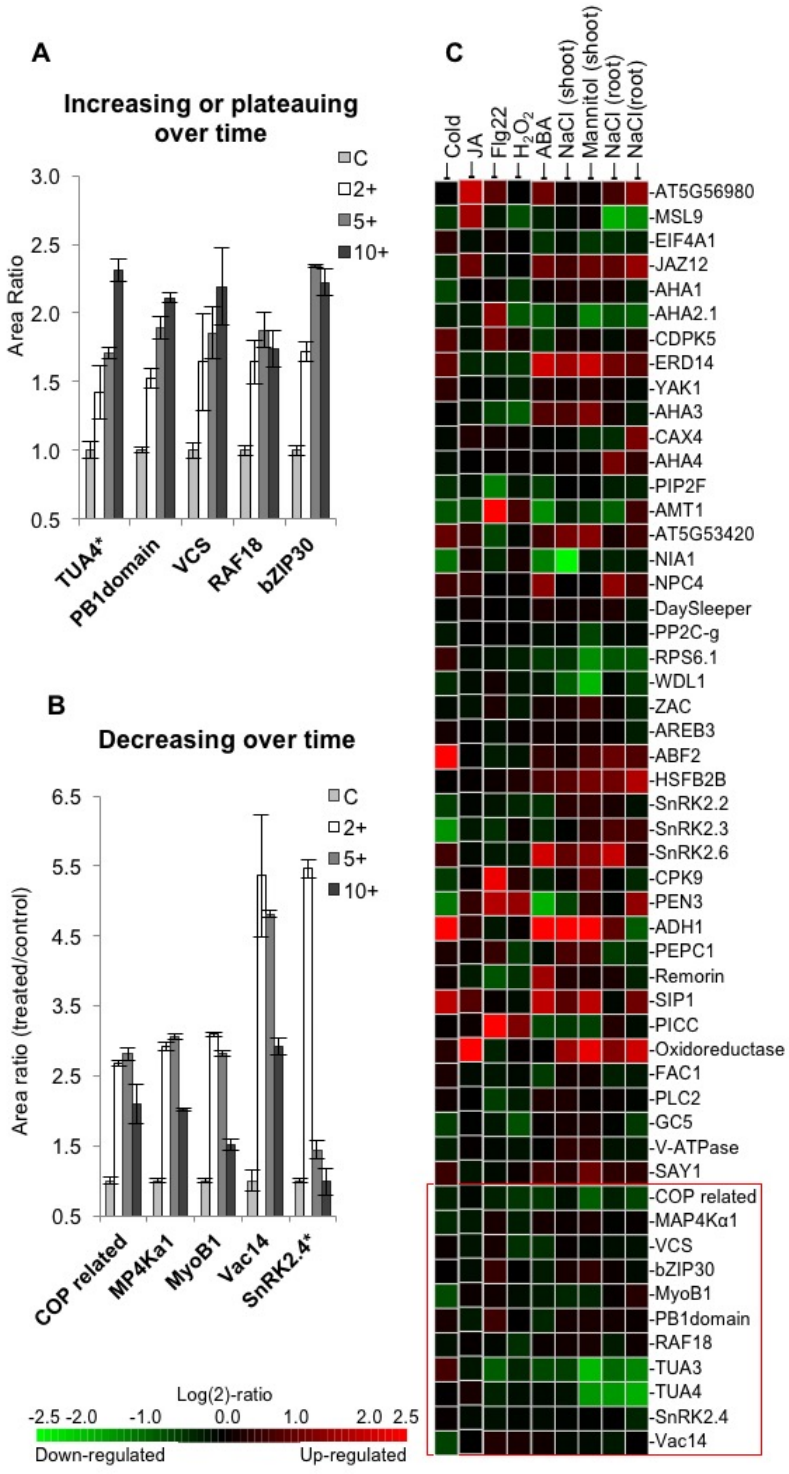
A
Increasing or plateauing over time
C
2+
5+
10+
Area Ratio
3.0
2.5
2.0
1.5
1.0
0.5
TUA4*
PB1domain
VCS
RAF18
bZIP30
B
Decreasing over time
Area ratio (treated/control)
6.5
5.5
4.5
3.5
2.5
1.5
0.5
COP related
MP4Kα1
MyoB1
Vac14
SnRK2.4*
Log(2)-ratio
-2.5 -2.0 -1.0 0.0 1.0 2.0 2.5
Down-regulated
Up-regulated
C
Cold
JA
Flg22
H2O2
ABA
NaCl (shoot)
Mannitol (shoot)
NaCl (root)
NaCl(root)
-AT5G56980
-MSL9
-EIF4A1
-JAZ12
-AHA1
-AHA2.1
-CDPK5
-ERD14
-YAK1
-AHA3
-CAX4
-AHA4
-PIP2F
-AMT1
-AT5G53420
-NIA1
-NPC4
-DaySleeper
-PP2C-g
-RPS6.1
-WDL1
-ZAC
-AREB3
-ABF2
-HSFB2B
-SnRK2.2
-SnRK2.3
-SnRK2.6
-CPK9
-PEN3
-ADH1
-PEPC1
-Remorin
-SIP1
-PICC
-Oxidoreductase
-FAC1
-PLC2
-GC5
-V-ATPase
-SAY1
-COP related
-MAP4Kα1
-VCS
-bZIP30
-MyoB1
-PB1domain
-RAF18
-TUA3
-TUA4
-SnRK2.4
-Vac14

Figure 2.8. *Phosphorylation timecourse and gene expression analysis of phosphoproteins used in our targeted proteomics experiment*. **A-B**. SRM measurement of phosphorylation induced over a 0.3M mannitol treatment timecourse. Phosphopeptides belong to osmotic-specific group in Figure 6A. Error bars represent standard error for three biological replicates. *Indicates non-unique peptides that match multiple gene family members. **C.** mRNA expression analysis of genes used in targeted proteomics study. Gene expression data was analyzed using Genevestigator. mRNA was collected from whole seedlings unless otherwise indicated. Microarray experimental details are found in SI Table 2.4. Red box = proteins found in the osmotic-specific phosphorylation block in Figure 6A.

Figure 2. 9

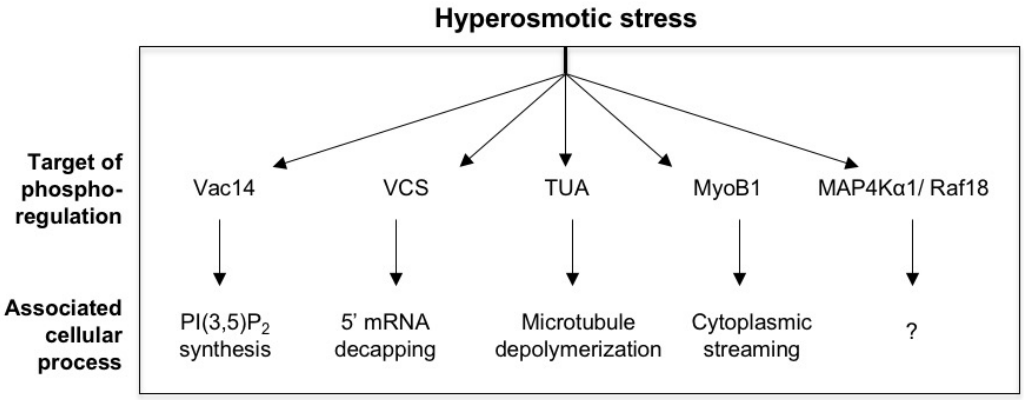

Figure 2.9. *Summery of select phosphorylation targets during initial osmotic stress response.*

Table 2.1

ATG accession	Protein	Phosphopeptide	Fold Change	Std Error	Targeted MS Validation
Kinases/signaling related					
AT2G01690	Vac14	AT[pS]GVPFSQYK	12.55	1.01	Yes
[1]AT1G10940	SnRK2.1/4/5/10	S[pT]VGTPAYIAPEVLSR	6.18	2.06	Yes
AT1G53165	Map4K alpha1	SS[pS]ASEDSISNLAEAK	4.87	0.72	Yes
AT1G16270	Map3K Raf18	TV[pS]GGGIETEAR	2.50	1.24	Yes
Proteasome/ubiquitin related					
AT2G26590	RPN13	AGNLVVPNLSSEV[pS]DVTSSSGPVK	3.84	0.23	n/a
AT2G47970	NPL4 family protein	SIPGAPPVTPAG[pS]FGR	2.29	0.18	n/a
AT3G63000	NPL41 (NPL4-LIKE)	GGPAVTPAG[pS]FGR	2.06	0.09	n/a
5'mRNA decapping					
AT5G13570	DCP2	[***pTS***]VGGNGTATVESQNR	4.48	0.04	n/a
AT3G13300	VCS (varicose)	TP[pS]ADYSVDR	5.69	0.95	Yes
		ESITSAS[pS]VAQALSR	5.50	2.01	n/a
		NLDVS[pS]VEEISR	2.18	0.002	n/a
		TSGLPSQTSGAGSAYATLPQLPL[pS]PR	0.49	0.06	n/a
AT3G13290	VCR (varicose related)	TS[pS]ADYFYVR	3.98	0.53	n/a
Cytoskeleton					
[1]AT1G04820	TUA2/4/6	TIQFVDWCP[pT]GFK	2.80	0.30	Yes
[1]AT5G19770	TUA1/3/5	TVQFVDWCP[pT]GFK	1.98	0.06	Yes
AT2G21380	Kinase motor related	[***pSSS***]TPTSTVYNSGGVTGSR	2.53	0.93	n/a
Channels/pumps					
AT3G58730	Vacuolar ATPase D subunit	GI[pS]INAAR	2.91	0.66	Yes
AT5G60660	Auquaporin PIP2F	ALGSFGSFG[pS]FR	2.48	0.11	Yes
		ALGSFG[pS]FGSFR	2.09	0.13	No
AT2G36380	ABC transporter PDR6	LP[pT]YDRLR	2.49	0.78	n/a
Vesicle trafficking related					
AT1G08800	MyoB1	ALLTQI[pS]ASR	5.65	0.07	Yes
AT4G19490	VPS54	SI[pS]DASSQSLSSILNNPHGGK	2.68	0.14	n/a
AT4G11740	SAY1	AASG[pS]LAPPNADR	1.92	0.09	Yes
AT1G79830	GC5	QN[pS]AFENGSLPR	2.78	0.004	Yes
Metabolism related					
AT1G77120	ADH1	IIGVDFN[pS]K	0.22	0.10	**No**
AT5G05600	Oxidoreductase	VQ[pS]LAESNLSSLPDR	3.20	0.49	**No**
AT5G40390	SIP1	SD[pS]GINGVDFTEK	1.51	0.06	Yes
AT3G58460	RBL15	[***pT***L***S***]TARDPTAPAGETDPNLHAR	2.04	0.13	n/a
Other/Unknown					
AT2G21230	bZIP 30	SI[pS]GEDTSDWSNLVK	2.70	0.19	Yes
AT1G72410	COP1-interacting related	LSLGGG[pS]ADFSK	4.73	0.26	Yes
AT3G03050	Cellulose synthase-like CSLD3	[pS]NLSTNSDAAEAER	2.10	0.01	n/a
AT2G01190	PB1domain containing	GF[pS]DSDTNVNR	2.29	0.25	Yes
AT5G64430	PB1domain containing	LFLFPASSGFG[pS]QSSTQSDRDR	2.00	0.42	n/a
AT2G32240	PICC defense responsive	DIDLSFS[pS]PTK	1.49	0.001	Yes
AT5G56980	A70 defense responsive	AP[pS]IIDR	1.55	0.02	Yes
AT5G35430	TPR domain containing	[***pTSS***]LLSSSVASDTLR	2.61	0.12	n/a
AT1G22060	Unknown	SVV[pS]GDLSGLAQSPQK	2.37	0.54	n/a
AT5G58510	Unknown	TN[pS]VNQSPTDAIR	2.10	0.01	n/a
AT5G42950	GFY domain containing	[***pS***P***SS***]DLLSILQGVTDR	2.00	0.23	n/a

[1]Peptide matches multiple family members.

Table 2.1. *Phosphorylation changes in response to 5 min of osmotic stress.* Phosphopeptides showing ≥ 2-fold change in phosphorylation in response to 5 minutes of 0.3M mannitol treatment and additional phosphopeptides selected for targeted proteomic analysis. [1]Indicates peptides that match multiple gene family members. Phosphorylation sites that could not be localized to one residue are indicated in bold, italicized font. MS/MS spectra for listed phosphopeptides are documented in SI Figure 1.

Table 2.2

Treatment	Concentration	Rationale
Mannitol	300mM	Osmotic stress (OS), validation of discovery results
NaCl	150mM	Ionic stress, OS
KCl	150mM	PM depolarization, OS
S-ABA	50uM	Drought stress hormone
Cold	0-4^{O}C	Freezing tolerance overlap with dehydration stress. Overlapping secondary messengers with OS
Flg22	1uM	Pathogen elicitor. Overlapping secondary messengers with OS
H_2O_2	5mM	ROS, secondary messenger
Fusicoccin (FC)	5uM	PM hyperpolarization
Methyl Jasmonate (JA)	50uM	Defense response hormone. Minimal overlap expected

Table 2.2. *Targeted MS treatment conditions.* Treatment conditions used for targeted proteomic analysis of 58 phosphopeptides.

Table S2. 1

SI Table 1 Mannitol responsive phosphopeptides identfied in untargeted 5 minute mannitol study
MS1 chromatograms were manually validated for all listed phosphopeptides
MS2 spectra were manually validated for phosphosite localization for all listed phosphopeptides. MS2 spectra can be found in **SI Figure 1**
Phosphorylation sites that could not be localized to one residue are indicated in bold, italicized text

ATG ID	Protein name	Protein Description	Peptide Sequence	Phosphorylation fold change; Average area ratio (treated/control)	Standard deviation	Mascot ion score	Alternate peptide intenfified in SI Table2
AT2G01690.1 AT1G10940.1/	Vac14		R.AT[pS]GVPFSQYK.H	12.55	1.43	37.91	No
AT5G08590.1/ AT5G63650.1/ AT1G60940.1	SNRK2.4/2.1/2.5/2.10	SNF1-RELATED PROTEIN KINASE 2.4; kinase	K.S[pT]VGTPAYIAPEVLSR.R	6.18	2.92	41.53	No
AT3G13300.1	VCS	VARICOSE; nucleotide binding / protein homodimerization	K.TP[pS]ADYSVDR.Q	5.69	1.35	52.9	Yes
AT4G05150	MYOB1	Myosin binding protein	K.ALLTQI[pS]ASR.G	5.65	0.09	46.54	Yes
AT3G13300.1	VCS	VARICOSE; nucleotide binding / protein homodimerization	K.ESITSAS[pS]VAQALSR.E	5.50	2.84	43.56	Yes
AT1G53165.1	MAP4Kalpha1	ATMAP4K ALPHA1; ATP binding / kinase/ protein kinase/ protein serine/threonine kinase/ protein tyrosine kinase	R.SS[pS]ASEDSISNLAEAK.L	4.87	1.02	58.28	Yes
AT1G72410.1	COP1-interacting protein-related		R.LSLGGG[pS]ADFSK.L	4.73	0.37	34.93	No
AT5G13570.1	DCP2	DECAPPING 2; hydrolase/ m7G(5')pppN diphosphatase/ mRNA binding / protein homodimerization	R.[***pTS***]VGGNGTATVESQNR.K	4.48	0.06	38.65	No
AT3G13290.1	VCR	VARICOSE-RELATED; nucleotide binding	K.TS[pS]ADYFYVR.Q	3.98	0.75	45.44	No
AT2G26590.1	RPN13	proteosome system (RPN13)	R.AGNLVVPNLSSEV[pS]DVTSSSGPVK.L	3.84	0.32	34.29	No
AT3G58730.1	V-ATPase D subunit	vacuolar ATP synthase subunit D (VATD) / vacuolar proton pump D subunit (VATPD)	R.GI[pS]INAAR.N	3.39	0.46	56.26	Yes
AT5G05600.1	oxidoreductase	2OG-Fe(II) oxygenase family protein	R.VQ[pS]LAESNLSSLPDR.Y	3.20	0.70	67.83	No
AT1G16270.1 AT1G64740.1/	Raf18	protein kinase family protein	R.TV[pS]GGGIETEAR.N	2.82	1.42	79.72	No
AT1G50010.1/ AT1G04820.1/ AT4G14960.1	TUA1/2/4/6	structural constituent of cytoskeleton	R.TIQFVDWCP[pT]GFK.C	2.80	0.43	45.74	Yes
AT1G79830.1	GC5	golgin candidate 5; protein binding	R.QN[pS]AFENGSLPR.K	2.78	0.01	54.9	No
AT2G21230.1	bZIP30	bZIP family transcription factor	R.SI[pS]GEDTSDWSNLVK.K	2.70	0.27	34.27	Yes
AT4G19490.1	VPS54		K.SI[pS]DASSQSLSSILNNPHGGK.S	2.68	0.14	42.37	No
AT5G35430.1	unknown protein		R.[***pTSS***]LLSSSVASDTLR.S	2.61	0.17	71.35	No
AT2G21380.1	kinesin motor protein-related		R.[***pSSS***]TPTSTVYNSGGVTGSR.S	2.53	1.32	49.85	No
AT2G36380.1	PDR6	pleiotropic drug resistance 6, ATPase, coupled to transmembrane movement of substances	R.LP[pT]YDRLR.K	2.49	1.10	28.29	Yes
AT5G60660.1	PIP2;4	PLASMA MEMBRANE INTRINSIC PROTEIN 2;4; water channel	K.ALGSFGSFG[pS]FR.S	2.48	0.15	47.42	Yes
AT1G22060.1	unknown protein		K.SVV[pS]GDLSGLAQSPQK.E	2.37	0.76	38.82	No
AT2G01190.1	PB1domain containing	octicosapeptide/Phox/Bem1p (PB1) domain-containing protein	R.GF[pS]DSDTNVNR.L	2.29	0.25	50.08	No
AT2G47970.2	NPL4 family protein	nuclear pore localized	R.SIPGAPPVTPAG[pS]FGR.K	2.29	0.25	39.64	No
AT3G13300.1	VCS	VARICOSE; nucleotide binding / protein homodimerization	R.NLDVS[pS]VEEISR.S	2.18	0.00	45.7	Yes
AT5G58510.1	unknown protein		R.TN[pS]VNQSPTDAIR.R	2.10	0.02	46.47	No
AT3G03050.1	CSLD3	CELLULOSE SYNTHASE-LIKE D3; cellulose synthase/ transferase, transferring glycosyl groups	R.[pS]NLSTNSDAAEAER.H	2.10	0.01	55.77	Yes
AT4G60660.1	PIP2;4	PLASMA MEMBRANE INTRINSIC PROTEIN 2;4; water channel	K.ALGSFG[pS]FGSFR.S	2.09	0.18	41.65	Yes
AT3G63000.1	NPL41	NPL4-LIKE PROTEIN 1	R.GGPAVTPAG[pS]FGR.K	2.06	0.13	46.68	No
AT3G58460.1	ATRBL15	ARABIDOPSIS RHOMBOID-LIKE PROTEIN 15	R.[***pT LS***]TARDPTAPAGETDPNLHAR.L	2.04	0.18	62.3	No
AT5G42950.1	GYF domain-containing protein		R.[***pS*** P***SS***]DLLSILQGVTDR.S	2.00	0.33	33.11	Yes
AT5G64430.1	PB1domain containing	octicosapeptide/Phox/Bem1p (PB1) domain-containing protein	R.LFLFPASSGFG[pS]QSSTQSDRDR.F	2.00	0.60	44.29	Yes
AT5G19770.1/ AT5G19780.1	TUA3/5	structural constituent of cytoskeleton	R.TVQFVDWCP[pT]GFK.C	1.98	0.09	54.21	Yes
AT4G13630.1	MYOB family protein	Myosin binding factor, DUF593 domian containing	R.SQ[pS]VSDTSYAFPQGK.S	1.97	0.12	27.19	No
AT3G04910.1	WNK1	WITH NO LYSINE (K) 1; kinase/ protein kinase/ protein serine/threonine kinase	R.QY[pS]NGNYPSNSSSLNR.Q	1.97	0.67	48.66	No
AT4G11740.1	SAY1	RabGTPase interacting	R.AASG[pS]LAPPNADR.S	1.92	0.12	29.08	Yes
AT3G13300.1	VCS	VARICOSE; nucleotide binding / protein homodimerization	K.VFCSQVSNL[p***ST***]EM#AR.D	1.90	0.09	40.2	Yes
AT4G38900.1	bZIP29	bZIP family transcription factor	R.SF[pS]GGECADWSK.S	1.87	0.34	47.54	Yes
AT2G35050.1	RAF24	Protein kinase superfamily protein with octicosapeptide/Phox/Bem1p domain	K.NVETNTPEHV[pS]QTETSAK.A	1.82	0.25	51.7	No
AT1G34260.1	FAB1D	phosphatidylinositol-4-phosphate 5-kinase family protein	R.SL[pS]GECSVDGNSCDR.G	1.81	0.98	31.42	No
AT1G72410.1	COP1-interacting protein-related		R.NL[pS]DLSLTDDSK.G	1.81	0.11	58.4	No
AT2G30930.1	unknown protein		K.[pS]LLQTFEAK.S	1.81	0.37	29.42	Yes
AT5G47930.1	Zinc-binding ribosomal protein family protein		R.LQEGC[pS]FR.K	1.80	0.11	25.33	No
AT2G33990.1	iqd9	IQ-domain 9; calmodulin binding	R.TV[pS]LSSVPAK.T	1.79	0.26	32.18	No
AT3G26400.1	EIF4B1	translation initiation factor	R.SS[pT]FGSSFGDSGQEER.R	1.78	0.33	71.07	No
AT3G59290.1	ENTH domain-containing protein	epsin N-terminal homology (ENTH) domain-containing protein	R.KF[pS]EQNIGAAPPSYEEAVSESR.S	1.74	0.09	47.67	No
AT4G37070.2	Phospholipase A	Patatin-related phospholipase A; PLA IVA; PLP1	R.SD[pT]MIKDSSNESQEIK.-	1.74	0.05	54.8	
AT1G67310.1	calmodulin binding / transcription regulator		R.VL[pS]M#SNSPEAR.Q	1.74	0.10	35.42	Yes
AT1G24300.1	unknown protein		R.NN[pS]LLSGIIDGGR.S	1.73	0.06	63.76	No
AT5G19320.1	RANGAP2	RAN GTPASE ACTIVATING PROTEIN 2; RAN GTPase activator	R.ELISEDSV[pS]PR.E	1.71	0.02	23.48	No
AT1G72710.1	CKL2	CASEIN KINASE 1-LIKE PROTEIN 2; ATP binding / kinase/ protein kinase/ protein serine/threonine kinase	K.DVVLSSS[pS]FLR.A	1.70	0.23	45.5	Yes
AT2G14835.1	zinc finger family protein	zinc finger (C3HC4-type RING finger) family protein	R.QN[pS]ETLYYADDEDGNR.K	1.70	0.23	37.65	No
AT5G27630.1	ACBP5	ACYL-COA BINDING PROTEIN 5; acyl-CoA binding	R.AS[pS]GLSYPER.F	1.69	0.40	27.2	No
AT1G29020.1	calcium-binding EF hand family protein		R.SDDQSITCDIS[pS]PR.R	1.69	0.18	51.74	No
AT5G14540.1	proline-rich family protein		R.SYG[pS]M#DSLEPSK.L	1.69	0.06	36.02	No
AT1G72410.1	COP1-interacting protein-related		R.LS[pS]DVSSSEKPILR.R	1.69	0.34	43.5	No

AT5G41950.1	unknown protein		R.NL[pS]GKAETMSTNVER.K	1.68	0.07	73.98	No
AT4G22740.1	glycine-rich protein		R.SG[pS]FGSGLVNR.E	1.67	0.07	47.13	No
AT1G35580.1	CINV1	cytosolic invertase 1; beta-fructofuranosidase	R.AVG[pS]HC[pS]LSEMDDLDLTR.A	1.66	0.31	46.1	Yes
AT4G24100.1	MAP4K5	ATP binding / kinase/ protein kinase/ protein serine/threonine kinase/ protein tyrosine kinase	R.***[pS*** D***S]*** NGNVEPVASER.E	1.60	0.06	56.5	Yes
AT5G57830.1	MYOB family protein	Myosin binding factor, DUF593 domian containing protein	R.NL[pS]SPFDGISSER.S	1.59	0.25	50.14	No
AT1G67230.1	LINC1	LITTLE NUCLEI1	R.[pS]VKDVVDDAK.A	1.59	0.09	34.81	Yes
AT4G17890.1	AGD8	ARF-GAP DOMAIN 8; ARF GTPase activator/ DNA binding / zinc ion binding	K.[pS]ISSAQYFGDQNK.N	1.59	0.42	60.02	No
AT1G56020.1	unknown protein		R.***[pSSS]*** SPGSFTGGPR.M	1.58	0.13	25.52	No
AT5G48430.1	aspartic-type endopeptidase		K.ALV[pS]TVSK.N	1.57	0.14	35.2	No
AT5G56980.1	unknown protein	defense response related	R.ST[pS]FGDGEDGVDAK.A	1.56	0.10	63.09	No
AT5G44460.1/ AT4G20780.1	CML42/43	calmodulin like; calcium-binding protein, putative	R.SP[pS]LNALR.L	1.56	0.40	53.75	No
AT1G29020.1	calcium-binding EF hand family protein		R.SDDQSITCDIS[pS]PR.R	1.56	0.03	51.74	No
AT5G56980.1	unknown protein	defense response related	R.AP[pS]IIDR.V	1.55	0.03	35.86	No
AT5G46750.1	AGD9	ARF-GAP DOMAIN 9; ARF GTPase activator/ DNA binding / zinc ion binding	K.SI[pS]SAQFFGNQNR.D	1.55	0.05	55.9	No
AT4G10730.1	MAP4K6	ATP binding / kinase/ protein kinase/ protein serine/threonine kinase/ protein tyrosine kinase	K.SA[pS]VGNWILDSK.M	1.54	0.44	40.62	Yes
AT2G11890.1	adenylate cyclase		R.FLQNAAVSAA[pS]PSPPR.C	1.52	0.23	52.78	No
AT4G26070.1/ AT4G29810	MEK1/MKK2	MAP KINASE/ ERK KINASE 1; MAP kinase kinase/ kinase/ protein binding	K.FLTQSG[pT]FKDGDLR.V	1.51	0.13	42.93	Yes
AT5G40390.1	SIP1	seed imbibition 1-like; galactinol-sucrose galactosyltransferase/ hydrolase, hydrolyzing O-glycosyl compounds	K.SD[pS]GINGVDFTEK.F	1.51	0.08	71.34	No
AT5G54440.1	TRAPPII	tethering factor	R.TN[pS]SPGNFESPLDRPM#R.L	1.49	0.13	45.8	No
AT2G32240.1	unknown protein		R.DIDLSFS[pS]PTK.R	1.49	0.00	51.67	Yes
AT1G79090.1	unknown protein		R.***[pSSS]***SGNYDGM#LGFGDLR.E	1.47	0.09	75.29	No
AT5G35180.1	phosphoinositide binding		R.QS[pS]TLVNDVR.G	1.47	0.06	58.94	No
AT1G80210.1	unknown protein		R.***[pSSS]***ARGDNPELDTSDTATTSGSK.G	1.46	0.04	49.08	No
AT4G01480.1	AtPPa5	Arabidopsis thaliana pyrophosphorylase 5; inorganic diphosphatase/ pyrophosphatase	R.IL[pS]SLSK.R	1.45	0.08	40.67	No
AT4G26130.1	unknown protein		R.TT[pS]IGDGGEEGVDDK.A	1.45	0.05	65.15	No
At1g79570	Raf20	Protein kinase superfamily protein with octicosapeptide/Phox/Bem1p domain	R.NSTLLGLDS[***pSS***]ANNLAELDVR.N	1.21	0.07	50.92	Yes
AT1G11310.1	MLO2	MILDEW RESISTANCE LOCUS O 2; calmodulin binding	R.SVENYP[***pSS***]PSPR.Y	0.66	0.10	34.56	No
AT2G43680.2	IQD14	calmodulin binding	R.QNPLA[pS]PAPSYSQPQR.D	0.66	0.06	29.45	Yes
AT2G34680.1	AIR9	protein binding	K.V***[pSS***]PSAGSSPSVSSSIR.S	0.65	0.01	37.17	No
AT5G63640.1	VHS domain containing	VHS domain-containing protein / GAT domain-containing protein	K.ASNANTESS[pS]FISNR.A	0.65	0.06	55.1	Yes
AT4G05150.1	PB1domain containing	octicosapeptide/Phox/Bem1p (PB1) domain-containing protein	R.EVSTLSDPG[pS]PR.R	0.64	0.03	56.97	Yes
AT3G21100.1	RNA binding	RNA binding / nucleic acid binding / nucleotide binding	R.GNF[pS]PGSSPSGM#DSR.D	0.60	0.05	43.19	No
AT5G40450.1	unknown protein		K.LE[pS]PSEVSEETSK.T	0.58	0.15	74.54	Yes
AT5G13260.1	unknown protein		R.SS[pS]PANSPAVSVR.A	0.57	0.06	58.93	Yes
AT5G47060.1	senescence-associated protein-related		R.NSQSYYYNQYSVS[pS]PR.S	0.55	0.17	32.55	No
AT4G27450.1	unknown protein		R.VD[pS]EGVLCGANFK.V	0.51	0.13	82.81	Yes
AT3G13300.1	VCS	VARICOSE; nucleotide binding / protein homodimerization	K.TSGLPSQTSGAGSAYATLPQLPL[pS]PR.L	0.49	0.08	55.6	Yes
AT1G10140.1	unknown protein		R.IEEEEETEEG[pS]VNPK.V	0.36	0.13	51.31	No
AT1G77120.1	ADH1	ALCOHOL DEHYDROGENASE 1; alcohol dehydrogenase	R.IIGVDFN[pS]K.R	0.22	0.14	33.37	No

Table S2.1. Mannitol-responsive phosphopeptides showing 1.5-fold or greater change in phosphorylation following 5 min of treatment.

Table S2. 2

SI Table 2. Mannitol responsive phosoproteins in which a secondary non-changing peptide has been identified
(Colums 2-8 are copied from SI Table 1)

Count	ATG ID	Protein name	Protein Description	Peptide Sequence	Phosphorylation fold change; Average area ratio (treated/control)	Standard deviation	Mascot Score (max)	Alternate Peptide Identified	Average area ratio (treated/ control)	Standard Deviation	Mascot Score (max)
1	AT3G13300.1	VCS	VARICOSE; nucleotide binding / pro K.TP[pS]ADYSVDR.Q		5.69	1.346	48.8	**K.ISEGSEGEDQPQITGK.I**	0.91	0.040	37.55
2	AT1G08800.1	MYOB1	Myosin binding protein	K.ALLTQ[pS]ASR.G	5.65	0.092	46.54	R.GIEFL[pS]PR.D	0.82	single hit	37.82
								K.SVI[pS]FNHLPDVGYTELK.I	1.44	single hit	39.26
3	AT1G53165.1	MAP4Kalpha1	ATMAP4K ALPHA1; ATP binding / kiiR.SS[pS]ASEDSISNLAEAK.L		4.87	1.016	58.28	K.EFS[pS]NANFSPLAR.F	0.91	single hit	45.36
4	AT3G58730.1	V-ATPase D subunit	vacuolar ATP synthase subunit D (V-R.GI[pS]INAAR.N		3.39	0.458	56.26	**K.TSSFALTEVK.Y**	1.08	single hit	33.41
								R.RVNALENVVKPK.L	0.91	single hit	45.4
	AT1G64740.1/ AT1G50010.1/										
5	AT1G04820.1/ AT4G14960.1	TUA1/2/4/6	structural constituent of cytoskeletR.TIQFVDWCPTGFK.C		2.80	0.428	45.74	**R.TIQFVDWCPTGFK.C**	0.95	0.003	50.02
		TUA2/3/4/5/6						**R.AVFVDLEPTVIDEVR.T**	0.95	0.050	50.71
6	AT2G21230.1	bZIP30	bZIP family transcription factor	R.S[pS]GEDTSDWSNLVK.K	2.70	0.265	34.27	R.SVI[pS]M#DSCFM#GK.L	1.21	single hit	55.96
7	AT2G36380.1	PDR6	pleiotropic drug resistance 6, ATPasR.LP[pT]YDRLR.K		2.49	1.100		R.SLAGAA[**pS** K5]FRDVFAPPTDDVFGR.S	0.91	single hit	25.28
8	AT5G60660.1	PIP2;4	PLASMA MEMBRANE INTRINSIC PR1K.ALGSFGS[pS]FGSFR.S		2.48	0.152		**K.DLDVNESGPPAAR.D**	1.18	0.238	95.85
	AT5G60660.1	PIP2;4	PLASMA MEMBRANE INTRINSIC PR1K.ALGSFGS[pS]FGSFR.S		2.09	0.181		**R.YGGGANELADGYNK.G**	1.04	0.315	79.59
9	AT3G03050.1	CSLD3	CELLULOSE SYNTHASE-LIKE D3; cellR.[pS]NLSTNSDAAEAER.H		2.10	0.013	55.77	R.M#GGD[pS]DDDEEM#NLSLVPK.K	1.08	0.019	56.24
10	AT5G42950.1	GYF domain-containing protein		R.[**pS PSS**]DLLSILQGVTDR.S	2.00	0.328	33.11	K.DIQGSDNAIPL[pS]PQWLLSKPGENK.T	1.03	0.053	58.73
								R.[**pS ASS**]PSQAVSQSSSQSK.S	0.99	0.061	57.4
11	AT5G64430.1	PB1domain containing	octicosapeptide/Phox/Bem1p (PB1)R.LFLFPASSGFG[pS]QSSTQSDRDR.F		2.00	0.601	44.29	K.FSYNSYPDSTDS[pS]PR.S	0.92	0.055	61.44
								R.DQEQQQQQEAVYR.R	1.08	0.070	67.52
	AT5G19770.1/ AT5G19780.1	TUA3/5	structural constituent of cytoskeletR.TVQFVDWCP[pT]GFK.C		1.98	0.092	54.21	**R.TVQFVDWCPTGFK.C**	0.94	0.075	64.21
13	AT4G11740.1	SAY1	RabGTPase interacting	R.AASG[pS]LAPPNADR.S	1.92	0.120	29.08	R.LAAPS[pS]PFDDDSDDVDEQPLVR.H	0.97	4.37E-04	69.87
								R.SG[pS]PEEEHASINPAER.G	0.94	0.021	44.42
14	AT4G38900.1	bZIP29	bZIP family transcription factor	R.SF[pS]GGECADWSK.S	1.87	0.336	47.54	R.SV[pS]VDSCFM#EK.L	1.20	single hit	27.21
15	AT2G30930.1	unknown protein		K.[pS]LLQTFEAK.S	1.81	0.367	29.42	**K.ESVTSTAESVTASLTDAEK.T**	0.99	single hit	62.06
								K.LVGGVTNLVSGAS[pS]STVANR.D	1.04	0.015	65.29
16	AT1G67310.1	calmodulin binding / transcription regulator		R.VL[pS]M#SNSPEAR.Q	1.74	0.099	35.42	R.QDVESTED[pS]EDEDILK.V	1.05	0.103	46.31
17	AT1G72710.1	CKL2	CASEIN KINASE 1-LIKE PROTEIN 2; AK.DVVLSS[pS]FLR.A		1.70	0.230	45.5	R.NSPIVSSEINKL[**pS S**]PSR.A	0.84	single hit	41.54
18	AT1G35580.1	CINV1	cytosolic invertase 1; beta-fructofurR.AVG[pS]HC[pS]LSEMDDLDLTR.A		1.66	0.309		**K.STGDLTLSETPECQK.G**	1.13	0.310	69.56
19	AT4G24100.1	MAP4K5	ATP binding / kinase/ protein kinasR.[pS]DSNGNVEPVASER.E		1.60	0.063	56.5	K.SA[pS]VGNWLEPK.M	1.22	0.195	36.78
								R.ASSNSL[pS]APIK.Y	0.87	0.153	54.49
20	AT1G67230.1	LINC1	LITTLE NUCLEI1	R.[pS]VKDVVDDAK.A	1.59	0.094	34.81	K.AQEVAAD[pS]LSNLDVDGQSR.M	0.99	0.015	66.72
								K.EVEVTNVN[pS]DGDQ[pS]DINSK.A	0.99	single hit	36.85
								K.EVEVTNVN[pS]DGDQSDINSK.A	0.94	0.138	52.88
21	AT4G10730.1	MAP4K6	ATP binding / kinase/ protein kinasK.SA[pS]VGNWILDSK.M		1.54	0.441	40.62	R.ASANSL[pS]APIK.S	0.96	0.055	54.07
23	AT4G26070.1/ **AT4G29810**	MEK1/**MKK2**	MAP KINASE/ ERK KINASE 1; MAP kiK.FLTQSG[pT]FKDGDLR.V		1.51	0.126	42.93	R.ISQLEPEVLL[pS]PIKPADDQLSLSDLDMVK.V	0.99	0.081	37.44
24	AT2G32240.1	unknown protein		R.DIDLSF[pS]PTK.R	1.49	0.001	51.67	**K.ELQAAQSSIDEQK.Q**	0.91	single hit	28.84
								K.TDAILSQALSNNSELEQK.L	0.99	single hit	76.34
25	AT2G43680.2	IQD14	calmodulin binding	R.QNPLA[pS]PAPSYQPQR.D	0.66	0.057	29.45	R.[pS]LSPKPPT[pS]PR.A	0.92	single hit	26.8
								R.QNPLA[pS]PAPSY*SQPQR.D	0.90	single hit	38.26
26	AT5G63640.1	VHS domain-containing	VHS domain-containing protein / GrK.ASNANTESS[pS]FISNR.A		0.65	0.063	55.1	R.ESQSV[pS]PSSILQK.A	0.87	0.009	36.87
27	AT4G05150.1	PB1domain containing	octicosapeptide/Phox/Bem1p (PB1)R.EVSTLSDPG[pS]PR.R		0.64	0.028	56.97	R.[**pS T**]PELPPPVFIKPE[pS]PEPVSTPK.S	1.04	single hit	42.22
								R.EVSTL[pS]DPG[pS]PRR.D	1.10	single hit	24.19
28	AT5G40450.1	unknown protein		K.LE[pS]PSEVSEETSK.T	0.58	0.148	74.54	K.QSLDTP[pS]EEETSK.T	0.88	0.023	33.88
								R.DIESL[**pS S**]VSK.T	1.07	single hit	27.82
29	AT5G13260.1	unknown protein		R.SS[pS]PANSPAVSVR.A	0.57	0.058	58.93	R.LSDIELK[pS]PGGPK.I	0.98	single hit	28.52
								R.NQTTNPLPVA[pT]PK.T	0.86	single hit	40.17
30	AT4G27450.1	unknown protein		R.VD[pS]EGVLCGANFK.V	0.51	0.131	82.81	**K.LPEETLNDFLLR.Y**	0.86	single hit	25.73
31	At1g79570	Raf20	Protein kinase superfamily protein \	R.NSTLLGLDS[**pS S**]ANNLAELDVR.N	1.21	0.071	50.92	R.L[**pS KS** DNS **LSS**]QFVTSESPANTAQQDSGK.I	1.10	0.033	68.2

Peptides in **bold** are non-phosphorylated
Italicized residues represent non-localized phosphorylation sites.
'Single hit' indicates that peptide was only identified in Experiment 1 or Experiment 2 and thus no standard deviation can be calculated between biological replicates.

Table S2.2. Proteins with secondary peptide identifications for quantifying protein abundance.

SI Table 3. Phosphopeptides used for targeted SRM analysis
Transitions in **bold** were used for quantificaiton

Protein name	Endogenous Peptide	Q1 mass**	Transition 1 Fragment ion/mass	Transition 2 Fragment ion/mass	Transition 3 Fragment ion/mass	Heavy-labeled Standard Peptide	Q1 mass**	Transition 1 Fragment ion/mass	Transition 2 Fragment ion/mass	Transition 3 Fragment ion/mass
*ABF2 pS86	QG[pS]LTLPR	476.24	**y4 / 486.31**	y5 / 599.4	y6-Pho / 668.42	QG[pS]LTLP[R+10]	481.24	**y4 /496.31**	y5 /609.4	y6-Pho /678.42
ADH1 pS229	IIGVDFN[pS]K	536.76	**y5 / 690.26**	y7-Pho / 748.33	y8-Pho / 861.46	IIGVDFN[pS][K+08]	540.76	**y5 /698.26**	y7-Pho /756.33	y8-Pho /869.46
AHA1 pT948	GLDIDTAGHHY[pT]V	739.83	y8 / 965.4	y9 / 1080.43	**y9-Pho / 982.21**	GLDIDTAGHHY[pT][V+06]	742.83	y8 /971.4	y9 /1086.43	**y9-Pho /988.21**
AHA2 pT947	GLDIETPSHY[pT]V	706.32	**y6 / 783.32**	**y7 / 884.37**	**y8 / 1013.41**	GLDIETPSHY[pT][V+06]	709.32	**y6 /789.32**	**y7 /890.37**	**y8 /1019.41**
AHA2 pS899	EAVNIFPEKG[pS]YR	530.59, 795.38	**y11(2)-Pho / 646.12**	**y7-Pho / 818.42**	**y8-Pho / 965.49**	EAVNIFPEKG[pS]Y[R+10]	533.92, 800.38	**y11(2)-Pho /651.12**	**y7-Pho /828.42**	**y8-Pho /975.49**
AHA3 pT948	GLDIETAGHY[pT]V	678.3	**y7 / 828.34**	**y8 / 957.39**	y8-Pho / 859.25	GLDIETAGHY[pT][V+06]	681.3	**y7 /834.34**	**y8 /963.39**	y8-Pho /865.25
AHA3 pT882	[pT]LHGLQNTETANVVPER	653.66	**y3 / 401.22**	**y4 / 500.29**	**y6 / 713.4**	[pT]LHGLQNTETANVVPE[R+10]	656.99	**y3 /411.22**	**y4 /510.29**	**y6 /723.4**
*AHA4/11 pT959	GLDIETIQQAY[pT]V	765.86	**b3 / 286.14**	**b7 / 742.4**	y3-Pho / 364.19	GLDIETIQQAY[pT][V+06]	768.86	**b3 /286.14**	**b7 /742.4**	y3-Pho /370.19
AMT1 pS488	[pS]PSPSGANTTPTPV	696.81	**b10 / 980.37**	**y4 / 413.25**	**y5 / 514.3**	[pS]PSPSGANTTPTP[V+06]	699.81	**b10 / 980.37**	**y4 /419.25**	**y5 /520.3**
AREB3 pS43	ALG[pS]MNLDELLK	692.34	**y10-Pho / 1101.58**	**y10(2)-Pho / 551.21**	y11(2) / 607.75	ALG[pS]MNLDELL[K+08]	696.34	**y10-Pho /1109.58**	**y10(2)-Pho /555.21**	y11(2) /611.75
Vac14 pS624	AT[pS]GVPFSQYK	632.79	y4 / 525.28	y5 / 672.35	**y6 / 769.4**	AT[pS]GVPFSQY[K+08]	636.79	y4 /533.28	y5 /680.35	**y6 /777.4**
AT5G53420 pS204	LGAGLVQ[pS]PLDR	653.33	**y4 / 500.29**	**y6-Pho / 697.32**	**y7 / 894.42**	LGAGLVQ[pS]PLD[R+10]	658.34	**y4 /510.29**	**y6-Pho /707.32**	**y7 /904.42**
AT5G56980 pS61	AP[pS]IIDR	426.21	y3 / 403.24	**y5-Pho / 585.34**	**y6(2) / 390.69**	AP[pS]IID[R+10]	431.21	y3 /413.24	**y5-Pho /595.34**	**y6(2) / 395.63**
PEPC1 pS11	MA[pS]IDVHLR	561.27	**y5 / 639.34**	**y6 / 752.44**	**y7 / 919.44**	MA[pS]IDVH[L+06]R	564.272	**y5 /645.377**	**y6 /758.461**	**y7 /925.46**
bZIP30 pS176	SI[pS]GEDTSDWSNLVK	859.37	y7 / 861.45	**y8 / 948.49**	**y9 / 1049.53**	SI[pS]GEDTSDWSNLV[K+08]	863.377	y7 /869.461	**y8 /956.493**	**y9 /1057.54**
CAX4 pS38	TV[pS]ASSLIR	507.26	y5 / 575.36	y7 / 813.39	**y7-Pho / 715.42**	TV[pS]ASSLI[R+10]	512.26	y5 /585.36	y7 /823.39	**y7-Pho /725.42**
*CDPK5/6 pS552	NSLNI[pS]MR	507.73	**y4-Pho / 488.27**	**y5-Pho / 602.31**	**y6 / 813.37**	NSLNI[pS]M[R+10]	512.73	**y4-Pho /498.32**	**y5-Pho /612.32**	**y6 /823.38**
COP1 related pS24	LSLGGG[pS]ADFSK	609.78	y8-Pho / 750.36	**y9 / 905.35**	**y9-Pho / 807.38**	LSLGGG[pS]ADFS[K+08]	613.78	y8-Pho /758.36	**y9 /913.35**	**y9-Pho /815.38**
CPK9 pS78	SN[pS]ILENAFEDVK	773.35	b3-Pho / 271.12	y8 / 951.46	**y9 / 1064.54**	SN[pS]ILENAFEDV[K+08]	777.35	b3-Pho /271.12	y8 /959.46	**y9 /1072.54**
CPK9 pT37	SVEVGVTNQDPPSY[pT]PQAR	709.00, 1062.99	y8 / 999.44	y9 / 1096.49	**y9(2) / 548.72**	SVEVGVTNQDPPSY[pT]PQA[R+10]	712.33, 1067.99	y8 /1009.44	y9 /1106.49	**y9(2) / 553.72**
DaySleeper pS155	SQNNA[pS]PYVAFNQDK	881.88	y4 / 504.26	**y6 / 722.36**	y9 / 1081.55	SQNNA[pS]PYVAFNQD[K+08]	885.88	y4 /512.26	**y6 /730.36**	y9 /1089.55
Remorin pT58	ALAVVEKPIEEH[pT]PK	580.96	y10(2) / 644.3	**y11(2) / 693.82**	**y12(2) / 743.36**	ALAV[V+05]EKPIEEH[pT]PK	582.641	y10(2) /644.303	**y11(2) /696.345**	**y12(2) /745.879**
DUF593 pS825	ALLTQI[pS]ASR	570.3	**y7 / 842.39**	**y7-Pho / 744.41**	y8-Pho / 857.49	ALLTQI[pS]AS[R+10]	575.3	**y7 /852.39**	**y7-Pho /754.41**	y8-Pho /867.49
EIF4A1 pT145	VHACVGG[pT]SVR	611.77	**b3 / 308.17**	y6 / 656.28	**y9 / 986.41**	VHACVGG[pT]SV[R+10]	616.78	**b3 /308.17**	y6 /666.28	**y9 /996.42**
ERD14 pS59	VHI[pS]EPEPEVK	448.54	b5 / 646.26	**y4 / 472.28**	y6 / 698.37	VH[I+06][pS]EPEPEVK	450.553	b5 /652.28	**y4 /472.277**	y6 /698.372
FAC1 pS203	SH[pS]VSGDLHGVQPDPIAADILR	788.71	**y10 / 1080.63**	**y8 / 868.55**	y9 / 983.57	SH[pS]VSGDLHGVQPDPIAADI[L+06]R	790.723	**y10 / 1086.625**	**y8 /874.545**	y9 /989.572
GC5 pS793	QN[pS]AFENGSLPR	700.31	y6 / 643.36	**y7 / 772.4**	y8 / 919.47	QN[pS]AFENGSLP[R+10]	705.31	y6 /653.36	**y7 /782.4**	y8 /929.47
HSFB2B pS222	TT[pS]CTTAPELVEENER	639.60, 958.90	**y5 / 676.29**	y6 / 775.36	**y9 / 1114.54**	TT[pS]CTTAPELVEENE[R+10]	642.94, 963.9	**y5 /686.3**	y6 /785.37	**y9 /1124.55**
JAZ12 pS97	NSTSI[pS]PVSSPALNR	805.38	y5 / 570.34	**y7 / 744.41**	y9 / 940.53	NSTSI[pS]PVSSPALN[R+10]	810.39	y5 /580.34	**y7 /754.41**	y9 /950.53
MAP4Ka1 pS477††	S[pS]SASEDSISNLAEAK	559.25, 838.36	**y10 / 1047.55**	**y7 / 732.4**	**y7 / 732.4**	S[pS]SASEDSISNLAEA[K+08]	561.91, 842.36	**y10 1055.55**	**y7 /740.4**	**y7 /740.4**
MSL9 pS124	EQFGAG[pS]FAR	575.24	y5-Pho / 519.18	**y7 / 745.31**	**y8 / 892.38**	EQFGAG[pS]FA[R+10]	580.24	y5-Pho /529.18	**y7 /755.31**	**y8 /902.38**
NIA1 pS537	SV[pS]SPFMNTASK	668.29	y10 / 1149.46	y6 / 651.31	**y8 / 895.43**	SV[pS]SPFMNTAS[K+08]	672.29	y10 / 1157.48	y6 /659.33	**y8 /903.45**
NPC4 pT158	WFASVPAS[pT]QPNR	770.85	y10 / 1136.52	**y8 / 950.42**	**y8-Pho / 852.36**	WFASVPAS[pT]QPN[R+10]	775.85	y10 / 1146.52	**y8 /960.42**	**y8-Pho /862.36**
Oxidoreductase pS29	VQ[pS]LAESNLSSLPDR	848.41	y10 / 1117.56	**y11 / 1188.59**	**y9 / 988.51**	VQ[pS]LAESNLSSLPD[R+10]	853.41	y10 / 1127.56	**y11 / 1198.59**	**y9 /998.51**
PB1domain pS218	GF[pS]DSDTNVNR	646.26	y5 / 603.33	y7 / 805.39	**y9(2)-Pho / 495.36**	GF[pS]DSDTNVN[R+10]	651.26	y5 /613.33	y7 /815.39	**y9(2)-Pho /500.36**
PEN3 pS40	NIEDIFSSG[pS]R	652.78	**y6 / 720.27**	**y9 / 1077.42**	y9-Pho / 979.45	NIEDIFSSG[pS][R+10]	657.78	**y6 /730.28**	**y9 /1087.43**	y9-Pho /989.46
PIP3B pS274	ALASFR[pS]NPTN	629.29	b8-Pho / 829.26	y3 / 331.16	**y8 / 1002.41**	ALAS[F+10]R[pS]NPTN	634.29	b8-Pho /839.26	y3 /331.16	**y8 /1012.41**
PIP2F pS286	ALGSFGSFG[pS]FR	656.79	**y4-Pho / 448.25**	**y5 / 693.28**	y6 / 780.31†	ALGSFGSFG[pS]F[R+10]	661.79	**y4-Pho /458.25**	**y5 /703.28**	y6 /790.32†
PIP2F pS283	ALGSFG[pS]FGSFR	656.79	**y8-Pho / 886.34†**	y2 / 322.19†	**y7-Pho / 739.34†**	ALGSFG[pS]FGSF[R+10]	661.79	**y8-Pho /896.34†**	y2 /332.2†	**y7-Pho /749.34†**
YAK1 pY284	TVYS[pY]IQSR	598.77	**y6 / 833.36**	**y7 / 996.42**	y7(2) / 498.71	TVYS[pY]IQS[R+10]	603.78	**y6 /843.36**	**y7 /1006.43**	y7(2) /503.78
PLC2 pS280	EVP[pS]FIQR	528.25	y3 / 416.26	**y6 / 827.38**	**y6(2) / 414.19**	EVP[pS]FIQ[R+10]	533.25	y3 /426.27	**y6 /837.39**	**y6(2) /419.21**
PP2C-g pS347	SI[pS]AEGLDLLK	613.31	**y6 / 658.41**	**y7 / 787.46**	**y8 / 858.49**	SI[pS]AEGLDLL[K+08]	617.315	**y6 /666.428**	**y7 /795.47**	**y8 /866.507**
RAF18 pS671	TV[pS]GGGIETEAR	628.78	**y10 / 1056.44**	**y10-Pho / 958.47**	y5 / 605.3	TV[pS]GGGIETEA[R+10]	633.78	**y10 / 1066.44**	**y10-Pho /968.47**	y5 /615.3
RPS6 pS240	SRL[pS]SAAAKPSVTA	713.36	**b8 / 824.37**	**b8-Pho / 726.39**	**b9-Pho / 854.48**	SRL[pS]SAAAKPS[V+06]TA	716.37	**b8 /824.37**	**b8-Pho /726.4**	**b9-Pho /854.48**
SAY1 pS313	AA[pS]GSLAPPNADR	653.8	**y6 / 669.34**	**y7 / 740.38**	y8 / 853.46	AA[pS]GSLAPPNAD[R+10]	658.8	**y6 /679.34**	**y7 /750.38**	y8 /863.46
SIP1 pS11	SD[pS]GINGVDFTEK	724.8	y5 / 639.3	**y7 / 795.39**	**y8 / 909.43**	SD[pS]GINGVDFTE[K+08]	728.81	y5 /647.31	**y7 /803.4**	**y8 /917.45**
SnRK2.2 pS177	[pS]TVGTPAYIAPEILLR	594.32, 890.97	**b5-Pho / 428.43**	**y6 / 740.47**	**y6(2) / 370.79**	[pS]TVGTPAYIAPEILL[R+10]	597.65, 895.97	**b5-Pho /428.43**	**y6 /750.47**	**y6(2) /375.79**
SnRK2.3 pS176	[pS]TVGTPAYIAPEVLLR	589.65, 883.96	**y6 / 726.46**	**y7 / 797.5**	y8 / 910.58	[pS]TVGTPAYIAPEVLL[R+10]	592.98, 888.96	**y6 /736.46**	**y7 /807.5**	y8 /920.58
*SnRK2.4 pS158	[pS]TVGTPAYIAPEVLSR	580.96, 870.94	**b5-Pho / 428.21**	**y11 / 1215.68**	y6 / 700.41	[pS]TVGTPAYIAPEVLS[R+10]	584.29, 875.94	**b5-Pho /428.21**	**y11 / 1225.68**	y6 /710.41
SnRK2.6.1 pS175	[pS]TVGTPAYIAPEVLLK	580.32, 869.96	**y11 / 1213.73**	**y6 / 698.46**	y7 / 769.5	[pS]TVGTPAYIAPEVLL[K+08]	582.98, 873.96	**y11 / 1221.73**	**y6 /706.46**	y7 /777.5

TRP1 pS214	AP[pS]PVNNPLLGSLPK	792.41	**y10 / 1052.63**	**y8 / 824.52**	y9 / 938.56	AP[pS]PVNNPLLGS[L+06]PK	795.423	**y10 / 1058.63**	**y8 /830.544**	y9 /944.587
*TUA3/5 pT349	TVQPVDWCP[pT]GFK	555.58	**b5 / 575.32**	**y5 / 629.27**	y6 / 789.3	TVQPVDWCP[pT]G[F+10]K	558.92	**b5 /575.319**	**y5 /639.297**	y6 /799.327
*TUA4 pT349	TIQPVDWCP[pT]GFK	839.87	**y11(2) / 732.8**	**y5-Pho / 531.29**	**y8 / 1090.41**	TIQPVDWCP[pT]GF[K+08]	843.87	**y11(2) /736.81**	**y5-Pho /539.44**	**y8 /1098.42**
PICC pS124	DIDLSFS[pS]PTK	645.29	**y7 / 833.34**	y8 / 946.43	**y9 / 1061.46**	DIDLSFS[pS]PT[K+08]	649.29	**y7 /841.36**	y8 /954.44	**y9 /1069.47**
V-ATPase pS241	GI[pS]INAAR	441.22	y5 / 544.33	y6 / 711.33	**y6-Pho / 613.35**	GI[pS]INAA[R+10]	446.22	y5 /554.33	y6 /721.33	**y6-Pho /623.35**
VCS pS692	TP[pS]ADYSVDR	595.74	**y5 / 639.32**	y6 / 754.34	**y9(2) / 545.18**	TP[pS]ADYSVD[R+10]	600.74	**y5 /649.32**	y6 /764.34	**y9(2) /550.18**
WDL1 pS6	SLSENAPNVG[pS]AER	755.83	**y8 / 909.39**	y8-Pho / 811.28	y9 / 980.43	SLSENAPNVG[pS]AE[R+10]	760.83	**y8 / 919.39**	y8-Pho / 821.28	y9 / 990.43
ZAC pS155	TPAFLSSSL[pS]K	609.29	**y8-Pho / 850.34**	**y9(2) / 510.15**	**y9-Pho / 921.25**	TPAFLSSSL[pS]K[+08]	613.3	**y8-Pho /858.34**	**y9(2) /514.15**	**y9-Pho /929.25**
								10.007		

Key

Bold transitions were used for phosphopeptide quantification

*Peptides map to more than one gene family member

**Peptides with 2 Q1 masses represent +2 and +3 charge states

††MP4Ka1pS477 peptide standard was used to measure endogenous peaks but **MAPKa1pS478** position was later confirmed as true endogenous phosphorylation site and thus reported in Figure 6A

†fragment ion is not unique for phosphopeptide isoform but peptide has unique chromatographic behavior that was used to differentiate peaks

Table S2.3. SRM methods for the targeted analysis of 58 phosphopeptides.

Table S2. 4

S1 Table 4: Targeted SRM phosphorylation data for 9 experimental conditions

			Area ratios (Treated/control)																				
ATG ID	Name	Peptide	Cold	Cold_P-value	JA	JA_P-value	NaCl	NaCl_P-value	H2O2	H2O2_P-value	KCl	KCl_P-value	Fig22	Fig22_P-value	Mannitol	Mannitol_P-value	ABA	ABA_P-value	FC	FC_P-valu
AT1G45249	*ABF2 pS86	QG[pS]LTLPR	1.54	0.05616	1.49	0.05833	2.16	0.01954	1.91	0.00747	2.63	0.00041	2.68	0.00043	3.51	0.00006	6.09	0.00009	1.05	0.49606
AT1G77120	ADH1 pS229	IIGVDPNI[pS]K	1.18	0.05360	1.04	0.59935	0.83	0.30741	1.40	0.06990	1.76	0.18649	1.58	0.03103	1.40	0.05019	1.00	0.99965	0.97	0.82966
AT2G18960	AHA1 pT948	GLDIDTAGHHY[pT]V	0.72	0.07736	0.99	0.96492	1.01	0.94997	0.61	0.00042	1.14	0.08375	0.95	0.50525	0.81	0.00482	0.96	0.72596	1.87	0.00023
AT4G30190	AHA2 pT947	GLDIETPSHY[pT]V	0.71	0.02434	1.03	0.77230	0.88	0.23377	0.57	0.01011	1.11	0.38817	1.03	0.80693	0.78	0.08815	0.94	0.49484	1.54	0.00527
AT4G30190	AHA2 pS899	EAV[NIFPEKG[pS]YR	1.02	0.80161	1.15	0.17199	1.18	0.05659	1.24	0.11287	1.42	0.11772	1.43	0.03170	1.05	0.49487	0.95	0.56252	1.04	0.77261
AT5G57350	AHA3 pT948	GLDIETAGHY[pT]V	0.87	0.27175	1.05	0.65993	1.01	0.90946	1.02	0.90554	1.34	0.80000	1.08	0.54717	0.96	0.74445	0.89	0.55343	1.39	0.01999
AT5G57350	AHA3 pT882	[pT]LHGLQNTETANVVPER	0.86	0.32957	1.18	0.09655	0.98	0.79112	0.89	0.35921	1.35	0.15706	0.96	0.75195	0.95	0.67772	0.92	0.76037	1.29	0.18380
AT3G47950	*AHA4/11 pT959	GLDIETIGQAAY[pT]V	0.93	0.76556	1.08	0.74119	1.55	0.09968	0.75	0.09622	1.41	0.13614	1.08	0.59667	1.01	0.93552	0.97	0.70825	1.53	0.03733
AT4G13510	AMT1 pS488	[pS]PSPSGANTTPTPV	0.96	0.72536	1.12	0.35978	1.04	0.74127	0.93	0.76981	0.98	0.61716	0.95	0.83532	0.75	0.33237	0.96	0.61974	0.67	0.01476
AT3G56850	ARE83 pS43	ALG[pS]MNLDELLK	0.75	0.20469	1.70	0.01889	2.63	0.01590	0.98	0.91482	3.23	0.00011	1.42	0.05552	4.99	0.00111	12.95	0.00010	0.97	0.65463
AT2G01690	Vac14 pS524	ATI[pS]GVPFSQVK	0.67	0.04614	1.06	0.71025	3.65	0.00009	1.56	0.00014	3.66	0.00006	0.90	0.06437	5.18	0.00000	1.34	0.00966	1.06	0.41039
AT5G53420	AT5G53420 pS204	LGAGLVQL[pS]PLDR	1.40	0.06169	1.21	0.28771	1.16	0.49936	1.06	0.70894	0.92	0.49605	0.90	0.48288	0.88	0.38827	0.93	0.26336	0.90	0.13684
AT5G56980	AT5G56980 pS61	AP[pS]IIDR	0.59	0.03939	1.22	0.24176	1.13	0.36161	1.04	0.77373	1.64	0.01880	1.38	0.05070	1.50	0.02275	1.14	0.23208	1.31	0.00428
AT1G53310	PEPC1 pS11	MA[pS]IIDVHLR	1.13	0.44185	1.10	0.49273	1.34	0.11128	1.68	0.01497	1.32	0.07033	1.41	0.08217	1.05	0.76066	0.96	0.50804	1.18	0.02704
AT2G21230	bZIP30 pS176	S[pS]GEDTSDWSNLVK	0.81	0.22056	1.22	0.19304	1.87	0.00886	1.16	0.05232	1.86	0.00348	0.97	0.65989	2.17	0.00017	1.12	0.09132	1.16	0.00850
AT5G01490	CAX4 pS38	TV[pS]ASSLIR	0.88	0.22427	1.15	0.28861	1.14	0.28345	1.03	0.76527	1.40	0.02521	1.03	0.83128	1.06	0.63127	1.09	0.49463	1.27	0.03056
AT4G35310	*CDPK5/6 pS552	NSLN[pS]MR	0.82	0.23391	1.28	0.08455	0.80	0.17875	0.58	0.03000	0.90	0.48633	0.68	0.05106	0.81	0.18236	1.02	0.90434	1.14	0.23819
AT1G72410	COP1 related pS24	LSLGGG[pS]ADFSK	1.06	0.49388	1.31	0.07382	2.82	0.00094	1.23	0.03663	2.76	0.00002	1.12	0.41435	2.84	0.00013	1.35	0.06484	1.17	0.11624
AT3G20410	CPK9 pS78	SN[pS]LENAFEDVK	2.97	0.00006	1.32	0.11445	1.88	0.00192	3.60	0.00057	2.44	0.00004	3.26	0.00009	1.49	0.02692	0.98	0.85345	1.55	0.01346
AT3G20410	CPK9 pT37	SVEVGVTNDDPPS[pT]PQAR	1.23	0.01085	1.16	0.04786	1.14	0.16910	1.41	0.02172	1.09	0.52353	1.52	0.01097	0.94	0.68731	0.98	0.79640	1.21	0.04803
AT3G42170	DaySleeper pS155	SQNNA[pS]PYVAFNQDK	0.97	0.76923	1.30	0.05721	1.06	0.59431	0.96	0.71751	1.00	0.93375	1.10	0.34666	1.02	0.84957	0.91	0.32876	1.03	0.80991
AT2G45820	Remorin pT58	ALAVVERPIEH[pT]PK	1.37	0.03577	1.16	0.18728	1.24	0.20033	1.27	0.02780	1.39	0.02661	1.78	0.00198	1.02	0.79854	0.95	0.50061	1.09	0.19086
AT1G08800	DUF593 pS825	ALLTQI[pS]ASR	0.77	0.10343	1.08	0.61253	1.93	0.00482	1.26	0.06427	1.92	0.00009	0.84	0.25132	2.23	0.00142	1.08	0.28242	1.06	0.36440
AT3G13920	EIF4A1 pT145	VHAGVGG[pT]SVR	0.62	0.00243	1.15	0.18172	1.62	0.00008	1.95	0.01361	1.23	0.68449	0.82	0.16680	1.01	0.93773	0.95	0.58625	1.04	0.45694
AT1G76180	ERD14 pS59	VHI[pS]EPEEYK	0.82	0.04915	1.04	0.54512	0.90	0.23810	0.82	0.17022	1.00	0.66191	0.69	0.02202	0.69	0.00577	1.06	0.71262	0.97	0.74538
AT2G38280	FAC1 pS203	SH[pS]YSGDLHSVQPDPIAADLR	0.93	0.63549	1.13	0.34262	1.34	0.13219	2.12	0.00027	1.38	0.01836	1.32	0.03163	1.28	0.02985	1.03	0.79142	1.35	0.00787
AT1G79830	GC5 pS793	QN[pS]AFENGSLPR	1.41	0.01850	1.25	0.16425	1.94	0.00657	2.41	0.00062	2.16	0.00115	1.99	0.00021	1.95	0.00051	1.19	0.08279	1.16	0.04595
AT4G11660	HSFB2B pS222	TT[pS]CTTAPELVENER	1.16	0.25067	1.22	0.15139	2.41	0.00260	1.77	0.00101	2.29	0.00042	2.33	0.00039	2.67	0.00002	2.62	0.00161	1.04	0.38314
AT5G20900	JAZ12 pS97	NSTS[pS]PVSSPALNR	1.04	0.71527	0.37	0.00176	0.94	0.58029	1.14	0.69046	1.09	0.76304	1.13	0.69338	0.70	0.40052	1.03	0.92434	1.23	0.02410
AT1G53165	MAPKKK14 pS478	SS[pS]ASEDSISMLASAK	0.86	0.31423	1.27	0.04508	2.85	0.00039	0.94	0.60389	1.97	0.00019	1.15	0.32171	3.10	0.00127	1.40	0.00229	0.99	0.72232
AT5G19520	MSL9 pS124	EQFGAG[pS]FAR	0.47	0.01108	1.19	0.47318	1.02	0.85690	0.98	0.79254	1.60	0.00095	1.17	0.07681	1.31	0.11946	1.12	0.59989	1.27	0.11527
AT1G77760	NIA1 pS537	SV[pS]SPFMNTASK	0.91	0.24851	1.08	0.40682	1.24	0.03249	1.37	0.01414	0.94	0.42017	0.92	0.21986	0.96	0.57929	0.87	0.12157	0.94	0.44656
AT3G03530	NPC4 pT158	WFASVPAS[pT]EQPNR	0.89	0.42425	1.02	0.88008	0.92	0.59817	0.86	0.26610	1.19	0.13388	1.16	0.25538	0.85	0.22185	1.06	0.48258	1.04	0.61886
AT5G05600	Oxidoreductase pS29	YQLpS]LAESNLSSLPDR	1.37	0.15899	0.86	0.46560	1.39	0.23447	1.20	0.46729	1.16	0.49019	1.09	0.74261	1.44	0.25395	1.24	0.04540	1.25	0.02181
AT2G01190	PB1domain pS218	GF[pS]DSDTWNR	1.03	0.70338	1.12	0.47187	2.13	0.00027	0.94	0.79236	1.41	0.03179	1.06	0.79389	2.00	0.01117	1.02	0.85015	1.11	0.39132
AT1G59870	PEN3 pS40	NIEDIFSSE[pS]R	1.81	0.00499	2.76	0.00047	1.35	0.05844	4.98	0.00006	1.19	0.37797	6.32	0.00016	1.27	0.13425	0.91	0.27814	1.24	0.09160
AT2G16850	PIP3B pS274	ALASFR[pS]NPTN	0.84	0.04094	1.06	0.38068	1.07	0.36115	1.01	0.95163	1.81	0.04155	0.96	0.80144	1.12	0.44426	1.01	0.95174	1.35	0.22948
AT5G60660	PIP2F pS283	ALGSFG[pS]FGSFR	1.06	0.34980	1.06	0.28888	1.17	0.18108	0.77	0.17142	1.14	0.34001	0.89	0.48333	1.11	0.48014	1.16	0.03595	1.34	0.02054
AT5G60660	PIP2F pS286	ALGSFGSFG[pS]FR	1.09	0.35761	1.16	0.14534	1.25	0.07204	2.21	0.00049	1.29	0.13651	1.55	0.00755	1.80	0.00433	1.05	0.62596	1.50	0.00623
AT5G35980	YAK1 pT284	TVYS[pT]PTGSR	0.98	0.86146	1.19	0.17143	1.01	0.91275	0.79	0.01730	0.86	0.14805	0.87	0.04315	0.78	0.02133	0.90	0.15204	0.97	0.70927
AT3G08510	PLC2 pS280	EVP[pS]FQR	1.68	0.00401	1.19	0.14592	1.44	0.06454	2.66	0.00035	1.48	0.00058	2.36	0.00024	1.26	0.02250	1.00	0.93815	1.16	0.06257
AT3G51470	PP2C-g pS347	SI[pS]AEGLDLLK	0.87	0.14866	1.11	0.50511	1.08	0.50570	1.09	0.74671	1.14	0.55641	1.00	0.99216	1.07	0.79338	0.90	0.46457	1.04	0.71812
AT1G16270	RAF18 pS671	TV[pS]GGGIETEAR	0.93	0.58272	1.12	0.37536	2.04	0.00360	1.08	0.29891	1.64	0.00039	0.98	0.76991	1.85	0.00042	0.93	0.19279	1.03	0.13774
AT4G31700	RPS6 pS240	SRL[pS]SAAAKPSVTA	1.07	0.35525	1.18	0.30857	0.98	0.83399	1.21	0.07230	1.05	0.63113	0.96	0.67328	0.92	0.37351	1.04	0.68488	1.17	0.16410
AT4G11740	SAY1 pS313	AA[pS]GSLAPPNADR	1.02	0.92742	1.06	0.73196	1.94	0.00308	1.59	0.00248	1.95	0.00094	1.69	0.00099	2.19	0.00013	1.09	0.09182	1.08	0.32404
AT5G40390	SIP1 pS11	SD[pS]IGNGVDFTEK	1.39	0.00080	1.07	0.28570	1.30	0.04210	1.31	0.00280	1.48	0.00121	1.26	0.01905	1.22	0.04439	0.95	0.42224	1.15	0.01172
AT3G50500	SnRK2.2 pS177	[pS]TVGTPAYVAPELLR	0.62	0.04899	1.30	0.12246	0.96	0.84428	0.86	0.43342	1.19	0.61999	1.15	0.41421	1.46	0.04849	6.14	0.00017	0.73	0.00129
AT5G66880	SnRK2.3 pS176	[pS]TVGTPAYVAPEVLR	0.82	0.21259	1.21	0.18236	1.02	0.89656	1.01	0.95348	1.33	0.38921	0.95	0.73011	1.27	0.10946	4.74	0.00020	0.76	0.00188
AT1G10940	*SnRK2.4 pS158	[pS]TVGTPAYVAPEVLSR	0.54	0.02345	1.08	0.62556	1.89	0.00359	2.50	0.00159	2.01	0.02187	0.90	0.15587	3.51	0.00059	1.83	0.00318	1.21	0.02613
AT4G33950	SnRK2.6 pS175	[pS]TVGTPAYIAPEVLLK	0.87	0.48937	1.39	0.11100	1.05	0.82794	1.59	0.02930	1.84	0.03425	1.08	0.40229	1.52	0.00187	6.29	0.00031	0.86	0.07866
AT1G80490	TRP1 pS214	AP[pS]PVNNPLLGSLPK	0.99	0.93906	1.16	0.16536	1.03	0.75712	0.96	0.56459	1.05	0.69448	1.10	0.27461	0.98	0.67599	0.94	0.33244	1.03	0.47760
AT5G19770	*TUA3 pT349	TVQFVDWCP[pT]GFK	1.33	0.06432	1.30	0.08870	1.95	0.00598	1.39	0.06184	1.33	0.03874	1.01	0.91491	1.72	0.97247	0.97	0.74277	0.83	0.08701
AT1G04820	*TUA4 pT349	TIQFVDWCP[pT]GFK	1.19	0.22244	1.37	0.04863	2.42	0.00068	1.55	0.03284	1.64	0.01283	1.13	0.44145	2.17	0.00582	0.99	0.94731	1.02	0.75981
AT2G32240	PICC pS124	DIDLSFS[pS]PIK	1.48	0.00807	1.24	0.09597	1.35	0.10764	1.21	0.02949	1.35	0.00460	2.34	0.00057	1.35	0.01263	0.95	0.51112	1.19	0.01780
AT3G58730	V-ATPase pS241	GI[pS]INAAR	1.81	0.00651	1.14	0.20110	2.17	0.00276	1.90	0.00036	2.31	0.00166	1.72	0.00101	2.56	0.00063	1.03	0.69072	1.19	0.11620
AT3G13300	VCS pS692	TP[pS]ADYSVDR	0.86	0.40525	1.20	0.25788	2.53	0.00204	1.03	0.74762	2.07	0.01252	0.97	0.17393	2.66	0.00000	0.99	0.92720	1.03	0.73894
AT3G04630	WD1 pS6	SLSENAPNVG[pS]AER	1.06	0.63614	1.30	0.10169	0.99	0.90427	1.21	0.17464	1.16	0.43363	1.29	0.22151	0.88	0.46852	0.80	0.16401	1.25	0.09109
AT4G21160	ZAC pS155	TPAFLSSSLp[pS]K	0.68	0.04343	1.29	0.09032	0.82	0.24498	1.02	0.79791	0.98	0.70477	1.03	0.79424	0.91	0.35311	1.08	0.05267	1.27	0.00095

*Peptides map to more than one gene family member

Table S2.4. SRM selective reaction monitoring phosphorylation data for the nine experimental conditions.

Table S2. 5

SI Table 5. Experimental details for gene expression studies used in Geneinve

Treatment	Code	Treatment length	Treatment concentration	Tissue
ABA	AT-00110	3 hrs	10 microM	seedlings
MethyJasmo	AT-00110	1 hr	10 microM	seedlings
Hydrogen Pe	AT-00185	1 hr	20 mM	seedlings
Cold	AT-00221	24 hrs	4 C	seedlings
Flg22	AT-00253	1 hr	1 microM	seedlings
NaCl	AT-00120	6-24 hrs	150 mM	root samples
Mannitol	AT-00120	6-24 hrs	300 mM	root samples
NaCl	AT-00120	6-24 hrs	150 mM	green tissue
Mannitol	AT-00120	6-24 hrs	300 mM	green tissue

Genevestigator experiments used in SI Figure 1 heatmap

Code
AT-00058
AT-00120
AT-00199
AT-00262
AT-00290
AT-00292
AT-00403
AT-00411
AT-00419
AT-00520
AT-00530
AT-00534
AT-00560
AT-00626
AT-00637

Table S2.5. Experimental details for gene expression studies used in Genevestigator mRNA analysis.

References

Bahn YS (2008) Master and commander in fungal pathogens: the two-component system and the HOG signaling pathway. Eukaryot Cell **7:** 2017-2036

Bak G, Lee EJ, Lee Y, Kato M, Segami S, Sze H, Maeshima M, Hwang JU, Lee Y (2013) Rapid structural changes and acidification of guard cell vacuoles during stomatal closure require phosphatidylinositol 3,5-bisphosphate. Plant Cell **25:** 2202-2216

Bonangelino CJ, Nau JJ, Duex JE, Brinkman M, Wurmser AE, Gary JD, Emr SD, Weisman LS (2002) Osmotic stress-induced increase of phosphatidylinositol 3,5-bisphosphate requires Vac14p, an activator of the lipid kinase Fab1p. J Cell Biol **156:** 1015-1028

Boudsocq M, Sheen J (2013) CDPKs in immune and stress signaling. Trends Plant Sci **18:** 30-40

Brodersen P, Sakvarelidze-Achard L, Bruun-Rasmussen M, Dunoyer P, Yamamoto YY, Sieburth L, Voinnet O (2008) Widespread translational inhibition by plant miRNAs and siRNAs. Science **320:** 1185-1190

Champion A, Picaud A, Henry Y (2004) Reassessing the MAP3K and MAP4K relationships. Trends Plant Sci **9:** 123-129

Charrier B, Champion A, Henry Y, Kreis M (2002) Expression profiling of the whole Arabidopsis shaggy-like kinase multigene family by real-time reverse transcriptase-polymerase chain reaction. Plant Physiol **130:** 577-590

Cheong YH, Sung SJ, Kim BG, Pandey GK, Cho JS, Kim KN, Luan S (2010) Constitutive overexpression of the calcium sensor CBL5 confers osmotic or drought stress tolerance in Arabidopsis. Mol Cells **29:** 159-165

Dereeper A, Guignon V, Blanc G, Audic S, Buffet S, Chevenet F, Dufayard JF, Guindon S, Lefort V, Lescot M, Claverie JM, Gascuel O (2008) Phylogeny.fr: robust phylogenetic analysis for the non-specialist. Nucleic Acids Res **36:** W465-469

Deyholos MK (2010) Making the most of drought and salinity transcriptomics. Plant Cell Environ **33:** 648-654

Dodd AN, Kudla J, Sanders D (2010) The language of calcium signaling. Annu Rev Plant Biol **61:** 593-620

Dove SK, Cooke FT, Douglas MR, Sayers LG, Parker PJ, Michell RH (1997) Osmotic stress activates phosphatidylinositol-3,5-bisphosphate synthesis. Nature **390:** 187-192

Dove SK, Johnson ZE (2007) Our FABulous VACation: a decade of phosphatidylinositol 3,5-bisphosphate. Biochem Soc Symp**:** 129-139

Dubiella U, Seybold H, Durian G, Komander E, Lassig R, Witte CP, Schulze WX, Romeis T (2013) Calcium-dependent protein kinase/NADPH oxidase activation circuit is required for rapid defense signal propagation. Proc Natl Acad Sci U S A **110:** 8744-8749

Duex JE, Nau JJ, Kauffman EJ, Weisman LS (2006) Phosphoinositide 5-phosphatase Fig 4p is required for both acute rise and subsequent fall in stress-induced phosphatidylinositol 3,5-bisphosphate levels. Eukaryot Cell **5:** 723-731

Franks TM, Lykke-Andersen J (2008) The control of mRNA decapping and P-body formation. Mol Cell **32:** 605-615

Franz S, Ehlert B, Liese A, Kurth J, Cazale AC, Romeis T (2011) Calcium-dependent protein kinase CPK21 functions in abiotic stress response in Arabidopsis thaliana. Mol Plant **4:** 83-96

Fricke W, Akhiyarova G, Wei W, Alexandersson E, Miller A, Kjellbom PO, Richardson A, Wojciechowski T, Schreiber L, Veselov D, Kudoyarova G, Volkov V (2006) The short-term growth response to salt of the developing barley leaf. J Exp Bot **57:** 1079-1095

Fujii H, Verslues PE, Zhu JK (2011) Arabidopsis decuple mutant reveals the importance of SnRK2 kinases in osmotic stress responses in vivo. Proc Natl Acad Sci U S A **108:** 1717-1722

Fujii H, Zhu JK (2009) Arabidopsis mutant deficient in 3 abscisic acid-activated protein kinases reveals critical roles in growth, reproduction, and stress. Proc Natl Acad Sci U S A **106:** 8380-8385

Fujita S, Pytela J, Hotta T, Kato T, Hamada T, Akamatsu R, Ishida Y, Kutsuna N, Hasezawa S, Nomura Y, Nakagami H, Hashimoto T (2013) An atypical tubulin kinase mediates stress-induced microtubule depolymerization in Arabidopsis. Curr Biol **23:** 1969-1978

Geiger D, Scherzer S, Mumm P, Stange A, Marten I, Bauer H, Ache P, Matschi S, Liese A, Al-Rasheid KA, Romeis T, Hedrich R (2009) Activity of guard cell anion channel SLAC1 is controlled by drought-stress signaling kinase-phosphatase pair. Proc Natl Acad Sci U S A **106:** 21425-21430

Haruta M, Sabat G, Stecker K, Minkoff BB, Sussman MR (2014) A peptide hormone and its receptor protein kinase regulate plant cell expansion. Science **343:** 408-411

Haruta M, Sussman MR (2012) The effect of a genetically reduced plasma membrane protonmotive force on vegetative growth of Arabidopsis. Plant Physiol **158:** 1158-1171

Ho CY, Alghamdi TA, Botelho RJ (2012) Phosphatidylinositol-3,5-bisphosphate: no longer the poor PIP2. Traffic **13:** 1-8

Hohmann S (2002) Osmotic stress signaling and osmoadaptation in yeasts. Microbiol Mol Biol Rev **66:** 300-372

Huttlin EL, Hegeman AD, Harms AC, Sussman MR (2007) Comparison of full versus partial metabolic labeling for quantitative proteomics analysis in Arabidopsis thaliana. Mol Cell Proteomics **6:** 860-881

Ichimura K, Tena G, Henry Y, Zhang Z, Hirt H, Wilscon C, Morris P, Mundy J, Innes R, Ecker JR (2002) Mitogen-activated protein kinase cascade in plants: a new nomenclature. Trends Plant Sci **7:** 301-308

Jakoby M, Weisshaar B, Droge-Laser W, Vicente-Carbajosa J, Tiedemann J, Kroj T, Parcy F (2002) bZIP transcription factors in Arabidopsis. Trends Plant Sci **7:** 106-111

Jiang Y, Yang B, Harris NS, Deyholos MK (2007) Comparative proteomic analysis of NaCl stress-responsive proteins in Arabidopsis roots. J Exp Bot **58:** 3591-3607

Jinek M, Eulalio A, Lingel A, Helms S, Conti E, Izaurralde E (2008) The C-terminal region of Ge-1 presents conserved structural features required for P-body localization. RNA **14:** 1991-1998

Jonas S, Izaurralde E (2013) The role of disordered protein regions in the assembly of decapping complexes and RNP granules. Genes Dev **27:** 2628-2641

Kawaguchi R, Girke T, Bray EA, Bailey-Serres J (2004) Differential mRNA translation contributes to gene regulation under non-stress and dehydration stress conditions in Arabidopsis thaliana. Plant J **38:** 823-839

Kline KG, Barrett-Wilt GA, Sussman MR (2010) In planta changes in protein phosphorylation induced by the plant hormone abscisic acid. Proc Natl Acad Sci U S A **107:** 15986-15991

Kumar MN, Jane WN, Verslues PE (2013) Role of the putative osmosensor Arabidopsis histidine kinase1 in dehydration avoidance and low-water-potential response. Plant Physiol **161:** 942-953

McLoughlin F, Galvan-Ampudia CS, Julkowska MM, Caarls L, van der Does D, Lauriere C, Munnik T, Haring MA, Testerink C (2012) The Snf1-related protein

kinases SnRK2.4 and SnRK2.10 are involved in maintenance of root system architecture during salt stress. Plant J **72:** 436-449

Meijer HJ, Divecha N, van den Ende H, Musgrave A, Munnik T (1999) Hyperosmotic stress induces rapid synthesis of phosphatidyl-D-inositol 3,5-bisphosphate in plant cells. Planta **208:** 294-298

Minkoff BB, Burch HL, Sussman MR (2014) A pipeline for 15N metabolic labeling and phosphoproteome analysis in Arabidopsis thaliana. Methods Mol Biol **1062:** 353-379

Munnik T (2014) PI-PLC: Phosphoinositide-Phospholipase C in Plant Signaling. *In* Phospholipases in Plant Signaling. Springer, pp 27-54

Munnik T, Vermeer JE (2010) Osmotic stress-induced phosphoinositide and inositol phosphate signalling in plants. Plant Cell Environ **33:** 655-669

Nick P (2008) Microtubules as Sensors for Abiotic Stimuli. *In* P Nick, ed, Plant Microtubules, Vol 11. Springer Berlin Heidelberg, pp 175-203

Nuhse TS, Bottrill AR, Jones AM, Peck SC (2007) Quantitative phosphoproteomic analysis of plasma membrane proteins reveals regulatory mechanisms of plant innate immune responses. Plant J **51:** 931-940

Olsson A, Svennelid F, Ek B, Sommarin M, Larsson C (1998) A phosphothreonine residue at the C-terminal end of the plasma membrane H+-ATPase is protected by fusicoccin-induced 14-3-3 binding. Plant Physiol **118:** 551-555

Park SK, Venable JD, Xu T, Yates JR, 3rd (2008) A quantitative analysis software tool for mass spectrometry-based proteomics. Nat Methods **5:** 319-322

Park SY, Fung P, Nishimura N, Jensen DR, Fujii H, Zhao Y, Lumba S, Santiago J, Rodrigues A, Chow TF, Alfred SE, Bonetta D, Finkelstein R, Provart NJ, Desveaux D, Rodriguez PL, McCourt P, Zhu JK, Schroeder JI, Volkman BF, Cutler SR (2009) Abscisic acid inhibits type 2C protein phosphatases via the PYR/PYL family of START proteins. Science **324:** 1068-1071

Peremyslov VV, Morgun EA, Kurth EG, Makarova KS, Koonin EV, Dolja VV (2013) Identification of myosin XI receptors in Arabidopsis defines a distinct class of transport vesicles. Plant Cell **25:** 3022-3038

Rodriguez MC, Petersen M, Mundy J (2010) Mitogen-activated protein kinase signaling in plants. Annu Rev Plant Biol **61:** 621-649

Ross PL, Huang YN, Marchese JN, Williamson B, Parker K, Hattan S, Khainovski N, Pillai S, Dey S, Daniels S, Purkayastha S, Juhasz P, Martin S, Bartlet-Jones M, He F, Jacobson A, Pappin DJ (2004) Multiplexed protein quantitation in

Saccharomyces cerevisiae using amine-reactive isobaric tagging reagents. Mol Cell Proteomics **3:** 1154-1169

Sato A, Sato Y, Fukao Y, Fujiwara M, Umezawa T, Shinozaki K, Hibi T, Taniguchi M, Miyake H, Goto DB, Uozumi N (2009) Threonine at position 306 of the KAT1 potassium channel is essential for channel activity and is a target site for ABA-activated SnRK2/OST1/SnRK2.6 protein kinase. Biochem J **424:** 439-448

Segonzac C, Zipfel C (2011) Activation of plant pattern-recognition receptors by bacteria. Curr Opin Microbiol **14:** 54-61

Shabala S, Shabala L (2011) Ion transport and osmotic adjustment in plants and bacteria. BioMolecular Concepts **2:** 407-419

Shabala SN, Lew RR (2002) Turgor regulation in osmotically stressed Arabidopsis epidermal root cells. Direct support for the role of inorganic ion uptake as revealed by concurrent flux and cell turgor measurements. Plant Physiol **129:** 290-299

Steinhorst L, Kudla J (2013) Calcium and reactive oxygen species rule the waves of signaling. Plant Physiol **163:** 471-485

Su SH, Bush SM, Zaman N, Stecker K, Sussman MR, Krysan P (2013) Deletion of a tandem gene family in Arabidopsis: increased MEKK2 abundance triggers autoimmunity when the MEKK1-MKK1/2-MPK4 signaling cascade is disrupted. Plant Cell **25:** 1895-1910

Sugiyama N, Masuda T, Shinoda K, Nakamura A, Tomita M, Ishihama Y (2007) Phosphopeptide enrichment by aliphatic hydroxy acid-modified metal oxide chromatography for nano-LC-MS/MS in proteomics applications. Mol Cell Proteomics **6:** 1103-1109

Sunkar R, Li YF, Jagadeeswaran G (2012) Functions of microRNAs in plant stress responses. Trends Plant Sci **17:** 196-203

Taylor NL, Fenske R, Castleden I, Tomaz T, Nelson CJ, Millar AH (2014) Selected reaction monitoring to determine protein abundance in Arabidopsis using the Arabidopsis proteotypic predictor. Plant Physiol **164:** 525-536

Tominaga M, Kimura A, Yokota E, Haraguchi T, Shimmen T, Yamamoto K, Nakano A, Ito K (2013) Cytoplasmic streaming velocity as a plant size determinant. Dev Cell **27:** 345-352

Torres MA, Jones JD, Dangl JL (2006) Reactive oxygen species signaling in response to pathogens. Plant Physiol **141:** 373-378

Tran LS, Urao T, Qin F, Maruyama K, Kakimoto T, Shinozaki K, Yamaguchi-Shinozaki K (2007) Functional analysis of AHK1/ATHK1 and cytokinin receptor histidine kinases in response to abscisic acid, drought, and salt stress in Arabidopsis. Proc Natl Acad Sci U S A **104:** 20623-20628

Tsugama D, Liu S, Takano T (2012) A bZIP protein, VIP1, is a regulator of osmosensory signaling in Arabidopsis. Plant Physiol **159:** 144-155

Umezawa T, Sugiyama N, Mizoguchi M, Hayashi S, Myouga F, Yamaguchi-Shinozaki K, Ishihama Y, Hirayama T, Shinozaki K (2009) Type 2C protein phosphatases directly regulate abscisic acid-activated protein kinases in Arabidopsis. Proc Natl Acad Sci U S A **106:** 17588-17593

Umezawa T, Sugiyama N, Takahashi F, Anderson JC, Ishihama Y, Peck SC, Shinozaki K (2013) Genetics and phosphoproteomics reveal a protein phosphorylation network in the abscisic acid signaling pathway in Arabidopsis thaliana. Sci Signal **6:** rs8

Urano K, Kurihara Y, Seki M, Shinozaki K (2010) 'Omics' analyses of regulatory networks in plant abiotic stress responses. Curr Opin Plant Biol **13:** 132-138

Urao T, Yakubov B, Satoh R, Yamaguchi-Shinozaki K, Seki M, Hirayama T, Shinozaki K (1999) A transmembrane hybrid-type histidine kinase in Arabidopsis functions as an osmosensor. Plant Cell **11:** 1743-1754

van Gisbergen PA, Li M, Wu SZ, Bezanilla M (2012) Class II formin targeting to the cell cortex by binding PI(3,5)P(2) is essential for polarized growth. J Cell Biol **198:** 235-250

Van Oosten MJ, Sharkhuu A, Batelli G, Bressan RA, Maggio A (2013) The Arabidopsis thaliana mutant air1 implicates SOS3 in the regulation of anthocyanins under salt stress. Plant Mol Biol **83:** 405-415

Wang C, Li J, Yuan M (2007) Salt tolerance requires cortical microtubule reorganization in Arabidopsis. Plant Cell Physiol **48:** 1534-1547

Wang C, Zhang L, Chen W (2011) Plant cortical microtubules are putative sensors under abiotic stresses. Biochemistry (Mosc) **76:** 320-326

Weber C, Nover L, Fauth M (2008) Plant stress granules and mRNA processing bodies are distinct from heat stress granules. Plant J **56:** 517-530

Wessel D, Flugge UI (1984) A method for the quantitative recovery of protein in dilute solution in the presence of detergents and lipids. Anal Biochem **138:** 141-143

Wohlbach DJ, Quirino BF, Sussman MR (2008) Analysis of the Arabidopsis histidine kinase ATHK1 reveals a connection between vegetative osmotic stress sensing and seed maturation. Plant Cell **20:** 1101-1117

Xiong L, Zhu JK (2002) Molecular and genetic aspects of plant responses to osmotic stress. Plant Cell Environ **25:** 131-139

Xu J, Chua NH (2012) Dehydration stress activates Arabidopsis MPK6 to signal DCP1 phosphorylation. EMBO J **31:** 1975-1984

Xue L, Wang P, Wang L, Renzi E, Radivojac P, Tang H, Arnold R, Zhu JK, Tao WA (2013) Quantitative measurement of phosphoproteome response to osmotic stress in arabidopsis based on Library-Assisted eXtracted Ion Chromatogram (LAXIC). Mol Cell Proteomics **12:** 2354-2369

Yoon JH, Choi EJ, Parker R (2010) Dcp2 phosphorylation by Ste20 modulates stress granule assembly and mRNA decay in Saccharomyces cerevisiae. J Cell Biol **189:** 813-827

Yoshida T, Fujita Y, Sayama H, Kidokoro S, Maruyama K, Mizoi J, Shinozaki K, Yamaguchi-Shinozaki K (2010) AREB1, AREB2, and ABF3 are master transcription factors that cooperatively regulate ABRE-dependent ABA signaling involved in drought stress tolerance and require ABA for full activation. Plant J **61:** 672-685

Zimmermann P, Hirsch-Hoffmann M, Hennig L, Gruissem W (2004) GENEVESTIGATOR. Arabidopsis microarray database and analysis toolbox. Plant Physiol **136:** 2621-2632

Zonia L, Munnik T (2004) Osmotically induced cell swelling versus cell shrinking elicits specific changes in phospholipid signals in tobacco pollen tubes. Plant Physiol **134:** 813-823

Zonia L, Munnik T (2007) Life under pressure: hydrostatic pressure in cell growth and function. Trends Plant Sci **12:** 90-97

CHAPTER 3

Genetic Characterization of Vac14, a Vacuolar Protein that Regulates Phosphatidylinositol 3,5 bisphosphate Biosynthesis and is Rapidly Phosphorylated in Response to Osmotic Stress.

This chapter represents a publication in preparation

Kelly E. Stecker, Magdalena Murray, Michael R. Sussman

Abstract

In the previous chapter, I demonstrated that the protein Vac14 was rapidly phosphorylated in response to osmotic stress in Arabidopsis seedlings and that the increase in this posttranslational modification was the greatest of all phosphorylated proteins identified in the discovery work. In this chapter I describe targeted reverse genetic experiments in which the gene encoding Vac14 was either knocked out, knocked down or overexpressed in Arabidopsis. These results demonstrate that Vac14 is an essential gene and that when plants expressed increased levels of Vac14 mRNA, large changes in vacuolar size and in the ability to control cellular water content were observed. Plants overexpressing Vac14 had pleiotropic growth defects including smaller leaves with greater water content and an increased ability for the plant to withstand drought. Equally important, I observed dramatic changes in the gravitropic response of shoots in plants with altered levels of Vac14 expression. These gravitropic phenotypes are consistent with other published vacuolar associated mutants that have significant defects in shoot gravitropism. These observations are discussed within the context of phosphoinositide signaling and its hypothesized role in vacuolar biology and on turgor mediated growth in plants.

Background

Phospholipid bilayers in living organisms consist of heterogeneous mixtures of lipid chains with various polar head groups. Phosphatidylinositol (PtdIns) represents one type of lipid species present in bilayers. The inositol head group of PtdIns can be phosphorylated at various positions to generate low abundance derivatives that have very important and diverse roles in cell biology, regulating processes such as vesicle trafficking and cell signaling (1, 2). The reversible phosphorylation state of PtdIns lipids allow them to function as transient signaling molecules in the membrane, acting as recruitment hubs for effector proteins that bind to specific PtdIns species (3, 4).

Singularly phosphorylated PtdIns molecules can undergo subsequent phosphorylation at specific positions to generate an additional class of signaling molecules. One of these doubly phosphorylated derivatives, phosphatidylinositol 3,5-bisphosphate ($PI(3,5)P_2$), has become increasingly of interest in recent years as scientists have realized its vital influence in cell biology(2, 4). $PI(3,5)P_2$ is present at very low levels in the cell (<0.01%) and is primarily localized to the endomembrane system (2). In yeast, $PI(3,5)P_2$ is localized to the vacuole and controls vacuole shape, fragmentation, and acidification through recruitment of protein complexes and direct regulation of ion channels and pumps (5). $PI(3,5)P_2$ is also involved in nutrient sensing through regulation of mTOR and recruitment of mTOR substrates to the vacuole membrane (3). In humans, $PI(3,5)P_2$ is localized to the lysosome and early and late endosomes and is essential for maintaining endomembrane homeostasis (6). $PI(3,5)P_2$ is required for proper lysosomal function and for vesicle maturation, trafficking, and fusion events in humans and mice(4). The similar role of $PI(3,5)P_2$ in yeast and mammals suggest a conserved function for $PI(3,5)P_2$ in all eukaryotes. Very little is known about the role of

$PI(3,5)P_2$ in plants, but its function in vacuole and endomembrane regulation is likely also conserved.

$PI(3,5)P_2$ levels are dynamically regulated in response to stimuli. The initial discovery of $PI(3,5)P_2$ less than 20 years ago arose from the finding that $PI(3,5)P_2$ levels are rapidly elevated by hyperosmotic stress. In yeast $PI(3,5)P_2$ levels increase 20-fold within minutes of exposure to hyperosmotic stress and this increase is essential for vacuolar volume adjustment (7-9). Mammalian adipocytes experiencing hyperosmotic stress also boost $PI(3,5)P_2$ levels within minutes (10); however, this response is not ubiquitous across all cell types in animals (11). It has been documented that osmotic stress induces $PI(3,5)P_2$ production in plant cell culture and pollen tubes, similar to observations in yeast and mammalian cells, but its effect or function is not well understood (12, 13).

The cellular machinery that controls $PI(3,5)P_2$ biosynthesis is highly conserved. $PI(3,5)P_2$ is generated through phosphorylation of precursor molecule phosphatidylinositol 3-phosphate (PI3P) by a trimolecular protein complex. In this complex, PI3P-5 kinase Fab1, responsible for $PI(3,5)P_2$ production, is bound by scaffold protein Vac14 along with $PI(3,5)P_2$ phosphatase Fig4 (**Figure 3.1**). The coordinated position of lipid kinase and lipid phosphatase within the same complex speaks to the highly controlled nature of $PI(3,5)P_2$ metabolism. The presence of all three of these proteins is required for normal $PI(3,5)P_2$ production. In yeast, the absence of Vac14 or Fig4 results in only 10% $PI(3,5)P_2$ levels compared to wild type, even though the Fab1 kinase is present (9). A similar trend is seen in animals (14). In Arabidopsis, there are several Fab1 and Fig4 homologues but only a single Vac14 gene.

To date, the majority of our understanding of $PI(3,5)P_2$ function in plants is derived

from mutant analysis of Fab1 homologs. There are four Fab1 family members in Arabidopsis, Fab1A-Fab1D. However, only Fab1A and Fab1B possess a PI3P lipid-binding FYVE domain in their protein sequence, making them bona fide PI3P-5 kinase homologues (15). Null mutations in the mammalian Fab1 homologue PIKfyve are lethal and, consistent with that observation, double knockout mutations in Arabidopsis of the two partially redundant fab1A/fab1B genes are also lethal (15). Arabidopsis knockdown studies of Fab1 family members result in pleiotropic phenotypes including vacuolar morphology and acidification defects similar to yeast Fab1 mutants (16). These observations support a conserved role for $PI(3,5)P_2$ in plants. Fab1 mutants also exhibited impaired root gravitropic response, suggesting defects in PIN localization and polar auxin transport (16, 17). In contrast to the recent studies on Fab1, Vac14 has not been genetically characterized in Arabidopsis or in any other plant.

Vac14 was initially identified in yeast as part of a screen looking for mutants with a similar enlarged vacuole phenotype to that of Fab1 kinase mutants (9, 18). Vac14 was found to be a general activator of Fab1 and specifically required for osmotic stress induced $PI(3,5)P_2$ production (9). In mammals Vac14 was identified through sequence homology and functions to regulate PIKfyve, the mammalian homolog of Fab1 kinase, in a similar manner (14). Null mutations in Vac14 are lethal in mice and point mutations in FIG4 phosphatase that binds Vac14 in the $PI(3,5)P_2$ biosynthesis complex are associated with epilepsy and several human neurodegenerative diseases including ALS and Charcot-Marie-Tooth (CMT) disorder (19-21). These associated diseases are consistent with the finding that $PI(3,5)P_2$ levels are critical for synaptic function in neurons, and that neurons are particularly sensitive to disruption of the Vac14 complex (22). The high sequence conservation of Vac14 across

eukaryotes is consistent in plants as *Arabidopsis thaliana* Vac14 shares 46% sequence identity with humans and 33% with *S.cerevisiae*, including conservation of critical Fab1 and Fig4 binding domains.

Initial insight into the function of Vac14 in plants comes from my previous work describing protein phosphorylation in Arabidopsis. Untargeted quantification of protein phosphorylation in response to osmotic stress identified Vac14 as a target of phosphoregulation in Arabidopsis. In my proteomic dataset, Vac14 displayed the largest phosphorylation increase out of approximately 1,300 phosphopeptides quantified in response to 5 minutes of 300 mM mannitol treatment *in planta* (23). This phosphorylation event was further characterized under a matrix of different treatment conditions and shown to be specific to osmotic stress. Measurement of Vac14 phosphorylation in a mannitol treatment time course found that phosphorylation levels are highest at 2 minutes of exposure to stress and decreased after 10 minutes (23). This pattern mirrors osmotic stress induced $PI(3,5)P_2$ production in yeast and *Chlamydomonas,* which peaks at 5 minutes and is reduced at 15 minutes follow treatment (12). Phosphoregulation of Vac14 has not been reported in other eukaryotes and, consistent with this observation, the C-terminal phosphorylation site is not conserved in yeast and mammals.

The presence of Vac14, Fab1 kinase, and Fig4 phosphatase genes in the Arabidopsis genome suggest a conserved function for these proteins in forming a complex to regulate $PI(3,5)P_2$ biosynthesis in plants. The unique phosphoregulation of Vac14 in Arabidopsis, however, indicates the presence of plant specific mechanisms for modulating protein function that are distinctly different from yeast and mammalian systems. More work needs to be done to understand the role of Vac14 in plants. Herein I report an initial genetic characterization

of Vac14 to interrogate the function of this highly conserved protein in Arabidopsis. My results indicate that Vac14 is an essential gene that is involved in regulating vacuole function and water content in cells. Vac14 expression levels influence seedling growth rate and result in overall dwarfed plants with elevated water content and defects in shoot gravitropism. Overall, Vac14 expression levels appear to influence cellular turgor, and this effect is likely the consequence of altered $PI(3,5)P_2$ levels in the cell.

Results

Vac14 homozygous T-DNA insertion mutants are not viable.

To characterize Vac14 function in Arabidopsis, two independent T-DNA insertion alleles were obtained: vac14-1 and vac14-2. The T-DNA insertion loci were verified by Sanger DNA sequencing and the vac14-1 insert was found to be at the splice junction between exon 7-8, while the vac14-2 insert sits in the middle of intron 13 (**Figure 3.2**). It is not known if these insertions represent true null alleles. Both lines failed to produce homozygous T-DNA progeny, indicating that homozygous T-DNA mutations in Vac14 are not viable. This finding is consistent with the fact that Vac14 is an essential gene in mice. It is also constant with the lethality of Arabidopsis Fab1A/Fab1B double homozygous mutations, supporting the notion that $PI(3,5)P_2$ is an essential lipid in plants and requires conserved biosynthetic machinery.

In the case of Fab1, the failure to generate homozygous null mutants is due to the pollen lethality of fab1a/b double mutant alleles (15). Pollen containing fab1a and fa1b mutations exhibit a collapsed shape with irregular vacuole morphologies, resulting in failed transmission of the fab1a/fab1b T-DNA alleles (15). It is currently not clear if this is also the case for vac14-1 and vac14-2 lines. Embryo lethality would result in a 66% transmission of the T-DNA mutant allele in a population of segregating progeny, while gamete lethality would result in 50% frequency. For vac14-1 lines I screened 50 seedlings derived from a heterozygous parent and found 30 heterozygous and 20 wild type plants. Surprisingly, I found only 13/35 seedlings to be heterozygous when the same analysis was conducted for vac14-2 lines. The 60% heterozygous frequency for vac14-1 lines suggests embryo lethality while the 37% frequency in vac14-2 lines is closer to, yet significantly under, a segregation

ratio representative of gamete lethality. To clarify these results, it will be necessary to perform reciprocal crosses with wild type and T-DNA lines and assess T-DNA transmission frequency. It is possible that vac14-1 and vac14-2 represent different Vac14 variants, as one may be a true null allele while the other generates a truncated protein product, each having different consequences during fertilization and development.

Vac14 overexpression causes swollen pavement cells and reduced leaf size.

To gain insight into the role of Vac14 in growth and development, I generated transgenic plants constitutively expressing a N-terminal GFP-Vac14 fusion protein driven by the cauliflower mosaic virus 35S promoter. These independent overexpression (OEx) lines exhibited several growth defects including an overall reduced rosette size with smaller, rounder leaves and shorter petioles compared to control lines expressing 35S:GFP alone (**Figure 3.3A-B**). To determine if smaller leaf size was due to reduced cell size, leaf disc samples were collected and cell walls were stained with propidium iodide to image epidermal cells. Contrary to expectations, Vac14 OEx lines consistently resulted in swollen, enlarged pavement cells compared to 35S:GFP controls (**Figure 3.3C**). The area of these enlarged pavement cells were 2.5-3X larger than control lines. Though this enlarged phenotype was not observed in every cell, it was consistently prevalent in both independent OEx lines. Furthermore, the swollen cell shapes observed in stably transformed Arabidopsis lines were also seen during transient overexpression of Vac14 in *N.benthamiana* leaves using both N-termal and C-termal GFP fusion constructs (**Figure 3.4A**). Leaves developed enlarged pavement cell morphology three days after infiltration and resulted in pigment loss and tissue damage in the subsequent 1-2 days (**Figure 3.4C**). These phenotypes were not observed with transient expression of 35S:GFP control construct (**Figure 3.4B**).

To determine if the Vac14 OEx lines possessing swollen epidermal cells contained more water than control lines, I measured the water content of harvested rosettes. Hydrated rosettes were weighed and later compared to their total desiccated biomass. Measurements revealed that Vac14 OEx lines contained approximately 30% more water per gram of tissue than wild type and control lines (**Figure 3.3D**). These measurements were performed in two independent experiments and the trends in the observed phenotype repeated. Taken together, these findings indicate that Vac14 expression has an important influence on organ and cell size, possibly through mediating vacuole water content and turgor.

Vac14 overexpression confers enhanced drought tolerance

Since Vac14 OEx lines contained higher water content in their aerial biomass, I wanted to test the hypothesis that Vac14 OEx influenced the plant's ability to withstand drought. For this purpose, I grew plants for 4 weeks under short day conditions and then withheld water for 3 weeks. 35S:GFP control lines developed high anthocyanin content during the third week of dehydration and then completely wilted and were unable to recover (**Figure 3.5A-D**). In contrast, Vac14 OEx lines maintained an overall rosette morphology that did not significantly differ from control conditions (**Figure 3.5A-D**). Rosettes remained green and were able to survive the entire period of dehydration and resume growth upon re-watering. Though this trend was true for both Vac14 OEx lines tested, there was some variation within the population and not every individual plant was able to recover after rehydration (**Figure 3.5E**). These results strongly suggest that Vac14 OEx plants have an increased drought tolerance. However, because the leaf size of Vac14 OEx plants is smaller than control plants, its is possible that Vac14 OEx lines appear more tolerant merely because they used up less of the soil water content. This would be due to a presumed lower rate of

transpirational water loss compared to controls. To confirm my preliminary results, this experiment must be repeated with plants of both genotypes grown in the same pot to better control for potential differences in soil water content between samples.

Vac14 overexpression causes increased rates of short-term water loss

My initial interest in Vac14 arose from the fact that it was identified in my screen for proteins whose level of phosphorylation was altered within 5 minutes of hyperosmotic stress. Given that Vac14 OEx lines posses phenotypes relating to water homeostasis, I wanted to test the sensitivity of Vac14 overexpression lines to conditions of short-term water loss. To examine this, Vac14 OEx lines were tested in a transpirational water loss assay. Rosettes from 4 week old soil grown plants were harvested and rates of water loss were measured over 4 hours. Compared to wild type plants and 35S:GFP control lines, Vac14 OEx plants showed a significantly increased rate of water loss (**Figure 3.6**). This result indicates that the regulation of stomata aperture is affected by Vac14 OEx. An increased rate of water loss may represent delayed stomata closure compared to wild type and control lines. Alternatively, increased transpiration in Vac14 OEx mutants may be due to a difference in stomata density. To determine which interpretation is correct, stomata density and stomata aperture must be quantified in Vac14 OEx and control lines.

Consistent with our findings, accelerated water loss due to impaired stomata response was also observed in fab1b x fab1c double mutants (24). Use of chemical inhibitors that block $PI(3,5)P_2$ production through inhibition of Fab1 kinase activity were also shown to inhibit ABA induced stomata closure (24). Taken together, our findings support published genetic and pharmacological data indicating that $PI(3,5)P_2$ production is required for stomata conductance and water loss in leaves.

Vac14 overexpression results in accelerated growth at early stages of development

To determine if Vac14 OEx had any effect on root sensitivity to osmotic stress growth conditions, I measured primary root lengths in a vertical root growth assay. Vac14 OEx seedlings were transferred after 4 days of germination to control plates or plates containing mannitol, and root lengths were measured over an 8 day period. Vac14 OEx lines displayed only minor reductions (ca. 10%) in normalized root growth on 100mM mannitol plates compared to 35S:GFP controls (data not shown). What was more striking however was the difference in root length between Vac14 OEx and control lines on normal media conditions. Vac14 OEx lines grew significantly faster, showing 50-70% longer roots than controls at day 2 post-transfer (**Figure 3.7A**). This difference in root length between Vac14 OEx and control lines started to decrease over time (**Figure 3.7B**), suggesting that Vac14 OEx does not cause a sustained increase in growth rate. It is known from my observation of mature plants that Vac14 OEx does not continue to promote faster growth, as Vac14 OEx lines are significantly smaller than controls and this size differential appears to enhance over time. Vac14 OEx seems to cause a growth advantage early on, as shown in primary root length and the onset of lateral root development (**Figure 3.7C**), but growth must slow later in development, as plants ultimately become stunted and small.

To test growth rate in another way, I measured hypocotyl elongation in dark grown seedlings. Seeds for each genotype were first size sorted to control for maternal effects; seeds falling within a 280-300 micron range were used for analysis. Hypocotyl measurements were then taken for sample sets grown for 4 days and 7 days in the dark. Results show that early on Vac14 OEx plants have approximately 25% longer hypocotyls compared to control lines (**Figure 3.7D**). However, after 7 days of growth in the dark, control lines significantly

surpass OEx lines in growth. Control hypocotyls were between 30-40% longer than Vac14 OEx lines, and this growth difference continued to increase over time (**Figure 3.7D**). In both cases OEx hypocotyls were visibly thicker than controls (**Figure 3.7E**). These findings support the idea that Vac14 OEx confers an initial growth advantage that is not sustained. Hypocotyl elongation requires polar cell expansion. The shorter and fatter hypocotyls in the mutant line suggest that Vac14 OEx may cause an inability to achieve proper polar cell expansion. This observation is also consistent with the shorter petioles seen in Vac14 OEx rosettes, as this phenotype is often associated with mutants defective in polar cell expansion (25-27).

Vac14 overexpression causes accelerated germination and enhanced tolerance to osmotic stress.

The increased root length of Vac14 OEx seedlings could be attributed to a faster germination rate and therefore a head start in growth compared to controls. To examine this I monitored germination under control and osmotic stress conditions using size-sorted seeds (280-300 micron). After three days of germination on control media almost all Vac14 OEx seeds had root radicals and emerged cotyledons while the vast majority of 35S:GFP control seeds only had root radicals. This observation indicates that Vac14 OEx seeds germinate faster than controls. After 5 days of growth all seedlings had fully germinated but Vac14 OEx lines displayed larger cotyledons than controls (**Figure 3.8A**). By day 6 this difference in cotyledon size was less significant (**Figure 3.8C**). Comparison of germination rates of seedlings on control media and media containing 250mM mannitol revealed that Vac14 OEx lines were much more tolerant to osmotic stress conditions. Only 56% of the control seedlings achieved full germination by 6 days of growth on stress media, measured as

emerged and expanded cotyledons, whereas Vac14 OEx lines achieved 90% full germination (**Figure 3.8B**). The majority of seeds failing to germinate in control lines did not even display emerged radicals. Furthermore, control seedlings that did successfully germinate on stress media had significantly smaller cotyledons than Vac14 OEx lines (**Figure 3.8C**). The difference in cotyledon size appears greater than the difference seen on corresponding 0.5xMS control plates at this growth stage. An even more striking difference in germination rates under osmotic stress conditions was observed when I analyzed germination on media containing 40% polyethyleneglycol (PEG). Only 40% of control seedling were able to initiate germination after 7 days of growth, measured by the appearance of an emerged radicals, while > 92% of Vac14 OEx seeds germinated (**Figure 3.8D-E**). These results indicate that OEx of Vac14 influences both the rate of germination and the ability to germinate under osmotic stress conditions. These phenotypes reflect an ability of Vac14 OEx seeds to hydrate faster and maintain turgor under water limiting conditions.

Vac14 overexpression causes severe defects in shoot gravitropism but does not affect root gravitropism

The most striking phenotype observed in Vac14 OEx lines is the impaired gravitropism of lateral branches. Lateral branches in Vac14 OEx plants consistently grow down, with direction of the gravity vector, not opposed to it (**Figure 3.9A**). The significantly altered gravitropic set point angles of lateral branches in Vac14 OEx lines displayed a range of phenotypic severity in the T1 population of transformants. Some Vac14 OEx lines displayed horizontal branches as opposed to downward facing branches (**Figure 3.9B**). This observation suggests that expression levels of Vac14 correlate with phenotypic severity. To test the gravitropic response of Vac14 OEx lines, plants pots were tipped on their side and

the reorientation of shoot growth was observed. Over a 24-hour period Vac14 lines showed no growth reorientation while control lines bent upward toward the light and against the direction of gravity (**Figure 3.9C**).

Gravity sensing in shoots requires the sedimentation of starch filled granules called amyloplasts in endodermal cells. The amyloplasts traverse through vacuole strands to settle at the bottom of cells. Following sedimentation, polar auxin transport is directed by asymmetrical distribution of auxin transporter PIN proteins. PIN efflux carriers direct auxin to one side of the organ tissue, thus promoting asymmetrical growth and reorientation with respect to gravity (28-30). In shoots, auxin maxima at the bottom of cells promotes elongation and ultimately growth upward, opposing the direction of gravity. In this way, proper gravity sensing in shoots relies on the vacuole and endomembrane system at two stages: first during amyloplast sedimentation, and second in directing PIN transporter reorientation (28). In roots, gravity sensing occurs in columella cells located at the root tip. Unlike shoot endoderm tissue, columella cells do not contain a large central vacuole structure (31). Therefore amyloplast sedimentation occurs in the cytosol and does not depend on proper movement through vacuole strands. Comparing shoot and root gravitropic response can aid in determining the contribution of the vacuole to the overall phenotype.

To determine which step of gravitropism is disrupted in Vac14 OEx plants I measured the gravitropic response of roots in Vac14 OEx seedlings. Three-day-old vertically grown seedlings were rotated 90^{o} and photographed every 2 minutes for 8 hours. Root growth and gravitropic response was then measured for each genotype. This work was done with the guidance and shared resources of Prof. Edgar Spalding's lab at UW-Madison. Results indicate that Vac14 OEx lines do not have a significantly different root gravitropic

response compared to controls (**Figure 3.10A**). Roots appear to initiate bending at the same time in all lines, although the rate of bending is slightly slower in Vac14 OEx seedlings. This indicates that there is not a significant defect in amyloplast sedimentation or polar auxin distribution and asymmetric growth in the roots of Vac14 OEx lines. The contrast in shoot and root gravitropic response suggests that vacuole defects caused by Vac14 OEx are contributing to the shoot gravitropic phenotypes. My findings are consistent with several shoot gravitropic mutants that do not display defects in root gravitropism and have mutations in SNARE proteins involved in endomembrane trafficking and vesicles fusing with the vacuole (32-35).

Measurements of growth were also calculated from 2-minute time interval photos taken over the experimental period. This analysis reveals that Vac14 OEx seedlings grow significantly faster than controls (**Figure 3.10B**). All genotypes display linear growth rates, with R^2 values > 0.995. The rate of root growth in seedlings OEx Vac14 is approximately 20% faster than controls. These results corroborate previous data indicating that Vac14 OEx causes an increased growth rate at early stages of development.

Vac14 knockdown mutants also show severe defects in shoot gravitropism

Since Vac14 homozygous T-DNA mutants are not viable, I generated artificial microRNA knockdown (amiRNA) lines targeting the Vac14 transcript. These plants are currently at the second generation after transformation (T2 stage) and are being screened for homozygous lines to use in future phenotypic analysis. Interestingly, I observed that T1 amiRNA plants exhibited the same shoot gravitropic phenotypes as Vac14 OEx lines. Positive transformants displayed severe gravitropic defects with lateral branches growing down in the direction of the gravity vector (**Figure 3.9D**). Some plants displayed milder

gravitropic defects with horizontal branches (**Figure 3.9E**), similar to the trend observed in the Vac14 OEx T1 population. The fact that OEx and reduction of Vac14 protein levels yield the same phenotype is consistent with published data on Fab1A OEx and amiRNA lines where both upregulation and downregulation of Fab1 resulted in the same phenotype (16).

The fact that both OEx and reduction in Vac14 protein levels results in impaired shoot gravitropism suggests that this is not a neomorphic phenotype derived from aberrant Vac14 activity. Rather, this observation suggests that phenotypes are a consequence of a disrupted process that requires specific Vac14 levels in the cell. Too much or too little protein equally manifests in a disrupted outcome. Given that the same relationship holds true for Fab1 protein expression, and the fact that Vac14 and Fab1 work together as part of the same PI(3,5)P_2 biosynthesis complex, it is likely that phenotypes reflect altered levels or subcellular distribution of PI(3,5)P_2 or its precursor PI3P. My results suggest that the PI(3,5)P_2 complex requires precise stoichiometry of Vac14 to correctly function within the cell.

Transient overexpression of Vac14 does not increase PI(3,5)P_2 levels.

To determine if Vac14 OEx directly influences PI(3,5)P_2 levels, measurements of ^{32}P labeled phospholipids from tissue extracts were conducted. Direct measurements of PI(3,5)P_2 lipid levels in plants presents a challenge due their extreme low abundance in a complex background of many PtdIns species. I attempted to measure PI(3,5)P_2 by radioactively labeling phosphorylated inositols *in vivo* using ^{32}P orthophosphate and quantifying lipids post-extraction using thin layer chromatography (TLC). I performed this work in the lab of Teun Munnik at the University of Amsterdam. At the time of analysis I did not have stably transformed Vac14 OEx lines. Therefore PI(3,5)P_2 levels were measured in *N.benthamiana*

leaf disc samples transiently overexpressing Vac14-GFP or GFP alone. My results indicated that basal PI(3,5)P_2 levels were extremely low, and I could not detect any changes in PI(3,5)P_2 induced by Vac14 OEx (**Figure 3.11A**). In addition to analyzing basal levels, I also looked at the influence of Vac14 OEx on PI(3,5)P_2 during osmotic stress. No significant changes were detected relative to osmotically stressed 35S:GFP controls (**Figure 3.11A**). The analysis was done in parallel with hydrogen peroxide treatment, as this is known to boost PI(3,5)P_2 levels and serves as a positive control for PI(3,5)P_2 TLC detection (Munnik, unpublished data).

The lack of altered PI(3,5)P_2 levels in Vac14 OEx tissues may not be surprising as Vac14 scaffolds both the lipid kinase and the phosphatase, so more protein does not necessarily relate to more lipid. Furthermore, given my findings that Vac14 amiRNA lines yield similar phenotypes, it is more likely that Vac14 OEx manifest in a disrupted biosynthetic complex causing less PI(3,5)P_2 lipid production. With the abundance of PI(3,5)P_2 teetering on the limit of detection, it is likely that any decreases to lipid abundance would not be accurately quantifiable in this assay. Additional support for the hypothesis that Vac14 OEx results in reduced PI(3,5)P_2 biosynthesis is the fact that increased levels of PI(3,5)P_2 are consistently found to cause small vacuoles (2, 36, 37). I found the opposite to be true in the case of Vac14 OEx, where leaf cells in mutant plants appear to have swollen, enlarged vacuoles. If increased PI(3,5)P_2 levels result in smaller vacuoles, these phenotypes could be caused by reduced PI(3,5)P_2 levels.

Failure to induce lipid accumulation is consistent with data from mammals where overexpression of Fab1 kinase alone was not able to boost PI(3,5)P_2 levels. In mammals, only overexpression of miss-regulated forms of Fab1, which posses activating point

mutations in regulatory domains, cause significant increases in $PI(3,5)P_2$ levels (22). This data from animal studies suggests that overexpressing components of the $PI(3,5)P_2$ metabolic complex alone may not be sufficient to increase $PI(3,5)P_2$ levels in a detectable manner.

Interestingly, although osmotic stress has been shown to increase $PI(3,5)P_2$ levels in plant cell cultures, significant increases in $PI(3,5)P_2$ were difficult to observe routinely during mannitol, sorbitol, or NaCl treatment. Several plant tissues were tested including Arabidopsis seedlings, Arabidopsis leaf discs, and *N.benthamiana* leaf discs. In addition, time-course studies were conducted over 2-10 min of osmotic stress (**Figure 3.11 C-D**). The difficulty in detecting robust $PI(3,5)P_2$ increases was surprising given that Vac14 is known to be rapidly and transiently phosphorylated in response to osmotic stress, suggesting that the $PI(3,5)P_2$ complex may be activated. It's possible that $PI(3,5)P_2$ increases that occur in response to osmotic stress remain below the limit of reliable quantification, as $PI(3,5)P_2$ levels are barely detectable (**Figure 3.11E**). Thus, measurements of $PI(3,5)P_2$ spot intensity may vary due to excessive background to signal ratio. It is also possible that osmotic stress activation occurs in only certain tissue types. These cell types may be either poorly labeled by ^{32}P, and thus not represented in the TLC analysis, or they may represent small contributions to the total lipid extraction of the whole seedling or leaf disc.

Vac14 partially co-localizes with endosomal Rab5 proteins.

To determine the subcellular localization of Vac14, Vac14-GFP fusion proteins were examined using a confocal microscope. Although stably transformed OEx lines at the T1 generation gave a GFP signal intensity that was easily detectable on an epifluorescent scope, GFP signal strength was not high enough in homozygous T2 populations to be detected, even when a more sensitive confocal microscope was used. This suggests a level of transgene

silencing occurring across generations. Therefore to examine subcellular localization, transient expression of Vac14-GFP in *N.benthamiana* leafs was employed. Vac14 appeared both in distinct punctate structures of varying size or diffusely located across what could be the vacuole membrane or cytoplasm (**Figure 3.12A**). Given the narrow space between the vacuole membrane and the plasma membrane in leaf pavement cells, it was difficult to discern if Vac14 was localized to the vacuole membrane or in the cytoplasm. In order to confirm the localization, Vac14 must be co-expressed with RFP markers for each organelle.

The punctate structures with Vac14 appeared to partially co-localized with Rab5 GTPase endosomal markers during co-infiltration experiments. Ara7 and Ara6 are Rab5 GTPases known to localize to distinct yet partially overlapping populations of endosomes in the cell (38). Vac14 puncta showed partial overlap with both Ara7 and Ara6, indicating that Vac14 is localized at least in part to vesicles associated with endosomes and the pre-vacuolar compartment (39, 40) (**Figure 3.12B-D**). In a time series analysis, Ara6-RFP and Vac14-GFP tracked together in vesicles moving across the cell (**Figure 3.12D**). Vac14 association with Rab5 endosomal markers is consistent with Fab1 subcellular localization, which was found to be partially overlapping with Ara7 (17). More work needs to be done to clarify these initial results and better characterize the subcellular localization of Vac14.

Discussion

In this chapter I present a genetic characterization of Vac14 for the first time in plants. In yeast and humans Vac14 functions as a scaffold protein that holds together the biosynthetic machinery responsible for PI(3,5)P_2 metabolism. This signaling lipid is essential in controlling endomembrane vesicle transport and fusion events and also regulates vacuole function, acidification, and morphology. My results demonstrate that Vac14 is an essential gene in plants and is required for proper vacuole function. The influence of Vac14 on vacuole function is demonstrated through OEx phenotypes that show overhydrated, swollen leaf cells with stunted overall growth, shoots and branches defective in gravity sensing, enhanced growth rates in young seedlings, and increased drought tolerance in mature plants and germinating seedlings. These diverse phenotypes are connected through their reliance on proper vacuolar plasticity and turgor. All together my results demonstrate that Vac14, likely through its influence on PI(3,5)P_2 metabolism, is important for regulating the vacuole and water homeostasis in cells.

Vac14 and turgor mediated growth

Plant growth occurs through turgor mediated cell expansion. Hydrated vacuoles impose a force on the plasma membrane and the adjacent cell walls that drives expansion, and in coordination with cellular machinery such as the cytoskeleton, this expansion is often asymmetric and tightly controlled. My results show that OEx of Vac14 affects growth rates and final organ size. These changes may occur through miss regulation of vacuole turgor leading to improper cell expansion.

My data shows that Vac14 OEx seedlings germinate faster, have larger cotyledons, and have faster rates of initial hypocotyl elongation and root growth. These phenotypes may

reflect an early growth advantage conferred by enhanced vacuole turgor. If Vac14 OEx results in overhydrated vacuoles and heightened water uptake, rates of seed imbibition and cell expansion may be faster. The growth phenotypes observed in Vac14 OEx seedlings therefore may reflect enhanced cell expansion due to increased vacuolar water content.

In contrast to the growth advantage early on, my results show that Vac14 OEx leads to stunted growth in mature plants. Rosette leaves are smaller and contain enlarged epidermal cells that are significantly wider than normal cells, however they maintain the highly lobed cell structure at their perimeter that is characteristic of pavement cells. This suggests that there is not a defect in proper cell patterning or development, but rather the cells expand more than normal and become bloated in appearance. The suggestion that cells are swollen and overhydrated is supported by my observations that Vac14 OEx plants contain significantly more water than wild type and 35S:GFP controls. It is possible that this miss-regulated cell expansion is responsible for the overall growth limitations in mature tissues of Vac14 OEx plants.

The growth disadvantage of Vac14 OEx is also seen in 7-day dark-grown hypocotyls. Early on, Vac14 OEx seedlings showed a faster rate in hypocotyl expansion but by 7 days of growth, control seedlings had significantly longer hypocotyls. This result suggests that Vac14 OEx may cause defects in polar cell expansion. This hypothesis is also supported by observations that Vac14 OEx leaves have shorter petioles, which is a hallmark of mutants defective in polar cell expansion (26, 27). The increase in cellular turgor that may be conferring a growth advantage early on may also be responsible for growth setbacks at later points in development when highly directed and controlled cell expansion is required.

Vac14 and dehydration tolerance

OEx of Vac14 resulted in an enhanced ability to withstand long-term drought and successfully germinate under osmotic stress conditions. Both of these observations support the hypothesis that Vac14 is involved in regulating water homeostasis in the cell. The increased water content in Vac14 OEx plants is likely responsible for their ability to withstand extended periods of dehydration. Similarly, the ability to maintain high turgor could allow for Vac14 OEx seedlings to successfully germinate in conditions of low water availability.

I also observed that Vac14 OEx lines had increased rates of water loss in a 4-hour transpirational water loss assay using harvested rosettes. The process of stomata closure requires deflation of guard cell turgor. If Vac14 OEx plants of have altered regulation vacuole water content leading to overly turgid cells, it is possible that rates of turgor adjustment and guard cell closure are slower in Vac14 OEx mutants. It has been documented that stomata closure coincides with vacuole fragmentation and acidification in the guard cell (24, 41). Both vacuole fragmentation and acidification are regulated by $PI(3,5)P_2$ in yeast (2). It is possible that these processes are disrupted in Vac14 OEx plants. This finding would be consistent with observation in fab1b/fab1d double mutants that show defective guard cell fragmentation, acidification, and closure (24).

Vac14 and gravitropism

A strong indication that Vac14 regulates vacuole function in plants comes from my observations of shoot gravitropic defects in Vac14 mutants. Gravitropic response requires amyloplast sedimentation to the bottom of cells. In shoots this sedimentation occurs in vacuole-filled endodermal cells where amyloplasts must traverse through vacuole strands. In

roots, gravity sensing occurs in the root tip where cells do not have a large central vacuole. My observation that Vac14 OEx lines display disrupted shoot, but not root, gravitropic response suggests that these phenotypes arise from improper movement of amyloplasts in the presence of a large central vacuole. It is unclear which element of vacuole function inhibits proper gravitropic response in Vac14 mutants, but the results support an important role for this protein in vacuole structure and plasticity.

My observation that Vac14 OEx does not cause significant root gravitropic defects is inconsistent with published data on Fab1 mutants. Fab1 OEx and amiRNA mutants are reported to have altered root gravitropic responses and improper redistribution of PIN auxin transporters upon root reorientation (16, 17). Furthermore, stable OEx of Fab1B does not cause obvious shoot gravitropic defects. This data suggests that although Vac14 and Fab1 function in the same complex, genetic manipulation of these proteins does not have the same consequence on growth and development.

Vac14 and PI(3,5)P_2

My preliminary analysis of Vac14 amiRNA knockdown lines indicates that increased and decreased levels of Vac14 yielded the same phenotypic response. Vac14 amiRNA lines displayed shoot gravitropic defects identical to Vac14 OEx lines. Importantly, this observation suggests that precise levels of Vac14 are required to achieve proper function in the cell. It is my hypothesis that PI(3,5)P_2 biosynthesis requires specific protein stoichiometry and if there is too much or too little of Vac14, the complex does not properly form. Therefore Vac14 mutant phenotypes are likely a reflection of reduced PI(3,5)P_2 levels or improper subcellular distribution of PI(3,5)P_2. This hypothesis is also supported by the fact that Vac14 OEx plants display enlarged vacuole phenotypes that are opposite to the

small fragmented vacuoles associated with high $PI(3,5)P_2$ levels in yeast and mammals (36, 37). Small vacuoles are thought to be one of the hallmark signatures of elevated $PI(3,5)P_2$ levels in cells (4, 22). My efforts to directly measure $PI(3,5)P_2$ in Vac14 OEx plants were not successful. However, as discussed more fully above, there is reason to believe this is due to technical limitations rather than a reflection of true cellular events.

Overall my work has demonstrated that Vac14 and $PI(3,5)P_2$ have essential functions in plants and their conserved role in regulating the vacuole and lysosome in other eukaryotes is likely also true in plants. Plants are unique in their cellular architecture, possessing a large central vacuole that occupies the vast majority of intracellular space and as the major repository of cellular water, also controls growth by regulating turgor pressure. This presents unique opportunities for Vac14 and $PI(3,5)P_2$ to possess regulatory functions that are not seen in other eukaryotes. Much work remains to be done to understand the mechanistic details behind Vac14 and $PI(3,5)P_2$ function in plants.

Materials and Methods

Plant material and growth conditions

Arabidopsis thaliana plants of ecotype Col-0 were grown in soil under continuous light conditions. T-DNA alleles used were the following: vac14-1 (At2g01690; GABI_647B12) vac14-2 (At2g01690; GABI_921C07). Plant lines were genotyped with the following primers: vac14-1 forward 5'-CAGGTGTGTTCAGTTGGCTTT-3', reverse 5'-AATAACGCACGAGCTGGTCT-3', T-DNA border 5'-ATATTGACCATCATACTCATTC-3'. vac14-2 forward 5'-GGGCTATCTTGCCTTGCATA-3', reverse 5'-ACCGCGCCTATAACGAGAT-3', T-DNA primer was the same as for vac14-1. For transpiration water loss assays and dehydration experiments, plants were grown in 10 hours of light under short-day growth conditions. In all experiments, seedlings were first germinated for 2 weeks on ½ MS plates containing ½ Murashige and Skoog (MS) media, 1% (w/v) sucrose, 0.05% (w/v) MES salt, and 1% (w/v) agar before being transplanted to soil. Media plates used for root growth and germination assays contained ½ MS media, described above, and 250mM mannitol or 40%PEG-8000. PEG plates were made using the protocol described in (42, 43).

Cloning Vac14 OEx and amiRNA constructs

Vac14 coding sequence was cloned from cDNA using forward primer 5'-ATGTCAGACGCT CTTTCTGC-3' and reverse 5'-TTAAAGCTGTAATTGACCAGGGC-3'. Overexpression GFP fusion constructs were generated using the T-DNA binary vectors pK7WGF2 and pK7FWG2 described in Karimi *et al*. (44). Mutagenesis was performed to remove the Vac14 stop codon in C-terminal GFP fusion constructs. GFP control lines were generated using pK7WGF2. Vac14 amiRNA lines were designed using WMD3 online tools

(http://wmd3.weigelworld.org/). The Vac14 amiRNA target sequence used was 5'-CAGCATGCGAGTGTCGTGATT-3' and is located in exon 17 (**Figure 3.2**). amiRNA cloning was constructed using the RS300 vector (45) and the following primers:

I 5'-gaTATCACGACACTCGCACGCTGtctctcttttgtattcc-3'

II 5'- gaCAGCGTGCGAGTGTCGTGATAtcaaagagaatcaatga-3'

III 5'- gaCAACGTGCGAGTGACGTGATTtcacaggtcgtgatatg-3'

IV 5'- gaAATCACGTCACTCGCACGTTGtctacatatatattcct-3'

The final amiRNA construct was cloned into T-DNA binary vector pEarlyGate 100 (46) for expression in Arabidopsis. All plasmids were cloned into *Agrobacterium tumefaciens* strain GV3101 for Arabidopsis transformation. Transformations were performed using the floral dip method (47).

Propidium iodide staining and confocal microscopy

Leaf slices taken from 5 week old rosettes were incubated in a propidium iodide (PI) solution (Sigma, P4864) for approximately 5 minutes and then washed 3-4 times using deionized water. Samples were imaged with a Zeiss LSM510 laser scanning confocal microscope using a plan-apochromat 20X objective. Excitation was conducted using a 488nm laser and emission was collected using 500-550nm (GFP) and 565-615nm (PI) band pass filters.

Vac14 transient expression and co-localization

Vac14 was transiently expressed in *N.benthamiana* following the detailed protocol published in Ma L. *et al.* methods paper (48). Briefly, 4 week-old leaves were co-infiltrated with 1mL of agrobacterium solution containing plant expression vectors and the silencing suppressor construct p19 (49). Leaf samples were then examined 2-3 days following

infiltration using a Zeiss LSM510 laser scanning confocal microscope and a plan-apochromat 20X objective. GFP was imaged using 488nm excitation and a 505-550nm band pass emission filter. RFP was imaged using 543nm excitation and a 585-615 band pass emission filter. Vac14-GFP was expressed using pK7WGF2 and pK7FWG2 vectors, as described above. Rab5 proteins were expressed using pUBC:Ara7-mRFP and pUBC:Ara6-mRFP constructs were provided by the Plant Physiology at the University of Amsterdam.

Root gravitropism measurements

Root gravitropism was measured as described in Brooks T.L. et al. (50). Briefly, seeds were first size sorted using 280um and 300um sieves and then vapor sterilized and plated on minimal media agar plates containing 1 mM KCl, 1 mM$CaCl_2$, 5 mM MES, and 1% agar adjusted to pH 5.7 with BisTris propane. Seeds were grown vertically in constant light for 3 days following stratification and then transferred to camera stages and allowed to requilibrate after plate handling for 1 hour before started the experiment. At time zero plates were rotated 90^O and roots were imaged every 90 seconds for an 8 hour period. Root growth and root angle were measured through automated image processing using in-house software. The experiment was conducted over 4 days, with each experimental batch measuring 9-12 seedlings per genotype.

^{32}P phospholipid analysis

Plant phospholipids were labeled, extracted, and quantified following the protocol described in detail in Munnik T. & Zarza X. methods paper (51). Experiments were conducted using 5 day-old Arabidopsis seedlings and 4 week-old *N.benthamiana* leaf discs. Samples were labeled using ^{32}P orthophosphate for 3-4 hours before experimental treatment

and lipid extraction. Stress treatments were applied for 10 minutes, unless otherwise stated, and lipids were immediately extracted following the published protocol (51). Treatment concentrations were as follows: 300mM sorbitol, 150mM NaCl, 40mM H_2O_2. For analysis of *N.benthamiana* leaves transiently expressing Vac14, leaves were infiltrated 2 days prior to labeling and lipid extraction, and protein expression levels were first verified using an epifluorescence microscope.

Figure 3.1

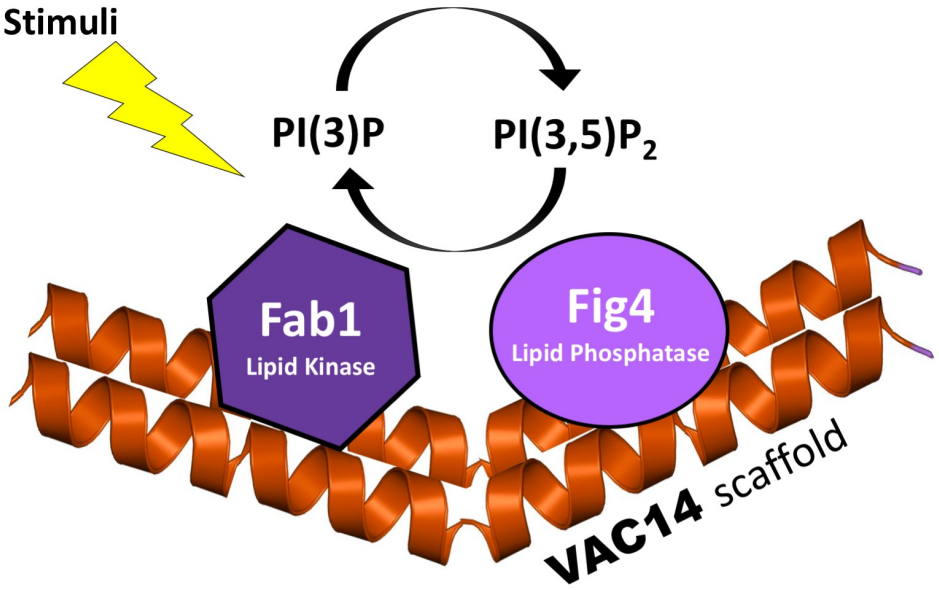

Figure 3.1. *PI(3,5)P_2 biosynthesis complex*.

Figure 3.2

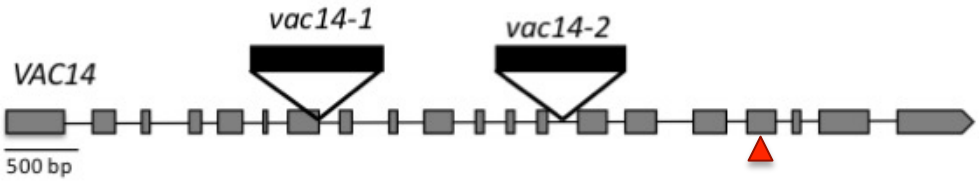

Figure 3.2. *Vac14 T-DNA alleles.* Black boxes represent T-DNA insertion loci. Red triangle represents the site of amiRNA hybridization in Vac14 knockdown lines.

Figure 3. 3

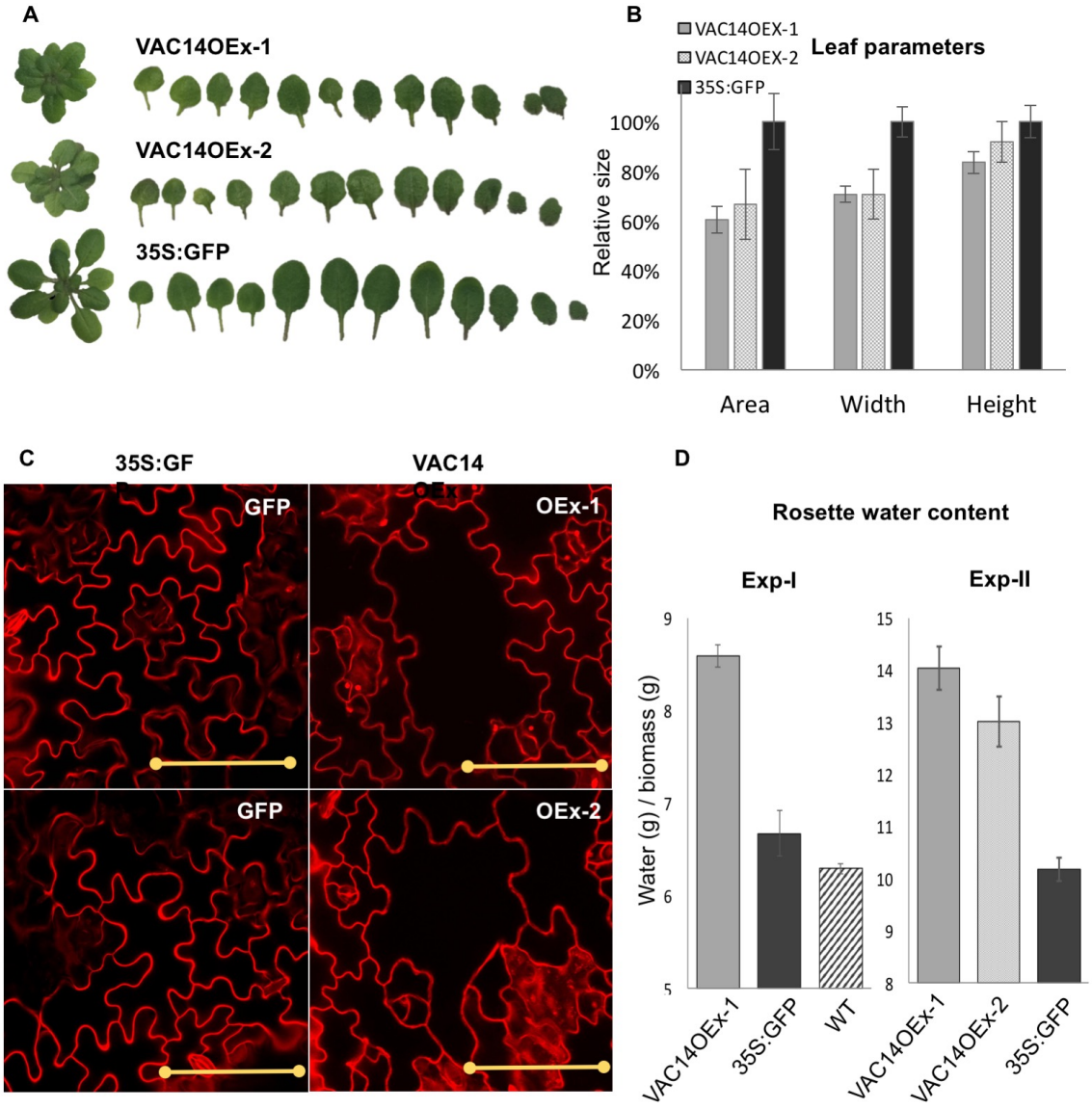

Figure 3.3. *Vac14 OEx results in reduced leaf size and enlarged pavement cells*. **A**. Dissected rosettes of 4 week-old plants grown in short-day conditions. **B**. Measurement of leaf area of 5 central rosettes leaves. Error bars indicate standard deviation. **C**. Pavement cells of 5 week-old rosette leaves stained with propidium iodide. Size bar indicates 100 um. **D.** Water content of 4 week-old rosettes. Error bars indicate standard error for 4-5 biological replicates.

Figure 3. 4

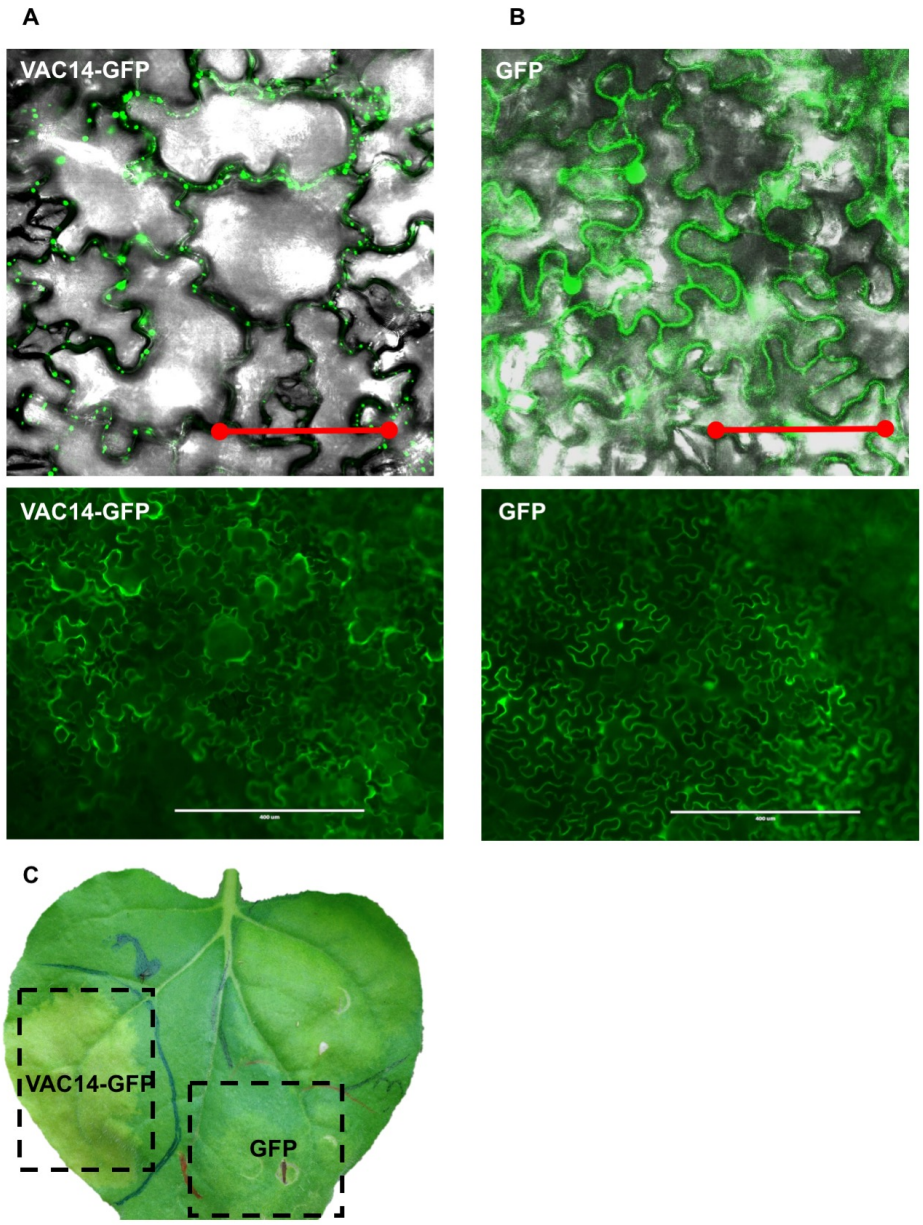

Figure 3.4. *Transient overexpression of Vac14 in N.benthamiana results in swollen pavement cells*. **A.** Vac14 OEx. Red size bar indicates 100um, white size bar indicates 400um. **B.** GFP OEx does not cause swollen pavement cell phenotype. Size bars same as in A. **C.** Vac14 OEx causes tissue damage in infiltrated leaves.

Figure 3. 5

Figure 3.5. *Vac14 OEx results in increased drought tolerance*. **A**. 4 week-old plants at the start of the dehydration experiment. **B**. Plants after withholding water for 3 weeks. **C.** Plants after 1 week of rehydration following drought period. **D**. 7-week-old plants grown in well-watered control conditions. **E**. Larger population of plants used in experiment. Image taken on same day as in B. Not all Vac14 OEx lines survived dehydration.

Figure 3. 6

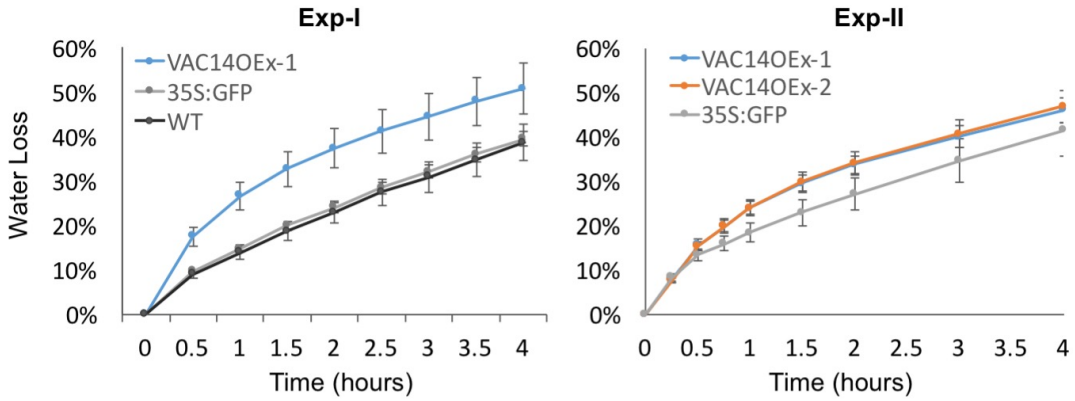

Figure 3.6. *Vac14 OEx causes increased rates of transpirational water loss*. Error bars represent standard error for 4-5 biological replicates. Experiment was conducted twice.

Figure 3. 7

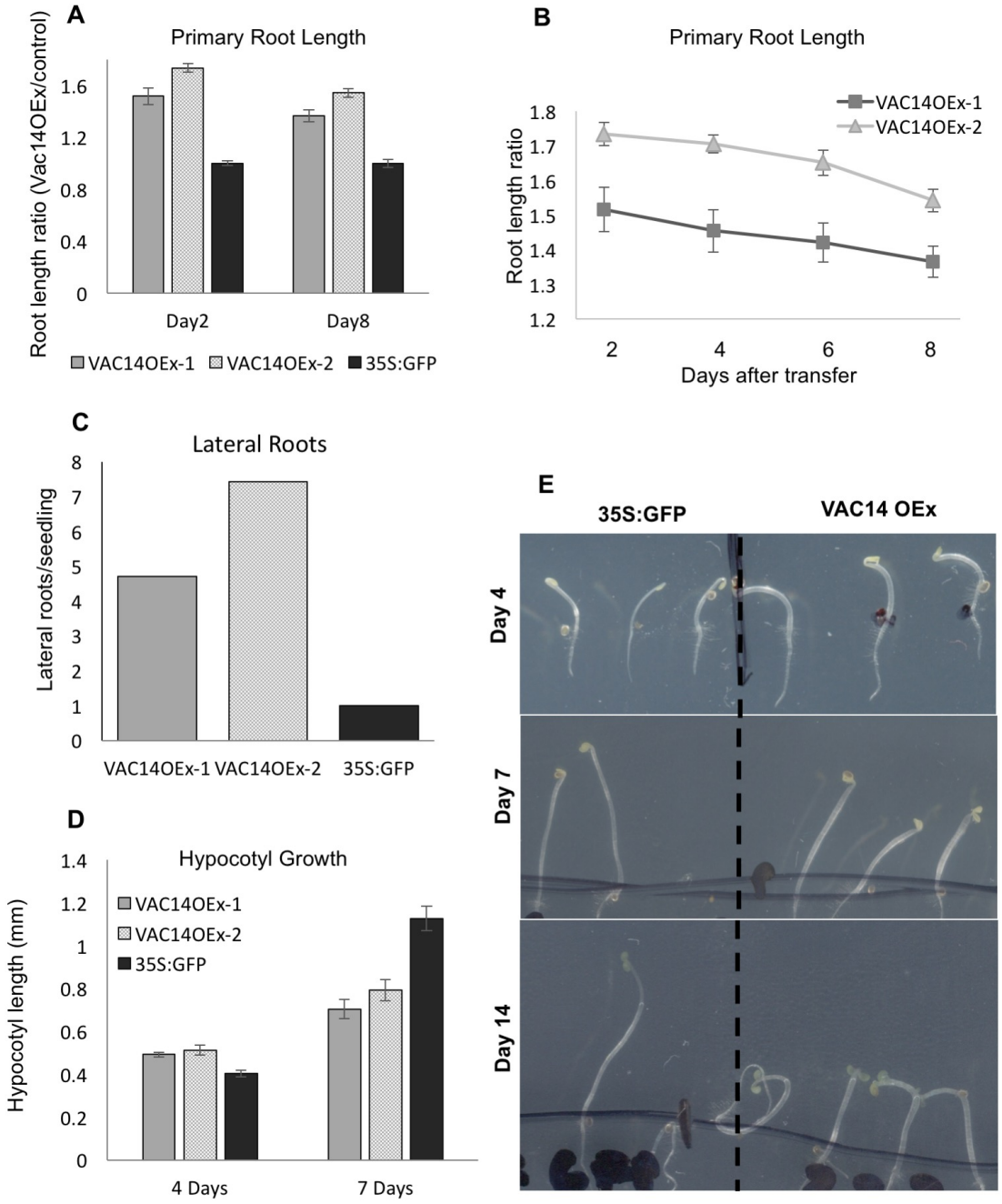
A
Primary Root Length
Root length ratio (Vac14OEx/control)
1.6
1.2
0.8
0.4
0
Day2
Day8
VAC14OEx-1
VAC14OEx-2
35S:GFP
B
Primary Root Length
Root length ratio
1.8
1.7
1.6
1.5
1.4
1.3
1.2
2
4
6
8
Days after transfer
VAC14OEx-1
VAC14OEx-2
C
Lateral Roots
Lateral roots/seedling
8
7
6
5
4
3
2
1
0
VAC14OEx-1
VAC14OEx-2
35S:GFP
D
Hypocotyl Growth
Hypocotyl length (mm)
1.4
1.2
1
0.8
0.6
0.4
0.2
0
VAC14OEx-1
VAC14OEx-2
35S:GFP
4 Days
7 Days
E
35S:GFP
VAC14 OEx
Day 4
Day 7
Day 14

Figure 3.7. *Vac14 OEx seedlings have an increased rate of initial growth*. **A**. Primary root length for seedlings grown on 1/2MS control media, shown as a relative ratio to 35S:GFP control plants. Time indicates days after seedling transfer. Error bars indicate standard error for 14 biological replicates. **B.** Primary root length difference between Vac14 OEx seedlings and controls decrease over time. Graph represents ratio values, calculated the same as in A. **C.** Average number of lateral roots per seedlings, calculated by counting the total number of lateral roots and dividing my the number of seedlings (n=14). **D.** Hypocotyl lengths measured for dark grown seedlings. Error bars represent standard error for 8-12 seedlings. **E.** Hypocotyls in Vac14 OEx seedlings appear thicker than 35S:GFP controls.

Figure 3. 8

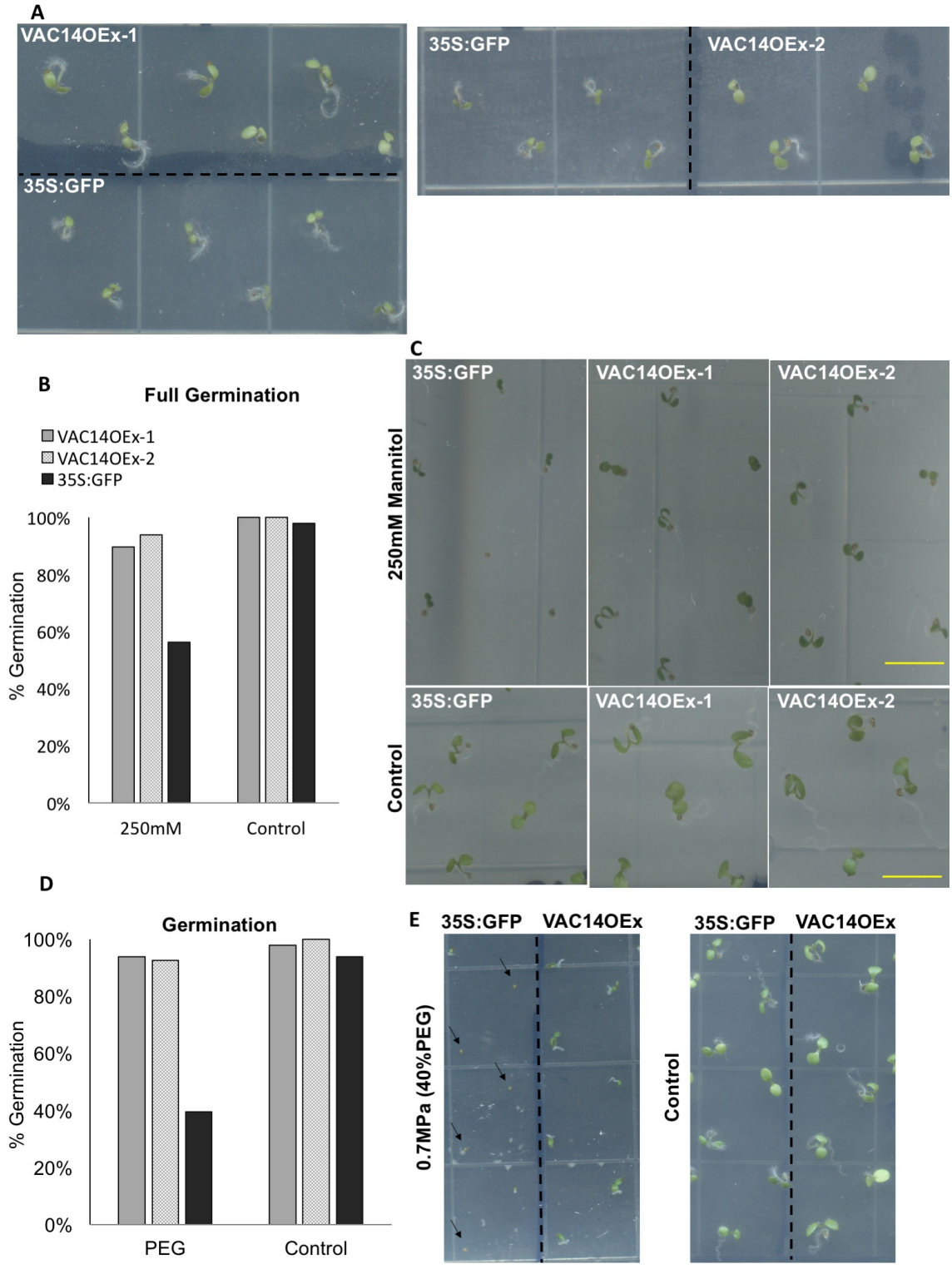
A
VAC14OEx-1
35S:GFP
35S:GFP
VAC14OEx-2
B
Full Germination
VAC14OEx-1
VAC14OEx-2
35S:GFP
% Germination
100%
80%
60%
40%
20%
0%
250mM
Control
C
35S:GFP
VAC14OEx-1
VAC14OEx-2
250mM Mannitol
Control
D
Germination
% Germination
PEG
Control
E
35S:GFP
VAC14OEx
0.7MPa (40%PEG)
Control

Figure 3.8. *Vac14 OEx seedlings are larger early on in development and display increased osmotic stress tolerance*. **A.** 5 day-old seedlings germinating on 1/2MS control media. Vac14OEx lines appear larger than 35S:GFP control. **B.** Vac14 OEx seedlings achieve full germination (expanded cotyledons) on 250mM mannitol osmotic stress media better than 35S:GFP controls. Germination scored at day 6 for 48 seedlings. Control data represents germination on 1/2MS media. **C.** 6 day-old seedlings germinating on control and osmotic stress media. Vac14 OEx seedlings appear significantly larger on 250mM mannitol plates. **D**. Vac14 OEx seedlings germinate on 40% PEG (8,000 MW) better than controls. Media plates containing 40% PEG represent a water potential of -0.7MPa (42, 43). Germination was counted as an emerged radical and scored on day 7. **E**. Image of seedling germination at day 7 on 40% PEG and control media. Black arrows point to 35S:GFP control seeds that failed to germinate on stress media.

Figure 3. 9

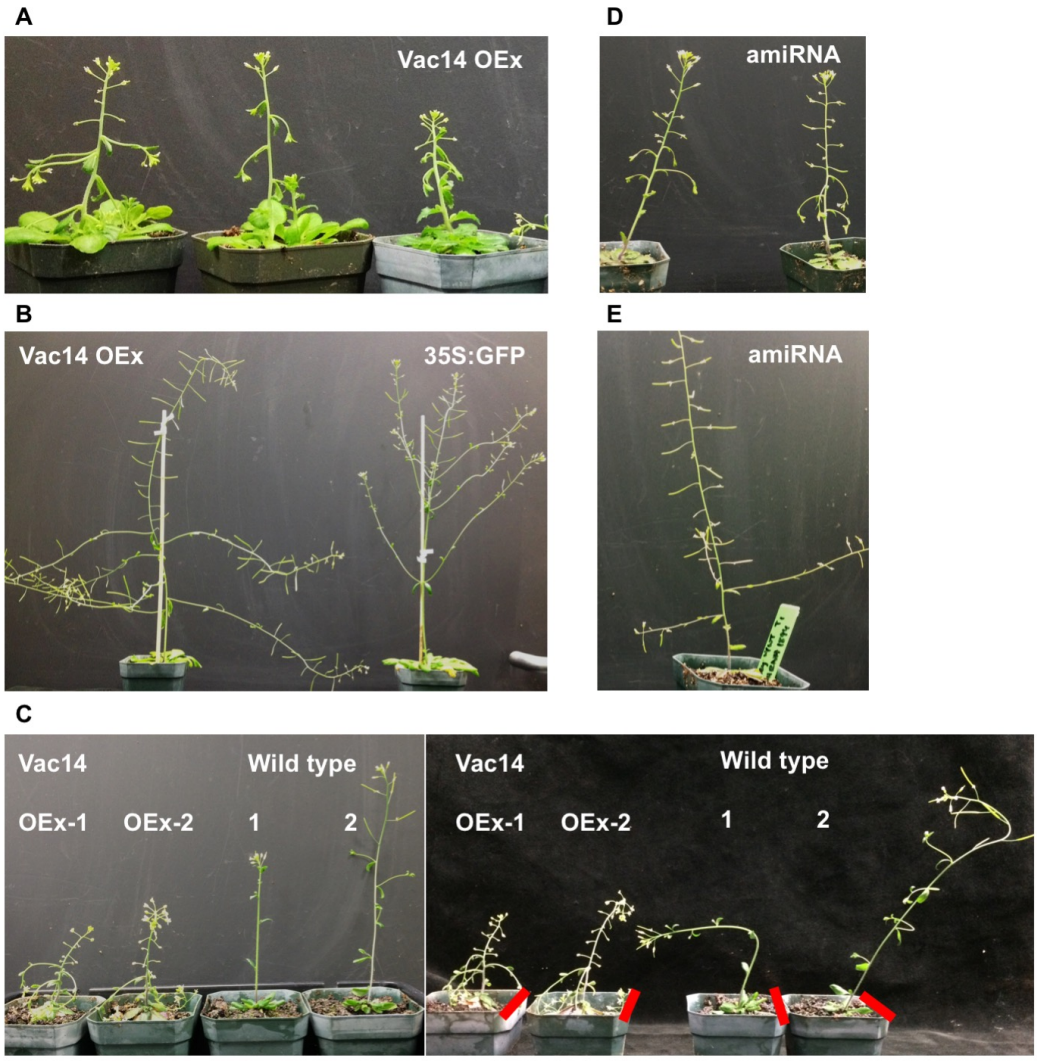

Figure 3.9. *Vac14 OEx and amiRNA knockdown lines have impaired shoot gravitropism*. **A.** Independent T1 Vac14 OEx lines with downward growing lateral branches. **B**. Vac14 OEx T1 plant showing intermediate gravitropic phenotype with horizontal branches. **C**. Vac14 OEx lines are not responsive to gravity. Plants on left were imaged before tilting. Plants on right imaged after being tipped on their side for 24-hours. Red lines indicate side that was laid on the bottom of the growth chamber. **D**. Vac14 amiRNA T1 plants showing same gravitropic phenotype as OEx lines in A. **E.** Vac14 amiRNA T1 plant showing intermediate phenotype similar to B.

Figure 3. 10

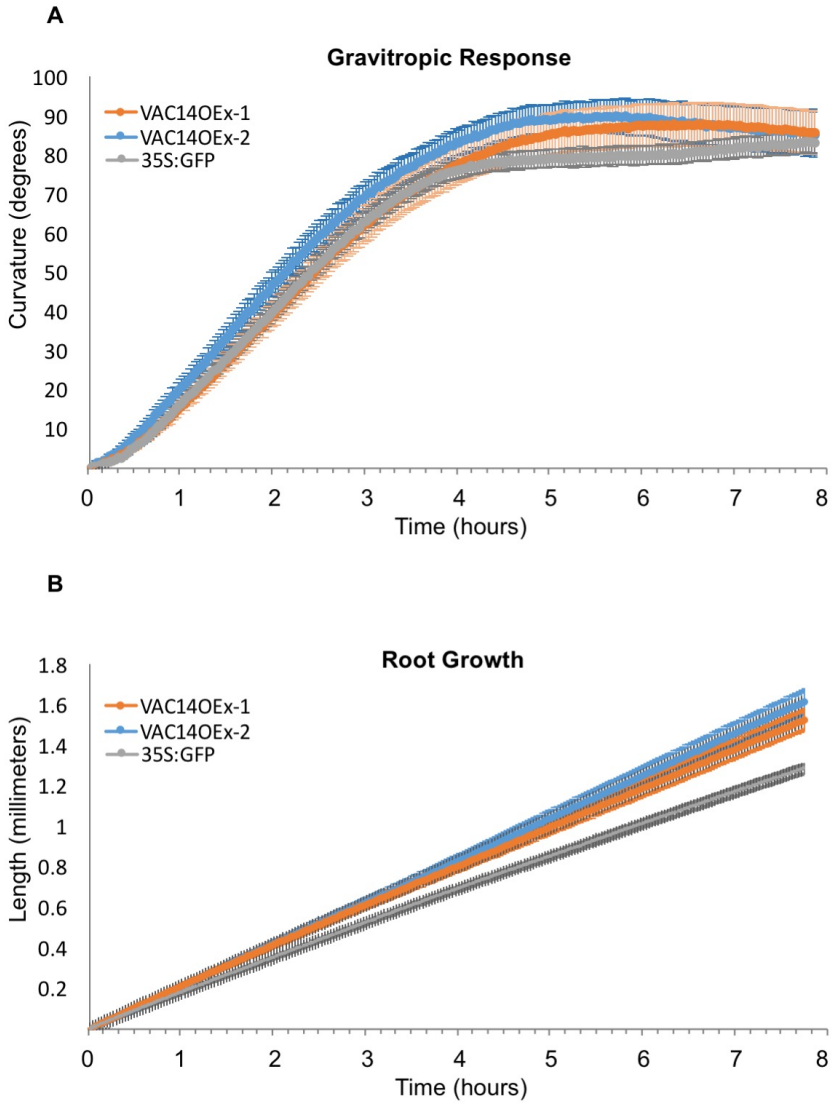

Figure 3.10. *Vac14 OEx seedlings do not display significant root gravitropic defects.* **A.** Root bending after 90^{O} reorientation. Root angle measured every 2 minutes. Error bars indicate standard error for 26-34 seedlings. **B**. Vac14 OEx seedlings show increased rate of growth. Root lengths measured every 2 minutes. Error bars indicate standard error for 26-34 seedlings.

Figure 3. 11

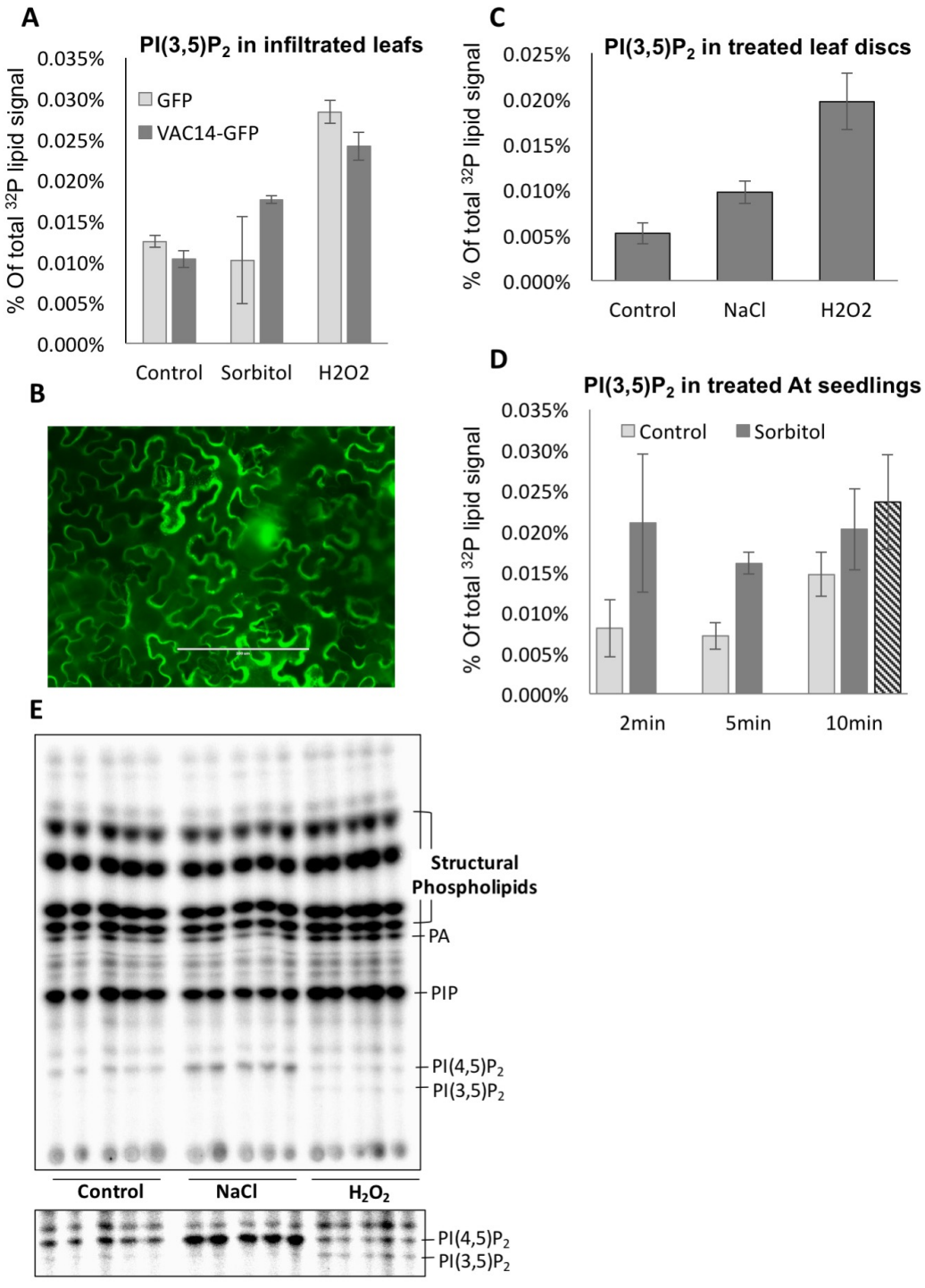
A
PI(3,5)P2 in infiltrated leafs
% Of total 32P lipid signal
0.035%
0.030%
0.025%
0.020%
0.015%
0.010%
0.005%
0.000%
GFP
VAC14-GFP
Control
Sorbitol
H2O2
B
C
PI(3,5)P2 in treated leaf discs
% Of total 32P lipid signal
0.025%
0.020%
0.015%
0.010%
0.005%
0.000%
Control
NaCl
H2O2
D
PI(3,5)P2 in treated At seedlings
% Of total 32P lipid signal
0.035%
0.030%
0.025%
0.020%
0.015%
0.010%
0.005%
0.000%
Control
Sorbitol
2min
5min
10min
E
Structural Phospholipids
PA
PIP
PI(4,5)P2
PI(3,5)P2
Control
NaCl
H2O2
PI(4,5)P2
PI(3,5)P2

Figure 3.11. *PI(3,5)P_2 measurements*. **A**. Vac14 OEx does not cause a significant difference in PI(3,5)P_2 levels. Lipids measured in *N.benthamiana* leaf disc sample collected from infiltrated leaves. Leaf discs were treated for 10 minutes before lipid extraction. Error bars indicate standard deviation for 4 biological replicates. **B.** Expression levels of Vac14-GFP in infiltrated leaves. **C.** PI(3,5)P_2 measurements in un-infiltrated *N.benthamiana* leaf discs. Error bars indicate standard deviation for 5 biological replicates. **D.** Timecourse measurement of PI(3,5)P_2 in stress treated Arabidopsis seedlings. Error bars indicate standard deviation for 3 biological replicates. **E**. TLC of data quantified in C. Bottom box represents over-exposure of TLC necessary for visualizing PI(3,5)P_2 spots.

Figure 3. 12

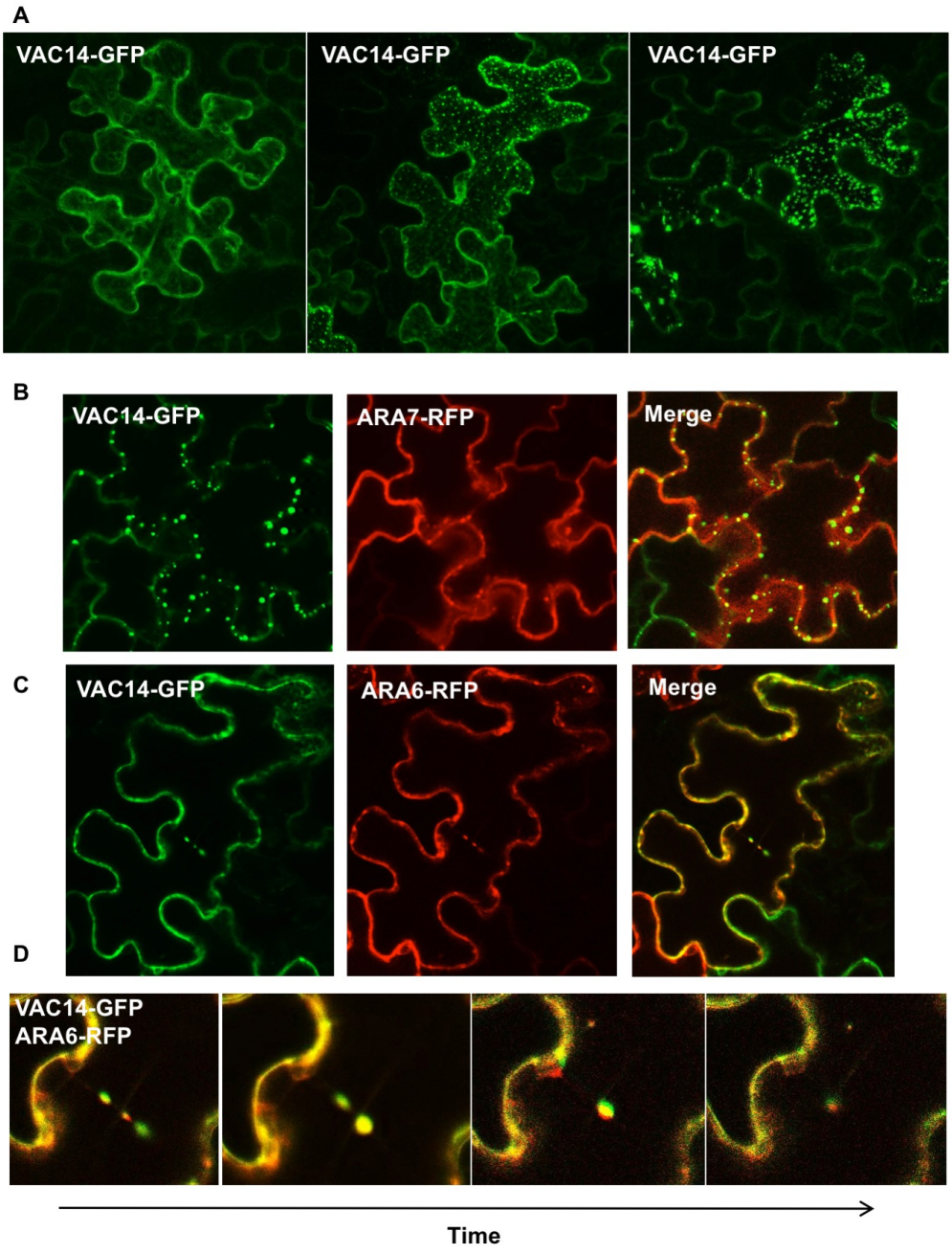

Figure 3.12. *Vac14 subcellular localization*. **A.** Vac14 appears in the cytosol or vacuole membrane and in distinct punctate structures. **B.** Vac14 partially co-localizes with Ara7. **C.** Vac14 partially co-localizes with Ara6 vesicles. **D.** Vac14 and Ara6 co-localize to moving vesicles in the cell.

References

1. Munnik T & Testerink C (2009) Plant phospholipid signaling: "in a nutshell". *J Lipid Res* 50 Suppl:S260-265.
2. Ho CY, Alghamdi TA, & Botelho RJ (2012) Phosphatidylinositol-3,5-bisphosphate: no longer the poor PIP2. *Traffic* 13(1):1-8.
3. Jin N*, et al.* (2014) Roles for PI (3, 5) P2 in nutrient sensing through TORC1. *Molecular biology of the cell* 25(7):1171-1185.
4. McCartney AJ, Zhang Y, & Weisman LS (2014) Phosphatidylinositol 3,5-bisphosphate: low abundance, high significance. *Bioessays* 36(1):52-64.
5. Li SC*, et al.* (2014) The signaling lipid PI(3,5)P(2) stabilizes V(1)-V(o) sector interactions and activates the V-ATPase. *Mol Biol Cell* 25(8):1251-1262.
6. Takatori S*, et al.* (2015) Phosphatidylinositol 3,5-bisphosphate-rich membrane domains in endosomes and lysosomes. *Traffic*.
7. Duex JE, Nau JJ, Kauffman EJ, & Weisman LS (2006) Phosphoinositide 5-phosphatase Fig 4p is required for both acute rise and subsequent fall in stress-induced phosphatidylinositol 3,5-bisphosphate levels. *Eukaryot Cell* 5(4):723-731.
8. Dove SK*, et al.* (1997) Osmotic stress activates phosphatidylinositol-3,5-bisphosphate synthesis. *Nature* 390(6656):187-192.
9. Bonangelino CJ*, et al.* (2002) Osmotic stress-induced increase of phosphatidylinositol 3,5-bisphosphate requires Vac14p, an activator of the lipid kinase Fab1p. *J Cell Biol* 156(6):1015-1028.
10. Sbrissa D & Shisheva A (2005) Acquisition of unprecedented phosphatidylinositol 3,5-bisphosphate rise in hyperosmotically stressed 3T3-L1 adipocytes, mediated by ArPIKfyve-PIKfyve pathway. *J Biol Chem* 280(9):7883-7889.
11. Jones DR*, et al.* (1999) The identification of phosphatidylinositol 3,5-bisphosphate in T-lymphocytes and its regulation by interleukin-2. *J Biol Chem* 274(26):18407-18413.
12. Meijer HJ, Divecha N, van den Ende H, Musgrave A, & Munnik T (1999) Hyperosmotic stress induces rapid synthesis of phosphatidyl-D-inositol 3, 5-bisphosphate in plant cells. *Planta* 208(2):294-298.
13. Zonia L & Munnik T (2004) Osmotically induced cell swelling versus cell shrinking elicits specific changes in phospholipid signals in tobacco pollen tubes. *Plant Physiol* 134(2):813-823.
14. Sbrissa D*, et al.* (2004) A mammalian ortholog of Saccharomyces cerevisiae Vac14 that associates with and up-regulates PIKfyve phosphoinositide 5-kinase activity. *Mol Cell Biol* 24(23):10437-10447.
15. Whitley P, Hinz S, & Doughty J (2009) Arabidopsis FAB1/PIKfyve proteins are essential for development of viable pollen. *Plant Physiol* 151(4):1812-1822.

16. Hirano T, Matsuzawa T, Takegawa K, & Sato MH (2011) Loss-of-function and gain-of-function mutations in FAB1A/B impair endomembrane homeostasis, conferring pleiotropic developmental abnormalities in Arabidopsis. *Plant Physiol* 155(2):797-807.

17. Hirano T, Munnik T, & Sato MH (2015) Phosphatidylinositol 3-Phosphate 5-Kinase, FAB1/PIKfyve Kinase Mediates Endosome Maturation to Establish Endosome-Cortical Microtubule Interaction in Arabidopsis. *Plant Physiol* 169(3):1961-1974.

18. Dove SK*, et al.* (2002) Vac14 controls PtdIns(3,5)P(2) synthesis and Fab1-dependent protein trafficking to the multivesicular body. *Curr Biol* 12(11):885-893.

19. Chow CY*, et al.* (2007) Mutation of FIG4 causes neurodegeneration in the pale tremor mouse and patients with CMT4J. *Nature* 448(7149):68-72.

20. Chow CY*, et al.* (2009) Deleterious variants of FIG4, a phosphoinositide phosphatase, in patients with ALS. *Am J Hum Genet* 84(1):85-88.

21. Baulac S*, et al.* (2014) Role of the phosphoinositide phosphatase FIG4 gene in familial epilepsy with polymicrogyria. *Neurology* 82(12):1068-1075.

22. McCartney AJ*, et al.* (2014) Activity-dependent PI(3,5)P2 synthesis controls AMPA receptor trafficking during synaptic depression. *Proc Natl Acad Sci U S A* 111(45):E4896-4905.

23. Stecker KE, Minkoff BB, & Sussman MR (2014) Phosphoproteomic analyses reveal early signaling events in the osmotic stress response. *Plant physiology* 165(3):1171-1187.

24. Bak G*, et al.* (2013) Rapid structural changes and acidification of guard cell vacuoles during stomatal closure require phosphatidylinositol 3,5-bisphosphate. *Plant Cell* 25(6):2202-2216.

25. Tsukaya H (2006) Mechanism of leaf-shape determination. *Annu Rev Plant Biol* 57:477-496.

26. Kim GT, Tsukaya H, & Uchimiya H (1998) The ROTUNDIFOLIA3 gene of Arabidopsis thaliana encodes a new member of the cytochrome P-450 family that is required for the regulated polar elongation of leaf cells. *Genes Dev* 12(15):2381-2391.

27. Hu Y, Poh HM, & Chua NH (2006) The Arabidopsis ARGOS-LIKE gene regulates cell expansion during organ growth. *Plant J* 47(1):1-9.

28. Strohm AK, Baldwin KL, & Masson PH (2012) Multiple roles for membrane-associated protein trafficking and signaling in gravitropism. *Front Plant Sci* 3:274.

29. Petrasek J*, et al.* (2006) PIN proteins perform a rate-limiting function in cellular auxin efflux. *Science* 312(5775):914-918.

30. Wisniewska J*, et al.* (2006) Polar PIN localization directs auxin flow in plants. *Science* 312(5775):883.

31. Zheng HQ & Staehelin LA (2001) Nodal endoplasmic reticulum, a specialized form of endoplasmic reticulum found in gravity-sensing root tip columella cells. *Plant Physiol* 125(1):252-265.

32. Sato MH*, et al.* (1997) The AtVAM3 encodes a syntaxin-related molecule implicated in the vacuolar assembly in Arabidopsis thaliana. *J Biol Chem* 272(39):24530-24535.

33. Silady RA*, et al.* (2004) The gravitropism defective 2 mutants of Arabidopsis are deficient in a protein implicated in endocytosis in Caenorhabditis elegans. *Plant Physiol* 136(2):3095-3103; discussion 3002.

34. Yano D*, et al.* (2003) A SNARE complex containing SGR3/AtVAM3 and ZIG/VTI11 in gravity-sensing cells is important for Arabidopsis shoot gravitropism. *Proc Natl Acad Sci U S A* 100(14):8589-8594.

35. Zheng H, von Mollard GF, Kovaleva V, Stevens TH, & Raikhel NV (1999) The plant vesicle-associated SNARE AtVTI1a likely mediates vesicle transport from the trans-Golgi network to the prevacuolar compartment. *Mol Biol Cell* 10(7):2251-2264.

36. Jefferies HB*, et al.* (2008) A selective PIKfyve inhibitor blocks PtdIns(3,5)P(2) production and disrupts endomembrane transport and retroviral budding. *EMBO Rep* 9(2):164-170.

37. Yamamoto A*, et al.* (1995) Novel PI(4)P 5-kinase homologue, Fab1p, essential for normal vacuole function and morphology in yeast. *Mol Biol Cell* 6(5):525-539.

38. Dettmer J, Hong-Hermesdorf A, Stierhof YD, & Schumacher K (2006) Vacuolar H+-ATPase activity is required for endocytic and secretory trafficking in Arabidopsis. *Plant Cell* 18(3):715-730.

39. Lee GJ, Sohn EJ, Lee MH, & Hwang I (2004) The Arabidopsis rab5 homologs rha1 and ara7 localize to the prevacuolar compartment. *Plant Cell Physiol* 45(9):1211-1220.

40. Kotzer AM*, et al.* (2004) AtRabF2b (Ara7) acts on the vacuolar trafficking pathway in tobacco leaf epidermal cells. *J Cell Sci* 117(Pt 26):6377-6389.

41. Andres Z*, et al.* (2014) Control of vacuolar dynamics and regulation of stomatal aperture by tonoplast potassium uptake. *Proc Natl Acad Sci U S A* 111(17):E1806-1814.

42. van der Weele CM, Spollen WG, Sharp RE, & Baskin TI (2000) Growth of Arabidopsis thaliana seedlings under water deficit studied by control of water potential in nutrient-agar media. *J Exp Bot* 51(350):1555-1562.

43. Verslues PE & Bray EA (2004) LWR1 and LWR2 are required for osmoregulation and osmotic adjustment in Arabidopsis. *Plant Physiol* 136(1):2831-2842.

44. Karimi M, Inze D, & Depicker A (2002) GATEWAY vectors for Agrobacterium-mediated plant transformation. *Trends Plant Sci* 7(5):193-195.

45. Warthmann N, Chen H, Ossowski S, Weigel D, & Herve P (2008) Highly specific gene silencing by artificial miRNAs in rice. *PLoS One* 3(3):e1829.

46. Earley KW*, et al.* (2006) Gateway-compatible vectors for plant functional genomics and proteomics. *Plant J* 45(4):616-629.

47. Clough SJ & Bent AF (1998) Floral dip: a simplified method for Agrobacterium-mediated transformation of Arabidopsis thaliana. *Plant J* 16(6):735-743.

48. Ma L, Lukasik E, Gawehns F, & Takken FL (2012) The use of agroinfiltration for transient expression of plant resistance and fungal effector proteins in Nicotiana benthamiana leaves. *Plant Fungal Pathogens: Methods and Protocols*:61-74.

49. Voinnet O, Rivas S, Mestre P, & Baulcombe D (2003) An enhanced transient expression system in plants based on suppression of gene silencing by the p19 protein of tomato bushy stunt virus. *Plant J* 33(5):949-956.

50. Brooks TL, Miller ND, & Spalding EP (2010) Plasticity of Arabidopsis root gravitropism throughout a multidimensional condition space quantified by automated image analysis. *Plant Physiol* 152(1):206-216.

51. Munnik T & Zarza X (2013) Analyzing plant signaling phospholipids through 32Pi-labeling and TLC. *Methods Mol Biol* 1009:3-15.

CHAPTER 4

Proteome-wide Conformational Analysis of Plant Proteins using Thermal Denaturation Profiling and Isotope-assisted Quantitative Mass Spectrometry.

This chapter represents ongoing research and a manuscript in progress.

Kelly E. Stecker, Jeremy D. Volkening, Heather Burch, Michael R. Sussman

Abstract

In my previous chapters I identified proteins involved in hyperosmotic stress response through measurement of rapid changes in protein phosphorylation induced by treatment with 0.3 M mannitol. In the work presented herein, I build upon recently published protocols developed with animal cell cultures, to develop a new method for identifying proteins participating in cell signaling. This procedure measures changes to a protein's conformational state and in conjunction with isotope-assisted mass spectrometry, can be used to interrogate the entire proteome. Conformational changes that cause a shift in the thermal stability of a protein are identified on a proteome-wide scale using untargeted quantitative mass spectrometry. I first validate my method by detecting conformational changes caused in vitro by MgATP binding in a cell extract and compare this data to published results. I next demonstrate the ability to detect post translation modifications that influence protein conformation by conducting enzymatic treatments of Arabidopsis extracts. Finally, I use thermal denaturation profiling to identify conformational changes induced from *in vivo* osmotic stress treatment of Arabidopsis seedlings. My results indicate that the plant proteome possesses a wide range of thermal stability and that proteins can undergo treatment-induced conformational changes that result in large shifts in their thermal denaturation profile. My results highlight the potential of this assay for identifying stress induced conformational changes *in vivo* and also addresses the challenges for its application to plant seedlings, a complex multicellular organism.

Background

Extracellular signals are perceived and rapidly communicated in cells through signal transduction pathways that rely primarily on protein post-translational modifications (PTMs). These rapid and often reversible chemical modifications to proteins allow external signals to translate into functional biochemical changes within the cell. PTMs may affect protein structure in a way that confers the ability to bind new targets, translocate within cells, or activate and deactivate enzymatic activity. The foundation of these modulating changes to protein function is the fact that PTMs can alter protein conformation. Changes in protein conformation can therefore be a direct readout of altered protein function and activity, but the development of technology to detect conformational changes directly in the entire proteome, e.g., complex cell extracts or living cells, has only recently been attempted (1).

The relationship between induced conformational change and modified protein function means that the ability to directly detect changes in protein conformation can be a valuable tool for probing cellular response. Measurements of conformational change could be a more direct and robust means to identify proteins involved in biologically significant cell signaling events. To be a useful tool for identifying new proteins involved in cellular response, however, measurements of conformational change must be conducted in a global, untargeted manner. To this point, large-scale global analysis has been difficult to achieve due to the density and heterogeneity of the proteome and the challenge of monitoring changes in a complex background.

Without a method to globally interrogate protein conformational changes in the context of cell signaling, efforts to identify proteins involved in signal transduction events have primarily relied on direct detection and measurement of PTMs. Measurement of PTMs

such as phosphorylation and acetylation have advanced the field tremendously in identifying and characterizing proteins involved in signaling pathways (2). Ultimately, however, quantification of protein PTMs serves as a proxy for modulation of protein function. The interpreted significance of PTM changes relies on the assumption that the monitored PTMs affect protein function. This may not necessarily be true. In the case of phosphorylation, for example, the ubiquitous nature of Ser/Thr/Tyr phosphorylation within the proteome can make it difficult to ascertain which phosphorylation events significantly influence protein function. For this reason, direct measurement of protein conformational changes, in addition to PTM detection, provides desirable information in discriminating significant from ineffectual PTMs.

Methods for determining protein conformation in simplified systems have been well established. These methods use purified protein *in vitro* and rely on exploitation of thermodynamic properties (3-6). For example, relative changes in a protein's stability over a temperature range are used to detect conformational changes in thermal shift assays (TSA) (7-9). Here the temperature at which a protein precipitates is related to its stability and conformation, and can be quantified in a variety of ways including light scattering and fluorescence based techniques (10-12). These assays are often used to measure protein ligand interactions in an isolated system with purified proteins (8).

A limitation in the utility of TSA is that fact that it requires purified targets and a simplified system. This does not make the technology useful for probing conformational changes *in vivo* and severely restricts which proteins can be targeted. Significant progress towards overcoming these purification requirements has recently been made with the advent of the cellular thermal shift assay (CETSA) (13, 14). CESTA applies the principles of TSA,

measurement of differential protein precipitation over a temperature gradient, but the assay is performed within the background of the whole cell. CESTA's heating and precipitation measures changes in protein thermal stability *in vivo* or in cell extracts (13, 14). To quantify thermal shifts in stability, western blot analysis is used to measuring soluble protein abundance over a set temperature range. Placing TSA measurements in a biologically relevant context significantly moved the field forward. As an example, the advancements of CESTA allowed for identification of drug targets in a cell by observing drug induced shifts in the thermal stability of target proteins *in vivo* (14).

A drawback and continued limitation of CESTA, however, is the fact that it approaches measurements of protein conformation in a targeted manner, meaning that only a small number of predetermined proteins can be examined. This prohibits the method from being a discovery-based tool for identifying new candidates involved in signaling and response. Recently, this large hurdle has been overcome by integrating CESTA with mass spectrometry based proteomic techniques to measure thermal shifts on a global scale (1). A quantitative proteomics approach was implemented in conjunction with the CESTA cellular thermal denaturation to transition the assay from a targeted, low-throughput characterization of protein conformation to an untargeted, high-throughput discovery tool (1, 15). By replacing western blots with quantitative shotgun proteomics, this powerful new platform allowed for untargeted identification of protein conformational changes by measuring protein thermal melting curves for thousands of targets *in vivo*. Referred to as the Thermal Proteome Pipeline (TPP), this experimental approach has been used to identify new drug targets and analyze off-targeted drug effects in vivo (1, 16).

In this chapter I present my initial efforts to establish a thermal denaturation experimental pipeline for measuring conformational changes in Arabidopsis plant proteins both *in vitro* and *in vivo*. Building on the methodology presented in the seminal TPP work investigating drug-ligand interactions in cultured animal cells (1), I have turned my focus to cell signaling events and *in vivo* response to short term hyperosmotic stress treatment. I first performed *in vitro* MgATP treatment of soluble extracts from Arabidopsis, humans, and yeast as part of a cross-species characterization of thermal denaturation profiles. I next examined post-translational modifications that affect protein conformation through *in vitro* enzymatic and chemical treatment of Arabidopsis extracts. Finally, I attempt for the first time to use thermal denaturation to detect *in vivo* conformational changes in multicellular a organism (Arabidopsis seedlings). My results demonstrate the potential of this assay and highlight areas in need of continued method development.

Results and Discussion

Plant proteins exhibit wide thermal stability range

To measure the thermal denaturation profiles of plant protein extracts I established an experimental pipeline that could be use to detect protein conformational changes from both *in vivo* and *in vitro* treated samples (**Figure 4.1**). To validate my pipeline, I first replicated an *in vitro* MgATP binding experiment that was performed by Savitski *et al*. in the seminal TPP publication (1). Arabidopsis seedling and Human K562 cell extracts were incubated with MgATP or control media for 10-15 min at room temperature. Thermal stability curves were then measured for proteins in both conditions and Tm values, defined as the temperature in which half of the protein has precipitated, were calculated. Modeling of thermal denaturation curves and calculation of Tm values was conducted using in-house R scripts written by fellow graduate student Jeremy Volkening in the Sussman lab. The ATP induced Tm shift, defined as the Tm difference between treatment and control samples, was calculated for each protein. In a global analysis of Tm shifts for proteins annotated as ATP binding, human K562 extracts showed nearly identical global Tm shifts as in the published data, providing confidence that the technology was successfully replicated (**Figure 4.2 A-B**). ATP binding proteins in human K562 samples displayed an average increased Tm shift of less than $2^{O}C$, experiencing a stabilizing effect on Tm when bound to ATP. This is in contrast to the majority of proteins not annotated as ATP binding, which showed no Tm shift upon incubation with ATP (**Figure 4.2B**). Strikingly, when this same experiment was conduced with Arabidopsis extracts, the effect of ATP binding on protein Tm was dramatically larger. In contrast to the modest $< 2^{O}C$ shift seen in K562 samples, Arabidopsis ATP binding proteins displayed Tm shifts of $> 5\ ^{O}C$, with subpopulations experiencing Tm shifts around

15 ^{O}C (**Figure 4.2C**). Additionally, ATP binding proteins showed both Tm stabilizing and Tm destabilizing shifts.

Thermal stability ranges correlate with environmental growth conditions

In my initial ATP analysis I observed that proteins from Arabidopsis extracts experienced a larger shift in Tm upon ligand binding than did human K562 proteins. Likewise, the overall range of Tm values displayed by Arabidopsis proteins was wider than humans (**Figure 4.2E**). This led me to wonder if there is a relationship between the global thermal stability of proteins from an organism and the temperature range experienced by that organism in their environment. K562 cells, being derived from a warm-blooded mammal, experience a very narrow temperature range in their environment. In contrast, plants are exposed to an extreme range in temperatures, and thus may require a broader range of thermal stability across the proteome. To gain additional evidence for this hypothesis, I repeated the in vitro MgATP incubation using yeast *S.cerevisiae* extracts. Yeast live within a much tighter temperature range than plants, but are more tolerant of temperature deviations than human K562 cells [Need reference]. Accordingly, I found that Tm shifts for yeast proteins upon ATP binding displayed a wider temperature range than K562 extracts (**Figure 4.2D**). Additionally, the overall profile of observed Tm values for yeast proteins was wider than K562 proteins (Figure 2E). All together, the yeast displayed a thermal stability profile that was closer to humans than Arabidopsis, but fell in between these two species in both magnitude of Tm shift and global distribution of Tm values. This preliminary evidence suggests there is a link between the environmental condition (temperature) in which an organism has evolved, and innate protein thermal stability.

Analysis of PTMs using thermal denaturation and in vitro treatments.

Identifying protein modifications that significantly contribute to conformation and stability is valuable information for understanding how proteins are regulated. Exposing proteins to enzymatic conditions that target specific PTMs is one way to evaluate which modifications are important for protein structure. To determine if the thermal denaturation assay could detect Tm shifts in Arabidopsis extracts exposed to different treatments targeting specific protein modifications, I conducted an *in vitro* experiment using enzymatic phosphatase and deubiquitinase treatment to target phosphorylation and ubiquitination PTMs, respectfully. In addition I exposed extracts to reducing conditions using DTT to identify proteins with redox sensitive conformational changes. To conduct these measurements I used the experimental pipeline outlined in Figure 1. All three conditions tested in my pilot study identified proteins responsive to *in vitro* treatments by changes in their Tm.

The *in vitro* condition that affected the most proteins and caused the largest shifts in thermal stability was phosphatase treatment. Soluble extracts were incubated for 2 hours at room temperature with a duel mixture of Lambda Protein Phosphatase and CIP Alkaline Phosphatase, each at 10uM. These generic phosphatases target Ser, Thr, and Tyr phosphorylation sites, while CIP Alkaline phosphatase can also dephosphorylates nucleic acids. Overall phosphatase treatment had a destabilizing affect on protein conformation, causing the majority of responsive proteins to precipitate at lower temperatures on the thermal denaturation curve. Approximately 175 proteins out of 1100 quantified displayed a phosphatase induced Tm shift. To further evaluate these findings, responsive proteins were searched against an online Arabidopsis phosphorylation database, PhosPhat 4.0 (17). From the list, 78% of the phosphatase responsive proteins have reported phosphopeptides identified

in previous mass spec phosphorylation studies. From my own untargeted phosphoproteomic data collected as part of the Stecker *et al*. 2014 publication, 22 proteins displaying phosphatase induced Tm shifts had identified phosphopeptides in this dataset. **Figure 4.3** shows several examples from this small subset of data.

Identifying proteins with conformational changes induced by phosphatase treatment indicates that these proteins possess phosphorylation sites that are influential to protein structure, and therefor are likely important for protein function. Many of the phosphatase induced Tm shifts were quite large, with over 30 proteins showing Tm shifts > $7^{O}C$. Interestingly, the large shifts in Tm seen in this study indicate that phosphorylation stoichiometry is high within the population of these proteins. If only a small percentage of a protein pool was phosphorylated, then the observed Tm response would be minimized due to a high background of proteins unresponsive to phosphatase treatment. At present, crucial information missing in this study is the identification of which phosphorylation sites have been modified to cause conformational shifts. Data from phosphatase treated and control samples were searched for phosphopeptides, however without an enrichment step for phosphorylated peptides prior to mass spec analysis, it is too difficult to confidently identify phosphopeptides in such a complex background. To confirm the reproducibility of these results with biological replicates, and to address the question of which phosphorylation sites are modified, this pilot study will need to be repeated. I will include a phosphopeptide enrichment step using titanium dioxide columns in parallel with thermal denaturation analysis to identified phosphorylation sites that are modified between treatment and control conditions. Additionally I will simplify the enzymatic treatment to only use Lambda Protein Phosphatase. Given that CIP Alkaline Phosphatase also dephosphorylates nucleic acids,

observed thermal shifts may be a consequence of altered DNA-protein binding rather than altered protein phosphorylation.

In contrast to phosphatase enzymes, deubiquitinase (DUB) treatment had significantly less influence on protein conformation. Arabidopsis extracts were treated for 2 hours at room temperature with human DUB enzyme USP2 prior to thermal denaturation. Pilot study results indicate that approximately 30 proteins showed DUB induced Tm shifts. The shifts were all stabilizing, i.e. an increase in Tm, indicating that removal of ubiquitin causes an increase in protein thermal stability. Unlike the large shifts seen with phosphatase treatment, delta Tm values for DUB treatment were smaller, frequently ranging between 3-5^{O}C. The observed smaller shifts may be due to ubiquitination having a smaller influence on the overall conformation state of a protein, or it could reflect of the fact that ubiquitination may occur at lower stoichiometry within a protein population. Contrary to phosphoproteome dataset repositories, minimal published data exists to validate protein ubiquitination sites in Arabidopsis. That being said, approximately 25% of the DUB responsive proteins were identified as containing ubiquitinated peptides in published mass spec datasets of Arabidopsis ubiquitinated proteins (18, 19). Examples of these DUB responsive proteins with reported ubiquitination sites are shown in **Figure 4.4**.

In addition to enzymatic treatment, I used the reducing agent DTT to identify proteins with redox sensitive amino acids important for protein conformation. I found that the number of proteins responsive to DTT treatment was similar to that of DUB, with around 20 proteins displayed Tm shifts. Almost all of these proteins showed a destabilization from DTT treatment and the magnitude of the Tm shift was quite large, ranging between 5 and 15^{o}C. Some examples of proteins destabilized by DTT treatment are shown in **Figure 4.5**.

Overall, my pilot study investigating the effect of *in vitro* enzymatic treatment of Arabidopsis extracts on protein thermal stability looks promising. *In vitro* analysis may be an effective tool for connecting significant posttranslational modifications to protein structure and therefore, increasing the likelihood that the PTM plays a biologically significant role. In addition, the data collected in this assay, particularly with phosphatase and DTT treatments, confirms my initial findings with the ATP experiment that plant proteins posses a very wide range of thermal stability. The *in vitro* analysis conducted in this pilot study must be repeated with biological replicates to confirm my initial findings.

Attempts to use of thermal denaturation profiling to measure in vivo changes in protein conformation in a complex eukaryotic organism.

Although the previously published work with untargeted thermal denaturation profiling had been performed with animal cell cultures or yeast cells, it remained possible that despite the heterogeneity and complexity of many different differentiated cell types, this method may also work to identify *in vivo* conformational changes in a multicellular eukaryote like intact Arabidopsis seedlings. To determine if I could use thermal denaturation to identify signaling events *in vivo*, I exposed Arabidopsis seedlings that were grown in liquid culture to brief hyperosmotic stress for 5 minutes, similar to the manner in which the prior phosphorylation studies had been performed (20, 21). After the tissue was homogenized, I then performed thermal denaturation profiling on soluble extracts from treated and control samples. I measured Tm values for thousands of proteins using untargeted mass spectrometry and the experimental pipeline outlined in **Figure 4.1**. The analysis was conducted using two biological replicates for both mannitol treatment and control conditions.

In total, thermal denaturation curves were calculated for approximetly 2500 proteins after filtering the data based on peptide spectral matches (PSM), co-isolation interference, and denaturation curve parameters (see methods section for details). The general trends I observed was that Tm calculations for any given protein were very stable across biological samples. A linear regression analysis of replicates gave an R^2 value ≥ 0.87 (**Figure 4.6A**). The difference in Tm values in a pairwise comparison of the biological samples displays a tight Gaussian distribution, with median delta Tm values $\leq 0.89^{O}C$ (**Figure 4.6B**). When comparing average delta Tm values between mannitol treated and control samples, the median difference was only $0.15^{O}C$ (**Figure 4.6B**). Importantly, this narrow deviation in calculated Tm values also holds true for proteins with a small number of PSMs, meaning that calculations made for less abundant proteins are not significantly more variable (**Figure 4.7**). The consequence of the highly reproducible Tm calculations seen in this dataset is that smaller differences in Tm between treated and control samples may be both statistically and biologically meaningful.

My primary interest in this study was to identify proteins whose thermal denaturation profile changed as a consequence of *in vivo* mannitol treatment. Such findings would indicate that these proteins are undergoing a stress induced conformational change, suggesting that they are participating in rapid stress response in the cell. In analyzing the data I observed that, in contrast to in vitro experiments, Tm shifts were much smaller between treated and control samples. Almost all of the changes I measured represent delta Tm values of $< 5^{o}C$ between treated and control samples. Furthermore, very few proteins appear to undergo conformational changes detectible in my assay. In total, approximately 20 proteins displayed stress induced Tm shifts larger than $2.5^{o}C$ in magnitude with thermal denaturation curves that

passed visual inspection. Another handful of proteins showed smaller changes in Tm, between 1.5 and 2.5^{o}C, but have very robust quantification parameters and thus might represent real changes. Thermal denaturation curves for a subset of candidate proteins are displayed in **Figure 4.8**.

To determine the validity of these observations, I compared my results to the pilot study I conducted of *in vivo* mannitol treatment. In this pilot study Arabidopsis seedlings were grown and stress treated for 5 min in the same manner as my current study, however the lysis method that was used to homogenize the plants differed from my current method. In the pilot study I employed the use of a homogenization probe and ground fresh plant material following treatment. I subsequently found this homogenization technique introduced too much variability and was potentially causing a stress response in the plants, so I transitioned to a method where the plant tissue was immediately flash frozen in liquid nitrogen post treatment and homogenized with a mortar and pestle in my current analysis. The very rapid cytosolic (30 seconds or less) calcium signaling that occurs in response to mechanical perturbation likely influences cytosolic conditions in a manner that can affect protein conformation. Therefore, handling of seedling samples for thermal denaturation analysis requires delicate consideration. Nonetheless, despite this difference in sample handling between datasets, I found that many of the mannitol responsive proteins also displayed a similar stress induced Tm shift in my pilot study (**Figure 4.8, second column**). The reproducibly seen with these proteins across experimental datasets provides confidence that the findings are real.

The protein with the largest conformational change in response to mannitol was Apoptosis Inhibitor Protein 5 (API5), displaying a stabilizing shift of 7^{o}C upon treatment

(**Figure 4.8A**). No publications exist describing this protein in Arabidopsis, but the API5 mammalian homolog is a major regulator of apoptosis whose upregulation is associated with several types of cancer (22-24). Human API5 has also been shown to be an important regulator of cell cycle progression through interaction with major regulatory transcription factors (25). API5 was not detected in my pilot study and therefore these results cannot be validated, but this finding nonetheless presents a potentially interesting link between osmotic stress, cell cycle control, and growth response.

The *in vivo* analysis also revealed Tm shifts around 5^{o}C for two proteins related to metabolism: Fatty Acid Binding Protein 3 (FAP3) involved in fatty acid metabolism and flavonoid biosynthesis (26), and Serine Hydroxymethyltransferase2 (SHM2) involved in one-carbon metabolism and photorespiratory Gly-to-Ser conversion (27). These proteins both showed reproducible thermal shifts in my pilot experiment, although the magnitude of the SHM2 shift was much higher in the original study (**Figure 4.8B-C**). The role of these proteins in rapid osmotic stress response is unclear, but SHM2 family member SHM1 was shown to be important for regulation of reactive oxygen species during salt stress (28). SHM1 is stabilized by ubiquitin specific protease 16 during salt stress, where SHM1 is converted from a poly-ubiquitinated to a mono-ubiquitinated state (28). It has not been documented if the same osmotic stress-induced regulation of SHM2 occurs, but thermal denaturation curves show a stabilizing shift for this protein upon mannitol treatment (**Figure 4.8C**).

Although some mannitol responsive proteins were identified in my *in vivo* study, the data does not look nearly as robust as my results from *in vitro* experiments. The limited number of proteins showing a measurable change in Tm and the overall reduced magnitude

of Tm shifts are likely a reflection of the heterogeneity found in a complex, multicellular organism. In order for Tm shifts to be detectable in my assay, the stress induced conformational changes must affect the majority of a protein population. This is a difficult requirement when measuring short-term responses in an entire seedling, where different tissue types may have unique biochemistry or operate on different temporal scales. Switching to a more homogenous cell population capable of a greater synchronized biochemical response is one way to significantly improve the robustness of this *in vivo* assay. Though plant cell culture does not reflect a true cell type *in planta*, its offers a good starting point for assay validation. Future in vivo thermal denaturation work should first be attempted using this simplified system.

Conclusions and Future directions

In this work I present the first attempt at performing proteome wide thermal denaturation of plant proteins as tool to measure treatment induced changes in protein conformation. By comparing similar experiments performed with animal, yeast, and plant cells, I demonstrated that plant proteins possess a wide range of thermal stability and undergo dramatic changes in thermal precipitation upon *in vitro* treatment. I demonstrate that thermal denaturation can be used with plant extracts to identify protein-ligand binding interactions and post-translational modifications that influence protein conformation. I also attempted for the first time to use thermal denaturation to monitor stress responsive conformational changes *in vivo* in a multicellular organism. All together my work demonstrates the potential of this assay and establishes a foundation for future thermal denaturation work. I have defined an experimental pipeline and also, highlighted limitations that still must be addressed. Adapting the thermal denaturation assay for plant proteomics presents some unique challenges. Below are some areas that need special consideration and improvement in future thermal denaturation work.

Challenges associated with TMT based quantification: co-isolation interference and TMT labeling efficiency.

Co-isolation interference

A well-documented limitation of protein quantification using isobaric tags is the problem of co-isolation interference. When peptides are measured in the Orbitrap mass spectrometer, they are first identified by their intact unfragmented exact mass MS1 spectra, and then selected for fragmentation during MS2. Quantification using isobaric tags occurs during MS2 fragmentation where TMT labels break apart, giving unique ion intensities that reflect the original peptide abundance for a given sample. Co-isolation interference occurs

when the m/z window for selecting parent ions for fragmentation is so wide that peptide ions in addition to he ones of interest, are included in the analysis. Contaminating peptide ions that fragment alongside desired peptides contribute to the TMT reporter ion intensity. This can lead to an inaccurate representation of the abundance of the target peptide. Co-isolation occurs when peptides with a similar m/z ratio co-elute and enter the mass spec at the same time. Therefor the problem of co-isolation increases with sample complexity.

In most experiments the ultimate consequence of co-isolation interference is signal suppression. This means that large fold changes in peptide abundance may seem smaller due to the presence of this contaminating background. However, overall it is not a significant problem because all samples labeled with TMT reagent are assumed to be at a 1:1 ratio and therefor the interfering fragment ions contribute equally across all channels, resulting in a minimal effect on ratio calculations of relative peptide abundance. Co-isolation interference presents a unique challenge during thermal denaturation experiments, however, because the underlying assumption that all TMT channels have the same total protein abundance is inherently not true in this assay. In fact, all channels have different protein abundances because they represent the remaining soluble fraction of a protein precipitation gradient. Therefore contaminating ions can markedly influence measurements of relative peptide abundance. The situation is exacerbated in thermal profiling of plant proteins because plants have a larger range of protein stability and Tm values across the proteome. This means that a co-isolated interfering peptide can have dramatic effects on the thermal denaturation curve. This concept is illustrated in **Figure 4.9**. In reality, one cannot simply predict if a co-isolated ion will significantly influence the thermal denaturation curve for a protein; each case must be examined individually.

To avoid the problem of inaccurate quantification due to co-isolation interference, PSMs that contain high interference levels are excluded during protein quantification. Due to the enhanced sensitivity of this assay to the problem of interference, co-isolation cut offs may need to be particularity stringent. However, the high sample complexity of plant protein extracts means that setting stringent co-isolation interference cut off results in excluding a very significant amount of data. Furthermore, reducing PSM counts can also have a negative consequence on accurate protein quantification. The analysis therefor becomes a trade off between sensitivity, depth of coverage, and quantification confidence.

To improve this dilemma moving forward the problem of co-isolation interference can be tackled at multiple levels. First, co-eluting contaminants can be minimized by reducing sample complexity. This can be achieved by enhancing prefractionation techniques and improving online-LC gradient separation to maximize peak sharpness and separation. Second, tightening ion m/z inclusion windows during MS2 acquisition can reduce the number of co-isolated ions. Narrow inclusion windows result in reduced ion intensity and lower signal, but there is likely a proper balance that can be met between signal intensity and purity. Different isolation windows should be tested during method development to maximize desired parameters. Third, one can attempt to improve the correction methods for co-isolation interference rather than purely excluding data. If data analysis methods can be developed that either back correct for co-isolation or determine the contribution of co-isolation to the thermal profile, then more PSMs can be included in the final analysis. The current method of excluding PSMs based on a predetermined co-isolation cut off is not flexible enough to address this large problem.

TMT labeling efficiency

Isobaric tags such as Thermo's TMT regent label free amines in protein fragments. This means the N-terminus of every peptide and the amino group of Lysine residues reacts with reagents to generate a fully labeled peptide. In classical TMT experiments, labeling efficiency of N-terminal amines and lysine sidechains are very high, achieving around 99% efficiency. Surprisingly, I have observed that during TMT labeling of thermal denatured samples N-terminal labeling efficiency significantly decreases. In some cases I observed N-terminal labeling efficiency as low was 60%. This has a significant consequence on data quality, as unlabeled peptides cannot be included in analysis. Through testing various sample handling variables, I have concluded that poor labeling efficiency is a consequence of low protein abundance, a feature that is inherent to thermal denaturation samples collected at high temperature ranges. Increasing protein abundance at high temperature ranges is not a plausible solution given the fact that proteins must be precipitated out of solution to define a denaturation curve. Therefore I have found that reducing the total reaction volume used for labeling can significantly improve N-terminal labeling efficiency. However, more work needs to be done to define the optimal conditions to maximize efficiency. This includes close examination of reaction volumes as well as aqueous to organic solvent ratios, and possibly additional variables such as temperature and sample mixing. Additionally, implementing data analysis tools that can assess per channel labeling efficiency can greatly improve method development and troubleshooting efforts.

Challenges associated with plant material: whole seedling analysis and lysis conditions.

Whole seedling analysis

Thermal denaturation analysis relies on the detection of Tm shifts within the entire population of a particular gene product (protein). This means that in order for changes to a protein's conformation to be detectable, they must occur at high stoichiometry. Traditional measurements of PTMs such as phosphorylation rely on relative increases or decreases to a modified residue and do not require knowing the overall stoichiometry of phosphorylation. For example, a 2-fold increase in phosphorylation may represent 4% of a protein population doubling to 8%, or 40% doubling to 80%. In the case of thermal denaturation, only the latter increase would be detectable. In reality PTMs such as phosphorylation and acetylation often occur at low stoichiometry in a cell (29, 30). This means that not all modifications may be detectable by thermal denaturation due to limitations of stoichiometry. Working with whole seedlings for thermal denaturation analysis only exacerbates the challenge of stoichiometry. Now not only do conformational changes have to occur within a large population of proteins in a cell, they must also occur within all cells of a tissue, and all tissues of an organism. This becomes a formidable challenge for detecting conformational changes *in vivo*. This challenge is especially limiting for plants, as other organisms are amenable to culturing particular cell types and thus are not limited to whole organism biology.

To improve the feasibility of measuring conformational changes arising from *in vivo* treatments, it is recommended to work with less complex starting material. This means extracting proteins from a particular tissue, for example roots grown in a hydroponic system, or switching entirely to cell culture. Though the latter scenario may be less biologically interesting, it provides an opportunity to observed a more synchronized biochemical response. Findings arising from cell culture experiments can attempt to be validated in more

biologically relevant tissues such as leaves or roots. Alternatively, in-vivo thermal denaturation experiments can focus on treatments that are likely to have a more uniform effect on proteins regardless of tissue type, such as incubation with inhibitors and pharmacological agents.

Lysis conditions.

Measurements of protein conformational change are extremely sensitive to sample handling conditions. The rapid calcium signaling occurring in plant cells in response to a myriad of conditions, including touch and mechanical perturbations, likely alter cytosolic conditions in a manner that can influence protein conformation, such as changes in pH. This means that methods used for tissue homogenization to lyse open cells require careful consideration and must occur rapidly and introduce as little sample handling as possible. During method development I attempted several methods of tissue homogenization including fresh grinding with a homogenization probe, fresh grinding with a vertical blender, and flash freezing material with liquid nitrogen and then grinding with a mortar and pestle. I found that data derived from flash frozen material was less noisy than freshly ground material. This likely is due to the delay time between exposing plants to the homogenization solution and achieving complete cell lysis. More work needs to be done to continue to improve homogenization conditions, making them as fast as possible with minimal exposure to mechanical and chemical stress (e.g., the extraction buffer constituents) while still achieving thorough lysis with high protein yields.

A major question in this consideration is what solution conditions to use for cell lysis. Measured conformational changes should reflect changes occurring in the cell, not response to solute conditions post-lysis. Therefor the chosen solution should mimic aqueous

conditions in the cell as much as possible. Plants present a unique challenge in that the cellular conditions in the large vacuoles are different than the cytoplasm, and one must generate a homogenization buffer than accommodates all soluble proteins. For the work presented in this chapter I adopted existing lysis buffer that has been used for previous work with cell extracts (31, 32). I did not optimize the lysis buffer conditions specifically for thermal denaturation. Future work needs to be done to ensure that selected buffer conditions are preserving in vivo protein conformational states as much as possible.

Methods

Plant growth conditions and method for in vivo treatment and homogenization

Arabidopsis Col-0 seeds were grown in liquid media under constant light for 11 days before experimental treatment. Liquid media consisted of ½ X Murashige and Skoog salts, 1% (w/v) sucrose, and .05% (w/v) MES salt, pH 5.7. After 11 days of growth, samples were either homogenized for *in vitro* analysis (see below) or treated *in vivo* as follows: sample media was replaced with fresh media and allowed to equilibrate for 4-5 hours prior to experimental treatment. Treatment was then applied by decanting existing media and replacing with control media or media containing 0.3M mannitol. After 5 minutes of treatment, plant samples were dunked in deionized water to rinse off treatment media, spun for several rotations in a salad spinner to remove excess water, and flash frozen in liquid nitrogen. The total duration of sample handling was routinely < 12 seconds. Frozen tissue was then homogenized with a mortar and pestle. Frozen ground material was resuspended in ice-cold homogenization buffer (see composition below) and processed in thermal denaturation pipeline, as described below. Two biological replicates were processed for each treatment condition.

Tissue Homogenization for in vitro treatments

Plant material used for in vitro treatment assays were homogenized using an upright blender. Seedlings were removed from growth media, dunked in deionized water to rinse, placed on an absorbent towel to remove excess water, and then placed in 70mL of homogenization buffer and blended for 30 seconds at maximum speed. **Homogenization buffer** contained the following base composition: 230mM sorbitol, 50mM Tris-HCl pH 7.5, 10mM KCl, 3mM EGTA. The following inhibitors were added to the homogenization solution on the day

of the experiments: 1mM Potassium MetaBisulfite , 1mM PMSF, 0.5µg/ml Leupeptin , 0.7µg/ml Pepstatin , and 1 protease inhibitor tablet (Roche) per 50 mL of buffer. Homogenized samples were processes in the thermal denaturation protocol described below

Treatment conditions used in vitro studies.

For ATP binding studies, samples were treated for 10-15 min with 2mM MgATP. Phosphatase treated samples were incubated on a rotating platform with 10uM Lambda Protein Phosphatase (Lambda PP; NEB), 10uM Calf Intestinal Alkaline Phosphatase (CIP; NEB), and 1mM MnCl for 2 hours at room temperature. Deubiquitinase treated samples were incubated on a rotating platform with 1uM Ubiquitin Specific Protease 2 (USP2; BostonBiochem) and 1mM DTT. DTT treated samples were incubated with 10mM DTT for 1 hour at room temperature. Each *in vitro* treatment was conducted using 2mL of sample extract.

General thermal denaturation protocol (written with practical notes for implementation)

1) *Start heating blocks for thermal denaturation*. It is important to let heating blocks equilibrate before use; therefore blocks are started at the beginning of the experiment. Set block temperatures and add appropriate volumes of mineral oil to heating wells (make sure tube volume displacement is accounted for when adding oil). For Arabidopsis experiments, block temperatures were set to cover the range of 25^{O}C-65 ^{O}C, split evenly across 10 blocks. Once heating block temperatures have stabilized, it is very important to record the actual temperature of each block using a digital thermometer. The digital block settings may not be accurate.
2) *Prepare biological material.* If samples are going to be treated *in vitro*, proceed to step 3A. If samples are treated *in vivo*, conduct treatment and proceed to step 3B.
3) *Homogenize samples*. Lyse cells using preferred, non-denaturing method. **A**. For samples prepared for the purpose of *in vitro* treatments, homogenize Arabidopsis

seedlings using a blender in the presence of ice-cold homogenization buffer as described in methods section above. **B**. For samples that were treated *in vivo*, cell lysis is a very critical step that should be conducted carefully. Sample quality can be greatly compromised if homogenization is to slow (see Future Directions section above). It is recommended that seedlings are immediately flash frozen after treatment and homogenized while froze, as described in methods section above. Frozen material can be aliquoted and resuspended in ice-cold homogenization buffer. Resuspended cell lysate should be kept cold.

4) *Remove large debris from lysate*. Filter homogenized solution through two layers of Mira-cloth (Calbiochem) to remove tissue debris. Perform filtering on ice in the cold room.

5) *Clarify cell lysate*. To isolate soluble proteins, ultracentrifuge lysate at 100,000xg for 20 min at 4^{O}C. Decant soluble fraction into a new tube.

6) *Prepare sample for in vitro treatment.* If *in vivo* treatment was performed, proceed to step 8. Aliquot clarified lysate into tubes for *in vitro* experiment. Lysate should be separated for treatment and control samples as well as for treatment replicates. The total sample volume needed for each *in vitro* treatment depends on the final volume used during heating in step 8. Flash freeze the remaining supernatant for use in later experiments.

7) *Perform in vitro treatment*. Allow sample to come to room temperature and add appropriate treatment reagents. Treatment conditions depend on the experiment being conduced. For example *in vitro* treatment experimental setups, see methods section above.

8) *Aliquot sample for heating.* Split samples evenly into sets of 10 pre-labeled tubes, (1 set of 10 per sample). At minimum there will be 20 tubes in an experimental pair (10 treated, 10 control). For practicality, it is not recommended to process more than 4 samples at one time (40 tubes). Additional samples can be heated as separate batches. The sample volume used for heating depends on the expected protein concentration in the sample, more concentrated samples require less total volume. For Arabidopsis

extracts, which are fairly dilute due to large volumes added during homogenization steps, I heated a minimum of 200ul and a maximum of 1mL.

9) *Heat samples*. Place tubes in preheated blocks for 10 min. It is important that the heating block wells contain mineral oil for proper thermal conductance.

10) *Cool samples.* Remove tubes from heating blocks and let sit for 10 min at room temperature. Tubes will be coated in oil so it is helpful to lay them on absorbent paper rather than place them in tube racks to reduce mess.

11) *Remove precipitated proteins.* Place tubes on ice and move them to the cold room. Spin tubes for 20 min at 17,000xg (max speed) at 4^{O}C. Note that it has been recommended to use an ultracentrifuge to separate soluble proteins at this step (15). A small volume ultracentrifuge was not readily accessible during my method development, so I cannot comment on the benefits of using a higher spin speed at this step.

12) *Save soluble fraction*. Transfer the supernatant to new pre-labeled tube. Make sure to not disrupt the pellet during transfer.

13) *Add calibrating BSA spike*. A uniform aliquot of BSA must be added to every single tube. BSA is used to normalize the 10-temperature point samples during thermal denaturation modeling (see method description below). The concentration of BSA added depends on the amount of protein the sample; therefore the BSA spike should be determined based on the expected total protein yield. The objective is to add enough BSA so that it is identified in the top 100 most abundant proteins during mass spec data acquisition. For Arabidopsis experiments, I added a total of 1ug of BSA to each tube. BSA can also be added to tubes prior to transferring the soluble fraction (step 12) for sample handling convenience. Samples can be frozen and processed at a later date after completing this step in the protocol.

14) *Protein extraction.* Perform methanol chloroform protein extraction on each sample as described in (33). Given the large number of samples, it is recommended to limit extraction volumes so that the protocol can be carried out using 1.7mL tubes and a tabletop centrifuge. This means that the maximum amount of sample volume that can

be used for the protein extraction is 180uL. After completing the protein extraction, resuspend protein pellets in 8M urea.

15) *Protein quantification*. Quantify protein concentrations in the extracted samples using an aliquot from the resuspended protein extracts. I used the 660nm Protein Assay Reagent kit (Peirce) to perform the quantification. This is assay is recommended because it remains stable at room temperature whereas the BCA Protein Assay reagents continue to develop color over time. Given the large number of samples, regent stability is a useful feature. Note that for *in vitro* experiments, all samples are originally aliquoted from the same plant extract. Therefore quantification can be performed on a subset of samples sets and used to approximate the concentration of the remaining sample sets, as protein concentrations are not likely to deviate significantly between aliquots.

16) *Protein digestion*. Dilute protein extracts to a final concentration of 4M urea using 50mM ammonium bicarbonate. Reduce samples with 5mM DTT for 45 min in a 40-50^{O}C water bath. Alkylate samples with 15mM IAA for 45 min in the dark at room temperature. Quench remaining IAA reagent by adding 5mM DTT and incubate for 5 min at room temperature. Digest samples with Lys C (Wako) at a 1:60 enzyme:protein ratio for 2 hours at 37^{O}C. Dilute samples to a final concentration of 1.2M urea and digest overnight at 37^{O}C with trypsin (Promega) using a 1:40 enzyme:protein ratio. For the higher temperature fractions, where there is very little protein present, I set a minimum amount of enzyme to add to each sample regardless of the protein concentration (i.e. no less than 0.1ug of Lys C or 0.2ug trypsin per sample).

17) *Desalt protein digests*. Digests must be cleaned up using solid phase extraction in preparation for TMT labeling. I use OMIX tips containing C18 resin and a 100uL sample volume capacity (Agilent) for this purpose. The desalting protocol is as follows: **A.** Acidify digests to pH < 3 using 20% using TFA (typically 4ul of 20% TFA for a 140ul digest). Verify pH before proceeding. **B.** Equilibrate OMIX tip with 75% acetonitrile (ACN). Conduct 3 rinses at 100ul each (3 x 100uL rinse). **C**. Equilibrate OMIX tip with 0.1% TFA wash solution (4 x 100uL rinse). **D**. Bind

sample to resin by pipetting the sample up and down 10X. **E**. Wash sample retained on resin using 0.1% TFA (2 x 100ul rinse). **D**. Wash sample with 0.01% TFA (1 x 100ul rinse). **E**. Elute sample using 75ul of 75% ACN, 0.1% formic acid (FA) solution into a low-bind microcentrifuge tube. **F.** Place samples in a vacuum centrifuge to remove volume for subsequent resuspension in TMT labeling buffer. It is important to not over rinse samples after binding them to the resin because isocratic elution can occur and some peptides may be lost. The additional 0.01% TFA rinse step in D is added to reduce the acidity of the solution because subsequent TMT labeling occurs under basic conditions. To elute samples in E, I first prepare all of the elution tubes and add the elution solution directly to the tube to eliminate the possibility of sample loss during initial solution pick-up.

18) *Label digested samples with TMT reagent*. Resuspend digests in 25uL of 150mM TEAB, 5% ACN solution. Samples can be sonicated in a water bath for 1 minute to aid in resolubilization. Resuspend 10-plex TMT reagents (ThermoFisher) in 100% ACN to the desired final concentration. I use 75 uL to generate a 10.66 ug/uL solution. Note that the necessary concentration of TMT reagent is calculated based on the desired final reaction volume protein and the concentration in your samples as TMT labeling ratios are calculated based on predetermined a label-to-protein ratio. Label each temperature point sample with a unique TMT label by adding the TMT reagent to your sample at the desired label:protein ratio. The ThermoFisher protocol suggests an 8:1 label:protein ratio, but I have found that a 3:1 ratio works just as well. This saves a considerable amount of reagent. Note that samples from higher temperature points will contain little to no protein. It is advised that TMT reagent is not continuously scaled down to maintain a fixed label:protein ratio for these samples. Instead, I set a fixed minimum label concentration to add to these samples. For example, samples representing the 4 highest temperature points all received the same amount of label. Each of the 10 samples should ultimately receive the same volume of ACN during labeling to maintain the same organic-to-aqueous solvent ratio. Since each sample receives a tailored amount of TMT label, additional ACN must be added to some samples to compensate for total volume discrepancies. For example, I have been using a total labeling reaction volume of 40uL, containing 40%

ACN and 60% TEAB. Therefore a total of 15 ul of TMT label + ACN are added to each sample. For lower temperature point samples containing more protein, the 15ul may be entirely TMT reagent, whereas the higher temperature point samples received 5ul of label and 10ul of ACN. Label samples for 1-2 hours at room temperature. Achieving efficient TMT labeling efficiency (>95%) at the N-terminus of peptides has been a problem for thermal denaturation samples (see comments above in Future Directions section). Therefore this step in the protocol should examined for continued improvement.

19) *Quench TMT reaction*. Add 5ul of 5% hydroxylamine solution to each sample. Incubate for 15 minutes at room temperature. Pool 10-plex labeled TMT samples representing 10 temperature points into one tube.

20) *Fractionate samples using offline HPLC and a high pH reverse phase column*. Vacuum centrifuge pooled samples to remove ACN content before HPLC fractionation. For fractionation I have used the equipment and protocol described below. Equipment: Waters 2795 Sepraration Module HPLC, Gemini C18 5um 110A 4.6mm x250mm column (Phenomenex), and a fraction collector (Gibson, model 201). Solvents: Buffer A (10mM ammonium formate), Buffer B (10mM ammonium formate, 80% ACN). HPLC gradient: 35 min total at a flow rate of 1mL/min, 5-60% B starting at 3min and ending at 23min, 100% B wash at 25-26min. 0%B for all other time periods in the gradient. Fractions were collected every minute and fractions 15-27 were used for mass spec analysis.

21) *Prepare samples for mass spec analysis*. Dry down fractions in a vacuum centrifuge and resuspend in 0.1% FA for injection on mass spec. Make sure to verify that the samples are pH < 3.

Mass spec methods and initial data processing

TMT labeled samples in this study were analyzed using an Orbitrap Elite mass spectrometer (Thermo). The following settings were used during data acquisition: MS1 data was acquired using a 120,000 resolving power and a mass range of 380-1800 m/z. Data dependent

acquisition and dynamic exclusion were used to analyze the top 10 ions for each scan period. Precursor ions were selected using a 2 m/z isolation window width and a 200 ms maximum inject time. Isolated peptides were fragmented using HCD and fragment ions were analyzed in the Orbitrap using a 30,000 resolving power and a mass range starting at 100m/z and extending to an upper m/z limited that was dynamically calculated based on the MS1 precursor mass (ca. 10% above MW). This data was collected in line with nanoflow HPLC separation (Agilent 1100) using a C18 column and the following solvents: A (0.1%FA), B(95%ACN, 0.1% FA). The flow rate used during separation was 300nL/min and samples were eluted over 2-hour gradient using the following LC method:

Time (min)	0-30	31	108	113	118	119	123-126
%B	0	3	30	50	95	95	0

Data collected from individual high pH fractions was combined together for database searching using Proteome Discover (Thermo). Data was searched using the Arabidopsis Information Resource (TAIR) Arabidopsis protein database (version 10). Peptide filtering was set at 'medium' (1% false discovery). Data tables were exported from Proteome Discoverer and the data was used for thermal denaturation models.

Data analysis methods for Thermal denaturation.

Modeling of the thermal denaturation data was performed using the MSTherm R package being developed in the Sussman lab (unpublished). Briefly, raw channel intensities were normalized to spike-in BSA levels (spectra weighted by intensity). The global normalized channel intensities were fit to the model below and the fitted values were used to calculate the final normalized scale factors for each channel. Protein-level quantification values were determined based on the sum of normalized spectrum-level values for each protein (see

http://dx.doi.org/10.1093/bioinformatics/btp610 for a justification of this approach). A baseline level for each protein was determined by calculating the mean of the first three temperature points and subsequently finding the mean of all temperature points within +/- 20% of that level. Experience suggested that this provides a more robust baseline than simply using the lowest temperature point for each protein, which was sensitive to errors in quantification of that channel.

Ratios were calculated for each temperature point relative to baseline and the resulting series were fitted to the following model:

$$P(n) = \frac{1-p}{1+e^{-k(T^{-1}-m^{-1})}} + p$$

where T is temperature, m is the melting point, p is the lower asymptote (i.e. "plateau"), and k determines the slope of the curve in concert with m. Fitting was performed by non-linear least squares regression with the *nls2* R package, using the "port" algorithm and limits of (0,0.4), (1,10^5), and (10,100) for the model parameters p, k, and m, respectively. In determining significance between treatment and control melting temperatures (T_m), p-values were calculated from the global distribution of ΔT_m using median absolute deviation for robust estimation of the standard deviation in the presence of outliers.

Inclusion parameters for data analysis

Protein thermal denaturation curves were filtered for quality control using the following settings: a minimum of 2 PSMs, a maximum lower plateau of 0.35, a Tm value of < 70^{O}C, and an R^2 value of >0.7.

Figure 4.1

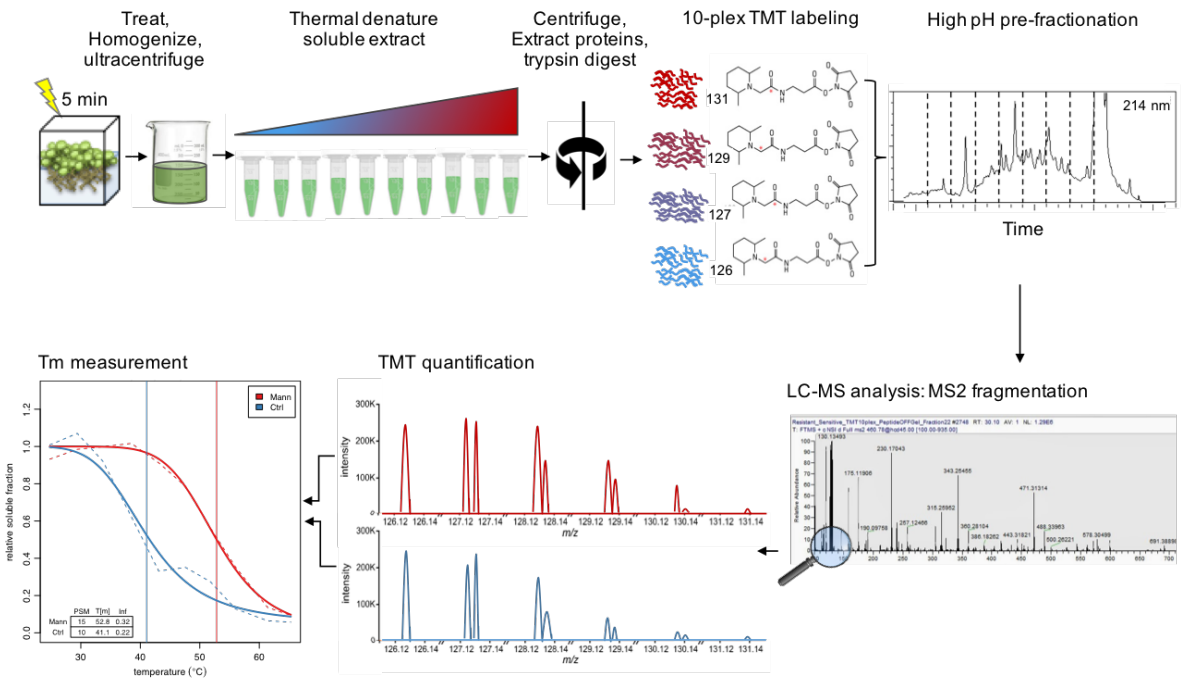

Figure 4.1 *Overview of the thermal denaturation profiling method.* The schematic outlines the workflow for *in vivo* treatments. For *in vitro* experiments, treatment is applied to the sample supernatant following ultracentrifugation.

Figure 4.2:

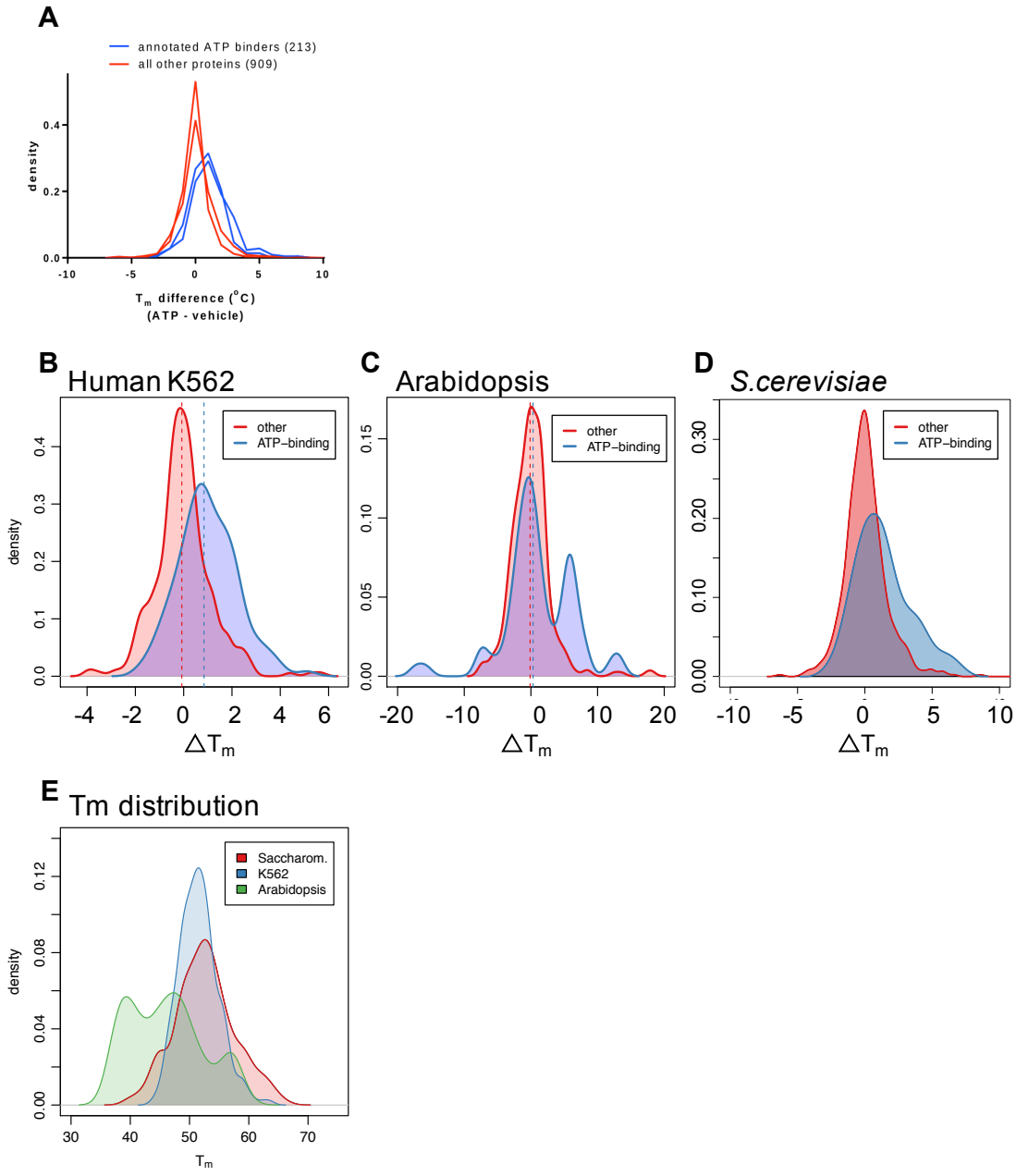

Figure 4.2: *In vitro mgATP binding*. **A.** Data published in Savitski MM, *et al*. (1) showing mgATP treatment of human K562 cells. **B-D**. Data generated using the Sussman Lab thermal denaturation pipeline. Vertical dotted lines represent median histogram values. Delta Tm values calculated as Tm_{ATP}- $Tm_{Control}$ for each protein. Histograms represent between 400-500 proteins. **E.** Overlay of the Tm distribution for all proteins in each species.

Figure 4.3

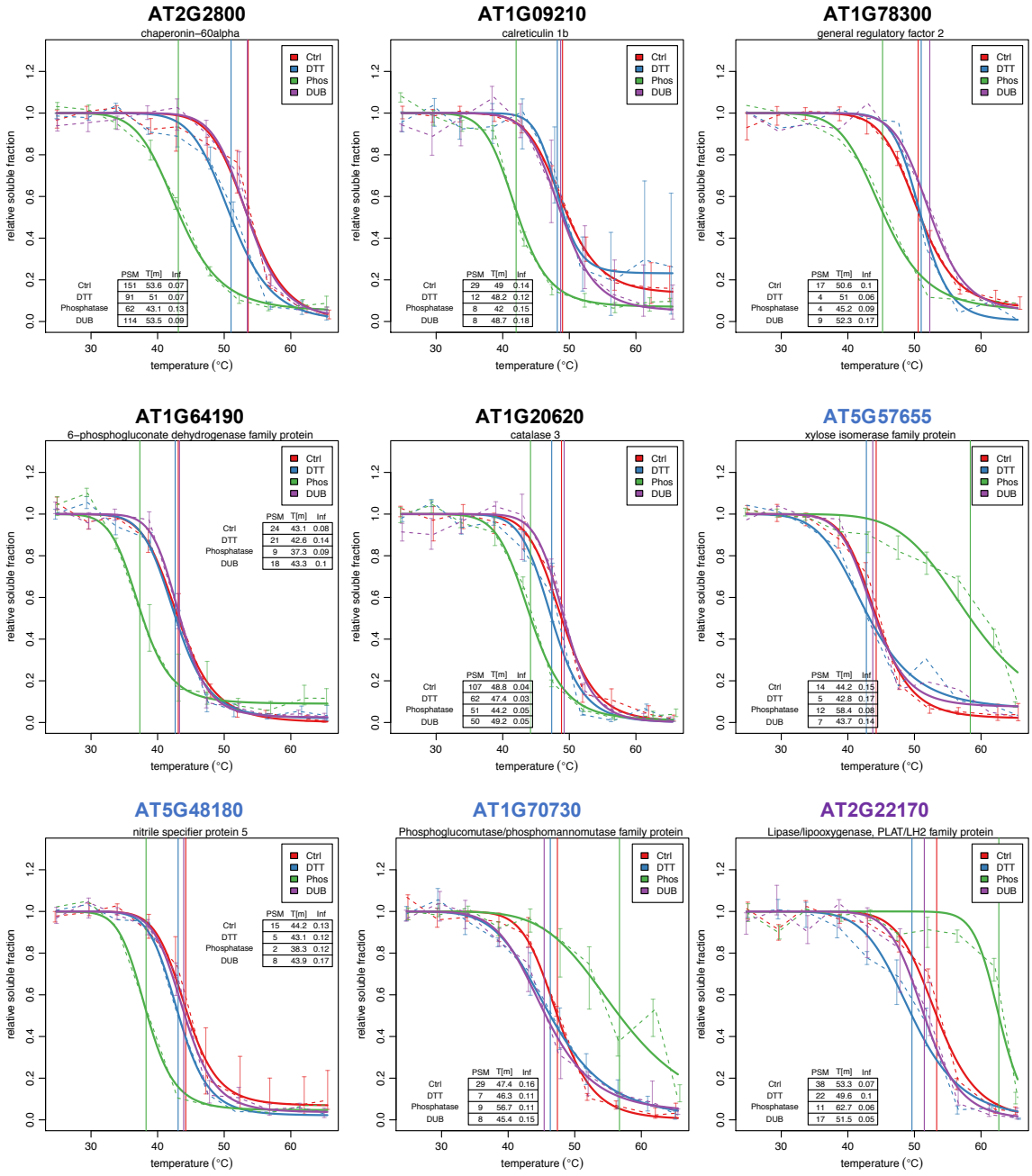
AT2G2800
chaperonin−60alpha
AT1G09210
calreticulin 1b
AT1G78300
general regulatory factor 2
AT1G64190
6−phosphogluconate dehydrogenase family protein
AT1G20620
catalase 3
AT5G57655
xylose isomerase family protein
AT5G48180
nitrile specifier protein 5
AT1G70730
Phosphoglucomutase/phosphomannomutase family protein
AT2G22170
Lipase/lipooxygenase, PLAT/LH2 family protein
Ctrl
DTT
Phos
DUB
relative soluble fraction
temperature (°C)
PSM T[m] Inf
Ctrl 151 53.6 0.07
DTT 91 51 0.07
Phosphatase 62 43.1 0.13
DUB 114 53.5 0.09
PSM T[m] Inf
Ctrl 29 49 0.14
DTT 12 48.2 0.12
Phosphatase 8 42 0.15
DUB 8 48.7 0.18
PSM T[m] Inf
Ctrl 17 50.6 0.1
DTT 4 51 0.06
Phosphatase 4 45.2 0.09
DUB 9 52.3 0.17
PSM T[m] Inf
Ctrl 24 43.1 0.08
DTT 21 42.6 0.14
Phosphatase 9 37.3 0.09
DUB 18 43.3 0.1
PSM T[m] Inf
Ctrl 107 48.8 0.04
DTT 62 47.4 0.03
Phosphatase 51 44.2 0.05
DUB 50 49.2 0.05
PSM T[m] Inf
Ctrl 14 44.2 0.15
DTT 5 42.8 0.17
Phosphatase 12 58.4 0.08
DUB 7 43.7 0.14
PSM T[m] Inf
Ctrl 15 44.2 0.13
DTT 5 43.1 0.12
Phosphatase 2 38.3 0.12
DUB 8 43.9 0.17
PSM T[m] Inf
Ctrl 29 47.4 0.16
DTT 7 46.3 0.11
Phosphatase 9 56.7 0.11
DUB 8 45.4 0.15
PSM T[m] Inf
Ctrl 38 53.3 0.07
DTT 22 49.6 0.1
Phosphatase 11 62.7 0.06
DUB 17 51.5 0.05

Figure 4.3: *Proteins displaying phosphatase induced Tm shifts*. Thermal denaturation curves are color-coded based on *in vitro* treatment condition. Vertical lines represent the calculated Tm value. Solid lines represent modeled thermal denaturation curves and dotted lines represent un-modeled data. Error bars indicate variation calculated by bootstrap analysis (6<PSMs required for bootstrapping). Table values represent the number of peptide spectral matches (PSMs) for the protein, the calculated Tm value, and the maximum co-isolation interference value for the most abundant PSM. Proteins that were identified in my previous in-house phosphoproteomics datasets are indicated with black titles. Proteins containing phosphopeptides identified in the PhosPhat4.0 online database are indicated in blue. Proteins not identified in either dataset are indicated in purple.

Figure 4.4

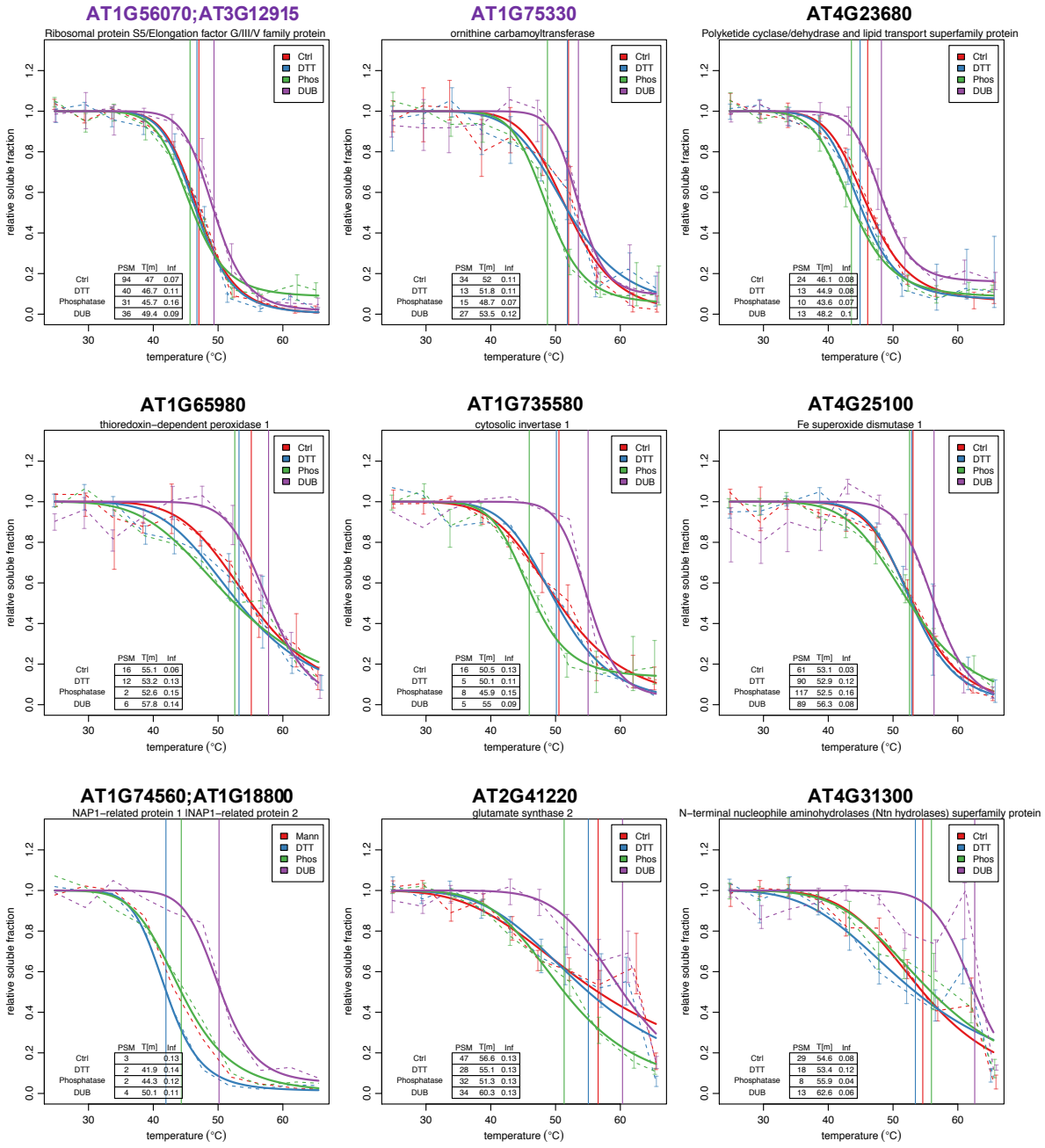

Figure 4.4: *Proteins displaying deubiquitinase induced Tm shifts*. Plot description is the same as in 4.3. Proteins identified in published datasets of ubiquitinated proteins are indicated with purple titles.

Figure 4.5

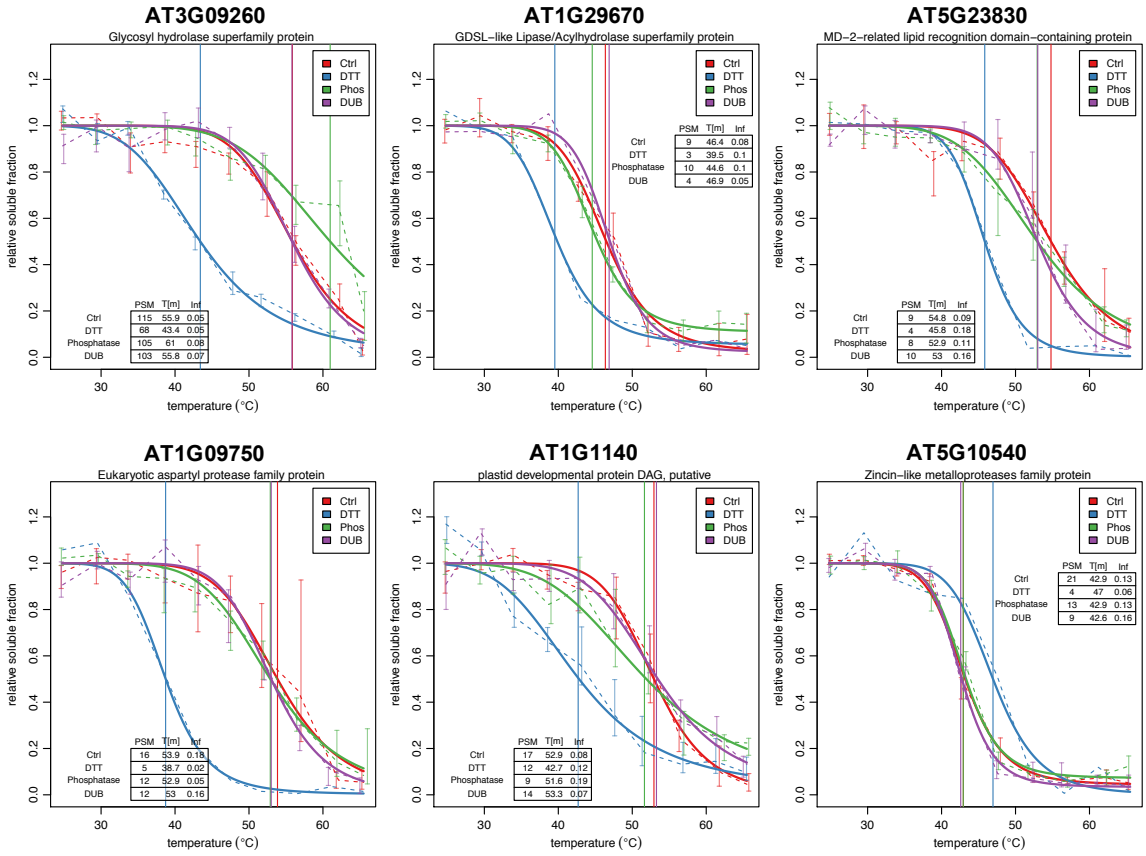

Figure 4.5: *Proteins displaying DTT induced Tm shifts*. Plot description is the same as in 4.3.

Figure 4.6

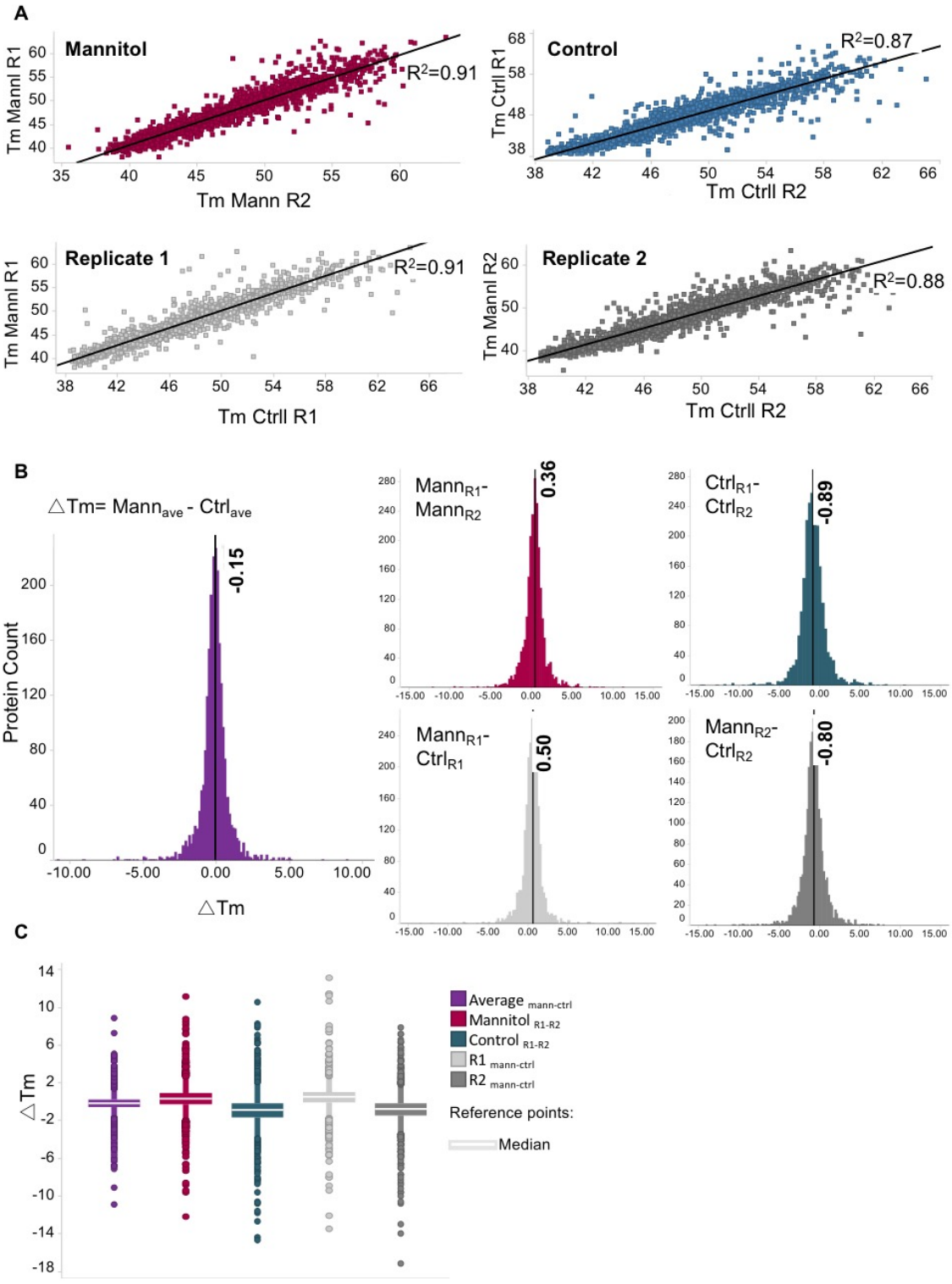
A
Mannitol
R²=0.91
Tm Mannl R1
Tm Mann R2
Control
R²=0.87
Tm Ctrll R1
Tm Ctrll R2
Replicate 1
R²=0.91
Tm Mannl R1
Tm Ctrll R1
Replicate 2
R²=0.88
Tm Mannl R2
Tm Ctrll R2
B
△Tm= Mann_ave - Ctrl_ave
-0.15
Protein Count
△Tm
Mann_R1- Mann_R2
0.36
Ctrl_R1- Ctrl_R2
-0.89
Mann_R1- Ctrl_R1
0.50
Mann_R2- Ctrl_R2
-0.80
C
△Tm
Average mann-ctrl
Mannitol R1-R2
Control R1-R2
R1 mann-ctrl
R2 mann-ctrl
Reference points:
Median

Figure 4.6. *In vivo dataset shows highly reproducible Tm calculations*. **A.** Pairwise comparison of Tm calculations in each sample. Data points represent calculated Tm values for individual proteins. **B**. Distribution of delta Tm values across different sample comparisons. **C**. Box plot analysis of delta Tm values calculated in pairwise comparisons.

Figure 4.7

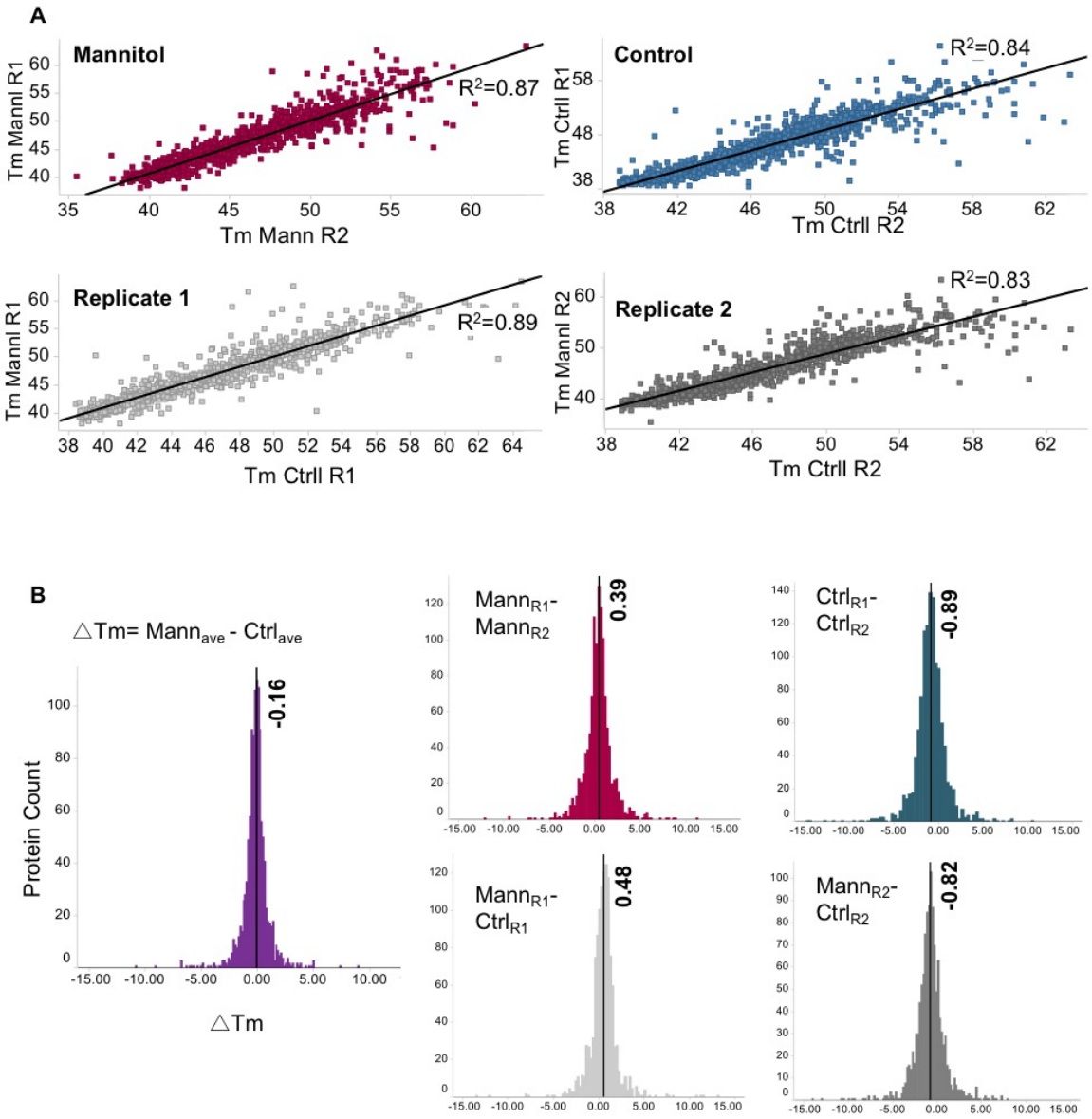

Figure 4.7: *Dataset analysis for proteins with 10 or fewer PSMs.* Data analysis was conducted that same way as in 4.6 **A.** Pairwise comparison of Tm calculations in each sample. Data points represent calculated Tm values for individual proteins. **B**. Distribution of delta Tm values across different sample comparisons.

Figure 4.8

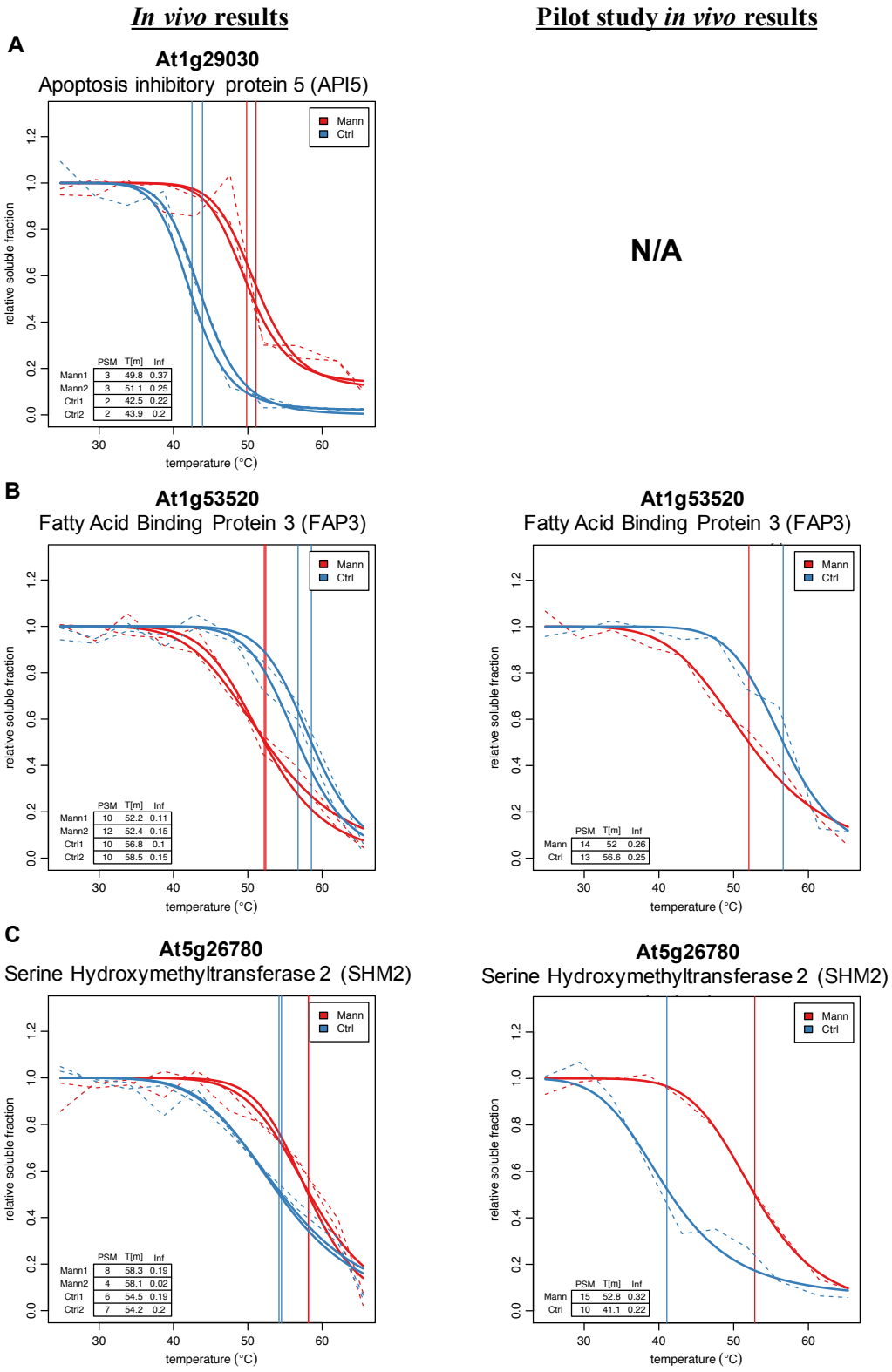
In vivo results
Pilot study in vivo results
A
At1g29030
Apoptosis inhibitory protein 5 (API5)
N/A
B
At1g53520
Fatty Acid Binding Protein 3 (FAP3)
At1g53520
Fatty Acid Binding Protein 3 (FAP3)
C
At5g26780
Serine Hydroxymethyltransferase 2 (SHM2)
At5g26780
Serine Hydroxymethyltransferase 2 (SHM2)
Mann
Ctrl
relative soluble fraction
temperature (°C)
PSM T[m] Inf
Mann1 3 49.8 0.37
Mann2 3 51.1 0.25
Ctrl1 2 42.5 0.22
Ctrl2 2 43.9 0.2
PSM T[m] Inf
Mann1 10 52.2 0.11
Mann2 12 52.4 0.15
Ctrl1 10 56.8 0.1
Ctrl2 10 58.5 0.15
PSM T[m] Inf
Mann 14 52 0.26
Ctrl 13 56.6 0.25
PSM T[m] Inf
Mann1 8 58.3 0.19
Mann2 4 58.1 0.02
Ctrl1 6 54.5 0.19
Ctrl2 7 54.2 0.2
PSM T[m] Inf
Mann 15 52.8 0.32
Ctrl 10 41.1 0.22

Figure 4.8

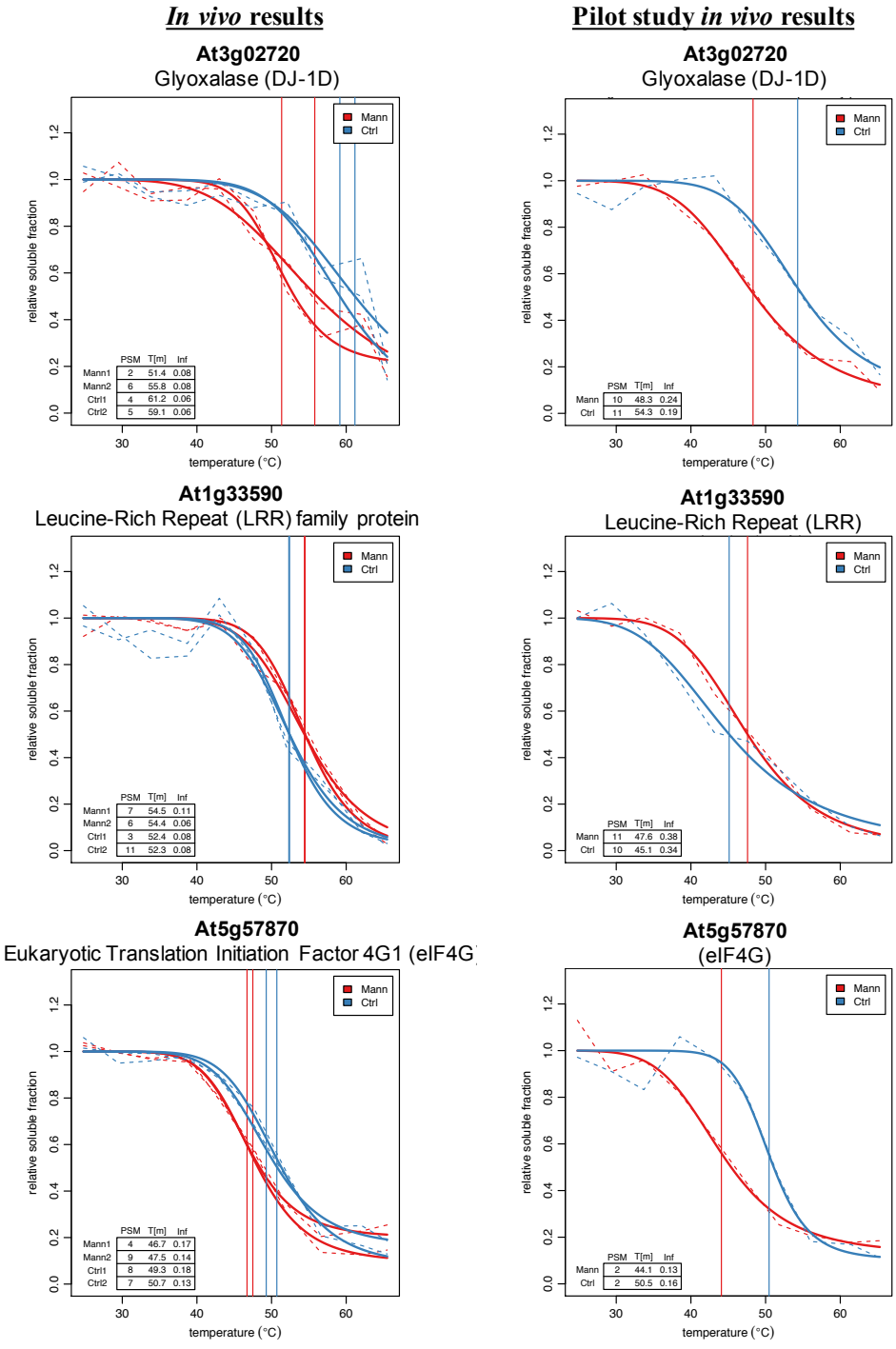
In vivo results
Pilot study *in vivo* results
At3g02720
Glyoxalase (DJ-1D)
At1g33590
Leucine-Rich Repeat (LRR) family protein
Leucine-Rich Repeat (LRR)
At5g57870
Eukaryotic Translation Initiation Factor 4G1 (eIF4G)
(eIF4G)
Mann
Ctrl
relative soluble fraction
temperature (°C)
PSM T[m] Inf
Mann1 2 51.4 0.08
Mann2 6 55.8 0.08
Ctrl1 4 61.2 0.06
Ctrl2 5 59.1 0.06
Mann 10 48.3 0.24
Ctrl 11 54.3 0.19
Mann1 7 54.5 0.11
Mann2 6 54.4 0.06
Ctrl1 3 52.4 0.08
Ctrl2 11 52.3 0.08
Mann 11 47.6 0.38
Ctrl 10 45.1 0.34
Mann1 4 46.7 0.17
Mann2 9 47.5 0.14
Ctrl1 8 49.3 0.18
Ctrl2 7 50.7 0.13
Mann 2 44.1 0.13
Ctrl 2 50.5 0.16

Figure 4.8

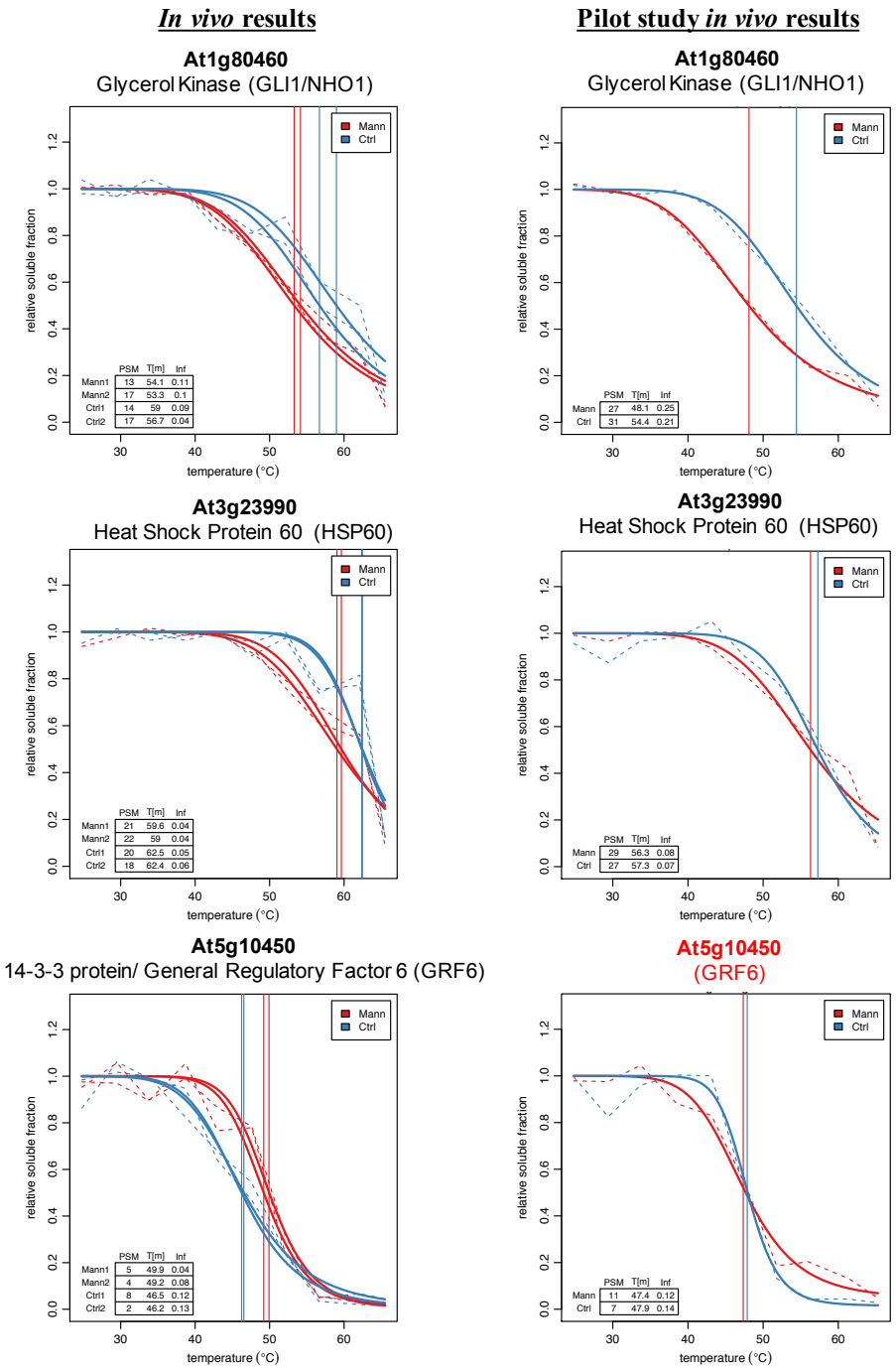

Figure 4.8: *Candidate proteins from in vivo mannitol treatment dataset.* Thermal denaturation curves calculate in the original pilot study are shown in the right column. Plot details are the same as described in 4.3. Red labels indicate proteins that did show reproducible delta Tm values in the pilot study.

Figure 4.9

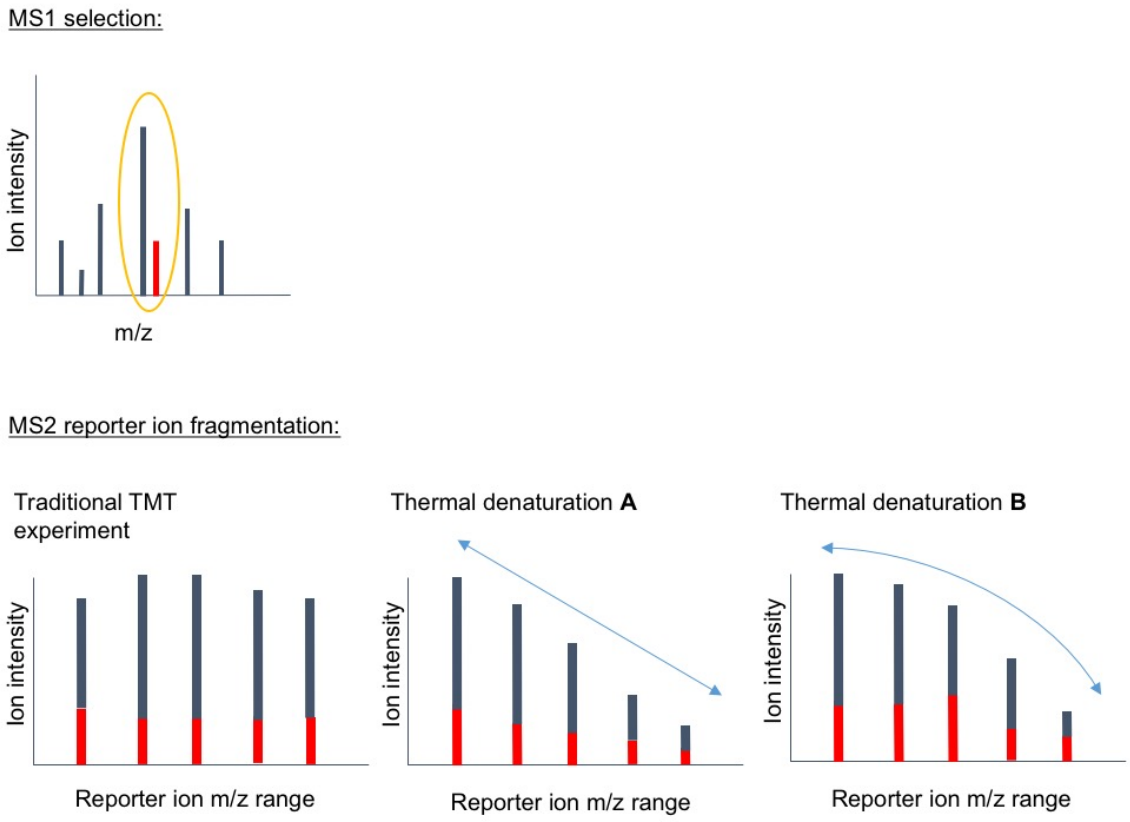

Figure 4.9: *Co-isolation interference*. Peptides ions are isolated from MS1 scans (yellow circle) for fragmentation and analysis in MS2. Isolation windows may allow in contaminating peptide ions (red line) in addition to the desired peptide (black line). The influence of the contaminating ions may be substantial in the calculations of protein abundance during thermal denaturation experiments (scenario A vs. scenario B). In scenario A, the interfering ion has an identical reporter ion abundance pattern to the target ion, and therefore has minimal influence on the total relative fragment ion intensities. In scenario B, the interference ion has a different reporter ion abundance that the target ion, and therefore influences the observed fragment ion ratios.

References

1. Savitski MM*, et al.* (2014) Tracking cancer drugs in living cells by thermal profiling of the proteome. *Science* 346(6205):1255784.
2. Humphrey SJ, Azimifar SB, & Mann M (2015) High-throughput phosphoproteomics reveals in vivo insulin signaling dynamics. *Nat Biotechnol* 33(9):990-995.
3. Kurganov BI (2002) Kinetics of protein aggregation. Quantitative estimation of the chaperone-like activity in test-systems based on suppression of protein aggregation. *Biochemistry (Mosc)* 67(4):409-422.
4. Kurganov BI, Rafikova ER, & Dobrov EN (2002) Kinetics of thermal aggregation of tobacco mosaic virus coat protein. *Biochemistry (Mosc)* 67(5):525-533.
5. Vedadi M*, et al.* (2006) Chemical screening methods to identify ligands that promote protein stability, protein crystallization, and structure determination. *Proc Natl Acad Sci U S A* 103(43):15835-15840.
6. Brandts JF & Lin LN (1990) Study of strong to ultratight protein interactions using differential scanning calorimetry. *Biochemistry* 29(29):6927-6940.
7. Pace CN & McGrath T (1980) Substrate stabilization of lysozyme to thermal and guanidine hydrochloride denaturation. *J Biol Chem* 255(9):3862-3865.
8. Pantoliano MW*, et al.* (2001) High-density miniaturized thermal shift assays as a general strategy for drug discovery. *J Biomol Screen* 6(6):429-440.
9. Straume M & Freire E (1992) Two-dimensional differential scanning calorimetry: simultaneous resolution of intrinsic protein structural energetics and ligand binding interactions by global linkage analysis. *Anal Biochem* 203(2):259-268.
10. Ericsson UB, Hallberg BM, Detitta GT, Dekker N, & Nordlund P (2006) Thermofluor-based high-throughput stability optimization of proteins for structural studies. *Anal Biochem* 357(2):289-298.
11. Niesen FH, Berglund H, & Vedadi M (2007) The use of differential scanning fluorimetry to detect ligand interactions that promote protein stability. *Nat Protoc* 2(9):2212-2221.
12. Senisterra GA*, et al.* (2006) Screening for ligands using a generic and high-throughput light-scattering-based assay. *J Biomol Screen* 11(8):940-948.
13. Jafari R*, et al.* (2014) The cellular thermal shift assay for evaluating drug target interactions in cells. *Nat Protoc* 9(9):2100-2122.
14. Martinez Molina D*, et al.* (2013) Monitoring drug target engagement in cells and tissues using the cellular thermal shift assay. *Science* 341(6141):84-87.
15. Franken H*, et al.* (2015) Thermal proteome profiling for unbiased identification of direct and indirect drug targets using multiplexed quantitative mass spectrometry. *Nat Protoc* 10(10):1567-1593.
16. Huber KV*, et al.* (2015) Proteome-wide drug and metabolite interaction mapping by thermal-stability profiling. *Nat Methods* 12(11):1055-1057.

17. Durek P, *et al.* (2010) PhosPhAt: the Arabidopsis thaliana phosphorylation site database. An update. *Nucleic Acids Res* 38(Database issue):D828-834.

18. Saracco SA, *et al.* (2009) Tandem affinity purification and mass spectrometric analysis of ubiquitylated proteins in Arabidopsis. *Plant J* 59(2):344-358.

19. Kim DY, Scalf M, Smith LM, & Vierstra RD (2013) Advanced proteomic analyses yield a deep catalog of ubiquitylation targets in Arabidopsis. *Plant Cell* 25(5):1523-1540.

20. Stecker KE, Minkoff BB, & Sussman MR (2014) Phosphoproteomic analyses reveal early signaling events in the osmotic stress response. *Plant physiology* 165(3):1171-1187.

21. Minkoff BB, Stecker KE, & Sussman MR (2015) Rapid Phosphoproteomic Effects of Abscisic Acid (ABA) on Wild-Type and ABA Receptor-Deficient A. thaliana Mutants. *Mol Cell Proteomics* 14(5):1169-1182.

22. Morris EJ, *et al.* (2006) Functional identification of Api5 as a suppressor of E2F-dependent apoptosis in vivo. *PLoS Genet* 2(11):e196.

23. Cho H, *et al.* (2014) Apoptosis inhibitor-5 overexpression is associated with tumor progression and poor prognosis in patients with cervical cancer. *BMC Cancer* 14:545.

24. Krejci P, *et al.* (2007) The antiapoptotic protein Api5 and its partner, high molecular weight FGF2, are up-regulated in B cell chronic lymphoid leukemia. *J Leukoc Biol* 82(6):1363-1364.

25. Garcia-Jove Navarro M, *et al.* (2013) Api5 contributes to E2F1 control of the G1/S cell cycle phase transition. *PLoS One* 8(8):e71443.

26. Ngaki MN, *et al.* (2012) Evolution of the chalcone-isomerase fold from fatty-acid binding to stereospecific catalysis. *Nature* 485(7399):530-533.

27. Engel N, *et al.* (2011) The presequence of Arabidopsis serine hydroxymethyltransferase SHM2 selectively prevents import into mesophyll mitochondria. *Plant Physiol* 157(4):1711-1720.

28. Zhou H, *et al.* (2012) Ubiquitin-specific protease16 modulates salt tolerance in Arabidopsis by regulating Na(+)/H(+) antiport activity and serine hydroxymethyltransferase stability. *Plant Cell* 24(12):5106-5122.

29. Johnson H, Eyers CE, Eyers PA, Beynon RJ, & Gaskell SJ (2009) Rigorous determination of the stoichiometry of protein phosphorylation using mass spectrometry. *J Am Soc Mass Spectrom* 20(12):2211-2220.

30. Olsen JV, *et al.* (2010) Quantitative phosphoproteomics reveals widespread full phosphorylation site occupancy during mitosis. *Sci Signal* 3(104):ra3.

31. Haruta M, *et al.* (2010) Molecular characterization of mutant Arabidopsis plants with reduced plasma membrane proton pump activity. *J Biol Chem* 285(23):17918-17929.

32. Haruta M & Sussman MR (2012) The effect of a genetically reduced plasma membrane protonmotive force on vegetative growth of Arabidopsis. *Plant Physiol* 158(3):1158-1171.

33. Minkoff BB, Burch HL, & Sussman MR (2014) A pipeline for 15N metabolic labeling and phosphoproteome analysis in Arabidopsis thaliana. *Methods Mol Biol* 1062:353-379.

APPENDIX 1

Rapid Phosphoproteomic Effects of ABA on Wildtype and ABA Receptor-Deficient *A. thaliana* Mutants

The work presented in this chapter has been published:

Minkoff, Benjamin B., **Kelly E. Stecker**, and Michael R. Sussman. "Rapid phosphoproteomic effects of abscisic acid (ABA) on wild-type and ABA receptor-deficient A. thaliana mutants." *Molecular & Cellular Proteomics* 14, no. 5 (2015): 1169-1182.

Contribution:

I developed the selected reaction monitoring (SRM) methods for targeted phosphopeptide analysis, ran the samples on the QTRAP5500 mass spectrometer, and assisted with data analysis. I also helped with revising the manuscript for publication.

Abstract

Abscisic acid (ABA) is a plant hormone that controls many aspects of plant growth including seed germination, stomatal aperture size, and cellular drought response. ABA interacts with a unique family of fourteen receptor proteins. This interaction leads to the activation of a family of protein kinases, SnRK2s, which in turn phosphorylate substrates involved in many cellular processes. The family of receptors appears functionally redundant. To observe a measurable phenotype, four of the fourteen receptors have to be mutated to create a multilocus loss-of-function quadruple receptor (QR) mutant, which is much less sensitive to ABA than wildtype (WT) plants. Given these phenotypes, we asked whether or not a difference in ABA response between the WT and QR backgrounds would manifest on a phosphorylation level as well. We tested WT and QR mutant ABA response using isotope-assisted quantitative phosphoproteomics to determine what ABA-induced phosphorylation changes occur in WT plants within five minutes of ABA treatment, and how that phosphorylation pattern is altered in the QR mutant. We found multiple ABA-induced phosphorylation changes that occur within five minutes of treatment, including three SnRK2 autophosphorylation events and phosphorylation on SnRK2 substrates. The majority of robust ABA-dependent phosphorylation changes observed were partially diminished in the QR mutant, whereas many smaller ABA-dependent phosphorylation changes observed in the wild type were not responsive to ABA in the mutant. A single phosphorylation event was increased in response to ABA treatment in both the WT and QR mutant. A portion of the discovery data was validated using Selected Reaction Monitoring (SRM)-based targeted measurements on a triple quadrupole mass spectrometer. These data suggest that different subsets of phosphorylation events depend upon different subsets of the ABA receptor family

to occur. Altogether, these data expand our understanding of the model by which the family of ABA receptors directs rapid phosphoproteomic changes.

Introduction

Abscisic acid (ABA) is a plant hormone involved in drought response as well as regulation of seed dormancy and germination. The core cellular ABA signaling pathway is mediated by three major events: (i) ABA binding to ABA receptor proteins, i.e. pyrabactin resistance/pyrabactin resistance-like/regulatory component of ABA receptor (PYR/PYL/RCAR) proteins, (ii) inhibition of clade A protein phosphatase 2C (PP2C) activity as a result of ABA:PYR/PYL/RCAR:PP2C ternary complex formation, and (iii) sustained activation via autophosphorylation of PP2C targets, snf-1 related kinase 2s (SnRK2s) [1]. Activated SnRK2s phosphorylate multiple substrates, including ion channels such as slow anion channel 1 (SLAC1)[2] and potassium channel in *Arabidopsis thaliana* 1 (KAT1)[3], transcription factors such as bZIP[4] and bHLH/AKS[5], and flowering time regulators[6]. Given that ABA signaling impacts many cellular processes, it is likely that the SnRK2s have additional, undiscovered substrates important for phosphosignaling, genetic regulation, and physiological effects.

Many proteins within the ABA signaling pathway are genetically redundant. There are 14 PYR/PYL/RCARs, nine clade A PP2Cs, of which at least six play a role in ABA signaling[1], and ten SnRK2s, of which three are known to play roles in ABA signaling[7]. This redundancy impeded the discovery of the receptor family until 2009[8, 9], when a multi-locus loss-of-function *pyr1/pyl1/pyl2/pyl4* quadruple receptor mutant (QR) was constructed. QR mutants are resistant to ABA-induced inhibition of germination[9], show reduced expression of ABA responsive genes, are deficient in ABA-mediated stomatal closure[10], have a higher stomatal conductance than wildtype (WT) plants, and show dramatically reduced reactive oxygen species-induced calcium influx upon ABA stimulation[11]. Loss-of-

function sextuple PYR/PYL/RCAR receptor mutants[12], triple SnRK2 mutants[13], and decuple SnRK2 mutants[14] have also been generated and all suffer from stunted growth and ABA insensitivity.

The reliance upon the SnRK2 family of protein kinases to transduce ABA signaling via changes in protein phosphorylation make quantitative mass spectrometry (MS)-based phosphopoteomics an ideal tool to study ABA signaling. The availability of faster and more sensitive mass spectrometers and new techniques for phosphopeptide enrichment have made proteome-wide comprehensive phosphorylation experiments feasible [15]. Previous experiments have used a quantitative phosphoproteomic approach to analyze ABA response in loss-of-function *snrk2.2/2.3/2.6* mutants[6, 16, 17], however, these focused on long ABA treatments (15 minutes and longer), even though ABA-responsive phosphorylation occurs as early as 5 minutes[17]. Additionally, none have been performed using the QR mutant, despite multiple phenotypes demonstrating its lack of ABA responsiveness[9-11].

The two most prevalent quantitative MS techniques for large-scale, untargeted work are *in vitro* labeling with isobaric tags (i.e. iTRAQ and TMT)[18, 19] and metabolic labeling with heavy isotope labeled inorganic nitrogen or amino acids in the growth medium (i.e. SILAC)[20, 21]. Metabolic labeling offers the ability to label proteins as an organism grows, and tissue from isotopic variants is combined immediately after treatment and processed together. Thus, sample processing affects both isotopic variant samples equally, and quantitative measurements are unaffected by inherent downstream processing error. Arabidopsis is uniquely suited for metabolic labeling since its small seed size allows labeling to 95 percent or greater in a span of approximately ten days[22, 23].

Untargeted discovery proteomic experiments using MS provide an unequaled means of identifying and quantifying large numbers of phosphorylation sites, but these large scale untargeted analyses are significantly affected by instrumental variability, which can have a large effect on statistical significance and reproducibility. Analyzing a complex sample multiple times can result in little overlap in peptide identifications between analyses. Low abundance species are not sampled in every analysis, resulting in variable observation and discrepancies in peptide identification between complex samples. One solution is to perform selected reaction monitoring (SRM)[24] assays with a triple quadrupole mass spectrometer (QQQ). SRM quantification uses ratios comprised of area under elution curves of fragment ions from endogenous phosphopeptides and identical measurements of their respective fragment ions from spiked in heavy-labeled synthetic phosphopeptides. Spiking identical amounts of a synthetic peptide mixture into every sample enables controlled quantification, and mass selection during analysis allows reproducible monitoring of handpicked phosphorylation events. Using a QQQ, SRM allows mass selection at both the precursor and fragment ion levels, improving signal to noise levels and enabling detection and quantification of low abundance species. Surprisingly, even with this well-established technique, the set of literature describing targeted MS experiments monitoring protein phosphorylation is noticeably small[25-30].

To identify early ABA-induced phosphorylation events mediated by the ABA receptors PYR1, PYL1, PYL2, and PYL4, we performed a quantitative phosphoproteomic analysis of WT plants treated with ABA for five minutes. This provided us with the foundation for understanding global ABA-responsive phosphorylation changes at this time point in WT plants. Next, because QR mutants are phenotypically much less sensitive to

ABA than wildtype plants[9-11], we aimed to determine whether or not this phenotype of QR plants corresponded to a loss of ABA-responsive phosphorylation following treatment. To that end, we used a combination of untargeted high-resolution mass spectrometry and targeted mass spectrometry to identify and confirm ABA-dependent phosphorylation events and measure their response to ABA in the QR mutant background. Our results demonstrate that a subset of ABA-responsive phosphorylation depends on a subset of the family of PYR/PYR/RCAR receptors that includes at least one within the group of four mutated in addition to at least one of the nine functional in the QR background, whereas the rest of the ABA-responsive phosphorylation depends on either the receptors knocked out in the QR mutant or at least one of the nine remaining. Altogether, this data suggests that different subsets of phosphorylation events may depend on the functional presence of different subsets of the ABA receptor family for full ABA-responsiveness. Further, we have identified putative SnRK2 substrates and found evidence of crosstalk between ABA and other plant stress signaling pathways. This analysis represents comprehensive analysis of early phosphorylation events in ABA signaling, and greatly expands the view of ABA-dependent phosphosignaling.

Materials and Methods

Arabidopsis metabolic labeling and untargeted MS.

Growth conditions, protein extraction, and digestion were all performed as previously described[17]. For the wildtype experiment, 2 A (^{14}N ABA-treated, ^{15}N mock-treated) replicates were used, and 3 B (^{14}N mock-treated, ^{15}N ABA-treated) replicates were used. Each A or B experiment consisted of material from 2 magenta boxes, combined at equal dry, frozen, and ground weights (Fig. S1). For the QR mutant experiments, three A and B replicates were used. When LysC digests were performed, trypsin was replaced with LysC in identical amounts. Offline SCX fractionation was performed solely on tryptic digests (not the LysC digests) with strong cation exchange chromatography using a method adapted from a previously published protocol[31]. Samples were resuspended into buffer A (5mM KH_2PO_4, 30% pH 2.65, 30% C_2H_3N), loaded onto a 200 x 9.4 mm polySULFOETHYL A column with 5µm beads with 200Å pores (PolyLC INC.) for 2 minutes, and eluted over 33 minutes with a gradient to 25% B (5mM KH_2PO_4, 350mM KCl, pH 2.65, 30% C_2H_3N), after which 100% B was flowed for 5 minutes, followed by a re-equilibration with 100% A for 20 minutes. HPLC flow was 3mL/min. Fractions were collected in 4-minute intervals and lyophilized. Fractions were chosen for analysis based on time of elution and intensity of chromatogram, based on 214nm and 280nm absorbance. Lyophilized fractions were resuspended in 0.1% TFA, desalted using Waters sep-pak columns, and dried down in a vacuum centrifuge. Phosphopeptide enrichment was performed on trypsin digested, SCX fractionated samples as well as lysC digested samples using 200µL spin-enrichment TiO_2-packed tips (GL Sciences, Inc.) using supplier protocol. This process is detailed in Figure S1.

Dried phosphopeptides were solubilized into Optima LC/MS-grade 0.1% formic acid in water (Fisher Scientific) for injection onto an LTQ Orbitrap XL using an Agilent 1100 LC system. Solvent A was 0.1% formic acid, and solvent B was 95% acetonitrile, 0.1% formic acid. Sample was loaded directly onto an analytical column of ID 75µm and OD 360µm house-packed with ~13cm C18 resin (Magic-C18, 200Å, 3µm, Michrom Biosources Inc.) at 0% B and a flow rate of 0.5µL/min from 0-45 minutes, then eluted from 45-235 minutes at a flow rate of 0.2µL/min and a gradient to 40% B, then from 235-255 minutes to 60% B, then from 255-260 minutes to 100% B. Column was then re-equilibrated by flowing 100% A from 260-278 minutes, stepping flow rate to 0.5µL/min at minute 265.

MS1 spectra were collected using the Orbitrap at resolution 100,000 with preview mode enabled. Top 5 MS2 per MS1 were collected in the LTQ, rejecting +1 and unassigned charge states, using CID with an isolation window of 2.5 m/z, normalized CE of 35, activation Q of 0.25, activation at 30ms, and a minimum MS1 signal threshold of 500. ETD analysis was performed with identical separation as listed for CID, with a reaction time of 100 ms, precursor charge state-dependent reaction time optimization, and supplemental activation for doubly charged precursor ions. Raw data were converted to .mgf files using default settings in the Trans-Proteomic Pipeline and searched using Mascot v2.2.2 and the Arabidopsis Information Resource (TAIR) protein database (version 9, June 19, 2009) with reverse sequences and common contaminants manually appended (62,522 sequences in total). The enzyme trypsin was specified as the protease and 1 missed cleavage was allowed. A precursor and fragment ion tolerance of 20ppm and 0.6Da, respectively, were used. Cysteine carbamidomethylation was set as a fixed modification, and methionine oxidation, serine/threonine/tyrosine phosphorylation, and asparagine/glutamine deamidation were set as

variable modifications. Mascot output was filtered to 1.0% false discovery rate using an in-house written script, and Census [32, 33] was used to extract ion chromatograms and quantify $^{14/15}$N area ratios. Census output was reformatted using an in-house written script, and data was median-normalized per injection. ^{15}N Mascot searches were performed for all .raw files, and phosphopeptide ratios that were not obtained for a given replicate using ^{14}N searching had ^{15}N search-produced ratios added and used in averaging and statistical analysis. Technical replicates were not performed, due to high instrument usage from multiple fractions for multiple biological replicates. Phosphopeptides of interest with Mascot score ≤ 30 or potentially ambiguous phosphorylation localization (i.e., multiple phosphoisoforms were identified) were manually validated by raw MS2 spectrum analysis. All data has been provided as supplemental Scaffold (Proteome Software) files, processed excel files (supplemental tables 2-4), and the raw data has been uploaded to and is publicly available via Chorus (https://chorusproject.org).

To obtain the values highlighted in this manuscript, phosphopeptides of interest had their ratios collapsed into a single data point by averaging all the values for the ^{14}Ntreat/^{15}Ncontrol experiment (A) and the inverse values of the ^{14}Ncontrol/^{15}Ntreat experiment (B). T-tests were performed using the spread of ratios from A experiments and from B experiments prior to inverting the B values.

SRM-MS

Plants were grown and treated as described above, solely in ^{14}N media. Three biological replicates of WT+ABA or Mock and QR+ABA or Mock were performed. Prior to digestion with trypsin/lysC mix, a mixture of heavy labeled internal peptide standards (IS) was added to samples. House-packed, offline TiO_2 columns were used for phosphopeptide enrichment,

as previously reported [23]**.** Samples were injected onto an AB SCIEX QTRAP 5500 using an Eksigent nanoflex cHiPLC system with a ChromXP C18-CL column (3μM beads with 120Å pore size packed into a 6mm x 200μM column) for trapping and a ChromXP C18-CL column (3μM beads with 120Å pore size packed into a 15cm x 75μM column) for chromatographic separation. Buffer A was 0.1% formic acid in water, and buffer B was 0.1% formic acid in ACN. Samples were loaded for 1 minute in 2% B, and an elution gradient from 2 to 35% B was run for 70 min., upped to 90% B in 2 min., flowed at 90% B for 2 min., dropped to 2% B in one min., then flowed at 2% B for 15 min. for a total run time of 90 min. All flow rates were 300nL/min. Precursor ions were scheduled within a 3- or 4-minute retention time windows, depending on instrument performance. Every condition save for QR+mock has at least 2 injection replicates, and most have 3. Method optimization was performed using MRMPilot software v1.0 (AB SCIEX).

Multiple fragment ions were tested for each peptide using both in silico predictions and acquired MS/MS spectra. The three to five most abundant parent ion-to-fragment ion transitions were selected, and collision energies were optimized to maximize fragment ion intensity. The developed method was pilot tested, and the number of transitions for each peptide was reduced to three through the removal of the lowest quality transitions that performed poorly in complex sample backgrounds. These were monitored during targeted analysis. Quantification was performed using Multiquant software v2.0 (AB SCIEX), and well-behaved (i.e. highest signal intensity, best chromatography) transitions for each peptide were used for quantification. For each peptide, 1-3 transitions were used for quantification with Multiquant's automatic MQ4 function to determine peak area under fragment ion chromatograms.

Further processing occurred in excel. Injection replicates were averaged per transition, and then transitions were averaged (when more than one was used for quantification) per biological replicate to obtain a ratio for a given peptide for that replicate. Ratios from the control (WT+mock and QR+mock) biological replicates (representing average area under chromatograms for endogenous peak:internal standard) were then averaged to get a single value for control condition, and then each WT+ABA or QR+ABA replicate was divided by the respective averaged control value to get a spread of ABA-induced fold changes. This spread was used to create the standard error bars shown in **fig. A1.4**. All reported p values were calculated using the spread of both +ABA and +mock biological replicate ratios.

Results

SnRK2 protein kinases and other proteins are phosphorylated in response to ABA in vivo within five minutes of treatment

We hypothesized that ABA phosphosignaling may function on a time scale shorter than the majority of plant phosphoproteomic studies have investigated. To test this, untargeted high-resolution MS in conjunction with metabolic labeling was used to examine the effect of five-minute ABA treatment on global phosphorylation in WT plants (Fig. S1). Ratios, calculated using area under extracted ion chromatograms for ^{14}N and ^{15}N versions for every phosphopeptide, were manually examined to find ABA-induced phosphorylation that had: i) a fold change of greater than 1.15 or less than 0.85, ii) at least one data point from both reciprocal experiments (see Fig. S1), and iii) extracted ion chromatograms that exhibited good signal to noise quality. We chose the threshold of 1.15 or 0.85 for fold changes of interest because of the short treatment time, the requirement to see a corresponding fold change in the reciprocal experiment, and because chromatograms were manually examined and validated for each phosphopeptide that passed the aforementioned requirements.

Within five minutes, ABA-dependent phosphorylation increased on residues within the autoactivation loops of SnRK2.2, 3, and 6 (**Fig. A1.1A**, Table S1), the three SnRK2 kinases previously demonstrated to be ABA-responsive[7]. A phosphopeptide that was ambiguous between SnRK2.1, 4, 5 and 10 (due to sequence homology) was also identified and showed a minor ABA-dependent change. We identified ABA-dependent phosphorylation on multiple transcription factors (**Fig. A1.1A**, Table S1) including the transcriptional repressor heat shock factor B2b (HSFB2b, AT4G11660), for which the largest ABA-responsive phosphorylation increase of the transcription factors was observed. Additional transcription factors that exhibited ABA-responsive phosphorylation increases include global

transcriptional element 3 (GTE3, AT1G73150), a basic leucine zipper (bZIP, AT2G21230), a basic helix-loop-helix/ABA-responsive kinase substrate (bHLH/AKS2, AT1G05805), and a zinc finger (AT2G14835). Interestingly, among these transcription factors, only bHLH/AKS2 has an annotated function. It is one of a family of 3 ABA-responsive kinase substrates (AKS1, 2, and 3). Upon phosphorylation, AKS1 represses transcription of KAT1, the inward-rectifying K^+ channel that positively regulates ABA-induced stomatal closure[5]. We identified ABA-induced phosphorylation on an analogous serine on AKS2 occurring within five minutes following treatment. Overall, 3,500 total unique phosphopeptides were sequences and quantified (Table S2); of these, less than one percent changed after five minutes of ABA treatment: 24 ABA-dependent phosphorylation events increased within this timeframe, and eight decreased (**Fig. A1.1B**, Table S1).

ABA-dependent phosphorylation increases on transcription factors within SnRK2 and MAPK phosphorylation motifs

To determine whether the phosphorylation sites that showed rapid changes were occurring on SnRK2 substrates, we analyzed the peptides showing increased ABA-responsive phosphorylation for enriched phosphorylation motifs using Motif-X[34, 35]. Using the *A. thaliana* proteome as a background, the most enriched, highest-scoring sequence motif identified was LXRXXS (**Fig. A1.2A**). This sequence has been demonstrated *in vitro* to be a preferential SnRK2 phosphorylation motif[4, 36], and its enrichment in the dataset suggests that some of these phosphoproteins may be ABA-dependent SnRK2 substrates. The second highest scoring motif was SP, which has been computationally predicted to be a target of mitogen-activated protein kinases (MAPKs)[37]. The full search results are shown in Fig. S2.

Of the identified phosphorylation increases, six contain an LXRXXS motif and two contain an RXXS motif, a weaker but still preferential SnRK2 phosphorylation motif (**Fig. A1.2B**)[4, 36]. Interestingly, of the five transcription factors identified, four contain the LXRXXS motif, and one contains the RXXS motif (**Fig A1.2C**). Given that phosphorylation occurs concurrent with or following SnRK2 activation and these sequences contain preferential SnRK2 phosphorylation motifs, these transcription factors are likely direct SnRK2 substrates. One of the transcription factors, bHLH/AKS2 (AT1G05805), has previously been shown to exhibit ABA-responsive phosphorylation[5], however, the kinase responsible is not known; our data suggest that the kinase responsible for ABA-responsive bHLH/AKS2 phosphorylation is one of the three SnRK2s we identified as ABA-responsive within the same timeframe. Seven of the 20 ABA-responsive phosphorylation increases contain the motif SP (**Fig. A1.2C**), a motif likely preferred by MAPKs[37]. MAPKs have been implicated in ABA signaling in many studies[38], and these data suggest that their ABA-responsive activity is occurring as early as five minutes after treatment. Interestingly, there is no overlap between the list of phosphopeptides that contains the SnRK2 phosphorylation motifs and the list that contains the MAPK phosphorylation motifs.

ABA-dependent phosphorylation in quadruple ABA receptor mutants exhibits distinct patterns

Quadruple ABA receptor (QR) mutants are far less sensitive to ABA than WT plants. This phenotype manifests as a loss of ABA-induced transcriptional changes[12], stomatal closure[10], calcium flux[11], and germination/growth inhibition[9]. We predicted that ABA-responsive phosphorylation patterns observed in WT plants would differ in the QR mutant background. To test this, we performed a metabolic labeling experiment with QR mutants to

quantify phosphorylation changes induced by ABA (Table S2). We observed that the SnRK2 kinases identified as significantly phosphorylated in response to five minutes of ABA treatment in wildtype plants are also responsive to ABA in the mutant background, albeit to a lesser degree (**Fig. A1.3A**). This indicates that the four mutated receptors only partially account for ABA-responsive SNRK2 phosphorylation. Interestingly, the phosphorylation event within the activation loop of SnRK2.1, 4, 5, and 10 was not ABA-responsive in the QR mutant background.

Many of the ABA-responsive phosphorylation changes observed in the WT dataset were identified as unresponsive to ABA in the QR mutant background (**Fig. A1.3B**), consistent with the idea that a portion of ABA-dependent phosphorylation relies entirely on at least one of the four knocked out receptors. Surprisingly, ABA-dependent phosphorylation on a single protein, bHLH/AKS2 (AT1G05805), was unaffected in the QR mutant background, indicating that some ABA-responsive phosphorylation events may occur independently of the four knocked out receptors.

In the untargeted studies, we could not compare all of the phosphorylation sites identified in the wildtype study to the QR mutant study. There was imperfect overlap in phosphopeptide identification between samples, an issue intrinsic to untargeted MS experiments. The nature of data-dependent MS is such that the same pool of low abundance peptides may not be identified in every analysis, and the effects of this are more apparent when analyzing phosphorylation, which can occur transiently and at low stoichiometries. Thus, we applied a targeted approach using triple quadrupole (QQQ)-based MS to reproducibly analyze phosphopeptides identified as ABA-responsive and as validation for the changes observed in the untargeted datasets.

Large ABA-responsive phosphorylation changes are reproduced in targeted analyses

Whereas untargeted mass spec can be made quantitative by metabolically labeling organisms as they grow prior to analysis, selected reaction monitoring (SRM), a type of targeted MS, uses synthetic heavy amino acid-labeled phosphopeptides. Mixtures of synthetic peptides are spiked into extracted protein samples prior to reduction, alkylation, and digestion. Quantification is achieved by comparing the area under extracted ion elution chromatograms of peptide fragment ions for the spiked in heavy isotope-labeled standards to the light, endogenous versions (Fig. S3). Comparing these ratios between samples allows large-scale experiments to be quantitative by focusing on a smaller number of peptides or phosphorylation events in every sample.

The panel of 21 phosphopeptides used for targeted analysis contained those identified from untargeted analyses in this study as well as those in a previously published untargeted study[17]. The ABA-responsive fold changes with the largest magnitude in the untargeted study were reproduced in the targeted study (**Fig. A1.4**, Table S4). Phosphopeptides corresponding to the activation loop of the SnRK2 kinases showed the same pattern of partially diminished ABA-responsive phosphorylation when in the QR mutant background. The SRM data revealed that ABA-dependent SnRK2.6 phosphorylation is indeed diminished in the mutant background, which could not be determined using theuntargeted data due to SnRK2.6 phosphorylation being observed in only one untargeted mutant sample. The ABF (AT1G45249, AT1G49720, AT4G34000, AT3G19290, AT3G56850) and AREB3 (AT5G56850) transcription factors are SnRK2 substrates that are phosphorylated in response to ABA[39, 40]. As expected given this relationship, our targeted SRM data indicate their phosphorylation pattern to be similar to that of the SnRK2 kinases in the mutant background.

The targeted SRM data also corroborated the ABA-responsive phosphorylation seen on bZIP transcription factor (AT2G21230), which we previously observed in the untargeted data. Additionally, targeted MS confirmed that ABA-responsive bHLH/AKS2 (AT1G05805) phosphorylation occurs fully in both WT and QR mutant background.

Targeted analysis using SRM revealed statistically significant differences that were not previously observed due inherent limitation of untargeted methods. For example, the transcriptional repressor HSFB2b (AT4G11660) shows diminished ABA-responsive phosphorylation in the QR mutant, similar to the SnRK2 kinases and the known transcription factor substrates. Additionally, we observed an ABA-responsive phosphorylation increase in the WT dataset on a phosphopeptide sequence ambiguous between the plasma membrane ATPases/proton transporters AHA4/11 (AT3G47950, AT5G62670). This phosphopeptide was not observed at all in the mutant untargeted dataset, and the QR response could not be compared to the WT response using the untargeted data. The SRM data revealed that, in the mutant background, an ABA-induced phosphorylation increase on AHA4/11 was not observed, suggesting ABA-induced AHA4/11 phosphorylation depends on at least one of the four mutated ABA receptors. AHA4 has been implicated in growth and salt resistance [41] and little is known about AHA11.

Both experimental and biological variability contribute to variation of small magnitude fold changes in targeted analyses

Interestingly, not all the ABA-responsive phosphorylation changes observed in the untargeted WT dataset were reproduced in the targeted dataset. Examples of this include the identified GTPase (AT4G21160), the phospholipase C NPC4 (AT3G03530), and a protein with unknown function accession AT5G53420 (**Fig. A1.4**). For the 14 phosphopeptides that

we obtained both untargeted and targeted data for in the WT+/-ABA experiment, we compared the fold changes observed using the two analytical techniques (Figure S4). Of these, eight had a fold change that was both trending the same direction and of a similar magnitude in the targeted vs. the discovery data, and six did not. All of the phosphorylation events that were increased 1.5-fold or greater in the discovery data in response to ABA, with the exception of NPC4 (AT3G03530), were validated by the targeted work, whereas none of the ABA-dependent decreases we monitored were replicated.

Phosphoproteomic experimental workflows involve many steps, making sample processing variability a reasonable concern. Furthermore, the lack of literature surrounding targeted MS protein phosphorylation experiments means widespread quality assurance measures have not been established. Due to this lack of consensus, we tested how much variability we observed in a controlled experiment. Specifically, we assayed the degree of biological variability as well as variability introduced by experimental processing (Fig. S5A). We treated four individual magenta boxes with ABA, then ground, processed and analyzed the material from the four boxes individually. Observed variability in this experiment was considered to be a result of processing and analysis or biological response variation between samples, given that all were treated and processed individually.

Samples were analyzed using an SRM panel of 55 synthetic peptides, monitoring 106 transitions, including those used in the ABA experiments (Table S4). This panel included 20 of the SRM peptides previously analyzed and 35 from a recently published targeted study from this laboratory[29]. A median coefficient of variation of 20% was observed after data was processed identically to the ABA experiment (Fig. S5B). Indeed, many of the small ABA-responsive fold changes fall within this range of variation, suggesting inherent

experimental and biological variability may account for discrepancies between discovery and targeted phosphoproteomic data when fold changes are small. The median represents this variability, which may occur at any step following protein extraction or be biological variation inherent to an *in vivo* system. This result is consistent with the previously published study, which indicated that statistical significance decreases drastically when monitored phosphorylation fold changes are ≤1.5[29].

Discussion

We used deep phosphoproteomic analyses to determine what ABA-regulated phosphorylation occurs in WT *A. thaliana* within five minutes of ABA treatment, a time point considerably earlier than has been previously examined in depth. We found ABA-induced phosphorylation changes on multiple proteins, including increased autophosphorylation of the SnRK2 kinases and increased phosphorylation on transcription factors not yet implicated in ABA signaling (**Fig. A1.1**). The two most enriched phosphorylation motifs in the set of ABA-responsive phosphorylation were those of the SnRK2 kinases and MAPKs, implicating these two pathways as the earliest activated in response to ABA stimulation (**Fig. A1.2**). We then asked if the pattern of observed ABA-responsive phosphorylation was altered in the quadruple ABA receptor mutant *pyr1/pyl1/pyl2/pyl4* (QR), a genetic background that is significantly less sensitive to ABA than WT plants[9-11]. Interestingly, the data demonstrated that a subset of phosphorylation events, including the autophosphorylation of the SnRK2 kinases, was lower in magnitude but still present and significantly ABA-responsive in the QR mutant background (**Fig. A1.3**). This suggests that these events depend on at least one of the four knocked out receptors in addition to at least one of the remaining nine receptors. Another subset of phosphorylation events was unresponsive to ABA in the QR mutant background, suggesting that these events depend on at least one of the four knocked out receptors to occur. A single ABA-induced phosphorylation event on the transcription factor bHLH/AKS2 (AT1G05805) occurred in both the WT and QR mutant background, suggesting its ABA-responsiveness depends on at least one of the nine functional receptors present in the QR mutant background. These untargeted phosphoproteomic studies were followed by targeted MS using a panel of 21

synthetic phosphopeptides (**Fig. A1.4**). Of the 14 SRM phosphopeptides monitored that were also identified and quantified in the reported untargeted studies, 8/14 (57%) were validated using targeted MS, a subset which included the large ABA-responsive changes (≥1.5) and a portion of the small ones. The remaining phosphopeptides monitored (6/14, 43%), which included small ABA-responsive changes (≤1.5) and ABA-responsive phosphorylation decreases, did not agree with the untargeted results. We tested the variability inherent to our targeted pipeline and found it to be 20%, consistent with the irreproducibility we observed when monitoring low magnitude fold changes in a targeted fashion. Altogether, the data provide comprehensive analysis of early ABA signaling events and expand the view of ABA-regulated phosphorylation signaling.

ABA-responsive phosphorylation occurs within five minutes of stimulation and is likely downstream of SnRK2 and MAP kinases

Our analysis of WT plants demonstrated that ABA-induced SnRK2 autophosphorylation occurred as quickly as five minutes following ABA treatment (**Fig. A1.1**). The largest ABA-responsive phosphorylation increases were on the three SnRK2 kinases responsible for ABA signaling, corroborating data from a recently published targeted study from this laboratory focusing on crosstalk between signaling pathways[29]. We also identified a phosphorylation event ambiguous between SnRK2.1, 4, 5, and 10 that increased in response to ABA treatment. None of these four SnRK2 kinases have yet been implicated in ABA signaling. Phosphoproteomic analyses also identified other ABA-responsive phosphorylation and dephosphorylation within this timeframe; about 1.0% of the quantified phosphoproteome was reproducibly responsive to ABA, and the majority of changes we observed were increased. Two recently published studies used untargeted phosphoproteomic

analyses to analyze ABA-responsiveness in *A. thaliana* on timescales ranging from 15-90 minutes[6, 16]. These longer studies found 1.6% and 5.3% of the quantified phosphoproteome were ABA-responsive, compared to our five minute study in which we found 1.0% of the quantified phosphoproteome was ABA-responsive. This reduced amount of identified ABA-dependent phosphorylation changes is consistent with the earlier time point following ABA treatment on which our experiments were focused. We compared fold changes for phosphorylation we identified as ABA responsive in WT plants to the same phosphorylation events observed and quantified in the previously published studies (Table S5). Though the quantification methods, time points, and growth conditions were different, our data support some of the smaller fold changes identified in these publications. Our threshold for consideration was 15% increased or decreased across multiple biological replicates, though many changes exceeded 20% or greater. Within the set of increased phosphorylation, the motifs LXRXXS and SP are enriched (**Fig A1.2**.). The first motif is a SnRK2 phosphorylation motif[4, 36], and its enrichment within the identified increased phosphorylation lends confidence to the dataset and is consistent with the SnRK2 activation observed within the same time frame. The second is a predicted MAPK phosphorylation motif[37], and its presence within the increased phosphorylation suggests that ABA-responsive MAPK signaling may be active within five minutes as well. This result is consistent with and may be linked to a recently published targeted MS analysis showing rapid ABA-dependent phosphorylation on a MAP4K[29]; however, the MAP4K family is poorly characterized in *A. thaliana*[42]. In *S. cerevisiae*, the MAP4K Ste20 activates the MAPK cascade responsible for osmotic adaptation in response to osmotic stress[43], but it is unknown if a similar network exists in Arabidopsis. Together, the two lists of

phosphopeptides containing the enriched motifs do not overlap and make up the majority of the identified increased phosphorylation, suggesting that the main phosphorylation cascades involved in ABA signaling at this early time point following treatment are the ABA-dependent SnRK2 and MAPK cascades.

ABA-responsive phosphorylation occurs on TFs and other substrates early in ABA signaling

In addition to the SnRK2 kinases, ABA-dependent phosphorylation also increased on five transcription factors (**Fig. A1.1**), HSFB2b (AT4G11660), GTE3 (AT1G73150), a bZIP (AT2G21230), a zinc finger (AT2G14835), and bHLH/AKS2 (AT1G05805). Of these, four contain the SnRK2 phosphorylation motif LXRXXS and one contains a weaker SnRK2 motif, RXXS. Because of the presence of these motifs within the protein sequences and the observation that phosphorylation increases concurrently with or following SnRK2 activation, we consider all of these transcription factors to be candidates of direct SnRK2 kinase phosphorylation. None of these have been previously reported as SnRK2 substrates, and of these, only HSFB2b and bHLH/AKS2 have known function.

HSFB2B (AT4G11660) and HSFB1 (AT4G36990) are heat-inducible transcriptional repressors. Together, they are necessary in *A. thaliana* for acquired thermotolerance[44] and play a role in pathogen defense signaling[45]. Our data indicate that HSFB2b phosphorylation within a SnRK2 motif increases quickly in response to ABA treatment. This is not the first data linking ABA and heat stress response. ABA treatment one hour before heat shock has been previously demonstrated to increase survival rate post heat shock, and ABI1, a PP2C in the core ABA signaling pathway, is necessary for basal heat shock resistance[46]. We predict that at least part of a combined response to ABA and heat shock begins as early as five minutes, and involves regulation of heat shock response transcription

factors, including HSFB2B. The SnRK2 phosphorylation motif, on which ABA-responsive phosphorylation occurred, is unique to HSFB2B, although HSFB2B contains a DNA binding domain that is highly conserved among both Class A and B heat shock factors.

Though HSFB2b phosphorylation has yet to be functionally linked to ABA signaling, bHLH/AKS2 is known to be phosphorylated in response to ABA at the site we observed *in planta*[5]. Analogous phosphorylation of AKS1 (AT1G51140) by SnRK2.6 was demonstrated *in vitro* to disrupt AKS1 binding to the promoter of the inward rectifying K^+ channel partially responsible for ABA-induced stomatal closure, KAT1. This binding event enhances KAT1 transcription, and phosphorylation prevents AKS1 binding, repressing transcription. Whether AKS2 functions similarly to AKS1 is currently unknown.

Mutant studies indicate dependence of phosphorylation events on subsets of the family of receptors

We next asked if the ABA-dependent phosphorylation observed is maintained in a genetic background containing multilocus loss of PYR1/PYL1/PYL2/PYL4 ABA receptor function. Interestingly, of the ABA-responsive phosphorylation observed in the WT background, we observed all three possible differences when examining ABA response in the QR mutant: (1) ABA-dependent phosphorylation that was as responsive in the mutant background as in the WT, (2) ABA-dependent phosphorylation that was unresponsive to ABA in the mutant background, and (3) ABA-dependent phosphorylation that was partially diminished in the mutant background when compared to the WT response (**Fig. A1.3**). The distribution was not equal; many of the phosphorylation events that were minimally responsive to ABA in the WT background were completely unresponsive to ABA in the mutant background, and only one event remained fully responsive, that on bHLH/AKS2

(AT1G05805). All of the SnRK2 kinases known to be ABA-responsive exhibit the partially sustained phosphorylation in the mutant background, as do well-known SnRK2 kinase substrates. This may be a result of the short time point sampled combined with the lower activity of the SnRK2 kinases. In this case, at longer time points following ABA treatment, ABA-responsive phosphorylation would eventually reach levels observed in the WT. However, this observation could also be the result of a threshold-based response. If this is the case, ABA-responsive SnRK2 autophosphorylation and downstream phosphorylation in the QR mutant background could never reach the levels observed in the WT plants without the presence of the complete set of fourteen PYR/PYL/RCAR ABA receptors. Future experiments to classify the nature of ABA-responsive phosphorylation will address this.

These data suggest that different subsets of ABA-responsive phosphorylation events depend on different subsets of the PYR/PYL/RCAR family of receptors to occur (**Fig. A1.5**). Those that are completely unresponsive to ABA in the QR mutant background depend upon the functional presence of at least one of the four mutated receptors. The phosphorylation events that are partially sustained in the QR mutant background depend upon a subset of ABA receptors that includes at least one of the four mutated receptors as well as at least one of the nine remaining in the QR mutant. These data are consistent with previously published data that demonstrate similar responses on a transcriptional level[12]. Taken together, these results suggest that diminished ABA-dependent transcriptional response in mutant backgrounds may be the result of lessened ABA-responsive phosphorylation on transcription factors responsible for ABA-stimulated gene regulation. This in turn may be the result of diminished ABA-responsive SnRK2 autophosphorylation in the mutant background. Finally, we identified a phosphorylation event on bHLH/AKS2 that occurred to a similar degree in

response to ABA in both the WT and the QR mutant background, a result that we verified with targeted experiments. Thus, this phosphorylation event depends entirely on at least one of the remaining nine receptors present in the QR mutant background to be ABA-responsive. Though only one instance of this was identified in these initial experiments, future experiments with other mutants and treatment time points may identify more phosphorylation events that follow an identical pattern.

The largest ABA-responsive phosphorylation changes were validated using SRM-based MS analyses

Some phosphorylation observed in the untargeted WT dataset could not be compared to the QR mutant dataset, due to intrinsic variability in phosphopeptide identification between samples in untargeted MS experiments. In addition, many of the phosphopeptides were only identified once or twice in the mutant data, preventing statistical analysis. To address this technical limitation, we used SRM-based targeted MS with a triple quadrupole instrument to monitor a panel of 21 phosphopeptides derived from these untargeted experiments and a previously published dataset [17].

The largest magnitude ABA-responsive fold changes (≥1.5) seen in the untargeted work were replicated using targeted assays (**Fig. A1.4**, Fig. S4). These included the SnRK2s and transcription factors that are likely ABA-responsive SnRK2 substrates, HSFB2b and bZIP AT2G21320. We also monitored phosphorylation on two peptides from ABFs1/2/3/4 (AT1G45249, AT1G49720, AT4G34000, AT3G19290, AT3G56850) and AREB3 (AT5G56850), known ABA-responsive SnRK2 substrates that were not identified in the discovery experiments performed for this study. The previous discovery work identified increased phosphorylation on ABFs1/2/3/4 and AREB3 only after thirty minutes of ABA

treatment[17], whereas the targeted work demonstrated that these transcription factors are highly phosphorylated within five minutes of treatment. Due to lack of identification at multiple time points in the previous study and in multiple replicates in the discovery data shown here, it is likely that the abundance of ABA-responsive phosphorylation on these transcription factors is too low this early in signaling to monitor without targeted assays, though it is clear that ABA induces their phosphorylation. The phosphorylation pattern on these transcription factors is identical to the SnRK2s, i.e. highly responsive to ABA treatment in WT plants, but only partially responsive to ABA in the QR mutant background. Interestingly, though we were unable to observe HSFB2b phosphorylation in the untargeted mutant dataset, our targeted analyses demonstrated a phosphorylation pattern identical to that of both the ABA-responsive SnRK2s and ABF1/2/3/4 and AREB3, providing further evidence that HSFB2b is an ABA-responsive SnRK2 substrate. These experiments demonstrate the ability of targeted assays to monitor phosphorylation events where abundance is too low for untargeted studies to reproducibly detect and quantify.

With respect to the small magnitude ABA-responsive fold changes identified in the untargeted data (≤1.5), some, but not all, were reproduced in the targeted data. The bHLH/AKS2 (AT1G05805) phosphorylation event increased 1.41 and 1.52 fold in the WT and QR mutant background, respectively, in response to ABA in the untargeted experiments (Fig. 3). This increase was repeated using targeted analyses, although lower fold changes were observed (Fig 4). The bZIP transcription factor (AT2G21230), observed in both approaches, exhibited similar ABA-responsive fold changes of 1.41 and 1.31 in the WT background in the untargeted and targeted experiments, respectively. However, other ABA-dependent phosphorylation changes identified in the untargeted analyses were not reproduced

using targeted analysis. For example, the identified ZAC GTPase (AT4G21160) phosphopeptide decreased in abundance upon ABA treatment in WT plants and was unresponsive in the QR mutant plants in the untargeted data. In the targeted dataset, this phosphopeptide appears unchanged upon ABA treatment in both wildtype and QR mutant plants. Of the 14 phosphorylation events we identified as ABA-responsive in the untargeted experiments and monitored using SRM analyses, eight were validated and six did not replicate (Fig. S4). Probing the literature led to a few reports of targeted phosphorylation experiments[25-30]. A single publication from another laboratory describes a similar experimental scheme with human breast cancer tissue samples from high-risk and low-risk patients[30]. In this study, a panel of 15 SRM peptides is used to validate an untargeted iTRAQ-based experiment. Of these, 66% (10/15) exhibited good correlation when comparing data points from the discovery and targeted experiments ($r^2 \geq 0.6$, as defined by the authors). This is slightly higher than what we found (57%).

To better understand the basis by which the targeted and untargeted experiments varied, we performed an experiment to determine what degree biological and processing variability affect the changes we can confidently quantify using targeted experiments using a panel of 55 SRM peptides. When treating, processing, and analyzing four plants identically, a median coefficient of variation (CV) of 20% was obtained when analyzing all the ratios of synthetic SRM peptide to endogenous peptide (Fig. S5). This CV value may explain why smaller magnitude fold changes are not reproduced; variation associated with experimental processing and biological variability is 20%, convoluting reproducible determination of smaller magnitude fold changes when performing targeted analyses using the described pipeline. This result is in line with a recent publication from this laboratory, which showed

that for fold changes determined by SRM to be ≤1.5, statistical significance greatly decreases[29]. Interestingly, when examining the targeted dataset, higher biological CVs were obtained when comparing the mutant data to the WT data (Table S3), suggesting a higher degree of variability in general in the mutant background, although the cause of this remains unclear.

Conclusion

Previously, we published a study examining ABA-responsive phosphorylation in WT *A. thaliana* at five, 15, and 30 minutes of treatment[17]. This work expands upon this previously published data by more deeply analyzing the five minute response, both in WT and in the multilocus loss-of-function *pyr1/pyl1/pyl2/pyl4* quadruple ABA receptor mutant. We have identified and quantified ABA-responsive phosphorylation changes in WT *A. thaliana* that occur within five minutes of treatment, representing approximately 1.0% of the reproducibly observable phosphoproteome. Two recently published studies also examining ABA-responsive phosphorylation in Arabidopsis found 1.6% and 5.3% of the identified phosphoproteome is affected when examining 15, 30, and 90 minutes and 30 minutes of ABA treatment, respectively[6, 16]. Considering we are examining an earlier time point after ABA treatment, our data is consistent with these published data. From the WT dataset, we identified multiple transcription factors whose phosphorylation is increased within five minutes of ABA treatment. A subset of these contain the SnRK2 preferential phosphorylation motif LXRXXS, and one contains the weaker RXXS motif, making these transcription factors candidates for direct phosphorylation by the SnRK2 family of protein kinases in response to ABA. Another subset, which doesn't overlap with the first, contains the MAPK phosphorylation motif SP. These data suggest that the SnRK2 and MAPK phosphorylation cascades are the most activated in the first five minutes following ABA stimulation. Using targeted analyses, the large magnitude ABA-responsive fold changes (≥1.5) and some small fold changes (8/14 total peptides) were validated. Conversely, six out of 13 phosphopeptides we monitored that were responsive to ABA in the untargeted experiments did not replicate using targeted analyses, all of which were small ABA-responsive fold changes in the

untargeted experiments (≤1.5). We found that 20% variation in targeted measurements can be attributed to biological and technical variability intrinsic to our targeted workflow. Hopefully, as more laboratories adopt similar workflows, some consensus can be reached in regard to the inherent variability of targeted phosphorylation analyses.

When compared to WT, ABA-responsive phosphorylation in the QR mutants exhibited distinct patterns. The largest ABA-responsive phosphorylation changes, the SnRK2s and transcription factors, showed partially diminished ABA-responsive phosphorylation in the QR mutant. Many of the small ABA-responsive phosphorylation changes were either unresponsive to ABA treatment or reduced to no statistical significance in the QR background. The exception to this was bHLH/AKS2, which maintained full ABA-responsive phosphorylation in the QR mutant background. Taken together, these data add a new layer of understanding to ABA-regulated phosphorylation signaling. Different ABA-induced phosphorylation events depend on different subsets of the family of PYR/PYL/RCAR receptors to occur. A subset of these events, responsive to five minutes of ABA treatment in the WT background, is unresponsive to the same treatment in the QR mutant background. Their ABA-responsive phosphorylation depends on a subset of the ABA receptors that includes at least one of the four mutated in the QR background. Another subset of ABA-responsive phosphorylation partially occurred in the QR mutant background after five minutes of ABA treatment when compared to the WT background, indicating their ABA-responsiveness depends on at least one of the remaining nine ABA receptors present in the QR mutant background in addition to at least one of the four mutated in the QR background. The SnRK2 kinases and some transcription factor phosphorylation events exhibit this partial dependence. Finally, in both the WT and QR mutant background,

phosphorylation observed on bHLH/AKS2 increased in response to ABA, indicating its occurrence depends entirely on the functional presence of at least one of the four knocked out receptors. It may be that yet undiscovered ABA-responsive phosphorylation events follow identical patterns, though they may depend on other receptors within the family. Much work by many laboratories has been performed to identify and quantify global phosphorylation changes in response to ABA treatment in *A. thaliana*, and we hope the data presented here can be used as a starting point for further *in planta* experiments to be performed within shorter time frames and with multiple permutations of mutants within the family of ABA receptors. Future studies will further elucidate details surrounding each of the PYR/PYL/RCAR receptors and their separate roles within the ABA-regulated phosphorylation network.

Acknowledgements - We thank the University of Wisconsin-Madison Biotechnology Center Core Mass Spectrometry Facility and Peptide Synthesis Facility, Greg Barrett-Wilt, Greg Sabat, and Melissa Boersma for technical assistance and consultation. We thank Leigh Anson and Lindsay Traeger for reading and editing the manuscript. This work was supported, by NSF Grants MCB-0929395 (M.R.S.) and DGE-1256259 (K.E.S.), University of Wisconsin-based Morgridge Fellowships (K.E.S. and B.B.M.), and an NHGRI training grant to the Genomic Science Training Program 5T32HG002760 (B.B.M.).

Figure A1.1

A

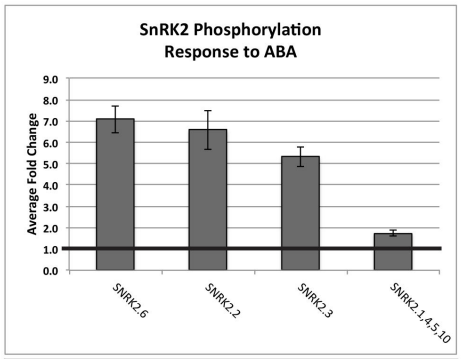

Accesion	Protein	Phosphopeptide
AT4G33950	SNRK2.6	K.ST*VGTPAYIAPEVLLK.K
AT3G50500	SNRK2.2	K.ST*VGTPAYIAPEILLR.Q
AT5G66880	SNRK2.3	K.ST*VGTPAYIAPEVLLR.Q
AT1G10940	SNRK2.1,4,5,10	K.ST*VGTPAYIAPEVLSR.R

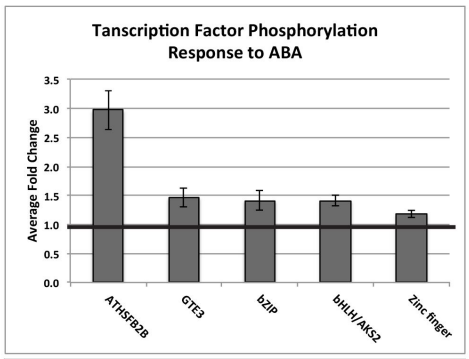

Accesion	Protein	Phosphopeptide
AT4G11660	ATHSFB2B	R.TTS*CTTAPELVEENER.L
AT1G73150	GTE3	AES*MTNPVKPAVLPVVPEK
AT2G21230	bZIP	R.SIS*GEDTSDWSNLVK.K
AT1G05805	bHLH/AKS2	S*SPADFFTYLASDK
AT2G14835	Zinc finger	R.QNS*ETLYYADDEDGNR.K

B

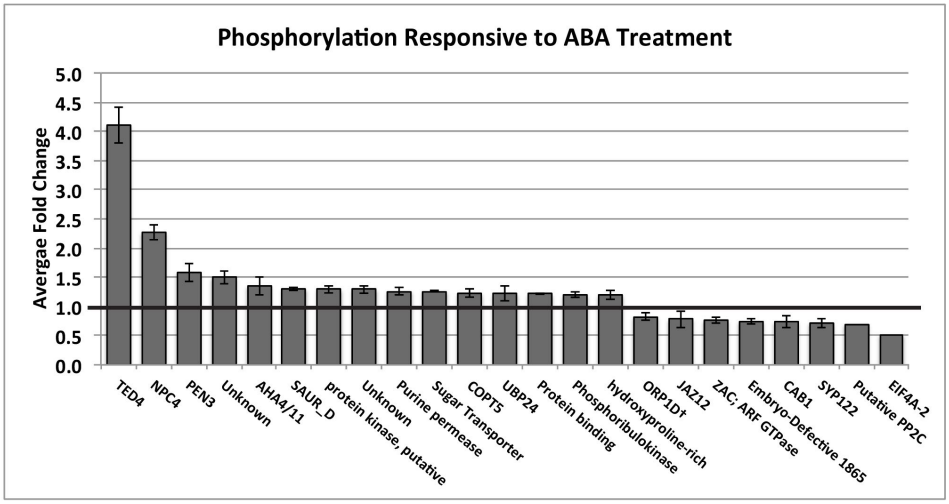

Figure A1.1. *ABA-responsive phosphorylation changes following five minutes of treatment identified using untargeted MS analyses*. Error bars represent standard error. Data displayed in full in Table S1. **A,** ABA-responsive SnRK2 and transcription factor phosphorylation. **B**, Additional ABA-responsive phosphorylation changes**.**

Figure A1.2

A

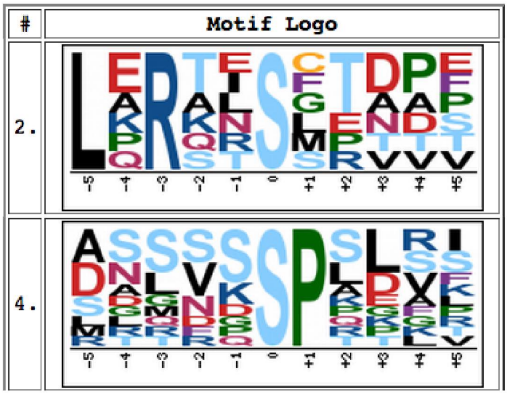

B

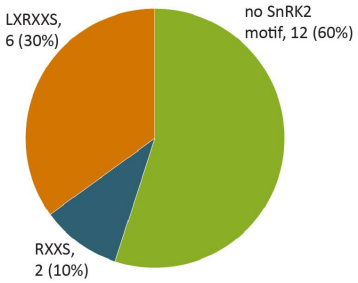

C

Sequences containing SnRK2 Motif

Accession	Protein	Sequence IDed plus Surrounding AA Content
AT4G11660	ATHSFB2B	GVVGGGS**LQR|*TT*S**** CTTAPELVEENER|LRKDNERLRK
AT1G73150	GTE3 - TF	KVVENRT**LER|AES*** MTNPVKPAVLPVVPEK|LVEEASANRD
AT2G21230	bZIP TF	KSPPLSS**LER|SIS*** GEDTSDWSNLVK|KEPREGFYKG
AT1G05805	bHLH Protein	SGSYS**LARQR|S*** SPADFFTYLASDK|NNFSLNQPTS
AT2G24400	SAUR_D	GSKSIKF**LKRT|LS*** FTDVTAVPK|GYLAVSVGLE
AT4G30890	UBP24	NDSDAK**LPR|KNS*** LRVPEHVVQNGIIK|EISESNKSLN
AT5G20650	COPT5	SSSRRAPPPP**R|SSS*** GVSAPLIPK|SGTRSAAKAA
AT2G14835	Zinc finger	RKGVPAVD**R|QNS*** ETLYYADDEDGNR|KKYSRRGPLR

Sequences containing SP Motif

Accession	Protein	Sequence IDed plus Surrounding AA Content
AT5G53420	Unknown	RAFSEGDIQK|LGAGLVQ**S*P**LDR|IIVSCTSEDR
AT3G09830	protein kinase, putative	MSEVLEMVNK|IVEASSGNG**S*P**QLVPLNSVK|ASRDARGKNN
AT2G32240	Unknown	EAMDVGVKSR|DIDLSFS**S*P**TK|RKSKKKPEAS
AT5G17010	Sugar Transporter	SSVSREFGK|SSGEI**S*P**EREPLIK|ENHVPENYSV
AT4G18220	Purine permease	QYLDETNLKK|SNEIPTTE**S*P**DRPEAEGSSEQSK|
AT1G73980	Phosphoribulokinase	LALPDDLKTK|LSLDDDTVS**S*P**K|EALSRASVDS
AT1G21580	hydroxyproline-rich	PSGGIVAVRR|DSVFPCDSLSS**S*P**R|LSRPLRSEIH

Figure A1.2. *Phosphorylation in response to five minutes of ABA treatment occurred on SnRK2 and MAPK motifs*. **A,** Two enriched motifs were identified, using MOTIF-X, as 10.49- and 3.04-fold enriched (Fig. S2) over the A. thaliana proteome at a significance threshold of 0.005. A window of 11 amino acids, centered on an S residue, with an occurrence threshold of six was used against the *A. thaliana* proteome as the background. Sequences fed into Motif-X had ten amino acids from the respective protein sequence before and after the identified sequence added for larger context. **B,** Of the phosphopeptides showing increased phosphorylation following ABA treatment, 30% of the increased phosphorylation occurred on the LXRXXS SnRK2 motif, 10% occurred on the RXXS SnRK2 motif. Peptides belonging to SnRK2 were removed form this analysis. **C,** Sequences containing identified SnRK2 motif and the MAPK motif. Identified sequences are highlighted with pipes, and motifs are shown in bold.

Figure A1.3

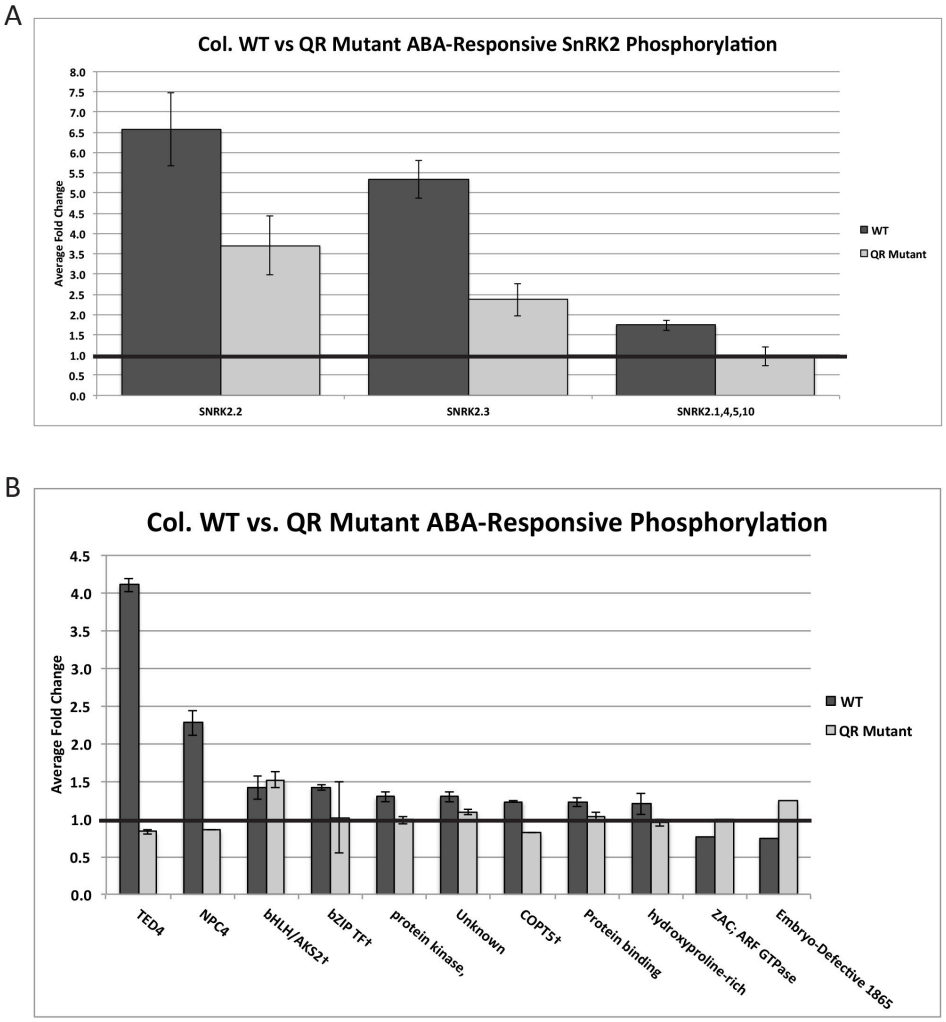

Figure A1.3. *Comparison of ABA-responsive phosphorylation changes in WT background to QR mutant background.* Error bars represent standard error. **A,** ABA-responsive SnRK2 kinase phosphorylation. **B,** ABA-responsive phosphorylation changes on other proteins identified and quantified in the QR mutant dataset.

Figure A1.4

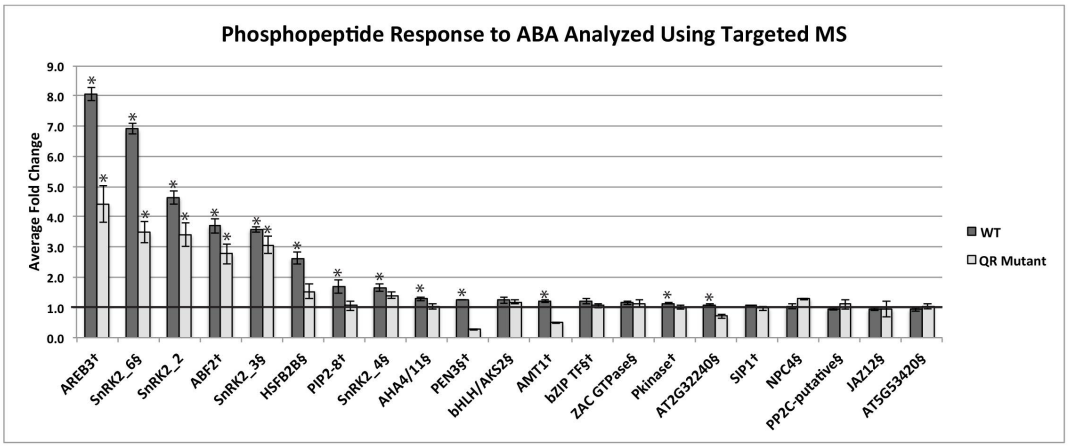

Figure A1.4. *Comparison of ABA-responsive phosphorylation changes in WT and pyr1/pyl1/pyl2/pyl4 (QR) mutant analyzed using targeted MS*. Phosphopeptides from the dataset presented here are designated with §, and phosphopeptides from previously published discovery work (Kline et al., 2010) are designated with †. Bars are marked (*) to indicate $p \leq 0.05$. See Table S3 for p values.

Figure A1.5

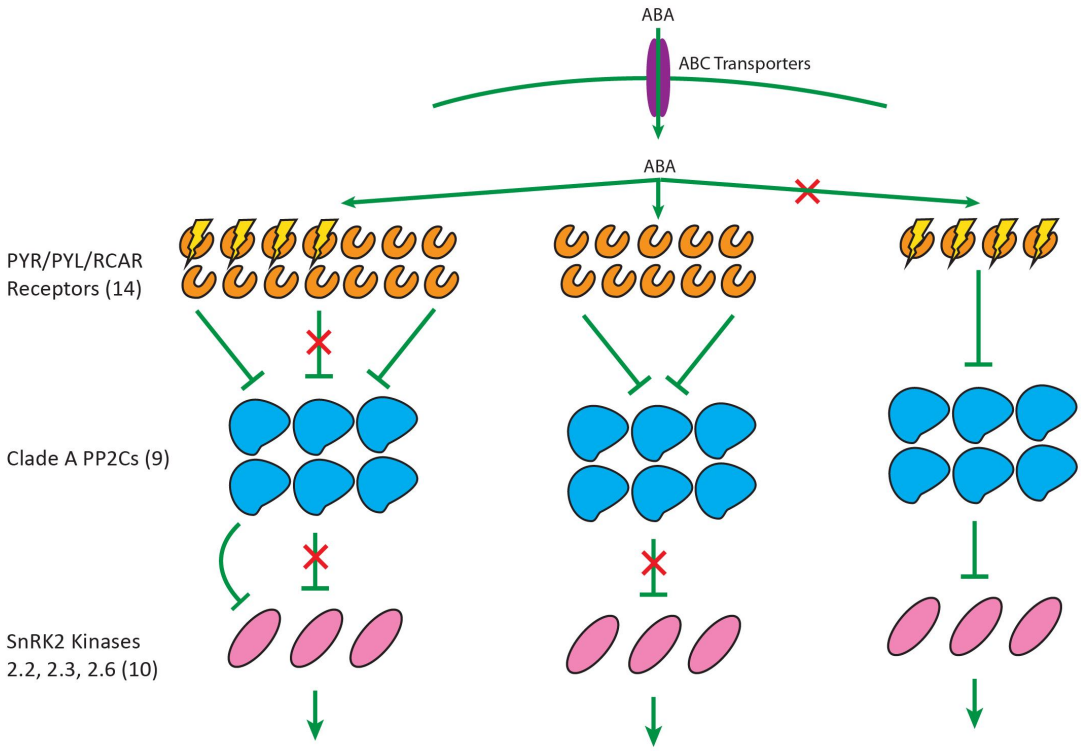

Protein whose phosphorylation falls into this category	Dimished response	Sustained response	No response
	SnRK2.6 SnRK2.2 SnRK2.3 SnRK2.[1,4,5,10] ABF[1,2,3,4] AREB3 HSFB2b AT2G32240	bHLH/AKS2	bZIP TF Pkinase - AT3G09830 COPT5 Protein Binding - AT4G19490 Hydroxyproline-rich - AT1G21580 Embryo-Defective 1865 PIP2;8 PEN3 AHA[4,11] Pkinase - AT5G35980

Figure A1.5. *Model of early ABA-responsive phosphorylation*. While a subset of ABA-responsive phosphorylation is diminished in the QR mutant, a single event is fully sustained in response to ABA, and another subset is completely unresponsive to ABA in the QR mutant. Proteins displayed had phosphopeptides identified in WT or both WT and QR mutant untargeted datasets shown in this report. Also included are proteins reported in previously published discovery data (Kline et al., 2010), which were followed up with targeted MS reported here. Phosphorylation identified as ABA-responsive in untargeted data but not reproduced in targeted analyses is not shown. Brackets indicate ambiguity in protein accession based on the phosphopeptide sequence identified and used for targeted study.

References

1 Cutler, S.R., *et al.* (2010) Abscisic acid: emergence of a core signaling network. *Annu Rev Plant Biol* 61, 651-679

2 Geiger, D., *et al.* (2009) Activity of guard cell anion channel SLAC1 is controlled by drought-stress signaling kinase-phosphatase pair. *Proc Natl Acad Sci U S A* 106, 21425-21430

3 Sato, A., *et al.* (2009) Threonine at position 306 of the KAT1 potassium channel is essential for channel activity and is a target site for ABA-activated SnRK2/OST1/SnRK2.6 protein kinase. *Biochem J* 424, 439-448

4 Sirichandra, C., *et al.* (2010) The Arabidopsis ABA-activated kinase OST1 phosphorylates the bZIP transcription factor ABF3 and creates a 14-3-3 binding site involved in its turnover. *PLoS One* 5, e13935

5 Takahashi, Y., *et al.* (2013) bHLH transcription factors that facilitate K(+) uptake during stomatal opening are repressed by abscisic acid through phosphorylation. *Sci Signal* 6, ra48

6 Wang, P., *et al.* (2013) Quantitative phosphoproteomics identifies SnRK2 protein kinase substrates and reveals the effectors of abscisic acid action. *Proc Natl Acad Sci U S A* 110, 11205-11210

7 Nakashima, K., *et al.* (2009) Three Arabidopsis SnRK2 protein kinases, SRK2D/SnRK2.2, SRK2E/SnRK2.6/OST1 and SRK2I/SnRK2.3, involved in ABA signaling are essential for the control of seed development and dormancy. *Plant Cell Physiol* 50, 1345-1363

8 Ma, Y., *et al.* (2009) Regulators of PP2C phosphatase activity function as abscisic acid sensors. *Science* 324, 1064-1068

9 Park, S.Y., *et al.* (2009) Abscisic acid inhibits type 2C protein phosphatases via the PYR/PYL family of START proteins. *Science* 324, 1068-1071

10 Nishimura, N., *et al.* (2010) PYR/PYL/RCAR family members are major in-vivo ABI1 protein phosphatase 2C-interacting proteins in Arabidopsis. *Plant J* 61, 290-299

11 Wang, Y., *et al.* (2013) PYR/PYL/RCAR abscisic acid receptors regulate K+ and Cl- channels through reactive oxygen species-mediated activation of Ca2+ channels at the plasma membrane of intact Arabidopsis guard cells. *Plant Physiol* 163, 566-577

12 Gonzalez-Guzman, M., *et al.* (2012) Arabidopsis PYR/PYL/RCAR receptors play a major role in quantitative regulation of stomatal aperture and transcriptional response to abscisic acid. *Plant Cell* 24, 2483-2496

13 Fujii, H. and Zhu, J.K. (2009) Arabidopsis mutant deficient in 3 abscisic acid-activated protein kinases reveals critical roles in growth, reproduction, and stress. *Proc Natl Acad Sci U S A* 106, 8380-8385

14 Fujii, H.*, et al.* (2011) Arabidopsis decuple mutant reveals the importance of SnRK2 kinases in osmotic stress responses in vivo. *Proc Natl Acad Sci U S A* 108, 1717-1722

15 Beltran, L. and Cutillas, P.R. (2012) Advances in phosphopeptide enrichment techniques for phosphoproteomics. *Amino Acids* 43, 1009-1024

16 Umezawa, T.*, et al.* (2013) Genetics and phosphoproteomics reveal a protein phosphorylation network in the abscisic acid signaling pathway in Arabidopsis thaliana. *Sci Signal* 6, rs8

17 Kline, K.G.*, et al.* (2010) In planta changes in protein phosphorylation induced by the plant hormone abscisic acid. *Proc Natl Acad Sci U S A* 107, 15986-15991

18 Zieske, L.R. (2006) A perspective on the use of iTRAQ reagent technology for protein complex and profiling studies. *J Exp Bot* 57, 1501-1508

19 Ross, P.L.*, et al.* (2004) Multiplexed protein quantitation in Saccharomyces cerevisiae using amine-reactive isobaric tagging reagents. *Mol Cell Proteomics* 3, 1154-1169

20 Everley, P.A.*, et al.* (2004) Quantitative cancer proteomics: stable isotope labeling with amino acids in cell culture (SILAC) as a tool for prostate cancer research. *Mol Cell Proteomics* 3, 729-735

21 Arsova, B.*, et al.* (2012) The use of heavy nitrogen in quantitative proteomics experiments in plants. *Trends Plant Sci* 17, 102-112

22 Huttlin, E.L.*, et al.* (2007) Comparison of full versus partial metabolic labeling for quantitative proteomics analysis in Arabidopsis thaliana. *Mol Cell Proteomics* 6, 860-881

23 Minkoff, B.B.*, et al.* (2014) A pipeline for 15N metabolic labeling and phosphoproteome analysis in Arabidopsis thaliana. *Methods Mol Biol* 1062, 353-379

24 Picotti, P. and Aebersold, R. (2012) Selected reaction monitoring-based proteomics: workflows, potential, pitfalls and future directions. *Nat Methods* 9, 555-566

25 Lam, M.P.*, et al.* (2012) An MRM-based workflow for quantifying cardiac mitochondrial protein phosphorylation in murine and human tissue. *J Proteomics* 75, 4602-4609

26 Mithoe, S.C.*, et al.* (2012) Targeted quantitative phosphoproteomics approach for the detection of phospho-tyrosine signaling in plants. *J Proteome Res* 11, 438-448

27 Lam, M.P.*, et al.* (2013) Site-specific quantitative analysis of cardiac mitochondrial protein phosphorylation. *J Proteomics* 81, 15-23

28 Kimura, A.*, et al.* (2014) Mass spectrometric analysis of the phosphorylation levels of the SWI/SNF chromatin remodeling/tumor suppressor proteins ARID1A and Brg1 in ovarian clear cell adenocarcinoma cell lines. *J Proteome Res* 13, 4959-4969

29 K, E.S.*, et al.* (2014) Phosphoproteomic Analyses Reveal Early Signaling Events in the Osmotic Stress Response. *Plant Physiol* 165, 1171-1187

30 Narumi, R.*, et al.* (2012) A strategy for large-scale phosphoproteomics and SRM-based validation of human breast cancer tissue samples. *J Proteome Res* 11, 5311-5322

31 Villen, J.*, et al.* (2007) Large-scale phosphorylation analysis of mouse liver. *Proc Natl Acad Sci U S A* 104, 1488-1493

32 Park, S.K.*, et al.* (2008) A quantitative analysis software tool for mass spectrometry-based proteomics. *Nat Methods* 5, 319-322

33 Park, S.K. and Yates, J.R., 3rd (2010) Census for proteome quantification. *Curr Protoc Bioinformatics* Chapter 13, Unit 13 12 11-11

34 Schwartz, D. and Gygi, S.P. (2005) An iterative statistical approach to the identification of protein phosphorylation motifs from large-scale data sets. *Nat Biotechnol* 23, 1391-1398

35 Chou, M.F. and Schwartz, D. (2011) Biological sequence motif discovery using motif-x. *Curr Protoc Bioinformatics* Chapter 13, Unit 13 15-24

36 Vlad, F.*, et al.* (2008) A versatile strategy to define the phosphorylation preferences of plant protein kinases and screen for putative substrates. *Plant J* 55, 104-117

37 van Wijk, K.J.*, et al.* (2014) Meta-Analysis of Arabidopsis thaliana Phospho-Proteomics Data Reveals Compartmentalization of Phosphorylation Motifs. *Plant Cell* 26, 2367-2389

38 Danquah, A.*, et al.* (2014) The role of ABA and MAPK signaling pathways in plant abiotic stress responses. *Biotechnol Adv* 32, 40-52

39 Kobayashi, Y.*, et al.* (2005) Abscisic acid-activated SNRK2 protein kinases function in the gene-regulation pathway of ABA signal transduction by phosphorylating ABA response element-binding factors. *Plant J* 44, 939-949

40 Furihata, T.*, et al.* (2006) Abscisic acid-dependent multisite phosphorylation regulates the activity of a transcription activator AREB1. *Proc Natl Acad Sci U S A* 103, 1988-1993

41 Vitart, V.*, et al.* (2001) Evidence for a role in growth and salt resistance of a plasma membrane H+-ATPase in the root endodermis. *Plant J* 27, 191-201

42 Champion, A.*, et al.* (2004) Reassessing the MAP3K and MAP4K relationships. *Trends Plant Sci* 9, 123-129

43 Bahn, Y.S. (2008) Master and commander in fungal pathogens: the two-component system and the HOG signaling pathway. *Eukaryot Cell* 7, 2017-2036

44 Ikeda, M.*, et al.* (2011) Arabidopsis HsfB1 and HsfB2b act as repressors of the expression of heat-inducible Hsfs but positively regulate the acquired thermotolerance. *Plant Physiol* 157, 1243-1254

45 Kumar, M.*, et al.* (2009) Heat shock factors HsfB1 and HsfB2b are involved in the regulation of Pdf1.2 expression and pathogen resistance in Arabidopsis. *Mol Plant* 2, 152-165

46 Larkindale, J. and Knight, M.R. (2002) Protection against heat stress-induced oxidative damage in Arabidopsis involves calcium, abscisic acid, ethylene, and salicylic acid. *Plant Physiol* 128, 682-695

APPENDIX 2

A Peptide Hormone and Its Receptor Protein Kinase Regulate Plant Cell Expansion

The work presented in this chapter has been published:

Haruta, Miyoshi, Grzegorz Sabat, **Kelly Stecker**, Benjamin B. Minkoff, and Michael R. Sussman. "A peptide hormone and its receptor protein kinase regulate plant cell expansion." *Science* 343, no. 6169 (2014): 408-411.

Contribution:

I operated the Orbitrap mass spectrometer for the untargeted phosphoproteome experiment and searched the mass spectral data against the protein database for peptide identification. I optimized and performed the selected reaction monitoring (SRM) to validate a part of the results arose from the discovery experiment.

Abstract

Plant cells are immobile; thus, plant growth and development depend on cell expansion rather than cell migration. The molecular mechanism by which the plasma membrane initiates changes in the cell expansion rate remains elusive. We found that a secreted peptide, RALF (rapid alkalinization factor), suppresses cell elongation of the primary root by activating the cell surface receptor FERONIA in*Arabidopsis thaliana*. A direct peptide-receptor interaction is supported by specific binding of RALF to FERONIA and reduced binding and insensitivity to RALF-induced growth inhibition in *feronia* mutants. Phosphoproteome measurements demonstrate that the RALF-FERONIA interaction causes phosphorylation of plasma membrane H^+–adenosine triphosphatase 2 at Ser^{899}, mediating the inhibition of proton transport. The results reveal a molecular mechanism for RALF-induced extracellular alkalinization and a signaling pathway that regulates cell expansion.

Introduction

Cell expansion is a fundamental cellular process driving plant growth, and regulation of its rate and direction is a highly dynamic process that changes during development, as well as during adaptation to variations in the external environment. To maintain appropriate cell expansion rates, plant cells fine-tune signal transduction pathways involving protein phosphorylation cascades catalyzed by protein kinases and protein phosphatases. For example, light and the growth-stimulating hormone auxin increase cell expansion rates and decrease apoplastic pH via phosphorylation of the penultimate Thr^{947} residue (1, 2) in a C-terminal regulatory domain of plasma membrane H^+–adenosine triphosphatase (H^+-ATPase).

RALF (rapid alkalinization factor), a 5-kD secreted peptide first discovered with assays searching for endogenous plant peptides with the ability to increase the pH of the media of cultured cells (3, 4), also induces a rapid increase in cytoplasmic calcium (5). Among more than 30 RALF-like genes in the*Arabidopsis* genome (fig. S1), RALF is most highly expressed in roots and was suggested to be involved in root development (6, 7) (figs. S2 and S3).We report here on signaling events at the plasma membrane that involve a peptide-receptor interaction leading to the suppression of root cell elongation. RALF mobilizes calcium in a manner resembling the signal transduction pathways of animal peptide growth factors, wherein the factor binds to a cell surface receptor that then autophosphorylates (8). We demonstrate that FERONIA receptor-like kinase binds to RALF and initiates a downstream phosphorylation signaling cascade that inhibits plasma membrane H^+-ATPase activity, increases apoplastic pH, and reduces cell elongation. We identify RALF and FERONIA as a ligand-receptor pair and provide a molecular mechanism for a

FERONIA-mediated growth-inhibitory signaling pathway that may also intersect with the innate immune response.

Results and Discussion

To obtain material for biochemical and genetic studies, we expressed RALF as an N-terminal 6×His fusion peptide in *Escherichia coli* that was purified to homogeneity using an affinity column and reversed-phase high-performance liquid chromatography (fig. S4, A-D). His-tagged RALF was biologically active in cytoplasmic calcium mobilization assays (fig. S4C). As a negative control, we also produced and purified an inactive RALF analog, RALF(Δ2–8), which lacks seven amino acids at its N terminus and is a biologically inactive analog (figs. S4E and S5)(9). To examine RALF-induced rapid changes in phosphorylation of plasma membrane proteins, we performed mass spectrometry–based quantitative phosphoproteomic profiling using an ^{15}N metabolic labeling technique (10,11)(**Figure A2.S6A**). Seedlings were treated with 1 μM RALF peptide or water as a control for 5 min, homogenized, and plasma membranes purified. For a biological duplicate, the samples were reciprocally labeled. Mass spectrometric analyses of phosphopeptides allowed the quantification of ~550 $^{14}N/^{15}N$ phosphopeptide pairs, with median linear ratio changes of 1.14 and 1.17 for samples A(^{14}N RALF/^{15}N control) and B (^{14}N control/^{15}N RALF), respectively (**Figure A2.S6, B-C; Figure A2.S7, A-B**. Among the phosphopeptides quantified, five proteins displayed a change in abundance, observed in a reciprocal manner, by a factor of at least 2.5 (table S1). Four of these proteins increased in abundance—FERONIA receptor kinase (pS871 and pS874, factor of 8.3 to 13.4, **Figure A2.1A**); plasma membrane H^+-ATPase 2 (AHA2; factor of 2.6 to 4.3, fig. S8); calcium-dependent protein kinase 9 (CPK9; factor of 4.0 to 12.1, fig. S9); and PEN3/ABCG36 transporter (factor of 4.17 to 4.52)—and one decreased: a second FERONIA-related receptor-like kinase we term ERULUS (ERU; factor of 0.22, fig. S10A).

We also observed the increased abundance of a FERONIA phosphopeptide containing a third serine phosphorylation site, pS858. Analysis was hampered by an unrelated peptide coeluting during the liquid chromatography–mass spectrometry analysis, but we manually reconstructed the chromatogram for the FERONIA phosphopeptide, SSDVYEGNVTDsR (**Figure A2.1B**). The pS858 phosphopeptide increased by a factor of ~20 in the RALF-treated tissues. Using selective reaction monitoring with a heavy isotope–labeled synthetic phosphopeptide containing pS858 (**Figure A2.S7, C-D**), we determined that pS858 is increased by a factor of 6.4 to 11.5 in RALF-treated seedlings. By analogy with the phospho-regulated mammalian epidermal growth factor receptor (12), we hypothesized that FERONIA was the receptor for RALF and that phosphorylation at the C terminus activated the kinase and initiated a RALF-induced signaling cascade (**Figure A2.1C**).

The FERONIA receptor-like kinase was first described with *Arabidopsis* mutants defective in pollen tube elongation arrest (13). During normal fertilization, the elongating pollen tube stops and releases its sperm nuclei at the egg, whereas in the *fer* mutant, the pollen tube overgrows and fails to release sperm nuclei, resulting in reduced fertility. FERONIA is among the most widely expressed members of the malectin receptor kinase family (14) (fig. S10B). In addition to changes in FERONIA, we detected another member of the malectin receptor family that responded to RALF, in this case with a decrease in abundance of the phosphopeptide containing pS497 located at the juxtamembrane domain (fig. S10C). Because FERONIA was named after the Etruscan fertility goddess, we have named this protein ERULUS, after a son of FERONIA in Etruscan mythology. To test the in planta function of these two receptor kinases (FERONIA and ERULUS) that show RALF-dependent changes in phosphorylation, we compared the growth of transferred DNA (T-

DNA) knockdown (*fer5*) and knockout (*fer4*) mutants with that of the wild type in the presence and absence of RALF. At 1 μM RALF, wild-type growth was inhibited, whereas the *fer4* null mutant was insensitive to RALF and the *fer5* knockdown mutant was moderately inhibited (**Figure A2.2A** and fig. S11A). In contrast, T-DNA mutants of ERULUS showed shorter root hair phenotypes (fig. S10, D-G), but there were no differences in sensitivity to RALF relative to the wild type (**Figure A2.2B**), despite changes in its phosphorylation in response to RALF. Inhibition of wild-type root elongation after RALF treatment was due to reduced cell elongation (fig. S11, B-D).

To characterize RALF-induced early cellular responses occurring within a few seconds after RALF treatment, we examined changes in cytoplasmic calcium of the *fer4* mutant using an aequorin-expressing*Arabidopsis* seedling as cytoplasmic calcium reporter. The RALF-induced calcium increase observed in the wild type was absent in the *fer4* mutant (**Figure A2.2C**), although a control experiment with ATP treatment showed that the *fer4* mutant fully responds to this calcium-mobilizing agonist and is thus not generally defective in the calcium response machinery (fig. S12). These results indicate that the *fer4* mutant is specifically deficient in the RALF-dependent calcium signaling system.

RALF and FERONIA are both highly expressed in the mature zone of the root during the seedling stage (fig. S13), and their mRNA expression patterns and RALF-induced root growth arrest suggest that the two proteins act by restricting cell elongation in the post-elongation zone. Consistent with this idea, transcriptome analyses after RALF treatment for 30 min revealed that the families of genes encoding proteins known to be involved in cell expansion—SAUR63 [small auxin up RNA (15)], expansin (16), and the rate-liming enzymes for biosynthesis of plant growth regulators, brassinosteroid-6-oxidase 2 (BR6OX2)

and gibberellin-3-oxidase 1—were all down-regulated (fig. S14) (17, 18). Genes associated with calcium and ethylene signaling, including calmodulin and ethylene response factors (19), were up-regulated by RALF treatment. The RALF-induced change of BR6OX2 expression was absent in the *fer4*mutant (**Figure A2.2D**).

A peptide derived from pathogenic bacterial flagellin, flg22, is sensed by the FLS2 receptor and also induces a phosphorylation change of AHA2 at Ser^{899} that coincides with apoplastic alkalinization (20, 21). An AHA2 S899D (Ser^{899}→Asp) mutant expressed in yeast demonstrated that this phosphomimetic mutation reduced growth relative to wild-type AHA2; thus, an increase in AHA2 phosphorylation at Ser^{899}after RALF treatment is predicted to down-regulate H^+-ATPase function, providing a molecular explanation for the observed RALF-induced apoplastic alkalinization (22). As a check on specificity of the RALF-FERONIA interaction, we examined the flg22 sensitivity of the *fer* mutant as well as the RALF sensitivity of the *fls2* mutant. The *fer4* mutant was insensitive to RALF but not to flg22 peptide, and the*fls2* mutant was insensitive to flg22 but not to RALF (fig. S15, A-B).We selected 17 other lines containing knockout mutations for receptor-like kinases and cell surface receptor–like proteins that are implicated in RALF signaling because they are co-regulated with RALF or are induced by RALF after 30 min of treatment (table S2). None of these other lines showed differences in RALF sensitivity of root elongation relative to the wild type (**Figure A2.2B**), and thus we conclude that the *fer4* response to RALF is specific.

The above observations suggest that FERONIA mediates RALF's inhibitory effect on root elongation by inhibiting the activity of AHA2, which secretes protons into the apoplast (23). Our model predicts that the H^+-ATPase activity is constitutively up-regulated in the *fer4* mutant; consistent with this prediction, experimental measurements showed

that *fer4* mutants acidify the bathing media faster than the wild type (**Figure A2.3A**). Moreover, in a root elongation assay in the presence of the inhibitory cation lithium, *fer4* mutant roots were hypersensitive and growth was poorer than in wild-type roots (**Figure A2.3B**). This response is a typical phenotype of mutant plants containing increased H^+-ATPase activity and a hyperpolarized plasma membrane, which causes increased uptake of the inhibitory cation into the cytoplasm (24). The effect of increased H^+-ATPase activity on root growth was examined by growing seedlings under blue light, which promotes root elongation (25). The roots of both *fer4* and *ralf* loss-of-function mutants were longer than wild-type roots (**Figure A2.3C** and fig. S16, A-D).

To test whether RALF binds to FERONIA, we performed coimmunoprecipitation of HisRALF or its inactive analog HisRALF(Δ2–8) with hemagglutinin (HA)–tagged FERONIA (FER-HA) expressed in*Nicotiana benthamiana*. FER-HA protein, with an apparent molecular mass of ~140 kD, bound HisRALF (~8 kD; **Figure A2.4, A-B**. His-RALF binding was greater than with the inactive analog by a factor of 4.5 to 6. The lack of effect of HisRALF(Δ2–8) when added together with HisRALF in root inhibition assays indicates that HisRALF(Δ2–8) lacks the ability to interact with the RALF receptor, and this was borne out by binding measurements (**Figure A2.4, A and C**, and fig. S17A). In a separate experiment with 25 nM RALF labeled with ^{125}I, we measured the binding of RALF peptide to plasma membranes isolated from wild-type or *fer4* plants in the presence or absence of an excess amount (25 μM) of nonradioactive RALF (**Figure A2.4D**). Approximately half of the iodinated RALF bound to the wild-type plasma membrane was reduced by an excess amount of nonradioactive RALF, indicating that this portion of the binding is not only specific but also saturable. In the *fer4* mutant, the saturable binding was

reduced by ~40% but not completely eliminated. The possibility that there are additional sites for RALF binding other than FERONIA in the plasma membrane of wild-type plants is supported by our observation that the *fer4* mutant is not completely insensitive to RALF at a higher concentration (5 μM) in both the root growth inhibition test and cytoplasmic calcium assay (fig. S15, D and E). Direct and specific binding of RALF to FERONIA was further confirmed with in vitro binding assays using the ectodomain of FERONIA (ectoFER) expressed as fusion proteins with either glutathione *S*-transferase (GST) or maltose binding protein (MBP) produced in*E. coli* (fig. S18, B to F). RALF specifically bound to GST-ectoFER as well as HisMBP-ectoFER; the inactive RALF analog showed little or no binding in pull-down assays with the ectoFER proteins (**Figure A2.4, E and F**).

Conclusion

Our results show that FERONIA is a receptor for RALF and that this receptor kinase mediates RALF's inhibitory effects on the cell elongation rate in *Arabidopsis* primary roots. Our demonstration that RALF is a naturally occurring ligand for FERONIA and that this kinase plays an important role in negatively regulating cell expansion provides an impetus for future work in evaluating the role that each RALF-like peptide plays in plant growth and development. The results also support the hypothesis that RALF, or another member of the 34 RALF-like peptides, is the ligand functioning in pollen tube arrest prior to fertilization.

Acknowledgements

We thank H. Burch for technical assistance; M. Ivancic for advice on mass spectrometry data analyses; R. Wrobel, B. Fox (National Institute of General Medical Sciences Protein Structure Initiative, U54 GM074901), and S. Litscher for assistance with *E. coli* expression experiments; G. Barrett-Wilt for mass spectrometric instrumentation; M. A. Beg, M. Hoffman, and O. Ginther for assistance with the iodination experiments; F. Li for advice on *Nicotiana* expression; S.-H. Su and the Plant Imaging Center for assistance with microscopy; and W. Aylward for advice on Etruscan mythology. Supported by NSF grant MCB-0929395 and U.S. Department of Energy Office of Basic Energy Sciences grant DEFG02-88ER13938 (M.R.S.), NSF grant DGE-1256259 (K.S.), and the National Human Genome Research Institute–University of Wisconsin Genomic Sciences Training Program (NIH grant 5T32HG002760, B.B.M.). Phosphoproteome data are deposited in PRIDE (Proteomics Identification Database) with accession numbers 31655 to 31656 and ProteomeXchange accession number PXD000515. Microarray data are deposited in ArrayExpress (E-MEXP-3994).

Methods (Relevant Sections)

Phosphopeptide sequencing and quantification

Phosphopeptides (8 uL) were analyzed with an LTQ Orbitrap mass spectrometer (LTQ XL, Thermo Scientific). Phosphopeptides were separated with a gradient of acetonitrile during a 240 min HPLC run using a C18 column and peptide ions were fragmented in the mass analyzer to obtain MS2 peak lists. Full description for operating the LTQ Orbitrap mass spectrometer is described in our previous report (*23*). Data file containing MS^1 and MS2 lists was searched against the *Arabidopsis thaliana* protein database (TAIR9 peptide) combined with the Arabidopsis reverse protein sequence database as a decoy (a total entry of 62, 522 sequences) using the MASCOT software (Matrix Science). The search was performed independently using both ^{14}N and ^{15}N protein masses with search parameters of fixed modification for cysteine carbamidomethylation and variable modifications for serine/threonine/tyrosine phosphorylation, methionine oxidation, asparagine/glutamine deamidation, and the amino terminal acetylation. Mass tolerance was set at 15ppm for the parent ion and 0.6 Da for fragment ions. Data was further processed to identify matching ^{14}N or ^{15}N peptide ion spectra and quantify ratios of ^{14}N phosphopeptide abundances over ^{15}N phosphopeptide abundances using Census software (*31*). In order to filter out peptides which are potentially falsely identified, a series of false discovery filters defined by the in-house script (*11*) were applied. The resultant protein identification datasets were manually compared with the above MASCOT protein identification results. Once we obtained four datasets, Experiment A (^{14}N RALF/^{15}N Control) with ^{14}N spectra search, Experiment A with ^{15}N spectra search, Experiment B (^{14}N Control/^{15}N RALF) with ^{14}N spectra search, and Experiment B with ^{15}N spectra search, the fold changes of phosphopeptide abundances were

compared to identify phosphopeptides showing RALF-treatment specific changes with a reciprocal manner. For data validation, raw mass spectra for ^{14}N or ^{15}N isotope envelopes of the peptide ions showing abundance changes were manually examined using the Qual Browser Xcalibur software (Thermo Scientific). Both, the ^{14}N and ^{15}N isotope envelops, were compared with the theoretical peptide isotope envelopes that were obtained from the ProteinProspector site (University of California, San Francisco). Whenever possible, peptide fragmentation b- and y- ion series were manually validated using the Scaffold (Proteome Software, Inc) and/or Xcalibur software.

Validation of phosphopeptide abundance changes via Selective Reaction Monitoring

The phosphopeptide-enriched samples prepared above were spiked with approximately 500 nM synthetic phosphopeptide containing heavy isotopes of ^{13}C and ^{15}N at the C-terminal Arg (Sigma). The phosphopeptides prepared above (4 uL) were separated by an on-line C18 microfluidic chip system (Eksigent) with an acetonitrile gradient of 0-35% in 0.1% formic acid during a 90 min run. Peptide parental ions and their fragment ions were selected and measured by a QTRAP5500 mass spectrometer (AB SCIEX). To quantify relative abundance of FERONIA pS858 phosphopeptide SSDVYEGNVTDsR, b4-, y7-, and phospho y7-fragment ions were monitored for peptides derived from synthetic standards and metabolically labeled ^{14}N and ^{15}N plants. Peak areas were calculated using MultiQuant software (AB SCIEX).

Figure A2.1

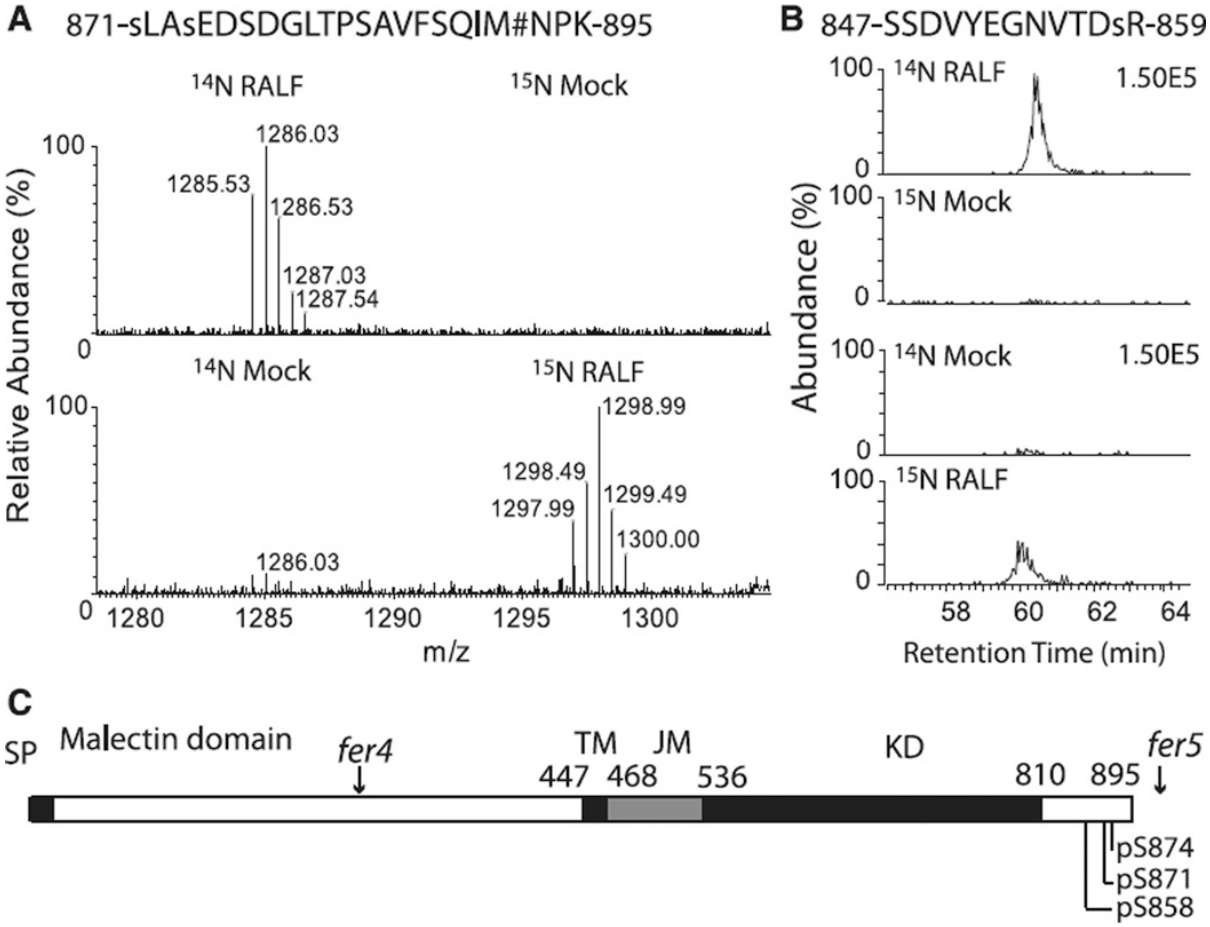

Figure A2.1. *RALF induces increased phosphorylation of FERONIA receptor kinase* **(A)** Mass spectrometric spectra showing an increased abundance of a FERONIA phosphopeptide containing pS871 and pS874 after RALF treatment. **(B)** Extracted ion chromatogram of a FERONIA phosphopeptide showing RALF-induced increase of phosphorylation at Ser858. **(C)** Structure of FERONIA receptor kinase. SP, signal peptide; TM, transmembrane domain; JM, juxtamembrane domain; KD, kinase domain. Arrows indicate the positions of T-DNA insertions in fer mutants. Abbreviations for amino acids: A, Ala; D, Asp; E, Glu; F, Phe; G, Gly; I, Ile; K, Lys; L, Leu; M#, oxidized Met; N, Asn; P, Pro; Q, Gln; R, Arg; S, Ser; T, Thr; V, Val; Y, Tyr; s, phosphorylated serine.

Figure A2.2

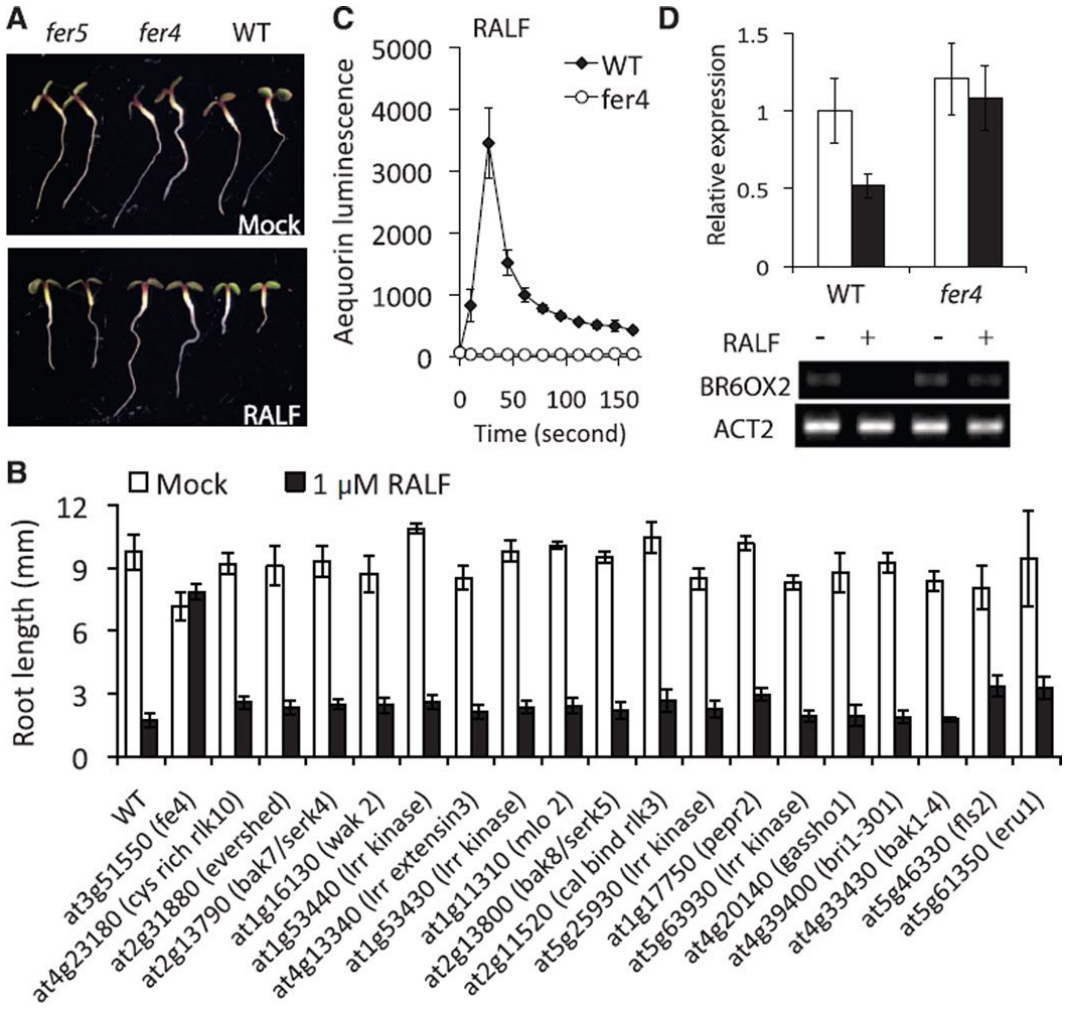

Figure A2.2. *Loss-of-function fer mutants are specifically insensitive to RALF* **(A)** The fer4 and fer5 plants show reduced sensitivity to RALF-induced root growth inhibition. Seedlings were treated with 1 μM RALF. **(B)** Insensitivity of fer mutants to RALF is specific. Mutants of 18 other receptor-like proteins respond to RALF normally. **(C)** Normal FERONIA function is required for RALF-induced cytoplasmic calcium increase. Aequorin-expressing seedlings were treated with 500 nM RALF, n=6. **(D)** RALF treatment causes a decrease of BR6OX expression in the wild type but not in the fer4 mutant. ACT2 denotes actin. Error bars in (B), (C), and (D) denote SEM

Figure A2.3

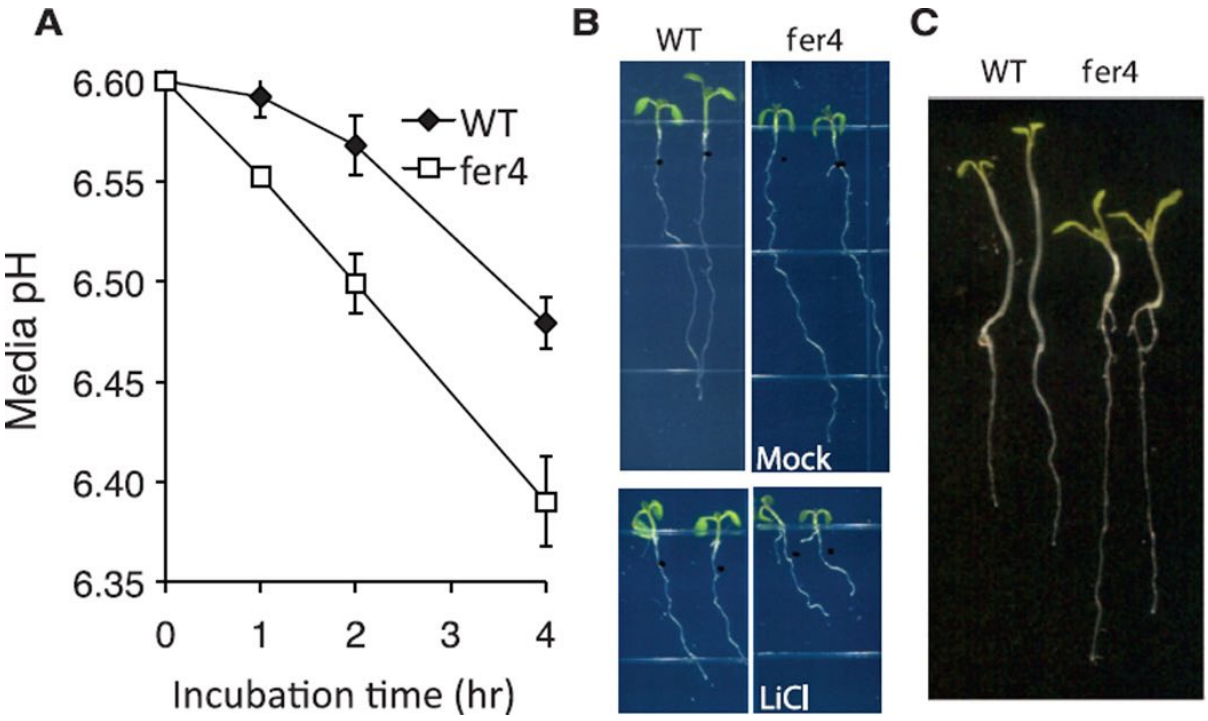

Figure A2.3 *Loss-of-function fer mutant exhibits the phenotype typical of plants with a higher plasma membrane H+-ATPase activity* **(A)** Seedlings of fer4 mutant acidify bathing media faster than the wild type (n = 7 each). Error bars denote SEM. **(B)** The fer4 root growth is hypersensitive to lithium ion stress, consistent with a hyperactive pump and a deeper membrane potential. **(C)** The fer4 mutant shows longer root length. Seedlings were grown under blue light for 7 days.

Figure A2.4

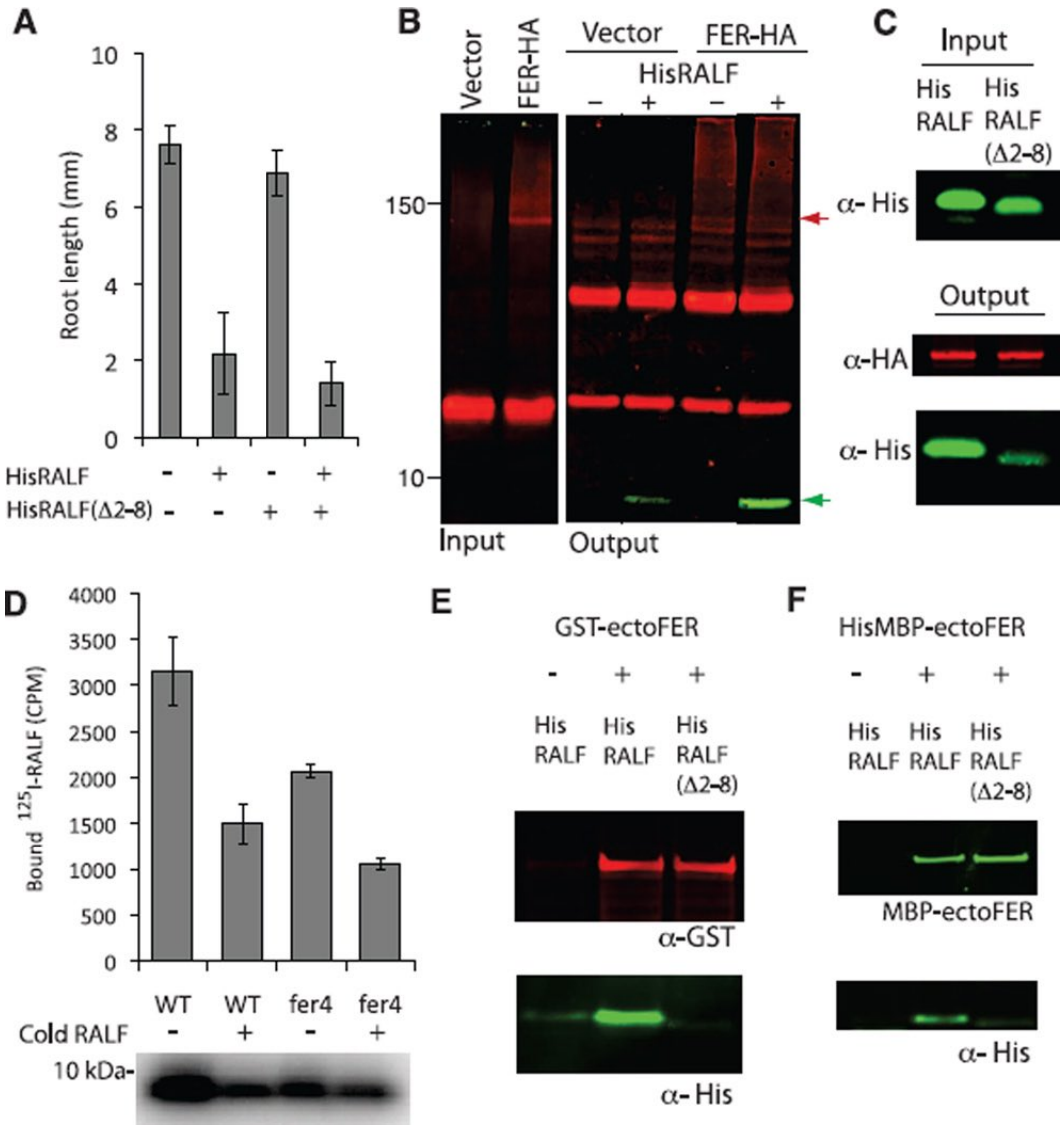
A
Root length (mm)
10
8
6
4
2
0
HisRALF - + - +
HisRALF(Δ2-8) - - + +
B
Vector
FER-HA
Vector
FER-HA
HisRALF
– + – +
150
10
Input
Output
C
Input
His RALF
His RALF (Δ2-8)
α- His
Output
α-HA
α- His
D
Bound 125I-RALF (CPM)
4000
3500
3000
2500
2000
1500
1000
500
0
WT WT fer4 fer4
Cold RALF - + - +
10 kDa-
E
GST-ectoFER
- + +
His RALF
His RALF
His RALF (Δ2-8)
α-GST
α- His
F
HisMBP-ectoFER
- + +
His RALF
His RALF
His RALF (Δ2-8)
MBP-ectoFER
α- His

Figure A2. *RALF binds to FERONIA* **(A)** HisRALF(Δ2–8) is an inactive analog of RALF and does not compete with RALF in root growth inhibition assay. Data are means ± SD (n = 6). **(B)** RALF binds to the FERONIA protein expressed in tobacco. Red arrow indicates FER-HA; green arrow indicates HisRALF. **(C)** Binding of RALF to FERONIA is sequence-specific, and binding of the inactive analog HisRALF(Δ2–8) to FERONIA is similar to background binding. Binding was immunodetected with antibodies to His tag (α-His) or HA (α-HA). **(D)** The fer4 mutant plasma membrane shows reduced saturable binding of 125I-RALF relative to the wild type. Data are means ± SE. Bound and released 125I-RALF detected in protein gel shows reduced binding in the fer4 mutant. **(E)** HisRALF, but not HisRALF (Δ2–8), binds to GST-tagged ectodomain of FERONIA receptor (GST-ectoFER). Data are representative of three experiments. **(F)** HisRALF, but not HisRALF(Δ2–8), binds to HisMBP-tagged ectodomain of FERONIA (HisMBP-ectoFER).

Figure A2.S6

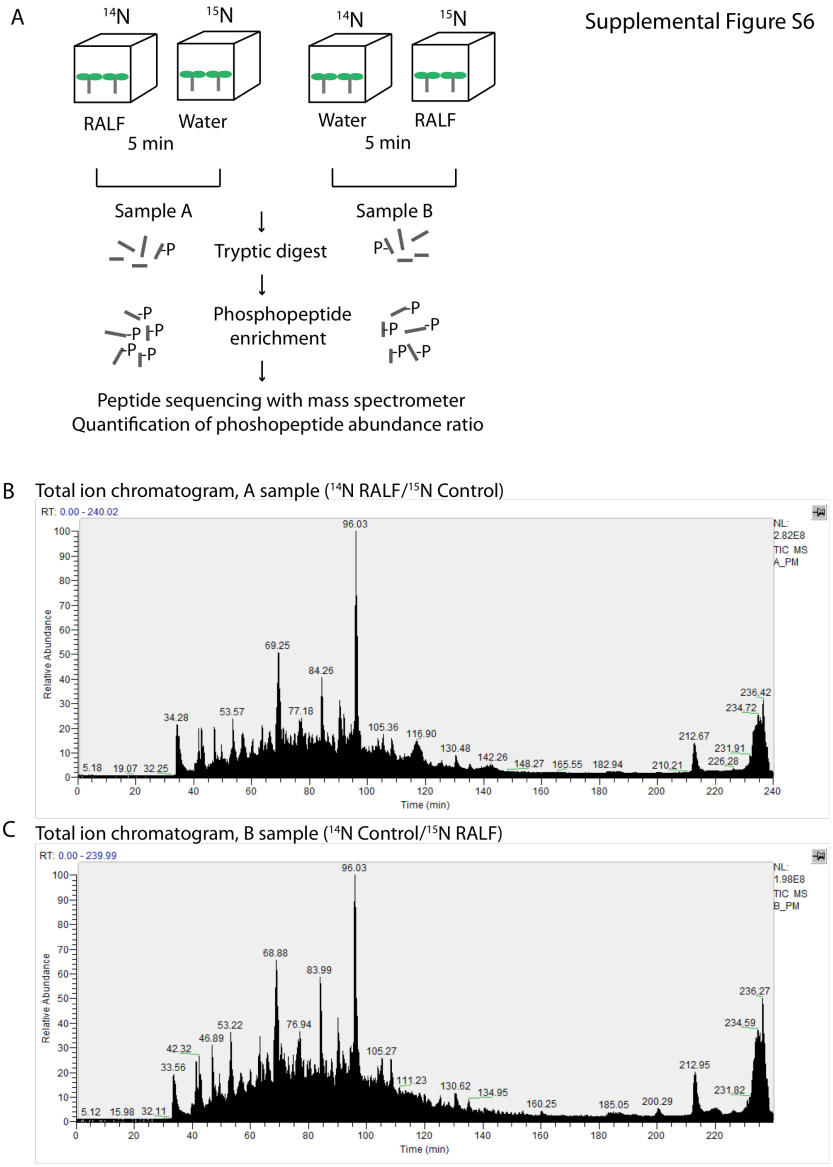
A
14N
15N
14N
15N
RALF
Water
Water
RALF
5 min
5 min
Sample A
Sample B
Tryptic digest
Phosphopeptide enrichment
Peptide sequencing with mass spectrometer
Quantification of phoshopeptide abundance ratio
Supplemental Figure S6
B Total ion chromatogram, A sample (14N RALF/15N Control)
RT: 0.00 - 240.02
NL: 2.82E8 TIC MS A_PM
Relative Abundance
Time (min)
C Total ion chromatogram, B sample (14N Control/15N RALF)
RT: 0.00 - 239.99
NL: 1.98E8 TIC MS B_PM
Relative Abundance
Time (min)

Figure A2.S6. *RALF-induced phosphoproteome and mass spectrometric analyses of phospho- enriched plasma-membrane peptides*. **(A)** RALF treatment of Arabidopsis seedlings grown in ^{14}N or ^{15}N media. Eight-day-old Arabidopsis seedlings were treated with RALF or water as a control for 5 min, and plasma membrane protein was extracted as described in the Materials and Methods section. Protein samples were trypsinized and subjected to phospho-enrichment prior to peptide sequencing and quantification via mass spectrometry. **(B)** Peptide ion chromatogram from the tissues composed of RALF-treated ^{14}N seedlings and water-treated ^{15}N seedlings. **(C)** Peptide ion chromatogram from the tissues composed of water-treated ^{14}N seedlings and RALF-treated ^{15}N seedlings.

Figure A2.S7

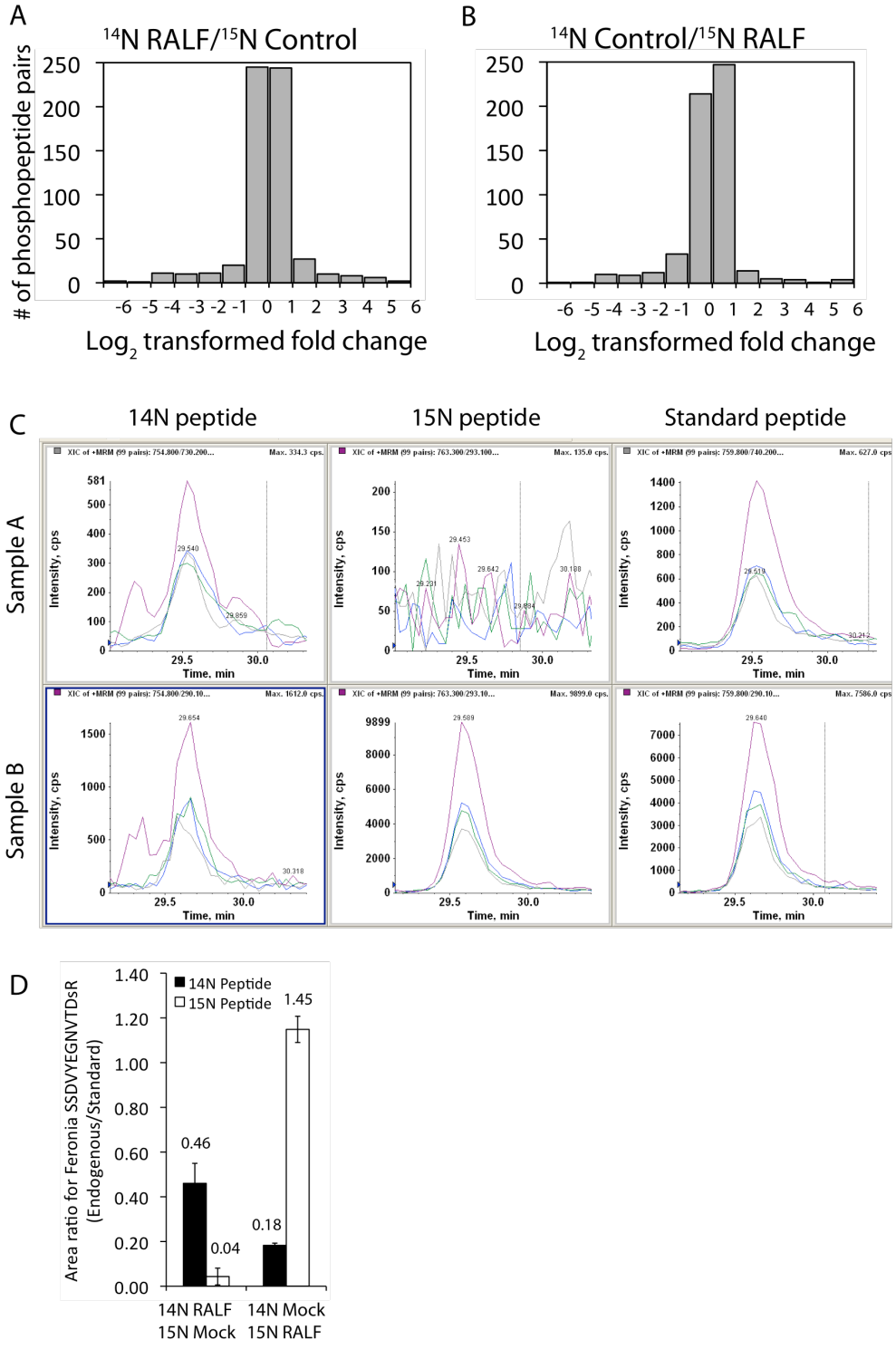
A
14N RALF/15N Control
# of phosphopeptide pairs
Log2 transformed fold change
B
14N Control/15N RALF
Log2 transformed fold change
C
14N peptide
15N peptide
Standard peptide
Sample A
Sample B
Intensity, cps
Time, min
D
14N Peptide
15N Peptide
Area ratio for Feronia SSDVYEGNVTDsR (Endogenous/Standard)
0.46
0.04
0.18
1.45
14N RALF 15N Mock
14N Mock 15N RALF

Figure A2.S7. *Phosphopeptide quantitation and RALF-induced changes of FERONIA pS858 peptide***. (A)** Histograms of peptide abundance ratio with the dataset of sample A. Approximately 550 phosphopeptide ^{14}N /^{15}N pairs were quantified. **(B)** Histograms of peptide abundance ratio with the dataset of sample B. **(C)** Selective Reaction Monitoring of FERONIA phosphopeptide containing pS858. The top panel plots are produced from Sample A (^{14}N RALF/^{15}N Control). The bottom panel plots are produced from Sample B (^{14}N Control/^{15}N RALF). Left, ion chromatogram of ^{14}N peptide (m/z, 754.8); middle, ion chromatogram of 15N peptide (m/z, 763.3; right, ion chromatogram of spike-in heavy standard peptide (m/z 759.8). **(D)** RALF- dependent increase of the pS858 phosphopeptide was observed in the both biological replicates.

References

1. Takahashi K, Hayashi K, Kinoshita T. Plant Physiol. 2012;159:632–641.

2. Kinoshita T, Shimazaki K. EMBO J. 1999;18:5548.

3. Pearce G, Moura DS, Stratmann J, Ryan CA., Jr Proc. Natl. Acad. Sci. U.S.A. 2001;98:12843–12847. 4. Haruta M, Constabel CP. Plant Physiol. 2003;131:814–823.

5. Haruta M, Monshausen G, Gilroy S, Sussman MR. Biochemistry. 2008;47:6311–6321.

6. Matos JL, Fiori CS, Silva-Filho MC, Moura DS. FEBS Lett. 2008;582:3343–3347.

7. Wu J, et al. Plant J. 2007;52:877–890.

8. Olsen JV, et al. Cell. 2006;127:635–648.

9. Pearce G, Yamaguchi Y, Munske G, Ryan CA. Peptides. 2010;31:1973–1977.

10. Kline-Jonakin KG, Barrett-Wilt GA, Sussman MR. Curr. Opin. Plant Biol. 2011;14:507–511.

11. Sanchez-Serrano JJ. Arabidopsis Protocols. New York: Springer; 2013.

12. Bertics PJ, et al. J Biol. Chem. 1988;263:3610–3617.

13. Escobar-Restrepo J-M, et al. Science. 2007;317:656–660.

14. Lindner H, Müller LM, Boisson-Dernier A, Grossniklaus U. Curr. Opin. Plant Biol. 2012;15:659–669.

15. Chae K, et al. Plant J. 2012;71:684–697.

16. Cosgrove DJ, Li ZC. Plant Physiol. 1993;103:1321–1328.

17. Nomura T, et al. J Biol. Chem. 2005;280:17873–17879.

18. Hu J, et al. Plant Cell. 2008;20:320–336.

19. Lee D, Polisensky DH, Braam J. New Phytol. 2005;165:429–444.

20. Felix G, Duran JD, Volko S, Boller T. Plant J. 1999;18:265–276.

21. Nühse TS, Bottrill AR, Jones AME, Peck SC. Plant J. 2007;51:931–940.

22. Rudashevskaya EL, Ye J, Jensen ON, Fuglsang AT, Palmgren MG. J Biol. Chem. 2012;287:4904–4913.

23. Haruta M, et al. J Biol. Chem. 2010;285:17918–17929.

24. Goossens A, de La Fuente N, Forment J, Serrano R, Portillo F. Mol. Cell. Biol. 2000;20:7654–7661.

25. Wu G, Spalding EP. Proc. Natl. Acad. Sci. U.S.A. 2007;104:18813–18818.

APPENDIX 3

Protein quantification using selective reaction monitoring for the publication: "Deletion of a Tandem Gene Family in Arabidopsis and Demonstration that Increased MEKK2 Abundance Triggers Autoimmunity when the MEKK1-MKK1/2-MPK4 Signaling Cascade is Disrupted"

The work presented in this chapter has been published:

Su, Shih-Heng, Susan M. Bush, Najia Zaman, **Kelly Stecker**, Michael R. Sussman, and Patrick Krysan. "Deletion of a tandem gene family in Arabidopsis: increased MEKK2 abundance triggers autoimmunity when the MEKK1-MKK1/2-MPK4 signaling cascade is disrupted." *The Plant Cell* 25, no. 5 (2013): 1895-1910.

Contribution:

I developed the selected reaction monitoring (SRM) assay for the targeted mass spectrometry based quantification of MEKK2 protein levels. I describe my contributions in this chapter and include relevant excerpts from the publication.

Publication Abstract

An *Arabidopsis thaliana* MAP kinase cascade composed of MEKK1, MKK1/MKK2, and MPK4 has been previously described as a negative regulator of defense response. *MEKK1* is a member of a tandemly-duplicated gene family with *MEKK2*, and *MEKK3*. Using T-DNA insertion lines, we isolated a novel deletion mutant disrupting this gene family and found it to be phenotypically wild-type, in contrast to the *mekk1* dwarf phenotype. Follow-up genetic analyses indicated that *MEKK2* is required for the *mekk1*, *mkk1 mkk2,* and *mpk4* autoimmune phenotypes. We next analyzed a T-DNA insertion in the *MEKK2* promoter and found that although it does not reduce the basal expression of *MEKK2*, it does prevent the upregulation of *MEKK2* that is observed in *mpk4* plants. This *mekk2* allele can rescue the *mpk4* autoimmune phenotype in a dosage-dependent manner. We also found that expression of constitutively active MPK4 restored *MEKK2* abundance to wild-type levels in *mekk1* mutant plants. Finally, using mass spectrometry we showed that MEKK2 protein levels mirror *MEKK2* mRNA levels. Taken together, our results indicate that activated MPK4 is responsible for regulating *MEKK2* RNA abundance. In turn, the abundance of MEKK2 appears to be under cellular surveillance such that a modest increase can trigger defense response activation.

Background for SRM method development

Quantification of a target protein is often achieved by western-blot analysis. Implementation of this strategy requires the use of an antibody that selectively binds the target protein. In the case of endogenous protein quantification, it can be challenging and expensive to successfully generate an antibody against the desired target proteins. Therefore alternate strategies for targeted protein quantification are desirable. Targeted mass spectrometry using selective reaction monitoring (SRM) is an example of an alternate strategy to western blot analysis. In this publication, SRM was used to quantify MEKK2 protein levels across four different genotypes.

Through the processes of developing a targeted SRM method for MEKK2 quantification, I encountered several challenges that are described below:

Peptide selection

It is very difficult to predict exactly how a peptide will behave in a mass spectrometer. Many *in silico* prediction tools exist for determining which peptides will be "proteotypic," meaning how well a peptide will behave in a mass spectrometer as a gas phase ions and therefore how easily it can be identified and quantified using mass spec. However, many people have found that *in silco* predictions have limited utility in accurately predicting how a peptide will behave and that peptide behavior can only really be determined empirically. I have also found this to be true in my targeted SRM work. This means that peptides for SRM analysis should be selected based on empirical evidence derived from acquired proteomic datasets.

In the case of MEKK2, however, there was no data showing detection of MEKK2 peptides in available plant proteomic datasets. Therefore I had no choice but to select

peptides based on *in silico* predictors. I found that length, acidity, hydrophobicity, and the presence of readily modified residues were important considerations for selecting tryptic peptides. It is important that selected peptides are short enough for feasible peptide synthesis (<20-25 residues), that they have a desirable 2+ charge state during ionization, and that they are neither too hydrophobic or too hydrophilic. It is also important to avoid peptides that can adopt many modification states, either through oxidation, multiple charge states, or miss-cleavage due to adjacent lysine and/or arginine residues. However, despite my efforts to select optimal peptides, I only achieved an ultimate success rate of 18% (2/11 endogenous peptides were successfully quantified). This fact reinforces the claim that empirical evidence is key for picking peptides that work in SRM analysis.

Sample prefractionation

The complexity of the entire Arabidopsis proteome can make the task of finding a few select peptides during SRM analysis seem akin to finding a needle a haystack. In order to mitigate this challenge, I found it important to implement sample fractionation prior to SRM analysis. To accomplish this goal first spiked in stable isotope labeled peptide standards into digested protein extracts, and then separated extracts using offline HPLC strong cation exchange chromatography. I then analyzed each collected fraction for the presence of standard peptides using SRM. This allowed me to determine where I would be able to find the corresponding endogenous peptides during sample analysis. In addition to orthogonal offline HPLC separation, I also tailored the online reverse-phase HPLC separation to maximize peptide detection. This means that for some sample fractions I ran a 4-hour separation gradient, as opposed to the standard 90-minute gradient. I also adjusted the steepness of the organic phase in the gradients as needed. By making use of standard

peptides, I was able to optimize LC separation and MS detection parameters to achieve the maximum signal for each target peptide. This work was done do develop a protocol that was then applied to the experimental samples.

In summery, the success of developing a SRM method for targeted protein quantification relies heavily on the ability to find peptides that behave well during mass spectrometry analysis, and this knowledge is acquired primarily through empirical data and trial and error. Making use of high-throughput, crude peptide synthesis platforms allows for more peptide standards to be purchased. The more peptides standards pursued, the higher the chance that a well-performing endogenous peptide can be identified. To streamline the process of identifying proteotypic peptides, it may be advantageous to first overexpression target proteins in *E.coli* and use digested protein extracts to determine directly which peptides perform well in a mass spectrometer.

Methods (publication excerpt)

Selective Reaction Monitoring Mass Spectrometry

Protein was extracted from the supernatant of homogenized three-week-old soil-grown seedlings using a previously described methanol/chloroform/water method (Wessel and Flüggee, 1984). Protein concentration was measured using a BCA assay kit (Thermo Scientific Pierce). Two mg of protein was reduced with 5mM DTT (45min, 50°C) and alkylated using 15mM iodoacetamide (45min, room temperature) before undergoing protease digestion. Samples were first digested with LysC (Wako Chemicals) in a 4M urea solution at a 1:50 enzyme-to-protein ratio for 3 hours at 37°C. Samples were then diluted to 1.2M urea using 50mM NH_4HCO_3 and digested with trypsin (Promega) at a 1:100 enzyme-to-protein ratio overnight at 37°C.

Samples were acidified using 0.5% FA to stop enzymatic digestion, and isotopically labeled peptides standards, synthesized by Sigma-Aldrich PEPscreen crude synthesis platform, were spiked in at known dilutions. Samples were de-salted using C-18 solid phase extraction (SPE) columns (Waters). Strong cation exchange (SCX) sample fractionation was performed using a polysulfoethyl aspartamide column (4.6 x 200mm; PolyLC) on a Waters Alliance 2795 HPLC. The gradient used for separation consisted of 0-40% buffer B [5mM KH_2PO_4, 350mM KCl, 30% ACN, (pH 2.65)] over 50 minutes at a flow rate of 1ml/min. The gradient was followed by an 80% buffer B wash and re-equilibration with buffer A [5mM KH_2PO_4, 30% ACN, (pH 2.65)]. Blanks were run between samples to ensure no carryover. Sample fractions were frozen, lyophilized, and desalted using SPE.

Peptide quantitation was performed using an Eksigent NanoLC-Ultra 2D system with cHiPLC nanoflex microfluidic C18 column (75μm, 120 Å) coupled to an AB SCIEX 5500

QTRAP mass spectrometer. SRM method development was performed using peptide standards and MRMPilot™ software (AB SCIEX). For each peptide, 3 parent ion to fragment ion transitions were monitored with a dwell time of 115msec. Analytical separation was performed using a linear gradient of 2-35% Buffer B [ACN, 0.1% FA] (Honeywell Burdick & Jackson) over 70 minutes at a flow rate of 300nL/min. Gradient was followed by a 90% buffer B wash and re-equilibration with buffer A [0.1% FA] (Honeywell Burdick & Jackson). Peak areas were integrated using the automatic MQ4 function in MultiQuant™ software (AB SCIEX). Peptide quantitation was achieved by comparing the area ratio of endogenous peptides to peptide standards within each run. For each sample, peptides were quantified from 2-4 injection replicates for three independent biological replicates. Tandem MS data acquisition was achieved using IDA methods in Analyst software (AB SCIEX). Three EPI scan were summed to generate MS/MS spectra.

Results (publication excerpt)

MEKK2 Protein Level Correlates with MEKK2 mRNA Level

The experiments described above indicate that the level of *MEKK2* mRNA is a key determinant of the autoimmune phenotypes displayed by *mekk1*, *mkk1 mkk2*, and *mpk4* mutant plants. We next wanted to determine if the relationship observed between *MEKK2* expression and plant phenotype could be extended to the protein level. For this experiment we used selective reaction monitoring (SRM) mass spectrometry to perform quantitative analysis of MEKK2 protein level in wild-type, *mekk2, mpk4, mekk2 mpk4,* and *mekk1/2/3* plants. The SRM method makes use of stable isotope-labeled peptide standards to quantitate protein abundance. Because the publically available proteomic databases contained very limited data regarding MEKK2, candidate MEKK2 peptides for SRM analysis were chosen using *in silico* predictions. For this analysis, only fully tryptic peptides with no missed cleavages were considered, and sequences containing residues prone to chemical modification during sample handling were also avoided (i.e., cysteine and methionine). All of the peptides chosen for analysis were unique to the MEKK2 protein based on the current annotation of the Arabidopsis genome.

We produced a list of 11 candidate peptides, obtained heavy-labeled synthetic versions of each, and performed a pilot experiment to determine if any of the corresponding MEKK2 endogenous peptides could be detected in Arabidopsis total-protein extracts. For this analysis, digested protein extracts were spiked with heavy-labeled MEKK2 peptide standards and prefractionated offline using strong cation exchange chromatography (SCX). SCX fractions were then analyzed independently using online nanoflow reverse-phase chromatography coupled to an AB SCIEX QTRAP 5500 triple quadrupole mass spectrometer. From this analysis we found that two of the MEKK2 peptides, corresponding

to amino acids 150 to 156 and 326 to 336, were reproducibly detectable in the wild-type, *mekk2, mpk4,* and *mekk2 mpk4* samples. As a negative control we also analyzed *mekk1/2/3* protein extracts and found, as expected, that both of these endogenous peptides were absent, consistent with the facts that the *MEKK2* gene is deleted in this genotype and these peptides are unique to MEKK2. The extracted ion chromatograms for the standard and endogenous peptides displayed the same transition patterns, indicating no interference from isobaric peptides (**Figure A3.1** and Supplemental Figure 6 [**Figure A3.2]**). Additionally, tandem mass spectrometry was used to confirm the peptide identities (Supplemental figure 7 [**Figure A3.3]**).

To quantify the relative abundance of MEKK2 protein, we measured the peak areas of the extracted ion chromatograms for each endogenous peptide as well as the corresponding heavy-labeled standard present in each sample. Three independent biological replicates were performed for each genotype, and peptide abundance was normalized to the average value observed for wild-type (**Figure A3.1**). The level of MEKK2 protein predicted from peptide abundance is 4- to 5-fold higher in *mpk4* dwarf plants when compared to wild-type, whereas the phenotypically wild-type *mekk2 mpk4* plants have an MEKK2 protein level that is not significantly different from wild-type. These results demonstrate that MEKK2 protein levels reflect *MEKK2* mRNA levels, and that the autoimmune phenotype correlates with elevated MEKK2 protein abundance.

Discussion (publication excerpt)

It has been established that mRNA and protein levels do not always correlate with each other for a given gene in a given population of cells (Greenbaum et al., 2003). For this reason, we used selective reaction monitoring (SRM), a highly sensitive mass spectrometry-based method, to directly quantitate the level of MEKK2 protein in our samples. Heavy-isotope labeled peptide standards were synthesized that corresponded to tryptic peptides predicted to be unique to MEKK2 in Arabidopsis based on an *in silico* analysis. By spiking known amounts of these labeled peptides into our samples we were able to obtain quantitative measures of the abundance of MEKK2 protein in plant total protein extracts from the various genotypes. Because MEKK2 is a relatively low-abundance protein, HPLC fractionation of the total protein extracts using SCX chromatography was implemented as an orthogonal separation technique to improve the sensitivity of detection. The high selectivity of SRM data acquisition allowed us to reproducibly identify and quantitate MEKK2, a protein that has otherwise been largely undetected in proteomic datasets. The results obtained from this analysis demonstrated that the relative levels of MEKK2 protein present in the various genotypes agreed with the levels of mRNA determined by RT-PCR. *mpk4* dwarf plants had the highest MEKK2 protein level, and the rescued *mekk2 mpk4* plants had MEKK2 level similar to that of *mekk2* and wild-type.

Figure A3.1

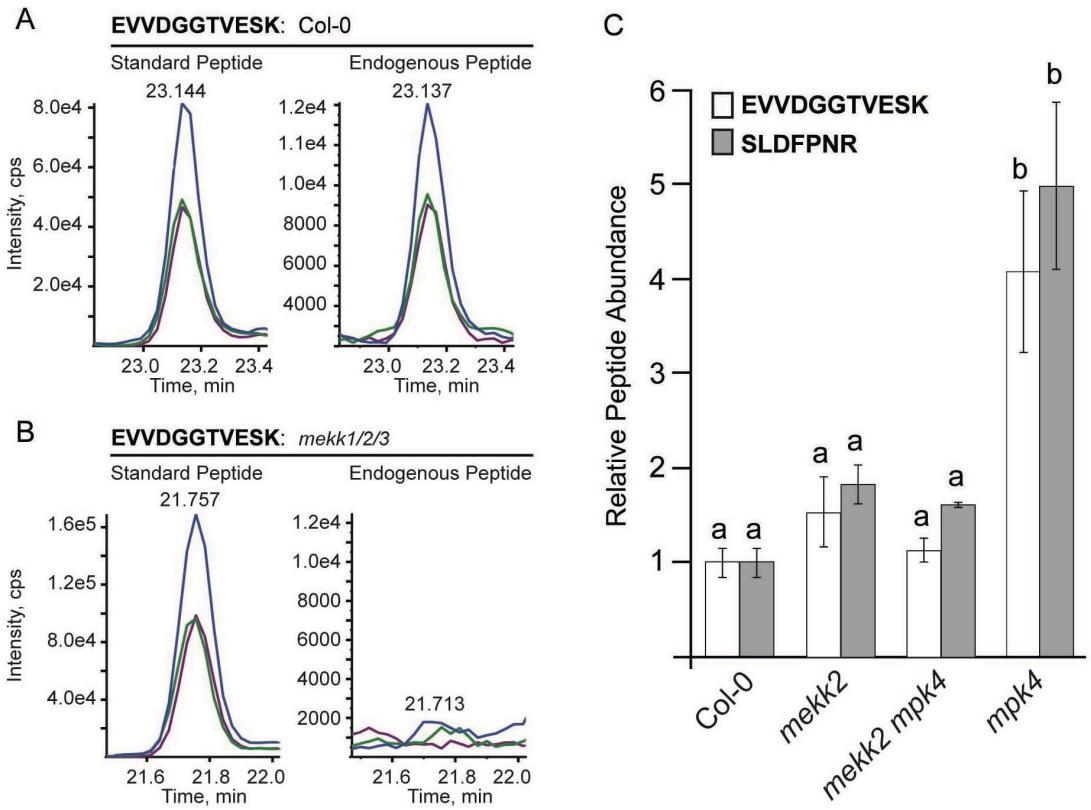
A
EVVDGGTVESK: Col-0
Standard Peptide
Endogenous Peptide
23.144
23.137
Intensity, cps
Time, min
B
EVVDGGTVESK: mekk1/2/3
Standard Peptide
Endogenous Peptide
21.757
21.713
Intensity, cps
Time, min
C
EVVDGGTVESK
SLDFPNR
Relative Peptide Abundance
Col-0
mekk2
mekk2 mpk4
mpk4

Figure A3.1. *MEKK2 Protein Abundance as Determined by SRM Mass Spectrometry*.
(A) Extracted ion chromatograms (XICs) for MEKK2 peptide EVVDGGTVESK. Three parent-ion to fragment-ion transitions were monitored for this peptide: y7 is represented by the purple trace, y8 by blue, and y9 by green. Only the strongest transition, y8, was used for quantification. The left panel displays XIC for the isotope-labeled peptide standard, while the right trace shows XIC for the endogenous peptide extracted from wild-type plants. The standard and endogenous peptides assayed in the same run have the same retention times and patterns of relative fragment ion intensity.
(B) XIC for protein extracted from *mekk1/2/3* plants as a negative control. No endogenous MEKK2 peptide was observed.
(C) The abundance of the indicated MEKK2 peptides is presented relative to their levels in wild-type Col-0. For each genotype, the abundance of the peptide was first determined relative to the isotope-labeled internal standard peptide. These values were then normalized to the average value obtained for wild-type Col-0. Three independent biological replicates were measured for each genotype, and each biological replicate was analyzed using two to four injection replicates.XICs for the SLDFPNR peptide are presented in **Figure A3.2**. ANOVA was performed separately for each peptide followed by Tukey's post-hoc analysis ($\alpha = 0.05$). Means not sharing the same letter are significantly different.

Figure A3.2

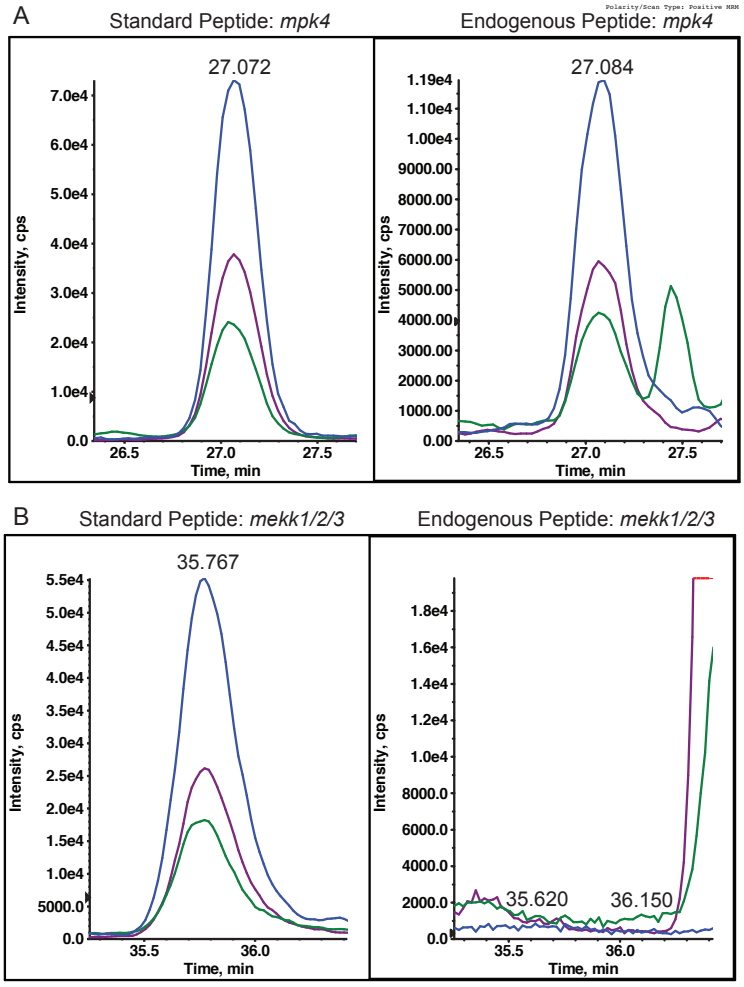

Supplemental Figure 6. Quantitation of the *MEKK2* Peptide SLDFPNR by Selective Reaction Monitoring Mass Spectrometry.

(A) Extracted ion chromatograms (XIC) for the MEKK2 peptide SLDFPNR. Three parent-ion to fragment-ion transitions were monitored for this peptide, y5 represented by the blue trace, y4 by purple, and y3 by green. Only the strongest transition, y5, was used for quantitation. Left panel displays XIC for the isotope-labeled peptide standard, and the right trace shows XIC for the endogenous peptide extracted from *mpk4* plants. The standard and endogenous peptides assayed in the same run have the same retention times and patterns of relative fragment ion intensity. **(B)** XIC for protein extracted from *mekk1/2/3* plants as a negative control. No endogenous MEKK2 peptide was observed.

Figure A3.3

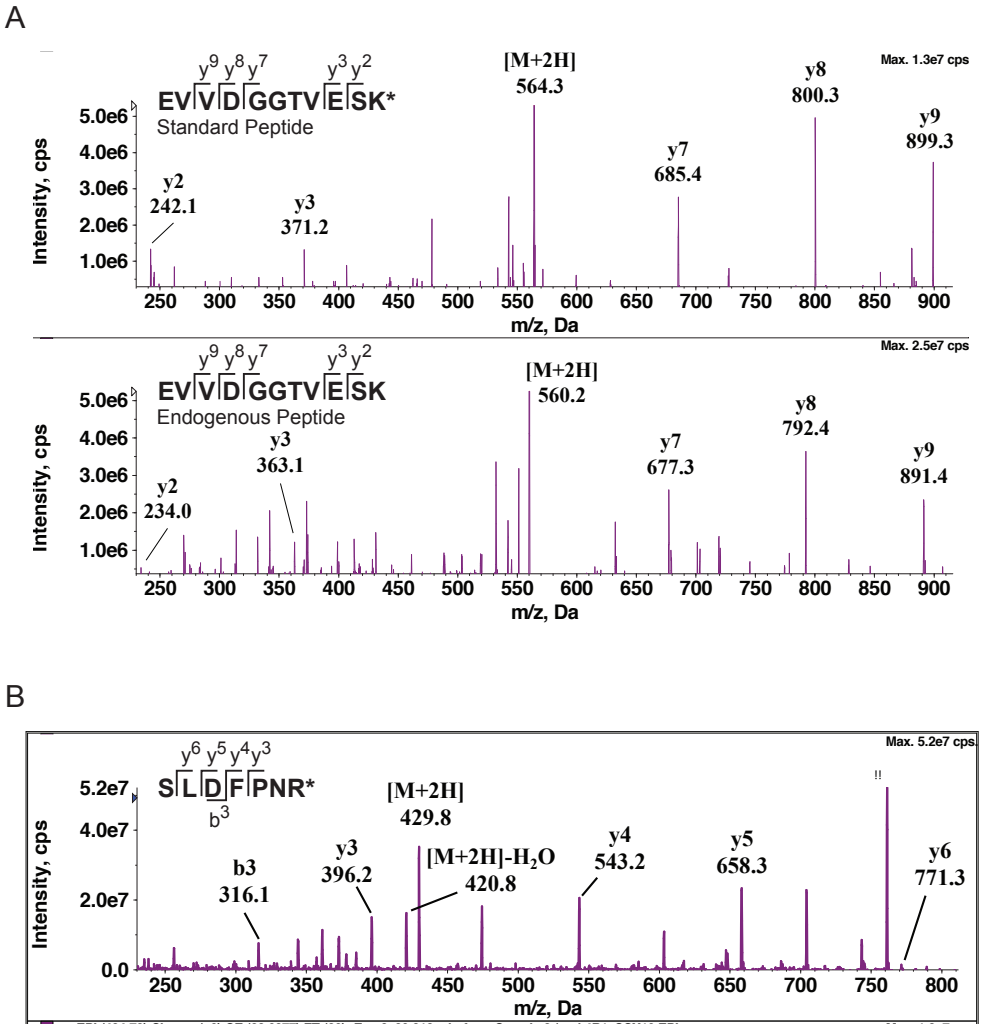

Supplemental Figure 7. Tandem Mass Spectrometry Analysis to Confirm the Identities of the MEKK2 Peptides.

(A) Tandem MS data for the EVVDGGTVESK peptide. The isotope-labeled standard is shown in the upper panel and the endogenous peptide in the lower. The standard is 8 Da heavier than the endogenous peptide. **(B)** Tandem mass spectrometry analysis of the SLDFPNR standard peptide. The standard is 10 Da heavier than the endogenous peptide. Good quality tandem MS data was not achieved for the endogenous SLDFPNR peptide because of co-eluting, contaminant spectra. When using the third quadrupole as a linear ion for tandem MS data acquisition, mass filtering capabilities can not reach those of SRM methods.